Effects of distribution of excitation energy transfer times and protein dynamics on spectral hole burning in pigment-protein complexes involved in photosynthesis

Nicoleta Herascu

A Thesis
In the Department
Of Physics

Presented in Partial Fulfillment of the Requirements
For the Degree of
Doctor of Philosophy (Physics) at
Concordia University
Montreal, Quebec, Canada

September 2013

CONCORDIA UNIVERSITY

SCHOOL OF GRADUATE STUDIES

This is to certify that the thesis prepared

By: **Nicoleta Herascu**

Entitled: **Effects of distribution of excitation energy transfer times and protein dynamics on spectral hole burning in pigment-protein complexes involved in photosynthesis**

and submitted in partial fulfillment of the requirements for the degree of

DOCTOR OF PHILOSOPHY (Physics)

complies with the regulations of the University and meets the accepted standards with respect to originality and quality.

Signed by the final examining committee:

_____ Chair
Dr. J. Kornblatt

_____ External Examiner
Dr. P. Juneau

_____ External to Program
Dr. J. Capobianco

_____ Examiner
Dr. L. Kalman

_____ Examiner
Dr. A. Champagne

_____ Thesis Supervisor
Dr. V. Zazubovits

Approved by _____
Dr. L. Kalman, Graduate Program Director

September 11, 2013

_____
Professor J. Locke, Interim Dean
Faculty of Arts and Science

ABSTRACT

Effects of distribution of excitation energy transfer times and protein dynamics on spectral hole burning in pigment-protein complexes involved in photosynthesis

Nicoleta Herascu, PhD

CONCORDIA UNIVERSITY, 2013

Understanding the spectral properties of natural photosynthetic complexes (the excited state lifetimes, electron-phonon couplings, distributions of "solvent shifts" of various pigments, and the interactions between them (manifestations of excitonic effects, excitation energy transfer, charge transfer) as well as pigments site energies, lowest-energy states and origin of various emission bands) is fundamental to advance the design of the artificial photosynthetic systems. Traditionally the spectral properties of natural photosynthetic complexes are explored by either time-domain or frequency-domain high-resolution spectroscopy methods, including non-photochemical spectral hole burning (NPHB).

The main goal of this thesis was the study of various effects of the distribution of excitation energy transfer times and protein dynamics on non-photochemical hole burning processes in photosynthetic pigment-protein complexes. In the first part of this

thesis we present our results concerning the inclusion of the distributions of excitation energy transfer (EET) rates (homogeneous line widths) and charge separation rates into treatment of the resonant and non-resonant NPHB processes in photosynthetic chlorophyll-protein complexes. Thus, the effects of the line width distributions resulting from Förster-type EET between weakly interacting pigments with uncorrelated site distribution functions, on the resonant NPHB process have been explored both theoretically and experimentally in isolated CP43 antenna from spinach. Furthermore, we have also demonstrated that inclusion of the effects of frequency-dependent EET rate distributions and burning following EET on the treatment of non-resonant NPHB spectra of trimeric Fenna-Matthews-Olson protein from *Chlorobium tepidum* leads to reasonable agreement between the theoretical and experimental data.

The second part of this thesis is focused on the analysis of HB spectral properties of the lowest energy states of Photosystem I (PSI) with the aims to gain better understanding of particular structural origins of these states as well as on the protein dynamics of PSI. We explored the satellite hole structures obtained after illumination at various wavelengths and the dependence of those structures on thermocycling. In order to explore the protein dynamics in PSI SHB experiments and compare it with SPCS observations special attention was devoted to the study of the influence of the P700 redox state on resonant and nonresonant NPHB spectra from cyanobacteria *Thermosynechococcus elongatus*.

ACKNOWLEDGEMENTS

I would like to thank my supervisor Prof. Valter Zazubovits for his guidance and support without which this thesis would not exist. I always appreciate his enthusiasm on approaching new and difficult scientific ideas. He has proven me many times how a difficulty can be seen as a great opportunity. I also thank him for his encouragements and help to attend several prestigious conferences and I would like to express my gratitude for introducing me to the distinguished photosynthesis scientific community.

I am very grateful to our group's collaborators for their constant and generous help with samples and scientific discussions. I thank them and my supervisor Prof. Valter Zazubovits for the great work they did on theoretical modeling and software development. I was very fortunate to benefit tremendously from this work.

I would like to thank to all of those who encouraged and helped me during the completion of this PhD degree. My special thanks to Prof. Laszlo Kalman for keeping me focused and motivated on this thesis.

I must also acknowledge Concordia University and NSERC for all the financial support provided during this PhD program.

Table of Contents

List of tables:

List of figures:

Figure 4. Structure of the photosynthetic apparatus including the light-harvesting antenna complexes in green sulphur bacteria. Reprinted with permission from ref. 33 Copyright (2007) National Academy of Sciences, USA.

Figure 5. The "special pair" and other cofactors in the PSI-RC from cyanobacteria *Thermosynechococcus elongatus*. The labels A and B refer to the two branches of the electron transfer chain. The QX (X=A or B) and F_Y (Y = X or A or B) indicate the quinone and iron-sulfur clusters. Reprinted by permission from Macmillan Publishers Ltd: Nature, ref. 29, copyright (2001).

Figure 6. **Frame A** cofactors of PSII from cyanobacteria *Thermosynechococcus elongatus*. The labels D1 and D2 refer to the two branches of the RC. Electron transfer occurs along the D1-branch. Also shown are the Mn_4Ca cluster and cytochrome c-550 Reprinted by permission from Macmillan Publishers Ltd: Nature, ref. 35, copyright (2005) **Frame B** The RC cofactors from purple bacteria *Rb. Sphaeroides*. Q_A and Q_B are immobile and mobile quinones, respectively. Arrows indicate the pathway of electron transfer. Reprinted from ref.39, Copyright (2002), with permission from Elsevier

Figure 7. Spectra of the impurity centers in a crystalline matrix (left) and amorphous matrix (right).

Figure 8. Spectral line shape of an impurity center in a solid matrix at low temperature. Γ_{hom} is the homogeneous line width, and ω_m is the mean phonon frequency. Reprinted with permission from ref.7. Copyright (2011) American Chemical Society.

Figure 9. Features of the single impurity spectral line (zero-phonon line and phonon side-band) depending on the strength of electron-phonon coupling. Reprinted with permission from ref.7. Copyright (2011) American Chemical Society.

Figure 10. Two-Level System model; where the barriers height in the ground and excited states are V_{grd} and V_{ex}; displacement between the two potential minima is denoted by d; the asymmetry of the TLS is Δ and hν is the excitation energy of the chromophore initially found in conformation A of the ground state. The tunneling frequency is $W=\omega_0 exp(-\lambda)$. Reprinted with permission from ref.7. Copyright (2011) American Chemical Society.

Figure 11. The spectral - hole profile (SDF is Site Distribution Function with Γ_{inh} being the inhomogeneous width, γ is the homogeneous width and 2γ is the hole width. Width is defined here and everywhere else within this thesis as the Full Width at Half Maximum, FWHM). Reprinted with permission from ref.7. Copyright (2011) American Chemical Society.

Figure 12. NPHB mechanisms accounting for two different hierarchical tiers on the energy landscape. Adapted with permission from ref. 66. Copyright (2012) American Chemical Society.

Figure 13. (A) HGK curve (noisy black curve) and its fit (red) for CP43 at 686.8 nm. (B) HGK curve (noisy black curve) and its fit (red) for CP29 at 681.7 nm. (C) HGK curve (noisy black curve) and its fit (red) for monomeric LHCII at 683.1 nm. (D) HGK curve (noisy black curve) and its fit (red) for trimeric LHCII at 684.2 nm. Reprinted with permission from ref.71. Copyright (2011) American Chemical Society.

Figure 14. HGK curves for 5, 6, 7, 8, 10, and 13 K. The smooth curves are the fits to HGK curves. The parameters of the Gaussian λ-distribution obtained from the fit to 5K HGK curve are $\lambda_0=10.2\pm0.1$, $\sigma_\lambda=1.1\pm0.1$, with $S=0.35\pm0.05$. The insert depicts the absorption spectrum of CP43 (black) with the site distribution function of the A-band

(red) and the B-band (blue). The down arrow indicates the burn wavelength. Reprinted with permission from ref.66. Copyright (2012) American Chemical Society.

Figure 15. Hole-recovery data for 21%-deep hole, noisy curve and circles. Smooth solid curve (good fit to experimental data) results from modeling in Gaussian λ-distribution framework (see Fig. 16A), while dashed curve results from modeling in uniform λ-distribution framework (see Fig. 16B). The insert represents a sample hole spectrum (ref. 15, 66, 71). The datapoints presented as circles are result of averaging of about 40 points of the raw data. The size of the symbols is approximately equal to the size of potential error bar, ~0.02.

Figure 16. (A) Calculated excited-state partial λ-distributions for Gaussian true full λ-distributions (black: 20% deep hole, a; blue: 55% deep hole, b). Areas under curves are normalized to 1. The red (c) and green (d) curves are integrals of the black and blue curves, respectively. The magenta curve (e) is the difference between these integrals. The dashed curve is the true full λ-distribution. (B) Same for the uniform λ-distribution. Reprinted with permission from ref.66. Copyright (2012) American Chemical Society.

Figure 17. **Frame A:** Indistinguishable HGK curves for different combinations of λ-distribution and line width distribution parameters (see below). **Frame B:** Easily distinguishable hole width dependences on the hole depth for the same parameters as in frame A. Red curve: line width distribution peaking at 3.0 cm^{-1} with fwhm = 3.0 cm^{-1}, λ_0= 10.0, and σ_λ = 1.0. Green: line width distribution peaking at 2.5 cm^{-1} with fwhm =2.1 cm^{-1}, λ_0 = 10.15, and σ_λ = 1.0. Black: line width distribution peaking at 2.0 cm^{-1} with fwhm = 1.3 cm^{-1}, λ_0 = 10.2, and σ_λ = 1.0. Blue: single line width 1.5 cm^{-1}, λ_0 = 10.5, and σ_λ = 1.0. Reprinted with permission from ref.60. Copyright (2011) American Chemical Society.

Figure 18A: Total SDF and sub-SDF in the case of two pigments with identical SDF. Blue curve is the absorption spectrum of a molecule with ZPL relatively low in energy, which is excited at higher energy via its phonon sideband or vibronic replicas. **Figure 18B:** the full SDF of three identical pigments with FMO 825 nm band parameters and three sub-SDF corresponding to the lowest-energy pigments (e), pigments with one donor and one acceptor (f) and highest-energy, two-acceptor pigments (d). Zero corresponds to 12116 cm^{-1}.

Figure 19. Example of sub-SDF for different EET rates for one-donor-one-acceptor pigments (V=3 cm^{-1}, the width SDF is 65 cm^{-1} and the SDF peak position: 12116 cm^{-1}). "ZPL width" includes only EET contribution to the width; pure dephasing and width corresponding to fluorescence lifetime are not included.

Figure 20. Dependence of the probability of EET on donor-acceptor ZPL gap for different values of inter-pigment coupling (where the probability functions for V=1cm^{-1}, V=5cm^{-1} and V=10cm^{-1} are the black, blue and red curve respectively; the green curve is the probability function resembling the step function of Jankowiak et al); all single-site spectrum parameters from FMO.

Figure 21. HB spectra taking EET into account to different degrees. V=3 cm^{-1} and no anti-hole was considered; the illumination dose was same in all three cases, The green curve has been obtained with SHB model that included the EET rate distributions at burn wavelength and no burning via EET, [60]; the black curve has been calculated including only wavelength dependent EET rate distribution; the blue curve has been calculated considering both the wavelength dependent EET rate distribution and burning via EET.

Figure 22. Blue: the result of convolution of two single-site spectra; with the width of the (truncated) peak being much smaller than the height. Black: corrected ZPL-ZPL contribution to spectral overlap (or line width) dependence on donor-acceptor gap. Red: Lorentzian function with same width and peak magnitude, for comparison.

Figure 23. The structure of the core antenna complex CP43. The increased spacing between luminal and stromal parts of the complex is introduced for clarity; note that Chl 46 (notation by Loll, ref. 93), located somewhat in between lumenal and stromal groups of pigments, is shown twice (pink). Reprinted with permission from ref.142. Copyright (2008) American Chemical Society.

Figure 24A The absorption spectrum of CP43 as well as the SDFs of the lowest-energy states according to various models discussed in the text (Reprinted with permission from ref.60. Copyright (2011) American Chemical Society. **Figure 24B.** The Q_y absorption band of CP43 at different temperatures (Reprinted from ref. 150, Copyright (1999), with permission from Elsevier); the lowest-energy band peaked at ~ 683-nm is clearly resolved only in spectra measured at liquid nitrogen and helium temperatures ($T < 77$ K).

Figure 25. Spectral overlap dependence on the ZPL-ZPL energy gap (black curve) for the single site spectra parameters in Table 2, two SDFs (solid red and blue curves), and deconvolution of those SDFs into sub-SDFs of fractions capable (dashed line) or incapable (dotted line) of EET. The dash-dotted green curve is the overlap integral dependence on energy gap according to Kolaczkowski et al, [133].Vertical solid arrows indicate contributions to the overlap from localized vibrations; the dashed arrow indicates minimal overlap. The dotted arrow indicates maximal overlap within the range of Fig.26. Reprinted with permission from ref. 60. Copyright (2011) American Chemical Society.

Figure 26. Overlap distributions (lower scale) and homogeneous line width distributions with V_{AB} = 5 cm^{-1} for EET between two bands with the SDFs resembling those of the two lowest-energy states of the CP43 complex (the inset contains its absorption spectrum and two SDFs). The blue curve is the distribution for A→B EET for λ_B = 680 nm, while the red curve is the distribution for B→A EET. The horizontal dashed arrow indicates the ~20% contribution of B-type pigments incapable of EET at λ_B. Reprinted with permission from ref. 60 . Copyright (2011) American Chemical Society.

N.B: Homogeneous line width reported in the figure does not include pure dephasing contribution (e.g, 1 GHz or 0.033 cm^{-1} at 5 K, [101]).

Figure 27. Left frame - Experimental dependence of the hole width on hole depth for λ_B = 680.15 nm. Black diamonds: high-resolution data. Blue diamonds: low-resolution data, corrected for the spectrometer resolution. The solid curve is the theoretical dependence for V_{AB}=5cm^{-1}, and the dashed curve is the theoretical dependence for V_{AB} =10 cm^{-1}. The dotted curve was obtained in the absence of the line width distribution.

Right frame –The dependence of the hole width on hole depth corrected for contribution of states other than A and B at λ_B = 680.15 nm.

Figure 28. Frame A - The locations of BChl molecules in a FMO monomer (Adapted from ref.32, Copyright (2006), with permission from Elsevier). The pigments within one selected monomer are highlighted, the pigments of other two monomers are presented as fainter shapes. **Frame B** - The low temperature absorption spectra of FMO protein. Dashed black curve: fit to the 825 nm band absorption (see text). Blue solid curve: emission spectrum measured for the same sample as absorption. Dashed blue curve: emission spectrum predicted assuming that emission origin coincides with the full 825

nm band SDF (i.e., there is no intra-825 nm-band, inter-monomer, EET). Insert shows the entire Q_y absorption band of *C. tepidum* FMO complex.

Figure 29A: Holes burnt at 821.0 (magenta), 823.0 (green), 825.0 (red), 826.5 (dark blue) and 828.4 (black) nm with a fluence of about 120 J/cm^2. Light-blue curve is the inverted full SDF of the 825 nm band. **Figure 29B:** Non-resonant holes produced by illumination at 814 nm with varying fluence. Smooth dark green curve represents the theoretical non-resonant hole in the presence of EET and the absence of an anti-hole.

Figure 30A. Emission origin calculated in trimeric model with slow EET: Black: total SDF of the 825 nm band of FMO, emission origin in case inter-monomer coupling is zero. Light green: $|V|=0.1$ cm^{-1}, Light blue: $V=0.5$ cm^{-1}, Red: $V=1.0$ cm^{-1}; Magenta: $V=2.0$ cm^{-1}; Blue: curve (e) from Figure 18B, valid for $V=3.0$ cm^{-1} and above. **Figure 30B:** best fit (red) to the FMO 5K emission spectrum (blue), $V=1.2$ cm^{-1}.

Figure 31A: ΔAbsorption of non-resonantly burned molecules and anti-holes (solid black curves) and their sum (dashed red curve) compared to a representative HB spectrum (blue) in the absence of EET. Non-resonantly burned spectra for other fluences are presented in grey. **Figure 31B:** Similar spectra as frame A, but in the presence of EET.

Figure 32A: Hole burnt at 821 nm and modeling results in the absence of EET and aberage blue shift of the anti-hole of 10 cm^{-1}. Red curve: perfect spectral memory [139], blue curve: no spectral memory. **Figure 32B:** Same hole and modeling results for two irradiation doses in the presence of EET. The small ~10 cm^{-1} shifts are not included, as it was assumed that their contribution is small when spectral memory in present (see red

curve in frame A). We did not attempt to simulate the higher-energy satellite hole at 816 nm.

Figure 33. The shift probability distributions for the middle (one donor and one acceptor) and higher (two acceptors) excitonic states of the trimer with identical FMO-like SDF parameters. **Frame A -** The NPHB shift of the lowest-energy pigment was assumed to be 10 cm^{-1} to the blue, and coupling V= 3 cm^{-1}. **Frame B** - The NPHB shift of the lowest-energy pigment was assumed to be 60 cm^{-1} to the blue and coupling V=1.5cm^{-1}. Courtesy of Stephanie Larocque.

Figure 34. The diagram of the two different charge separation pathways in the PSII RC from spinach. Reprinted with permission from ref. 88. Copyright (2010) American Chemical Society

Figure 35. The absorption spectrum of the isolated PSII RC complex. The arrows indicate the burn wavelengths of 680 and 686 nm, the latter within a weak shoulder at ~684 nm, Reprinted with permission from ref. 60. Copyright (2011) American Chemical Society.

Figure 36. Persistent hole depth versus irradiation dose data for λ_B = 686 nm. The noisy curves are HGK curves; symbols refer to data extracted from the hole spectra. The numbers refer to the intensity (in mW/cm^2) used to obtain the data.

The fastest two HGKs (red and magenta) were obtained in fluorescence excitation mode. Also presented is the best fit (solid black line) to the lowest-intensity transmission mode data (noisy green curve + open circles). See the text for line width distribution details, Reprinted with permission from ref. 60 . Copyright (2011) American Chemical Society

Figure 37. Experimental persistent hole width vs depth data (open and solid circles represent two complementary data sets) for λ_B = 686 nm and theoretical fits with the same distribution as in figure 36 (solid curve), with the distribution from ref 87 (dashed curve) and without any line width distribution (dotted curve). The solid triangles represent the experimental data obtained at 680 nm. The data was obtained at high resolution (~30 MHz) with 4 cm^{-1} scan range. Therefore, errors do not exceed the size of the symbols Reprinted with permission from ref. 60. Copyright (2011) American Chemical Society

Figure 38. Absorbance difference vs. burn fluence (Figure 11 Reprinted with permission from ref. 172. Copyright (2004) American Chemical Society and fractional hole depth vs. burn fluence (our data) for PSII core (RC+CP43+CP47) from spinach in $S_1(QA^-)$ at T= 2.5 K and 5 K, respectively. Black line, triangles, and circles: HGK in PSII core from spinach, in $S_1(QA^-)$ state, Red line and diamonds: HGK curve obtained at T= 5K and λ_B = 686 nm in CP43 (our data); Green: fit to HGK curve measured in transmission at the lowest intensity, T= 5K, λ_B = 686 nm; isolated PS II RC (our data).

Figure 39. Structural arrangement of the cofactors in the reaction center of Photosystem I, where P_A and P_B designate the two components of the special pair (primary electron donor, P700); A_0 refers to the primary electron acceptor (Chl a) and A_1 is the phylloquinone (PhQ_A); the terminal electron acceptors are three iron-sulfur clusters Fx, F_A and F_B,. Adapted from ref. 174, Copyright (2002), with permission from Elsevier

Figure 40. Red chlorophyll assignment in PSI from cyanobacteria where in the notation of Krauß et all chlorophylls B31, B32 and B33 are referred to as trimer **a**. The dimers **b, c** and **d** are made up of chlorophylls A32/ B7, A38/A39 and B37/B38 (from ref. 175, 177,

180). The three-fold axis of symmetry is perpendicular to the page and located above the top view of PSI. Adapted with permission from ref. 180. Copyright (2002) American Chemical Society

Figure 41. 5 K fluorescence spectra of PS I trimers from *T. elongatus* with P700 in the reduced (solid line), oxidized (dashed line) and mixture of reduced-oxidized state (dash–dotted line). Reprinted from ref. 181, Copyright (Year), with permission from Elsevier

Figure 42. The low-temperature (5 K) absorption and non-resonant hole structures for PSI from *T. elongatus* (frame A) and *Synechocystis PCC 6803* (frame B). Hole spectra are labeled (to the right) with illumination wavelengths

Figure 43. 5 K fluorescence spectrum of mostly reduced sample B. Comparison with figure 41 (from [181]) above shows that while the sample mostly has P700 in reduced state (hence the peak at 741 nm, solid arrow) some contribution from samples with oxidized P700 is also present, yielding a shoulder at ~730 nm, dashed arrow.

Figure 44. Frame A: Green curve: difference between two consecutively measured spectra. Blue: result of exposure of the sample to dim room light (several nW/cm^2). Black: after one minute of illumination at 732 nm. Red: after 16 minutes of illumination at 732 nm. Dashed line indicates the cut-off wavelength of a long-pass filter, 730 nm. **Frame B:** NPHB-free $P700^+$ minus P700 spectra produced with illumination at 753 nm through 750 nm long-pass filter. Green: difference between the first two spectrometer scans. Blue: after seven spectrometer scans, further scanning does not increase the hole. Black: after 10 minutes of illumination at 753 nm. Red: after further 20 minutes of illumination at 753 nm.

Figure 45. Fluorescence excitation spectra of sample B, cooled down in the dark. Black to green curves represent consecutive scans from 735 to 670 nm. Magenta curve was recorded after an attempt to measure the HB action spectrum covering 735 to 700 nm range. Spectra are equally distorted (longer-wavelength range is amplified) by the transmission dependence on wavelength of the supposedly neutral density filters used for beam attenuation. The spectra were left uncorrected since in uncorrected spectra the red state region is artificially amplified and its evolution is clearer.

Figure 46. Left Frame: Hole spectra after thermocycling to indicated excursion temperatures. Spectra are shifted along vertical axis for clarity. Arrow indicates the burn wavelength of 725 nm. Right frame: several hole spectra (color coding same as in the left frame) overlaid together.

Figure 47. Sample A with mostly oxidized P700. Black: hole spectrum after illumination at 714.5 nm, probing both C715 and C719 states. Blue: hole spectrum after illumination at 725 nm, probing only C719 state. Arrows indicate burn wavelengths. Red: $P700^{+}$ minus P700 signature from sample B, Figure 44, presented for comparison.

Figure 48. Left Frame: Hole spectra with λ_B=719 nm after thermocycling to indicated excursion temperatures. Spectra are shifted along vertical axis for clarity. The burn wavelength was 719 nm. Right frame: several hole spectra (color coding same as in the left frame) overlaid together.

Figure 49. Frame A. Hole spectra for λ_B of 660 nm (blue) and 532 nm (red). Frame B: the difference between spectra in frame A. Frame C: The difference between spectra for λ_B of 714.5 and 725 nm (see Figure 47). Frame D: the hole spectra for λ_B of 714.5 nm (black) and 532 nm (blue).

List of Acronyms:

BChls - Bacteriochlorophylls

C. Tepidum - *Chlorobium Tepidum*

CD spectra - Circular Dichroism spectra

CGS units – Centimeter, Gram, Second units

Chls - Chlorophylls

EET - Excitation Energy Transfer

FLN and ΔFLN - Fluorescence Line Narrowing

FMO - Fenna-Matthews-Olson

FWHM - Full Width at Half Maximum

HB - Hole-Burning

HGK - Hole Growth Kinetics

LHC I - Light Harvesting Complex I

NPHB - Non-Photochemical Hole Burning

PSB - Phonon Side Band,

PSBH - Phonon Side Band Hole

PSI - Photosystem I

PSII - Photosystem II

PSII RC - Photosystem II Reaction Center

RC - Reaction Center

SDF - Site Distribution Function

SHB - Spectral Hole Burning

SPCS - Single Photosynthetic Complex Spectroscopy

T. elongatus - *Thermosynechococcus elongatus*

TLS - Two-Level Systems,

ZPH - Zero Phonon Hole

ZPL - Zero–Phonon Line

1. Motivation and outline of the thesis

The natural energy resources and energy supply capabilities provide the main support for all societies and global economic growth. However, all the currently available energy resources (e.g. reserves of fossil fuels, nuclear and currently employed renewable resources) combined will not be able to satisfy the world's expanding needs which are estimated to triple (> 46TW) by the end of the 21st century [1-3]. Therefore, harnessing additional viable energy sources is one of the most challenging issues addressed by scientists from various fields of research. The global climate change imposes additional pressure on energy challenge [1-5]. The prospective energy sources must be abundant and sustainable for both developed and developing countries and preferably come from carbon-neutral sources [1-5]. The most abundant source of clean energy is the sunlight [1-6]. However, the enormous potential (Sun energy delivered to Earth, $P_{sun} = 4.3 \times 10^{20}$ J / hour) of this natural resource is not fully exploited yet. The large-scale solar energy production and utilization is currently limited by several factors including the short term storage issues, and either low conversion efficiency of solar energy or high costs of production of most effective and widespread silicon devices [1-3, 6].

As the natural photosynthesis is the most important solar-energy conversion process on Earth, artificial photosynthesis may be the most viable solution for energy challenge. Similar to natural photosynthetic organisms, artificial photosynthetic systems capture the sunlight and transfer the excitation energy to the artificial reaction centers where primary photochemistry takes place [1-3, 6]. Therefore, understanding the chemical and physical principles of photon capture as well as mechanisms of efficient sunlight conversion (> 90%) and storage in natural photosynthetic pigment-protein complexes is fundamental to

advancing the design of the "molecular circuits" in artificial photosynthetic systems [1-3, 6]. Achieving these goals requires the elucidation of the electronic structure of both the ground and excited states of photosynthetic pigments, the mechanisms of charge and excitation energy transfer (EET) in natural photosynthetic pigment networks as well as mapping out the energy landscape of the photosynthetic proteins. Chapter 2 provides introduction to photosynthesis and pigment-protein complexes.

The spectral properties of photosynthetic complexes (e.g. the excited state lifetimes, electron-phonon couplings, distributions of "solvent shifts" of various pigments, and the interactions between them (manifestations of excitonic effects, excitation energy transfer, charge transfer)) are traditionally explored by either time-domain or frequency-domain high-resolution spectroscopy methods, including spectral hole burning (SHB). Persistent non-photochemical hole burning (NPHB) - a variety of SHB - is a mature and powerful tool employed for the last ~30 years to study optical properties of photosynthetic complexes. Since the non-photochemical spectral holes are due to the rearrangement of the local environment of the pigments, the pigment molecules themselves remain chemically intact and their network is preserved for the purpose of energy transfer [7]. Therefore, the NPHB is a reliable method to study the excitation energy transfer (EET) in photosynthetic complexes. Introduction to NPHB will be presented in Chapter 3.

Despite being around for ~30 years, NPHB still has potential for improvement, both in terms of technique and in terms of data analysis. This research will focus on the study of various effects influencing the hole burning processes in pigment-protein complexes and on ways developed to reliably extract various relevant parameters. As the effects of EET rate distributions on hole burning spectra have not yet been explored quantitatively,

in this thesis we present our new results concerning the inclusion of such distribution into treatment of SHB spectra. Determining EET time distributions is important from three key viewpoints. First, sometimes one just needs to know the average EET time at certain wavelength, while SHB tends to probe the longer-time end of the distribution, if such distribution is present. Thus, understanding effects of EET rate distributions on SHB will result in more precise EET rate determination. Second, knowledge of the whole EET time distribution will bring additional information on the site energies (transition energies in the absence of inter-pigment interactions) and inter-pigment couplings of different photosynthetic pigments which in turn will lead to the refinement of the structure-based calculations of the optical spectra. Various optical spectra of multi-pigment systems are usually calculated by finding eigenvalues and eigenvectors of a Hamiltonian matrix with site energies as diagonal elements and inter-pigment couplings as off-diagonal elements. There is no universally accepted approach to calculating site energies. Therefore, in practice, site energies are determined from the simultaneous fit of as many different optical spectra as possible to modeling results. The more complicated the system (e.g. Photosystem I has 96 chlorophylls per monomer), the more different types of data one needs for reliable site energies determination. Wavelength-dependent distributions of EET times represent one useful type of such additional data. Third, one is often employing SHB to explore barrier parameters of the protein energy landscapes. Thus, it is essential to be able to disentangle the effects of EET rate distributions and barrier distributions on SHB data.

Theory common for all multi-pigment systems will be presented in the introductory part of Chapter 4. Several different complexes will be considered in detail. Chapter 4.4.1

will present estimating inter-pigment couplings in plant CP43 based on SHB data, Chapter 4.4.2 will discuss Fenna-Matthews-Olson (FMO) complex of green sulfur bacteria, while Chapter 4.5 will describe our attempts to test if various published distributions of charge transfer rates are in agreement with SHB results for Photosystem II reaction center (PSII RC).

We are also going to explore spectral properties of the lowest energy states and protein dynamics of Photosystem I (PSI), one of the two major photosynthetic protein complexes involved in photosynthesis. Here the focus will be on analyzing the whole satellite holes spectra of PSI from *Thermosynechococcus elongatus (T. elongatus)* upon excitation at different wavelengths and the effects of P700 redox state on these structures. These results will be presented in Chapter 5.

2. Introduction

2.1. Photosynthesis and photosynthetic pigments

Photosynthesis is a natural process in which solar energy is captured, transformed into chemical energy and stored by photosynthetic organisms, to further generate products essential to their metabolism [8-11]. To perform photosynthesis, plants, algae and bacteria possess dense networks of chlorophylls (or bacteriochlorophylls) and other pigments such as carotenoids embedded in trans-membrane proteins [8-12] (as well as phycobilisomes in cyanobacteria).

The chlorophylls (Chls) are a large group of tetrapyrrolic pigments with similar structure, function and spectral properties. At the center of tetrapyrrolic ring there is a magnesium atom; all chlorophyll molecules have long phythyl tail; different chlorophylls possess different side groups (e.g. methyl group in Chl *a* molecule, formyl group in Chl *b* molecule, etc) [8-12]. A large number of different types of chlorophyll-like pigments has been identified in photosynthetic organisms [8-12]. However, the most common chlorophyll-like pigments in photosynthetic organisms are chlorophylls *a* and *b* and bacteriochlorophylls *a* and *b* [8-12]. Chlorophyll *a* has been identified in all oxygenic photosynthetic organisms and it has the major role in all primary steps of photosynthesis - namely in light-harvesting, energy transfer and charge separation. Chlorophyll *b* occurs selectively in some organisms or some complexes and not others. It is the major accessory antennae pigment in all higher plants and green algae. The Chl*b*:Chl*a* occurrence ratio widely varies between species and even within same species depending on environmental conditions [8-12].

The main spectral features of Chlorophylls *a* and *b* (Chl *a* and Chl *b*) are the two intense characteristic absorption bands peaked in the blue and red regions of the visible spectrum [8-12]. The absorption spectra of Chl *a* and *b* are not identical due to their slightly different molecular structure. The major distinction between them is the blue shift of the Chl *b* Q_y band and the red shift of the Chl *b* Soret band (Figure 1) [8-12].

Bacteriochlorophylls (Bchls) are the major antenna pigments in purple and green sulfur bacteria involved in non-oxygenic photosynthesis. Bchl *a* is the most abundant pigment identified in majority of photosynthetic bacteria while the group of Bchls *c/d/e/f* occurs only in the chlorosomal antenna of green sulfur bacteria [8-12]. In photosynthetic organisms the absorption spectra of (bacterio)chlorophyll-binding proteins differ dramatically with respect to pigments in solution due to both pigment-pigment and pigment-protein interactions [8-12].

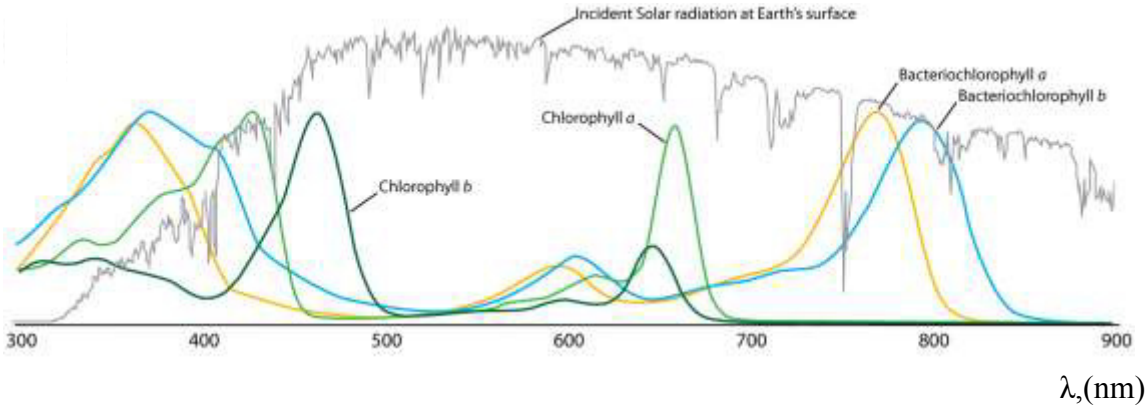

Figure 1. Absorption spectra of chlorophylls *a* and *b* and bacteriochlorophylls *a* and *b* in methanol and ethanol. For comparison, the solar radiation spectrum is presented as well. Reprinted from ref. 13, Copyright (2010), with permission from Elsevier

The carotenoids are the second large group of pigments identified in all photosynthetic organisms. They play an important role in light-harvesting as well as in photo-protection of antennae pigments embedded in photosynthetic proteins [8-12].

2.2. Light harvesting antennae

In order to effectively harvest and transfer solar energy to the reaction center (RC), various photosynthetic organisms living in different environments are equipped with specific light-harvesting antennae [6-15]. Although the peripheral light-harvesting complexes and the core antennae perform similar functions in photosynthesis, they exhibit clear structural differences. Usually, all these antennae complexes are arranged to optimize the energy flow from the peripheral light-harvesting antennae towards the core antenna complexes and then towards the RC [6-15].

The core of Photosystem II (PSII) of higher plants, algae and cyanobacteria is made up of several subunits including the reaction center (RC) protein subunits (D1/D2) and the core antenna complexes CP43 and CP47 (Figure 2). The lowest energy state and the primary electron donor of PSII RC is referred to as P680. More details on the core antenna complex CP43 and PSII RC will be presented in Chapter 4. In higher plants and algae the major LHC II (Light Harvesting Complex II) protein and the three minor antenna proteins CP24, CP26, and CP29 are membrane-intrinsic peripheral antennae of PSII which bind Chl *a* and Chl *b* in different ratios (Fig.2). The LHC II, binding approximately 65% of PSII chlorophylls, naturally exists as a trimeric complex and each of its monomers contains 14 Chl (8 Chl *a* and 6 Chl *b*) molecules arranged approximately in two layers [16-18]. Thus, an isolated LHCII trimer contains 21–24 chlorophylls *a*, 15–18 chlorophylls *b*, 2 luteins and 1 neoxanthin [16-18] while the minor peripheral antenna CP29 binds 8 Chls *a* and 5 Chls *b* [19].

The cyanobacteria, green algae, and higher plants the Photosystem I (PSI) core is made up of two large protein subunits (PsaA/PsaB) that hold a large core antenna system

and the reaction center (RC, with lowest state, primary donor in electron transfer, referred to as P700). The core antenna network is comprised of a large number of pigments that funnel the excitation energy to P700 [9, 20-28]. In cyanobacteria (e.g. *Thermosynechococcus elongatus*), the PSI core antenna network contains about 96 Chl *a* and 22 carotenoid molecules per monomer while in higher plants the core contains about 100 Chl *a* molecules and more than 20 carotenoids [9, 20-28]. Interestingly, the position of 92 of these chlorophylls has been conserved for all species explored so far [26]. In cyanobacteria the PSI core is trimeric.

In plants, the peripheral antennae system of (monomeric) PSI is known as the Light Harvesting Complex I, LHC I, (Figure 3). The LHC I consists of four chlorophyll-binding proteins (Lhca 1-4) closely connected to one side of the monomeric PSI core [9, 20-28]. The LHC I contains up to 61 Chl *a* and *b* molecules (15 Chls / Lhca1, 14 Chls / Lhca2, 17 Chls / Lhca3 and 15 Chls / Lhca4), [21]. The "contacts" between each LHC I proteins and PSI core subunits is interfaced by several chlorophylls [9, 20-28]. In cyanobacterial PSI the membrane-intrinsic peripheral antennae generally do not exist (but in case of iron-deficient environment core PSI may be surrounded by multiple copies of *IsiA* protein, also known as CP43' of PSII) but there is a large membrane-extrinsic antenna system known as the phycobilisomes [9, 20-28]. Both plant and cyanobacterial PSI possess chlorophylls or groups of chlorophylls that absorb at longer wavelengths than the primary electron donor P700.

The largest and most efficient light-harvesting complex in Nature is the major peripheral antenna complex of the green bacteria namely the chlorosome. The main difference between the chlorosome and all the other antenna complexes is that

chlorosome is a self-assembled (without protein) network of Bchls [8,30,31]. The chlorosome is built from more than 150000 Bchl c, d, and e [8,30,31]. In green sulphur bacteria the large peripheral chlorosome antenna is connected to the reaction center by a membrane-attached Fenna-Matthews-Olson (FMO) protein. These two peripheral antennae are unique to green sulphur bacteria [9, 32-34]. More details about the structure of the FMO protein are provided on Chapter 4.4.2. The structure of the photosynthetic apparatus of the green sulphur bacteria is presented in Figure.4

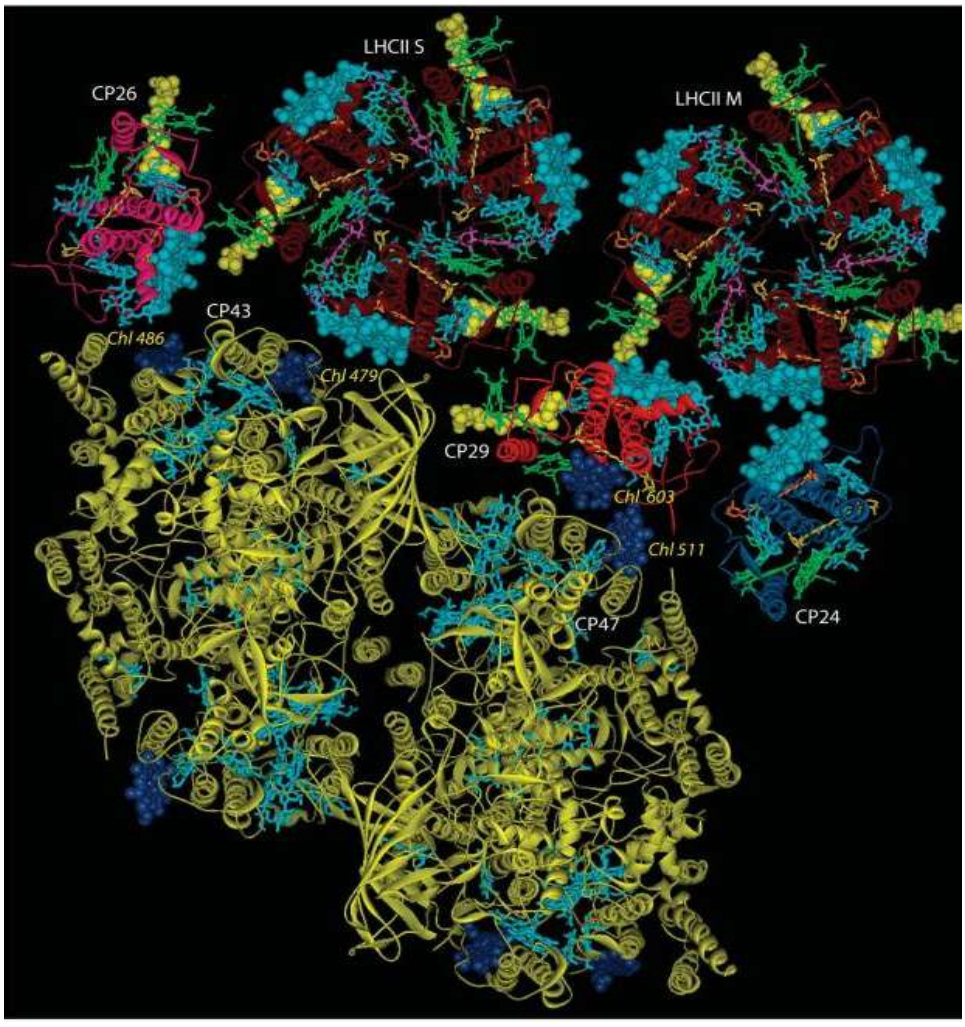

Figure 2. The structure of the PSII in plants where the yellow ribbon diagram shows the structure of PSII- core (from ref. 14). Note that the core is dimeric. Reprinted by permission from Macmillan Publishers Ltd: EMBO, ref. 14, copyright (2009).

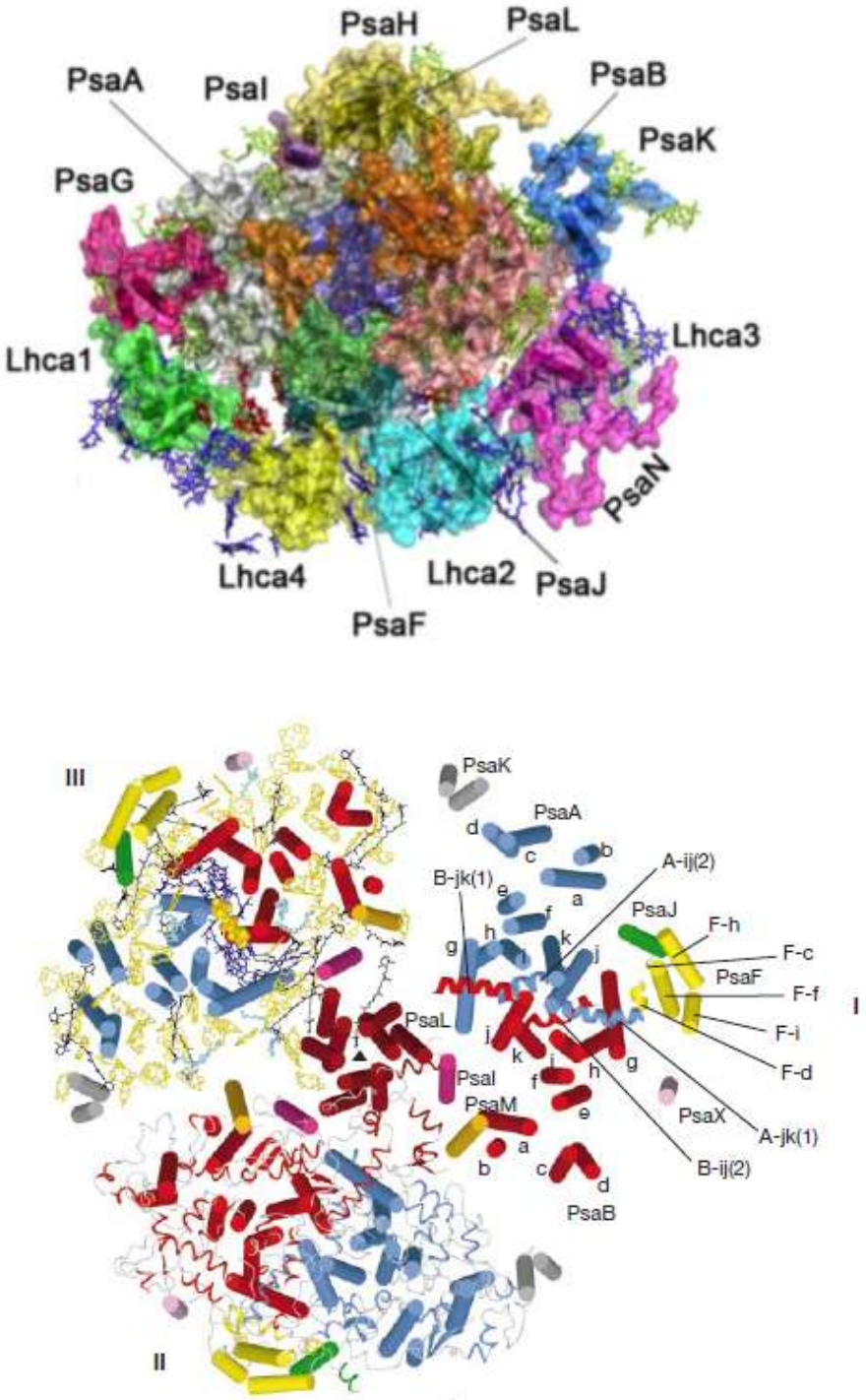

Figure 3. Structural details of PSI from plants (top; from Ref. 21, reprinted with permission from American Society for Biochemistry and Molecular Biology) and cyanobacteria *Thermosynechococcus elongatus* (bottom; Reprinted by permission from Macmillan Publishers Ltd: Nature, ref. 29, copyright (2001). Monomers are oriented with PsaL protein subunits towards three-fold symmetry axis.

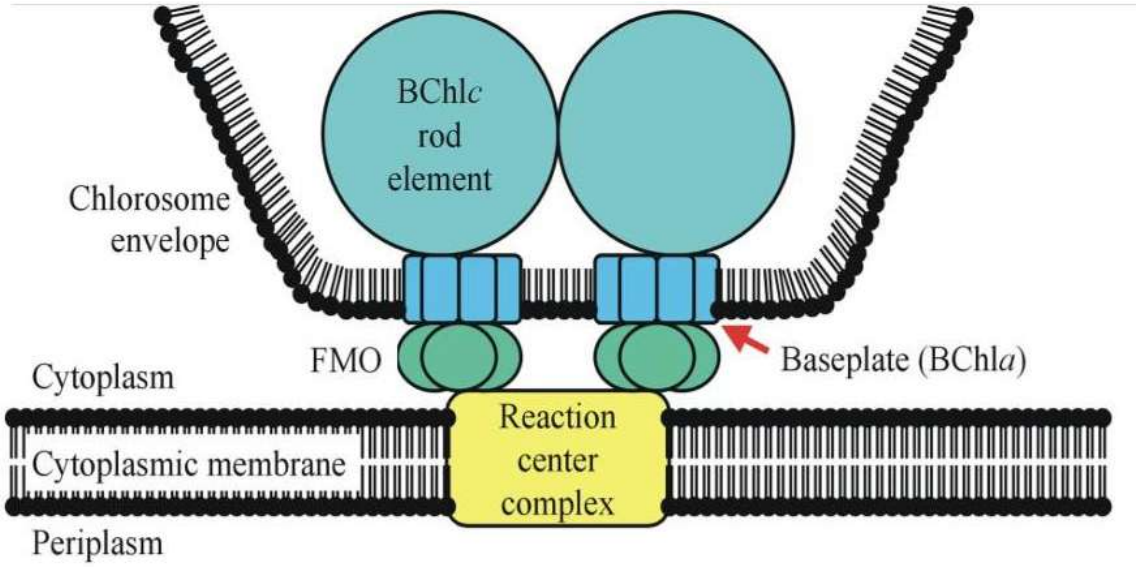

Figure 4. Structure of the photosynthetic apparatus including the light-harvesting antenna complexes in green sulphur bacteria. Reprinted with permission from ref. 33 Copyright (2007) National Academy of Sciences, USA.

2.3. Reaction centers

The photosynthetic reaction center is very efficient solar energy conversion machine. The solar energy absorbed by light-harvesting antennae is funneled down to the reaction center (RC) where the primary charge separation occurs. Note that all RCs contain chlorophylls and therefore can absorb solar energy directly as well [8, 9, 15, 35, 36]. The reaction center is a trans-membrane pigment-protein complex which contains the special pair of chlorophyll-like pigments that is usually the primary electron donor and the electron transfer cofactors including the quinones or the iron sulfur centers [8, 9, 15, 35, 36]. Thus, based on the terminal electron acceptor type the reaction centers are usually divided into quinone-type (Figure 6) and iron-sulfur RCs (Figure 5). The quinone-type RCs are present in purple bacteria and PSII of cyanobacteria, algae and higher plants while the iron sulfur type RCs are found in green sulfur bacteria and PSI of cyanobacteria, algae and higher plants [8, 9, 15, 35, 36].

In oxygenic photosynthesis both photosystems possess a specific primary electron donor. In PSI this is a chlorophyll *a*/chlorophyll *a'* heterodimer referred to as the "special pair" of PSI (P700), [22, 23, 36]. In PSII the situation is somewhat more complicated. Unlike in PSI and bacterial RC, where the electrostatic coupling between pigments of the "special pair" is clearly the strongest, in PS II all nearest-neighbor couplings are similar (except for peripheral chlorophylls Z, See Figure 6A). Combining this with static energy disorder results in variable composition of the lowest-energy state of the RC, and variability in the nature of the primary donor. The primary electron donor is either P_{D1} Chl *a* or Chl_{D1} and charge separation pathways vary accordingly [37-38]. More details about the processes that determine the two charge separation pathways in PSII-RC are provided in Chapter 4.5.

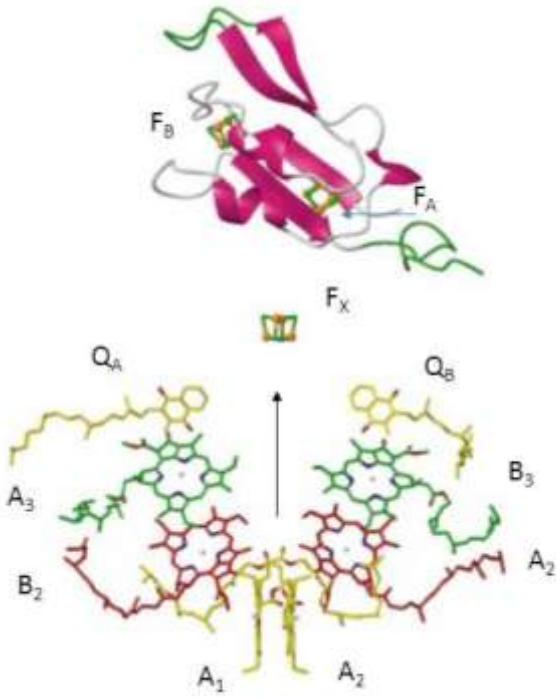

Figure 5. The "special pair" and other cofactors in the PSI-RC from cyanobacteria *Thermosynechococcus elongatus*. The labels A and B refer to the two branches of the electron transfer chain. The QX (X=A or B) and F_Y (Y = X or A or B) indicate the quinone and iron-sulfur clusters. Reprinted by permission from Macmillan Publishers Ltd: Nature, ref. 29, copyright (2001).

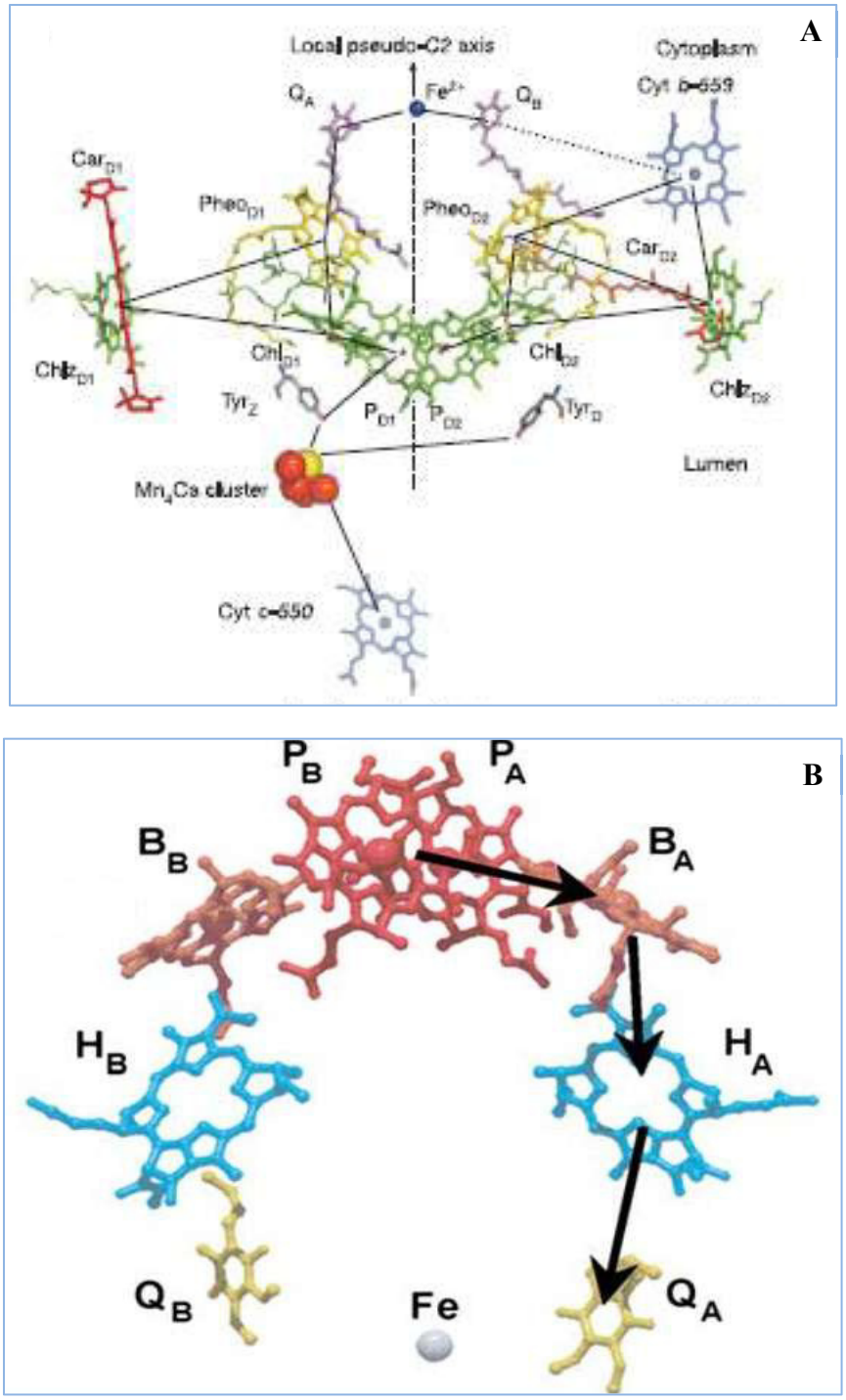

Figure 6. **Frame A** cofactors of PSII from cyanobacteria *Thermosynechococcus elongatus.* The labels D1 and D2 refer to the two branches of the RC. Electron transfer occurs along the D1-branch. Also shown are the Mn_4Ca cluster and cytochrome c-550 Reprinted by permission from Macmillan Publishers Ltd: Nature, ref. 35, copyright (2005) **Frame B** The RC cofactors from purple bacteria *Rb. Sphaeroides*. Q_A and Q_B are immobile and mobile quinones, respectively. Arrows indicate the pathway of electron transfer. Reprinted from ref.39, Copyright (2002), with permission from Elsevier

Unlike PS II of oxygenic photosynthetic organisms, purple bacteria exhibit a pair of uniquely strongly coupled BChl *a* molecules which absorb at a wavelength ranging from ~870 nm to ~960 nm, depending on the particular species (e.g. P870 in *Rb. Sphaeroides*) [8, 9, 15, 35, 36]. Interestingly, despite the apparent C_2 symmetry of the reaction centers (see Figures 5 and 6), the electron transfer in all organisms occurs along the A (PSI) / D1 (PSII) /L (in bacterial RC) branch.

3. Persistent Non-photochemical Hole Burning (NPHB) and its Applications to Photosynthetic Complexes

3.1. Spectral line shape and other properties of an impurity center in solid matrices

Biological macromolecules including photosynthetic pigment-protein complexes can be viewed as soft condensed matter systems. Thus, their spectral properties can be analyzed the same way as in the case of impurity centers (or "dopants") in amorphous solid matrices (e.g. glasses and polymers). In the case of photosynthetic pigment-protein complexes the chlorophyll-like pigment is not exactly a dopant, since it is naturally present in the system. Nevertheless it is used in the same manner as dopants / impurity centers, to report on its local environment. Typically, it acts as a local probe for dynamics in photosynthetic proteins [7, 40-45] as well as for energy or charge transfer processes.

Since in photosynthetic pigment-protein complexes the chlorophyll-like pigments experience different local environments (strains, random electric fields, and interactions between different closely-spaced centers/chromophores, [7 and ref. therein]) even in the same protein site, their absorption spectra exhibit inhomogeneous broadening [7, 40-45]. The inhomogeneous broadening hides remarkable information about the electronic structure of the ground and excited electronic states of pigments, manifestations of excitonic effects, as well as about the excitation energy and charge transfer in photosynthetic complexes. One needs to access the widths and positions of the narrow (at low temperatures) homogeneously-broadened lines that contain detailed information on the properties and functioning of photosynthetic proteins, and to do that one needs to circumvent the inhomogeneous broadening.

The spectral properties of the impurity centers in solid matrices are determined by the nature of the matrix (Fig. 7). Moreover, the nature of the matrix affects the lifetime of the electronic transition by introducing new radiationless decay channels, [7, 40-45]. In the case of a crystalline (perfect) matrix doped with impurities in low concentration, the guest molecules are subject to identical local environment and therefore their spectral properties (e.g. transition frequencies / solvent shifts, line width, homogeneous line shape) coincide. If the impurity molecules are embedded in an amorphous matrix they experience different local environment and therefore the absorption spectrum of the ensemble of molecules presents an inhomogeneous broadening [7, 40-45]

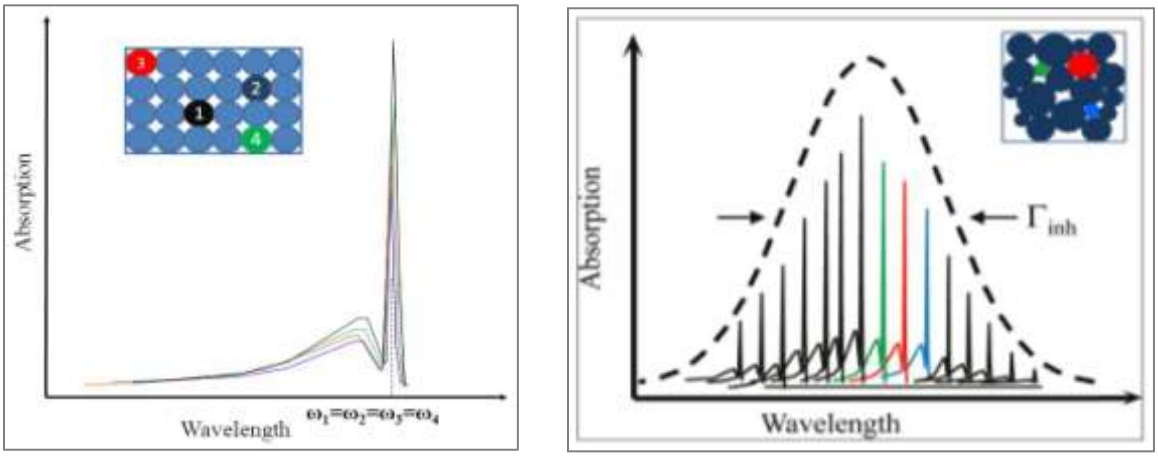

Figure 7. Spectra of the impurity centers in a crystalline matrix (left) and amorphous matrix (right).

The inhomogeneous absorption band is the convolution of the "single site spectrum" with the site distribution function [46, 47]. The site distribution function (SDF) describes the probability to find a molecule with the purely electronic (0-0) S_0-S_1 transition at a certain frequency, [48].

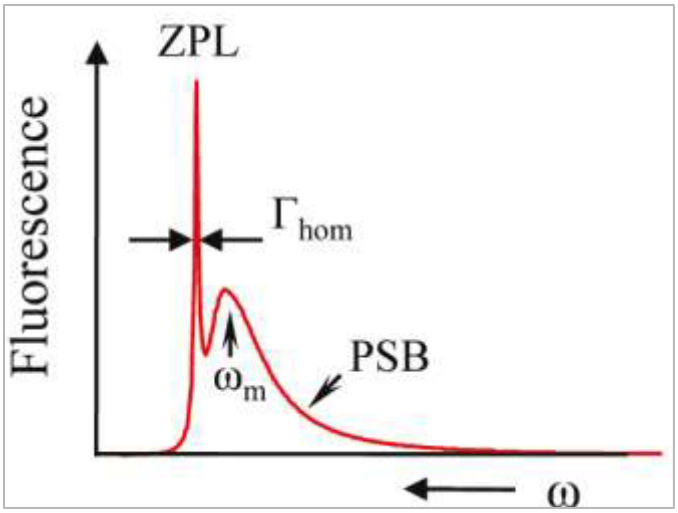

Figure 8. Spectral line shape of an impurity center in a solid matrix at low temperature. Γ_{hom} is the homogeneous line width, and ω_m is the mean phonon frequency. Reprinted with permission from ref.7. Copyright (2011) American Chemical Society.

The low-temperature homogeneous line shape of a single impurity center in a solid matrix presents two main features, [7, 40-45]: (a) the zero–phonon line, ZPL and (b) the phonon side band, PSB (fig.8). The ZPL has a Lorentzian lineshape and represents the purely electronic transition, without creation or elimination of phonons (delocalized lattice vibrations). The homogeneous line width, is determined by the electronic relaxation time (τ_1) and pure dephasing time (τ_2^*).

$$\Gamma_{hom} = \frac{1}{c\pi\tau_2} \quad \frac{1}{\tau_2} = \frac{1}{2\tau_1} + \frac{1}{\tau_2^*},$$

All the quantities in equation above are given in CGS units, as follows: Γ_{hom} is the homogeneous line width in cm^{-1}, τ_2 is the total dephasing time in s and c is the speed of light in cm/s [7, 40-45].

The phonon side band corresponds to the electronic transition accompanied by creation or destruction of phonon(s). The strength of the electron-phonon coupling is described by the Debye – Waller factor (α) which represents the relative intensity of the zero-phonon line [7, 40-45].

$$\alpha = \frac{I_{ZPL}}{I_{Total}} = \frac{I_{ZPL}}{I_{ZPL} + I_{PSB}} = \exp(-S),$$

Here I_{ZPL} is the integral intensity of the zero-phonon line, I_{Total} is the total intensity and I_{PSB} is the integral intensity of the phonon sideband. The Huang-Rhys factor (S) determines the average number of phonons/vibrations of particular frequency excited during electronic transition. For weak electron phonon coupling (S<1) the intensity of the pure electronic transition is much higher than that of the phonon transitions and the ZPL and phonon sideband are well resolved. In contrast to the weak coupling, in the case of the strong electron-phonon coupling (S>1) the transitions involving phonons dominate the spectral line shape (Fig.9.), [7, 40-45]. The strength of the electron-phonon coupling is related to the difference in generalized coordinate between ground and excited electronic states, as shown in Figure 9. The intensity of each transition depends on the overlap of vibrational wavefunctions (Franck-Condon principle). The transitions are represented by vertical lines, indicating that during electronic transition massive nuclei do not have time to shift (Born-Oppenheimer approximation).

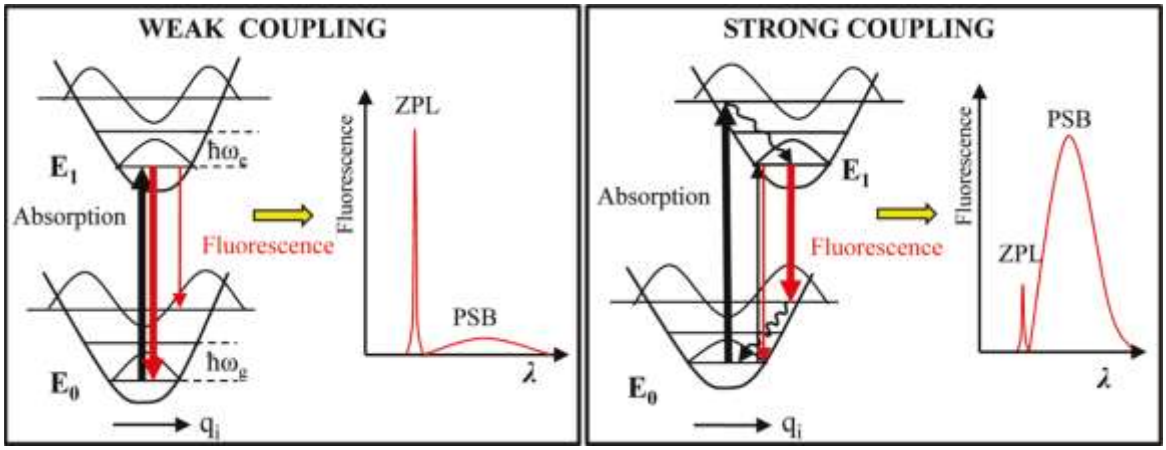

Figure 9. Features of the single impurity spectral line (zero-phonon line and phonon side-band) depending on the strength of electron-phonon coupling. Reprinted with permission from ref.7. Copyright (2011) American Chemical Society.

Both Debye-Waller factor and the zero-phonon line width are temperature-dependent. Since at low temperatures electronic relaxation is much slower than vibronic relaxation, the ZPL width is much narrower and ZPL is more prominent than PSB.

However, due to strong temperature dependence of pure dephasing the ZPL broaden and at temperatures above 50 K ZPL merges with PSB and homogeneous width (now defined as the combined width of the resulting feature) increases drastically [7, 40-45]. Therefore the essential requirement to measure the homogeneous ZPL of the chromophores embedded in solid matrices is to perform these measurements at low temperature using a narrow laser source ($\Delta\nu_{laser} << \Gamma_{hom} << \Gamma_{inhom}$) [7, 32-49].

3.2. Spectral Hole Burning (SHB)

Spectral Hole Burning is a frequency-domain spectroscopy technique initially used to unravel spectral characteristics hidden under the inhomogeneously broadened absorption spectra of chromophores embedded in crystalline and glassy matrices. Depending on the actual mechanism of burning one can distinguish the photochemical (e.g. photodissociation, proton phototransfer / tautomerization, electron transfer, etc) and non-photochemical hole burning. The latter is the rearrangement of the environment surrounding the optically excited chromophore without chemical changes in the chromophore itself [7, 15, 49-55]. The non-photochemical hole burning (NPHB) was first observed in glasses, by Personov and co-workers [50]. Theoretically this physical phenomenon has been explained by Small and co-workers [51]. NPHB at low temperature in glasses is treated as being due to the tunneling between different bistable configurations of glass-chromophore systems referred to as two-level systems, TLS. These asymmetric double-well potentials are characterized by the displacement, *d* between the two potential minima, the asymmetry Δ and barrier height, *V* between configurations A and B ($V_{ex} < V_{grd}$, Figure 10) [7, 15, 49-55]. The "strength" of the

barrier can be described by the tunneling parameter, λ that is given by the equation, [7, 15, 49-55]:

$$\lambda = d\,(2mV)^{1/2}/\hbar \qquad (1)$$

where *m* is the effective mass of the entity rearranging during the conformational change.

The tunneling of TLS is triggered by excitation of the chromophore initially found in conformation A and occurs while the chromophore is in its excited state ($V_{ex} < V_{grd}$, Figure 10). Upon tunneling (yellow arrow in figure 10) between configurations A and B the chromophore returns to the ground state. As the TLS exhibits different asymmetry in the ground and excited electronic states the absorption of the chromophore in conformation B will be shifted (antihole), [7, 15, 44, 46-54].

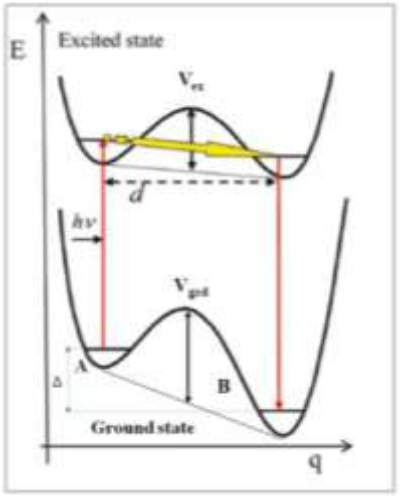

Figure 10. Two-Level System model; where the barriers height in the ground and excited states are V_{grd} and V_{ex}; displacement between the two potential minima is denoted by d; the asymmetry of the TLS is Δ and hν is the excitation energy of the chromophore initially found in conformation A of the ground state. The tunneling frequency is $W=\omega_0\exp(-\lambda)$. Reprinted with permission from ref.7. Copyright (2011) American Chemical Society.

To obtain a hole-burning (HB) spectrum the following steps are required. First, the absorption (or fluorescence excitation) spectrum is measured before burning (i.e.,

"pre-burn" spectrum), then, after burning with a narrow band laser the absorption spectrum is measured again ("post-burn" spectrum) and actual HB spectrum is obtained as the difference between these two spectra [49-55].

The HB spectrum exhibits a sharp Zero Phonon Hole (ZPH) at the burn frequency ω_B and two features at the high and low energy sides of the ZPH which are referred to as the real Phonon Side Band Hole (PSBH), and the pseudo-PSB, respectively (Figure 11). The last feature is the mirror image of the real-PSB and is due to the electronic transitions at lower energy than ω_B which are excited through their phonon sidebands (or non-resonantly burned) [7, 15, 49-55]. Since vibrational relaxation is fast, faster than fluorescence lifetime, the tunneling most likely occurs from the zero vibrational level of the excited state.

Another feature of the HB absorption spectrum is the anti-hole or "photoproduct" which is due to the molecules that resonantly absorb at ω_B (state A in Fig. 10) but subsequently shifted their absorption frequencies (state B in Fig. 10) [7, 15, 49-55]. In the case of NPHB no photochemistry occurs, and it is somewhat misleading to call anti-hole a "photoproduct". In the case of NPHB the anti-hole is usually located next to the resonant hole, while in the case of photochemical hole burning the product may be shifted fairly far in terms of energy [7, 15, 49-55].

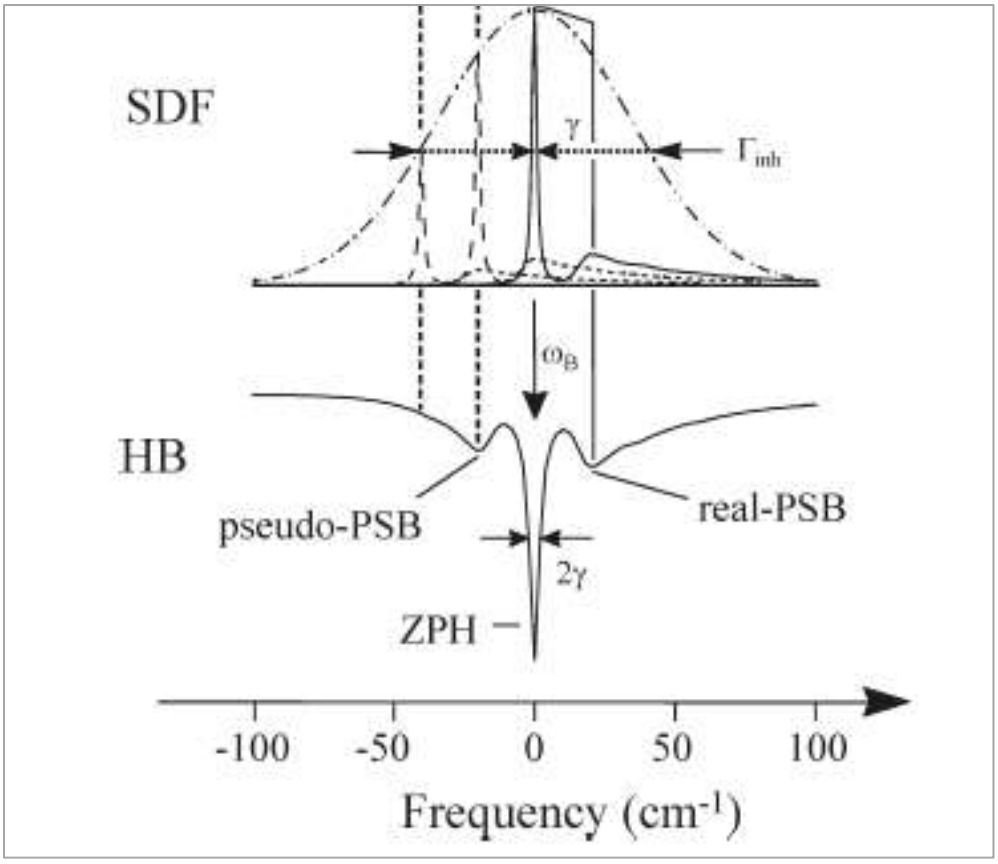

Figure 11. The spectral - hole profile (SDF is Site Distribution Function with Γ_{inh} being the inhomogeneous width, γ is the homogeneous width and 2γ is the hole width. Width is defined here and everywhere else within this thesis as the Full Width at Half Maximum, FWHM). Reprinted with permission from ref.7. Copyright (2011) American Chemical Society.

Although at low temperatures proteins behave as amorphous solids, proteins show somewhat different properties compared to glasses. While behavior of glasses can be described considering only interaction between the pigment and one-two TLS (see Figure 12), the proteins are better explained in terms of a complicated multi-well energy landscapes. The term "energy landscape" was introduced to describe the high-dimensional energy surface of a protein and it features hierarchical tiers of conformational substates (CS), Figure 12, [7, 56, 57]. In the energy landscape model each hierarchical tier is characterized by specific distribution of energy barrier parameters and each minimum represents a different conformation of the protein [7, 56, 57].

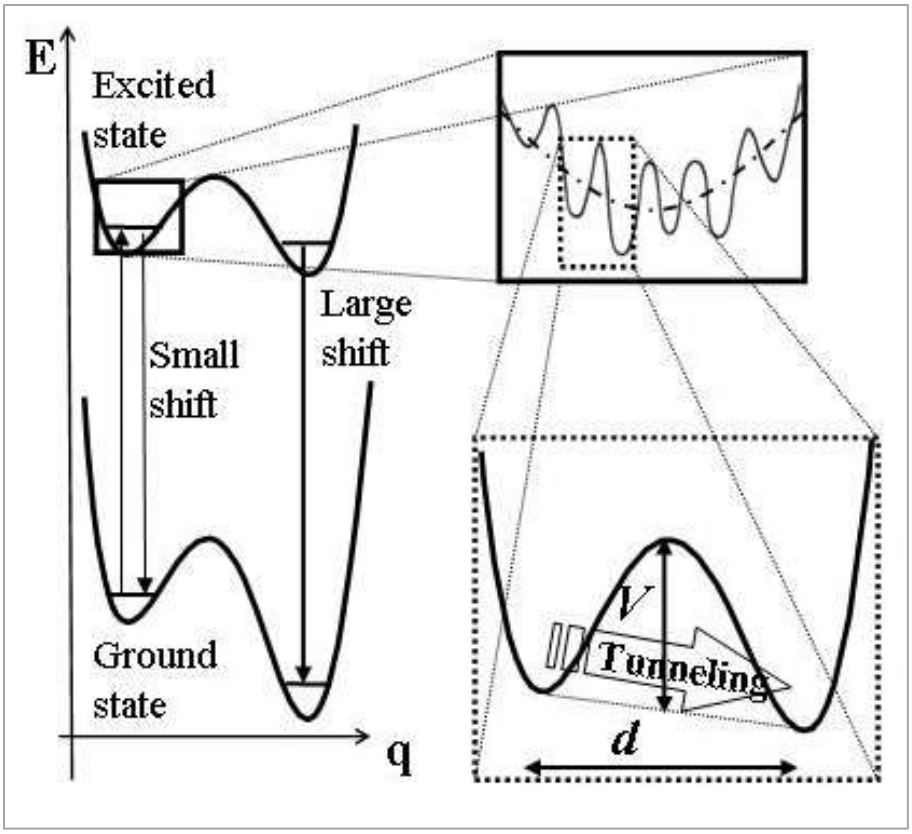

Figure 12. NPHB mechanisms accounting for two different hierarchical tiers on the energy landscape. Adapted with permission from ref. 66. Copyright (2012) American Chemical Society.

The concept of energy landscape is important in explaining the protein functions, motions and folding processes [7, 56-65]. Transitions between different conformational sub-states are possible, with the rates depending on the barrier parameters [65]. At low temperatures, these transitions are sufficiently slow for convenient exploration of the energy landscape properties [65]. Due to the inherent disorder in proteins the energy landscape parameters (e.g. barrier shapes, heights, widths, tunneling parameter, etc.) are subject to distributions. Conformational fluctuations of proteins result in fluctuations in the local interactions and changes in the electronic transition frequencies of the chromophore. Often the conformational changes are optically triggered, and in this case one is dealing with the NPHB. Therefore, dynamics of proteins can be monitored by

optical spectroscopy techniques and understood in terms of protein energy landscapes rather than just two-level systems [7, 56-65]. Low-temperature spectral hole burning techniques have been used to measure these distributions in glasses and proteins, [7, 56-65]. The hole growth kinetics (HGK) experiments have been used to probe the distribution of barriers in the excited electronic state of a pigment-protein system, whereas the distribution of barriers in the ground state has been explored by observing the recovery of the previously burnt holes [65] at a fixed temperature (burning temperature), or as a result of thermocycling [60-71].

As mentioned above in the case of NPHB the excitation of the chromophore triggers the rearrangement of its local environment which changes chromophore-host interactions [51]. Since it is the inherent structural disorder of amorphous solids that allows for reorganization and change in chromophore-host interactions, the NPHB is effective only in amorphous systems [7, 15, 49, 50, 51]. SHB has been used to probe static and dynamic properties of pigments naturally embedded in trans-membrane proteins of various photosynthetic organisms [7, 15, 49, 50, 51]. In the last two decades SHB studies of photosynthetic complexes provided several classes of parameters as follows [7]:

- lifetimes of the zero-point level of S_1(Qy)-states due to excitation energy transfer EET or electron transfer (ET), as determined by the widths of zero-phonon holes ($\Gamma_{hole} = 2\gamma = 2/\pi c\tau_2$; τ_2 is the total dephasing time);
- Γ_{inh} values, typically ~50 - 200 cm^{-1} derived from the SHB action spectrum, i.e. the profile of ZPHs burned at different wavelengths under constant irradiation dose conditions;

- the extent of correlation and excitonic interaction between the absorption bands of different Qy-states, using satellite hole-burning;
- Franck-Condon factors and frequencies of Chl modes active in $S_0 \rightarrow S_1$, Qy transitions as determined by vibronic satellite HB spectroscopy;
- Pure dephasing of Qy-optical transitions due to coupling with the "bistable configurations" (TLS) of proteins.

However, the actual distributions of barrier parameters have not been explored in photosynthetic proteins before us. The same is true for distributions of energy transfer times.

A model for NPHB of the S_0 - S_1 origin absorption bands of chromophores in amorphous hosts which we used as a starting point in further developments described below has been developed for glasses in ref. 46. In the absence of energy transfer the master equation for the SHB-modified absorption spectrum and the NPHB yield can be expressed as suggested in [7, 51, 53]:

$$D(\Omega, t) = 1.5 \int d\omega L(\Omega - \omega) G(\omega) \int d\lambda f(\lambda) \times$$

$$\times \int d\alpha \sin\alpha \cos^2\alpha \, e^{-P\sigma\phi(\lambda,\Gamma)L(\omega_B - \omega)t\cos^2\alpha} \tag{2}$$

$$\phi(\lambda, \tau_{EET}) = \frac{\Omega_0 \exp(-2\lambda)}{\Omega_0 \exp(-2\lambda) + \tau_1^{-1}} \tag{3}$$

Here:

- ω_B is the burn/excitation frequency, P is the photon flux and t is the burn time;
- σ is the integral absorption cross section

- ϕ is the HB quantum yield (essentially probability of conformational change)
- G(ω) is the Gaussian distribution of ZPL frequencies (site-distribution function, SDF);
- L(Ω–ω) is the single site absorption spectrum that consists of the ZPL and PSB;
- λ and f(λ) are the tunneling parameter and (Gaussian) distribution thereof, with mean λ_0 and standard deviation σ_λ.
- α is the angle between laser polarization and pigment's transition dipole
- τ_1 is, in the absence of energy transfer, fluorescence lifetime (note: in the case energy transfer is present, the EET time, τ_{EET}, should be used in the above equation as τ_1, see below)
- $\Omega_0 \exp(-2\lambda)$ is the NPHB rate and Ω_0 = 7.6 x 10^{12} s^{-1} is a constant pre-factor, the physical meaning of which is the attempt frequency. The numerical value, though somewhat exaggerated, has been kept the same as in [54, 59, 60, 69, 70] to allow for easy comparisons between λ–distribution parameters observed in various classes of systems (i.e., proteins versus simple organic glasses).

3.3. Spectral Hole Recovery

Although NPHB involves triggering small conformational changes by light, not all conformational changes are light-induced. Changes occurring in the dark (in the electronic ground state of the pigment-protein system) result in gradual recovery of spectral holes. In a hole recovery or temperature cycling experiment, first the protein is labeled with a narrow spectral hole at low temperature (e.g., T_b ~ 5 K) [61-66]. After burning, the hole is either allowed to recover at a fixed (burn) temperature (e.g. 5 K) or is

"thermocycled". In the latter experiments, the temperature is repeatedly cycled up and down again to the burning temperature, T_b and at this point the hole is measured again [61-68]. The highest temperature of the cycle is referred to as the excursion temperature, T_{ex}. Essentially, during recovery it is interesting to monitor the shape, the area, and the width of the hole. As to the shape, the Lorentzian profile of the hole is preserved during the temperature cycle [61-68]. The changes in the area and width of the hole provide information about energy landscape and hence yield information on the possible conformational changes of the protein. Area recovery and spectral diffusion broadening are considered independent processes [66-68]. In glasses these processes are attributed to extrinsic (TLS_{ext}, associated with the guest dye molecule and its inner shell of solvent molecules) and intrinsic (TLS_{int}, associated with the glassy host) TLS [69, 70]. In proteins they are assigned to different hierarchal tiers of the protein energy landscape. The change in hole area during a temperature cycle is associated with the number of molecules that returned from the product state (i.e. from the antihole, discussed in section 3.2) to the initial state at a given excursion temperature and hence, yields information on the barrier heights between these two conformational states. In case of proteins, one could argue that hole broadening is due to conformational changes on the fastest, smallest-barrier tier of the protein energy landscape (Figure 12), while the hole area decrease is due to relaxation on the next, higher-barrier tier [66 and references therein]. It was usually assumed (before us) that the holes recover exclusively due to barrier hopping upon thermocycling, with the probability of crossing barriers of height V being temperature-dependent and proportional to $exp(-V/k_BT)$ [66 and references therein].

Typically, the distribution of the barrier heights is derived from the equation of area recovery [61-68].

$$\frac{A(T)}{A_0} = \int_{V_T}^{V_{max}} p(V)dV$$

where:

- $A(T) / A_0$ is the ratio of the hole area after a complete temperature cycle and hole area immediately after burning (at temperature, T_b);
- V_{max} and V_T are the maximum barrier height and the barrier height which can be overcome at T_{ex}, respectively.
- p(V) is barrier height distribution [61-68].

Inversely, the experimentally measured dependence of hole area on excursion temperature is differentiated to obtain the barrier height distribution. We also include into consideration the effects of tunneling on hole recovery, which are actually dominant up to a certain temperature [66].

3.4. Parameters of the protein energy landscape in photosynthetic complexes

In the next chapter we are going to explore the effects of distributions of energy transfer rates on HB in photosynthetic complexes. Proper modeling of the hole spectra requires the knowledge of relevant parameters of the protein energy landscapes, namely the tunneling parameter distribution, which allows one to successfully disentangle the effects of tunneling and EET rate distributions (both cause dispersion of HB rates). Thus, we recently determined the parameters of the tunneling distribution for the lowest-energy pigments of several photosynthetic complexes in [71]. The HGK curves for a number of simple photosynthetic complexes including CP43, CP29, trimeric LHCII and monomeric LHCII have been reported in ref. 71. Parameters for B800 band of LH2 antenna complex of purple bacteria have been determined in [59]. Examples of the theoretical and experimental HGK curves are presented in Figure 13 and the tunneling distribution parameters are summarized in the Table 1 [59, 71].

Table 1. Tunneling distribution parameters used to fit the HGK curves (from ref. [59] and [71]).

	LH2[a]	**CP43, A-state**	**CP29**	**LHCII monomer**	**LHCII trimer**
λ_0	10.3±0.2	10.2±0.2[b]	10.2 ±0.2	11.3±0.2	11.2±0.2
σ_λ	0.7±0.2	1.0±0.05	1.4±0.2	2.0±0.2	2.3±0.2
S	0.45 ± 0.05	0.30±0.05	0.60±0.05	0.80±0.05	1.3±0.1

[a] from [59]
[b] corrected value for CP43 is given according to [71].

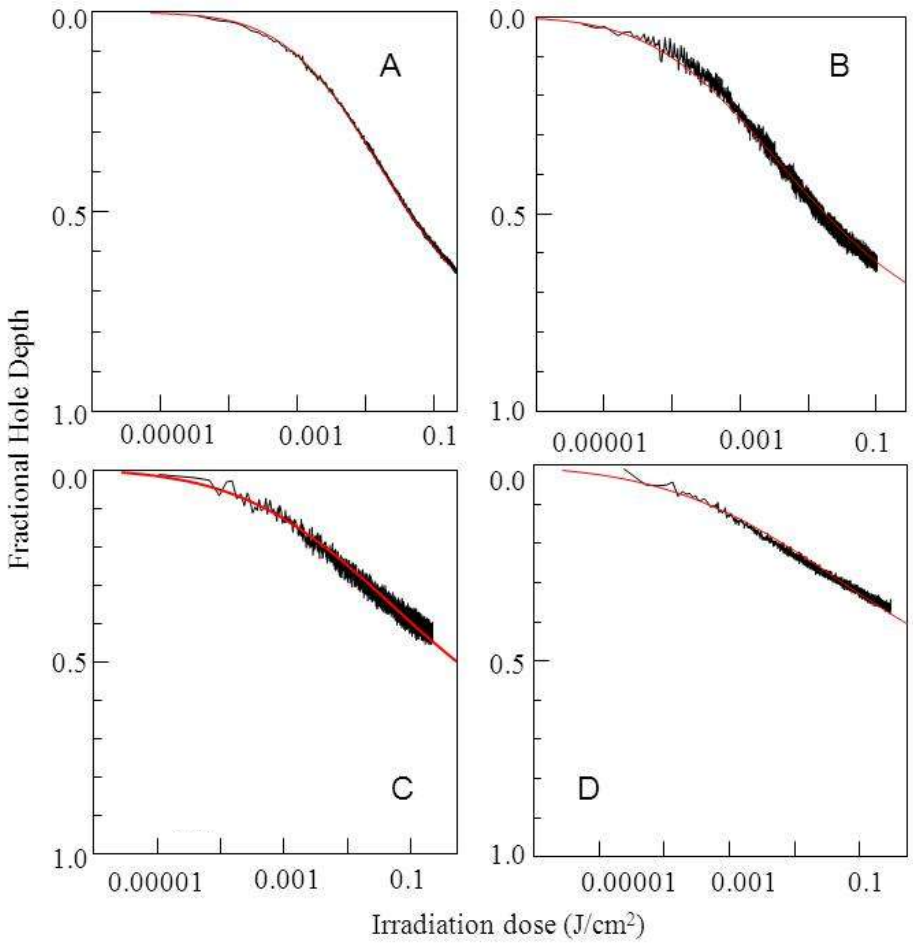

Figure 13. (A) HGK curve (noisy black curve) and its fit (red) for CP43 at 686.8 nm. (B) HGK curve (noisy black curve) and its fit (red) for CP29 at 681.7 nm. (C) HGK curve (noisy black curve) and its fit (red) for monomeric LHCII at 683.1 nm. (D) HGK curve (noisy black curve) and its fit (red) for trimeric LHCII at 684.2 nm. Reprinted with permission from ref.71. Copyright (2011) American Chemical Society.

It needs to be stressed that when HGK curves are being fitted, most of the parameters present in Eq 2 are fixed to values obtained from independent measurements. The PSB parameters can be obtained from analysis if either SHB or FLN spectra. The shape of the SDF is determined by measuring the HB action spectrum (hole depth dependence on wavelength for fixed illumination dose), etc. The burning parameters (laser excitation frequency, photon flux and burning time) and pigment photophysical properties (fluorescence lifetime and integral absorption cross section) are also known

from the literature. Thus, only the parameters of the line width and tunneling parameter distributions are treated as free parameters during simulations or fitting procedures.

The tunneling distribution parameters as well as the hole burning yields are significantly different in photosynthetic complexes than in molecular glasses (hyperquenched glassy water, [72-74] ethanol and methanol, [74] and ortho-dichlorobenzene, [75]). The latter exhibit λ_0 values around eight. This effect is most likely due to larger and heavier tunneling entities in proteins than in the amorphous host [60, 71].

3.5. Brief example of joint treatment of NPHB and recovery experiments: CP43

In the most of the studies performed in glasses [61-68] it was assumed and indeed apparently (see discussion below) observed that the ground-state barrier distribution *p(V)* is proportional to $V^{-1/2}$. However, there is a notable exception in the work of Love et al., who observed a Gaussian barrier distribution in the ground state of a glass-like mixed crystal, namely Tb^{3+} in the glasslike mixed crystal $Ba_{1-X-Y}La_xTb_yF_{2+x+y}$ [67]. Combination of Gaussian and $V^{-1/2}$ terms has been observed for proteins [67, 79]. On the other hand, HGK analysis is usually based on assumption of Gaussian distribution of tunneling parameter in the excited state. Recently we demonstrated that Gaussian barrier distributions more properly explain both the HB and recovery behavior of the CP43 complex. The details will be presented in the thesis of the fellow graduate student, Mehdi Najafi. Briefly, first we rigorously confirmed that tunneling is indeed the dominant mechanism behind hole burning in photosynthetic complexes (this is still a matter of debate, see for example ref. 61). The hole growth kinetics (HGK) curves at 686.1 ± 0.1 nm obtained for different temperatures are shown in Figure 14. The respective modeling

results (shown as smooth red lines) were based on the NPHB model presented in Section 3.2 [59 and references therein], assuming that the HB yield is temperature independent, and only the homogenous line width and Huang-Rhys factor S depend on temperature. The homogeneous line width dependence on temperature can be found in ref. 101.

It is apparent that the burning process exhibits a slowdown with increasing temperature (solid arrow), [66]. The good agreement between the experimental data and the fits to HGK indicates none or very weak temperature dependence of the SHB yield between 5 and 13 K [66]. At 13 K there is a small fraction of the systems that experiences somewhat accelerated burning in the beginning (shown by the dashed arrow) [66] which may indicate the onset of barrier-hopping. These results confirm tunneling in the excited state is the dominant mechanism of SHB in CP43, as barrier hopping would have much stronger temperature dependence.

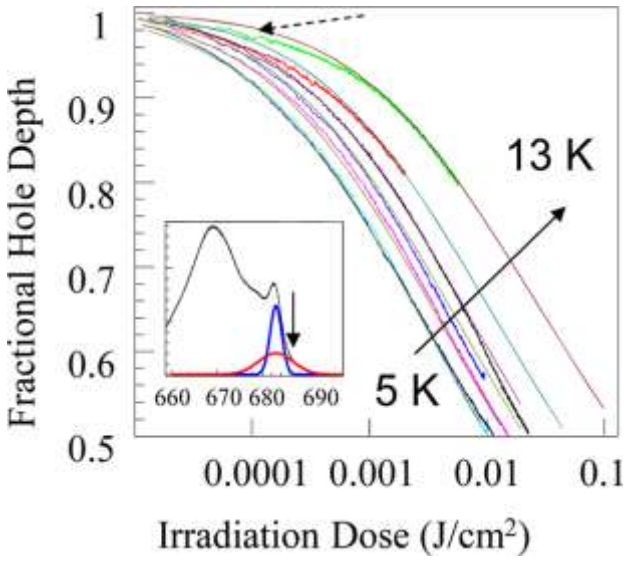

Figure 14. HGK curves for 5, 6, 7, 8, 10, and 13 K. The smooth curves are the fits to HGK curves. The parameters of the Gaussian λ-distribution obtained from the fit to 5K HGK curve are λ_0=10.2±0.1, σ_λ=1.1±0.1, with S=0.35±0.05. The insert depicts the absorption spectrum of CP43 (black) with the site distribution function of the A-band (red) and the B-band (blue). The down arrow indicates the burn wavelength. Reprinted with permission from ref.66. Copyright (2012) American Chemical Society.

The upper limit of md^2 parameter, characterizing the entities participating in conformational changes, was estimated as $md^2 = 1.0 \times 10^{-46}$ kg·m^2 [66]. However, there are some indications that 1.0×10^{-46} kg·m^2 is the true value of the md^2 and not its upper limit. If this is true, the tunneling entities can be either protons or the lighter of the protein side chains, such as a methyl group of alanine, for example. If the tunneling involves a proton, the respective distance, d, would be 2.45 Å, which is a typical hydrogen bond length. If it is a methyl group, the displacement along the generalized coordinate, d would be around 0.37 Å. Since the tunneling within a sufficiently long hydrogen bond is described by double-well potentials with d several times smaller than the hydrogen bond length [77, 78], the structural elements involved in tunneling in the CP43 protein are most likely the protein side chains, although proton tunneling cannot be excluded at this point [66 and references therein]. More details about the nature of the tunneling entities and its significance for the photosynthetic proteins structure are presented in ref. 66.

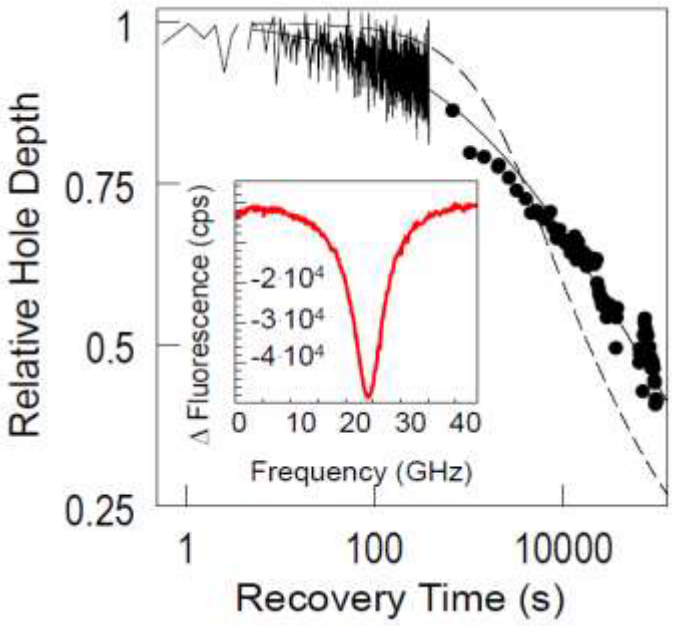

Figure 15. Hole-recovery data for 21%-deep hole, noisy curve and circles. Smooth solid curve (good fit to experimental data) results from modeling in Gaussian λ-distribution framework (see Fig. 16A), while dashed curve results from modeling in uniform λ-distribution framework (see Fig. 16B). The insert represents a sample hole spectrum (ref. 15, 66, 71). The datapoints presented as circles are result of averaging of about 40 points of the raw data. The size of the symbols is approximately equal to the size of potential error bar, ~0.02.

We also demonstrated that hole recovery measurements, especially fixed-temperature ones, can be used to determine the shape of the tunneling parameter and/or barrier height distributions (see discussion above on Gaussian versus $V^{1/2}$ barrier distribution). One should note that non-saturated holes are dominated by pigment-protein systems with smaller barriers, as these systems burn first. Figure 15 depicts recovery of the non-saturated holes of 21% fractional depth. The existence of the dependence of recovery rate on the depth of the hole (not shown) indicates that CP43 exhibits a significant degree of spectral memory [66]. This means that holes recover mostly as a result of the previously burnt molecules returning to ω_B, [66]. If holes were refilled by all systems, both burned and unburned, with identical barrier distributions (no spectral

memory), the dependence on depth would not be present. Perfect spectral memory is the only possibility in the case of pigment interacting with one TLS, see Figure 10, but in proteins with their multi-well landscapes the spectral memory may in principle not be present.

The partial excited-state λ-distributions, which actually contribute to the holes of the fractional depths of 21 and 55% for the Gaussian and uniform λ-distributions have been calculated and are shown in Figure 16. In the case of the uniform λ distribution model, corresponding to the barrier height distribution ~ $V^{-1/2}$, the shape of the partial distributions is highly asymmetrical, while Gaussian λ-distribution yields nearly Gaussian partial distributions as well. We showed that the uniform full λ-distribution corresponding to the barrier height distribution ~ $V^{-1/2}$ is in disagreement with the hole recovery experimental results (see Fig. 15).

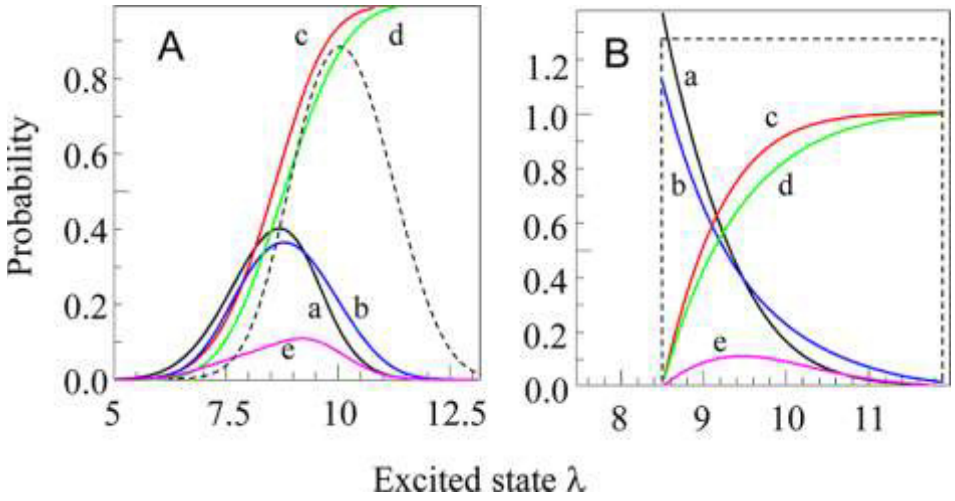

Figure 16. (A) Calculated excited-state partial λ-distributions for Gaussian true full λ-distributions (black: 20% deep hole, a; blue: 55% deep hole, b). Areas under curves are normalized to 1. The red (c) and green (d) curves are integrals of the black and blue curves, respectively. The magenta curve (e) is the difference between these integrals. The dashed curve is the true full λ-distribution. (B) Same for the uniform λ-distribution. Reprinted with permission from ref.66. Copyright (2012) American Chemical Society.

The results of the hole thermocycling experiments yield a Gaussian barrier distribution as well. Thus, there is no evidence for $\sim V^{-1/2}$ barrier distributions in CP43. Importantly, the above line of reasoning, based on partial distributions is not specific to proteins, which makes us question if the models leading to $\sim V^{-1/2}$ barrier distributions are correct even for glasses. Thus, one of the two energy-landscape tiers observed in this work and characterized by Gaussian distributions may reflect the dynamics of the amorphous host surrounding the protein (i.e., the frozen buffer/glycerol glass), rather than of the protein itself. These issues have been addressed in refs. [79, 80] but more experiments are necessary to clarify the origins of various tiers of the spectral diffusion dynamics in protein−chlorophyll complexes [66]. These studies include performing similar HB, recovery and thermocycling experiments in simpler protein systems (such as Cytochrome b_6f, possessing one Chl *a* molecule per protein monomer) and chlorophyll-doped organic glasses, as well as exploring the effects of deuteration on protein dynamics (work in progress).

4. Effects of the distribution of excitation energy transfer rates on NPHB spectra from photosynthetic complexes

4.1. Introduction. The excitation energy transfer (EET) processes in photosynthetic pigment-protein complexes determine the lifetimes of the excited states [82-85]. Due to the energy disorder imparted by the protein environment the EET rates as well as the charge separation rates in the reaction centers (RC) must be subject to distributions [86-89]. Although it has been known for a long time that SHB in pigment-protein complexes preferentially probes the slow EET rate wing of the distribution (as HB usually provides somewhat longer lifetimes than time-domain methods), this effect has not been explored quantitatively. Namely, to the best of our knowledge no one has discussed what errors are introduced by ignoring the EET rate distributions while interpreting the results of the SHB experiments in various systems. Although Reinot et al. briefly considered the effects of the (Weibull) distribution of homogeneous line widths due to irregularities of pure dephasing for Al-phthalocyanine in hyperquenched glassy water and ruled these effects negligible [90], the distribution parameters may be very different in the case of EET in photosynthetic complexes. Note that the distribution of EET rates originates from energetic disorder in photosynthetic complexes, not from differences from molecule to molecule in fast spectral diffusion as was the case in ref. 90.

In the absence of the distribution of homogeneous line widths, the hole burning process is governed by the distributions of the tunneling parameter λ, by the distribution of angle between the laser polarization and the transition dipole, as well as by ω-distribution reflecting non-resonant burning [90, 91], Equation 2. The combined influence of all distributions, including that of EET rates (homogeneous line widths) was

never explored in detail for photosynthetic complexes. Some time ago Riley et al. made [86] the first attempt to incorporate the homogeneous line width distribution into the SHB model of Hayes et al., [91] which does not include dispersion of the tunneling rates. As was suggested by Prokhorenko and Holzwarth, the excited state lifetime (in this case reflecting the primary charge separation time) of the P680 state of the RC of plant Photosystem II (PSII RC) is subject to a broad distribution [87]. Riley et al employed the (fast part of the) line width distribution from ref. 87 and successfully fitted the triplet bottleneck (transient) holes using the same site distribution function (SDF) and electron-phonon coupling parameters as for persistent holes burnt at the same wavelengths [86]. (Transient (usually triplet bottleneck) holes are the difference of absorption spectrum measured while the burning laser is on and the pre-burn absorption spectrum. Since in this case the burning mechanism is photochemical (even if reversible), the distribution of tunneling parameter is irrelevant here.) Thus, it was demonstrated that the electron-phonon coupling for both P680 and P684 states of the PSII RC (with P684 probably corresponding to a subpopulation of more intact RCs; see Chapter 4.5 for more details on this system) might be much weaker than previously believed. Therefore, the impact of the line width distributions on the hole spectra in photosynthetic complexes can be quite significant and cannot be neglected. Since the analysis of ref. 86 did not include λ- and α-distributions, the fitting of the persistent holes with one and the same set of parameters (including the burn dose) for all holes was impossible. Thus, persistent SHB data obtained for PSII RC from spinach will be discussed in the Section 4.5.2. In the case of Light Harvesting complex 2 (LH2), [59] we demonstrated that taking into account the line width distribution from ref. 59 does improve the agreement between spectral hole

simulations and experiment. The main focus of ref. 59 was, however, on protein energy landscapes and light-induced spectral diffusion, not on the line width distributions. The results of Ref 59 were subject of my M.Sc. thesis and will not be discussed here in detail.

One could also ask an even more ambitious question: can one reliably determine, from the SHB data, the whole EET time distribution at a given wavelength? This distribution could then be compared to theoretical predictions based on structural data, which in turn could yield additional information on transition energies in the absence of inter-pigment interactions ("site energies"), couplings of different Chls, and improved overall understanding of light-harvesting antennae. Calculations of optical spectra and EET rates between Chl molecules in various pigment-protein photosynthetic complexes became possible after the structures of these complexes were determined at high enough resolution by means of X-ray crystallography [29, 93-95]. A number of structure-based calculations were performed previously for example on cyanobacterial Photosystem I (PSI) [96, 97] and PS II [98], LH2 antenna complex of purple bacteria [99, 100], and FMO [99]. These simulations yielded new insight into the excitonic structure of these complexes, as well as important results in terms of possible origins of the lowest-energy antenna states, EET times, and trapping times. However, additional comparisons between the theory and experiment are necessary for refinement of the parameters of such calculations - namely, the sets of both inter-pigment coupling energies and the site energies. The conflicting information on these parameters, especially the site energies, is currently impeding the progress in matching the features of calculated and experimental spectra in most of the photosynthetic complexes. For example, in the case of the CP43 core antenna complex of PSII, [93] several assignments of quasi-degenerate lowest-

energy A and B bands (figure 14), [101] to different Chl molecules are possible [102]. In fact, by now, 8 out of 13 Chls have been suggested to be the lowest energy ones, contributing to either localized or delocalized states. Any such assignment requires certain assumptions about the site energies of the Chls. The same is true for PSII RC, FMO, and also for PSI, for which at least two sets of site energies are available in the literature, and different assignments of the lowest-energy antenna states are reported [96, 97, 103-106]. It is also not clear which EET theories yield the best agreement with experiment in cases when the energy donor or acceptor or both are states delocalized over a large number of strongly coupled molecules [107-108]. One of the ways to distinguish the "correct" chlorophyll-to-band assignments and/or EET theories would be through comparing theoretical predictions and observations concerning the excited state lifetimes (and their distributions) at various wavelengths.

One could argue that single photosynthetic complex spectroscopy (SPCS), when performed on a sufficiently large number of complexes, is capable of delivering the desired information on the EET rate distributions. In practice, however, low-temperature SPCS experiments are relatively difficult to perform; collecting statistically meaningful amounts of data takes a long time; and one often cannot be sure that SPCS results are free of systematic distortions originating from particular sample preparation procedures. For example, the sum of the many LH2 single complex excitation spectra from ref. 110 does not yield the bulk excitation spectrum, which may indicate that in SPCS samples the LH2 complex does not reside in the same local environment as LH2 complexes in the bulk samples. With respect to sample preparation, in ref. 111 it has been recently demonstrated that the nature of the solvent/matrix (buffer solution, glycerol/buffer mixtures, and PVA

films) determined the shape of the SDF and spectral diffusion parameters in the fluorescence emission of single PSI from cyanobacteria *T. elongatus* at cryogenic temperature (1.4 K). Hussels and Brecht showed that glycerol induces some suppression of conformational flexibility in individual PSI proteins and in the environment of the C708 chlorophyll molecules in particular [111]. (See Chapter 5 for discussion on various red states of cyanobacterial PSI.) In addition, small fluctuations of width and position of the spectral lines systematically affect the results of SPCS experiments [112], increasing the line width averages beyond those corresponding to the results of SHB and even of the time domain measurements. Obviously, the distributions of EET times should also be apparent in the time-domain experiments. Finally, SPCS experiments by necessity use very large excitation intensities, which may induce local heating of the sample.

Time-domain experiments do not exhibit detection preference for slower kinetics. However, the common practice is to fit the time-domain results with a minimal number of decay exponents (see, for example, refs 102 and 113 for CP43 and refs 88 and 114-116 for PSII RC, as well as refs 117-119 for other complexes). Note that even in refs 89, 120, and 121, although the likely lifetime distributions have been reported, for instance as lifetime density maps, the fitting of the time-dependent behavior at each point still involved just several (3-6) exponents.

Consequently, it would be of considerable interest to explore if it is possible to develop a methodology of reliably extracting EET rate distributions from the SHB data. To achieve this goal, one would have to develop a detailed understanding of the combined influence of EET rate distributions and other factors affecting the shape of the hole spectra and their time (irradiation dose) evolution and to learn disentangling these

effects. The range of tunneling parameters typical for photosynthetic proteins has recently been determined, see Section 3.4 [59, 71]. A brief summary of the effects of the tunneling parameters on the shape of the spectral holes is also presented in that section. All this provides the background necessary to start fitting the results of spectral hole burning experiments (whole hole shape evolution experiments as in refs 104 and 122 and hole growth kinetics (HGK) measurements as in refs 123 and 124) in photosynthetic complexes with the purpose of determining the EET rate distributions. We will also examine some EET (or charge separation, [86]) rate distributions from the available literature and analyze their agreement or disagreement with the SHB data.

4.2. Model Basics. The first step would be to incorporate EET rate (or homogeneous line width) distributions into the model from ref. 60 described in the previous chapter:

$$D(\Omega,t) = 1.5\int d\omega L(\Omega-\omega,\tau_{EET})G(\omega)\int d\lambda f(\lambda)\int d\Gamma h(\Gamma)\times$$

$$\times\int d\alpha \sin\alpha\cos^2\alpha\, e^{-P\sigma\phi(\lambda,\Gamma)L(\omega_B-\omega,\tau_{EET})t\cos^2\alpha} \quad (4)$$

$$\phi(\lambda,\tau_{EET}) = \frac{\Omega_0\exp(-2\lambda)}{\Omega_0\exp(-2\lambda)+\tau_{fl}^{-1}+\tau_{EET}^{-1}} \quad (5)$$

h(Γ) is the distribution of homogeneous line widths, which are proportional to EET rates. The hole burning yield now explicitly depends on the EET time, and is reduced if EET is present. The homogeneous line widths, the widths of the Lorentzian ZPL part of *L(ω)* have been modified as follows [60]:

$$\Gamma = (2\pi c\tau_{EET})^{-1} + (2\pi c\tau_{fl})^{-1} + (\pi c\tau_2{}^*)^{-1} \quad (6)$$

Here τ_2* is pure dephasing time, temperature-dependent. The effects of the EET rate / homogeneous line width distributions on the SHB spectra of several photosynthetic complexes will be presented in Chapter 4.4 of this thesis.

It is obvious that modeling spectral holes in the presence of multiple distributions requires significant computational resources. To improve calculations speed, the angular integral was treated as

$$F(x) = 1.5\int d\alpha \sin\alpha \cos^2\alpha \cdot e^{-x\cos^2\alpha} = \frac{1.5}{x}\left[\frac{\sqrt{\pi}}{2}\frac{erf(\sqrt{x})}{\sqrt{x}} - e^{-x}\right] \quad (7)$$

which in turn was fitted with a polynomial for x<10 and with $(1/x)\sqrt{9\pi/16x}$ for x>10 [70]. Integrals over λ and the homogeneous line width were calculated as sums with up to 100 (usually less) components each; the fast Fourier transform algorithm was utilized for convolution / integration over ω. We assumed that there is no correlation between the SHB rate $\Omega_0\exp(-2\lambda)$ (governed by the protein energy landscape parameters) and the energy transfer time (governed by the inter-pigment interactions and spectral overlaps). This means that the probability of a certain combination of Γ and λ is proportional to $f(\lambda) \cdot h(\Gamma)$. In complicated enough excitonically coupled systems with multiple EET pathways, depending on particular realizations of disorder, the latter assumption may not always be valid. Namely, certain states may be dominated, even at the same fixed wavelength, by different Chls in different complexes, which may exhibit distinct distributions of HB yields and transfer excitation energy along distinct paths characterized by distinct distributions of EET rates [60].

As a first step, one can experiment with simple Gaussian distributions of EET rates. Although this may sound artificial and oversimplified, EET rate distributions resembling Gaussian are possible, for instance they have been suggested for B800-B850

EET in the LH2 complex of purple bacteria, and result from including the whole density of states, including upper excitonic states of B850 ring, into consideration of EET in so-called extended Főrster models [59, 107-109]. This has been discussed in detail in the M.Sc. thesis of Somaya Ahmouda, so we only present a brief summary here.

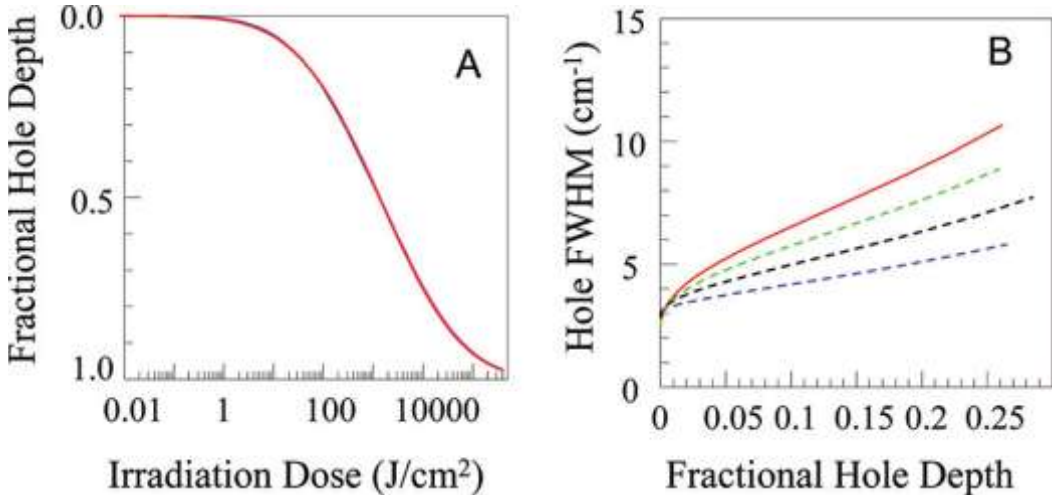

Figure 17. **Frame A:** Indistinguishable HGK curves for different combinations of λ-distribution and line width distribution parameters (see below). **Frame B:** Easily distinguishable hole width dependences on the hole depth for the same parameters as in frame A. Red curve: line width distribution peaking at 3.0 cm^{-1} with fwhm = 3.0 cm^{-1}, λ_0= 10.0, and σ_λ = 1.0. Green: line width distribution peaking at 2.5 cm^{-1} with fwhm =2.1 cm^{-1}, λ_0 = 10.15, and σ_λ = 1.0. Black: line width distribution peaking at 2.0 cm^{-1} with fwhm = 1.3 cm^{-1}, λ_0 = 10.2, and σ_λ = 1.0. Blue: single line width 1.5 cm^{-1}, λ_0 = 10.5, and σ_λ = 1.0. Reprinted with permission from ref.60. Copyright (2011) American Chemical Society.

It appears one can develop a procedure to determine the parameters of both line width and λ-distributions without pre-existing knowledge of any of them (it is only assumed that both are Gaussian): First one should fit the HGK under the assumption of the absence of a line width distribution. This will provide: (i) a reasonably close estimate of σ_λ; (ii) the lower limit of the mean of the line width distribution, and (iii) the upper limit for the tunneling distribution mean, λ_0. If in fact the line width distribution is present, the theoretical hole width dependence on depth calculated with these parameters will deviate

significantly from the experimental one. Then one is supposed to vary the line width distribution until good fit to hole FWHM dependence on fractional depth is achieved.

Figure 17A shows both the HGKs and hole width dependences on hole depth obtained for different combinations of λ_0, σ_λ, and the mean and width of the line width distribution [60]. Suppose that the red solid curves in Figure 17 (calculated with $\lambda_0 = 10$ and $\sigma_\lambda = 1$, with the mean and the width of the line width distribution both being 3 cm^{-1}) represent the experimental data. One can notice that Figure 17A contains indistinguishable HGK curves while Figure 17B exhibits easily distinguishable hole width dependences on hole depth for the same combinations of parameters as in Figure 17A. Note that σ_λ essentially does not change between different data sets, while λ_0 changes only a little. All dependences in frame B extrapolate to approximately the same width at zero depth (the first 1% of the curve can be ignored if we assume a realistic S/N ratio of 100 in experimental data). Thus, we concluded that simultaneous fitting of both types of data can yield the parameters of both distributions [60].

4.3. EET rate distributions for simple Förster – type model

4.3.1. Effects of EET on resonant HB. Another, qualitatively different class of homogeneous line width distributions can be obtained for a simple model describing Főrster-type EET [125] between relatively weakly coupled pigments with uncorrelated site distribution functions (SDF). This approach is appropriate for small antenna proteins such as CP43 [101, 126], CP43' (or *IsiA* (CP43'), peripheral antenna complex of cyanobacterial PSI in the case of iron-deficient environment) [127], CP29 [71] and LHCII [114] where the majority of the pigments are weakly interacting. Detailed discussions on the applicability of the Förster model and different variations of the

Redfield model (density-matrix based approach) can be found in refs 128-132 (Dexter EET, involving electron exchange, is not present for pigment molecules separated by several nanometers. For these distances, dipole-dipole approximation is reliable for calculating inter-pigment interaction energies.) Roughly, for weak enough inter-pigment coupling ($V \leq 10\text{cm}^{-1}$) leading to slow enough excitation energy transfer between ($\tau_{EET} >$ 10 ps) the EET process can be described by Förster theory and the inter-pigment coupling $V_{1,2}$ can be can be calculated in dipole-dipole approximation, [8, 9]:

$$V_{1,2} = f\kappa \frac{\mu_1 \mu_2}{R^3}.$$

Here τ_1 and τ_2 are transition dipole moments of pigments 1 and 2, κ is the orientation factor (-2…+2), f is the local field correction factor, depending on dielectric constant, and R is the distance between the molecules.

In 2007 Zazubovich and Jankowiak [126] introduced a model describing non-resonant spectral hole burning and HB action spectra for the case of two quasi-degenerate bands belonging to pigments connected by relatively slow excitation energy transfer (slow enough to obey Förster theory [60]). The first version of the model, not including spectral overlaps, has nevertheless been successful in qualitatively explaining the shapes of various non-resonant HB spectra and the HB action spectrum in CP43, as well as its fluorescence spectrum. Later the model has been extended to the CP43' ring of the CP43'-PSI supercomplex, with each A or B-type pigment having five nearest neighbors of A and B variety (still, with no treatment of spectral overlaps) [60]. Here we essentially report proper inclusion of real single-site spectral shapes and spectral overlaps into Förster-based model.

In Főrster theory, EET rate depends on the parameters of the single-molecule spectra according to:

$$k_{ET}(\sim \Gamma_{\text{hom}}) = \frac{2\pi V^2}{\hbar} \int E_D(E) A_A(E) dE \,, \qquad (8)$$

where E_D and A_A are single-site donor emission and acceptor absorption spectra, including various vibronic contributions, normalized to unity on the energy scale, and V is the inter-pigment coupling energy. The integral in the equation above is the spectral overlap integral. Equation 8 illustrates that, in addition to inter-pigment interaction energies, the EET rates are governed by the overlaps between the donor emission and acceptor absorption spectra. This is the consequence of conservation of energy; availability of phonons or vibrations necessary to achieve energy balance affects the EET probabilities. A simple theory of dispersive kinetics of (low-temperature) EET resulting from the distribution of spectral overlaps has been developed by Kolaczkowski et al., [133] but their approach has significant limitations. That is, some of the approximations made in ref 133 are in fact not valid at liquid helium temperatures, where SPCS and SHB experiments are normally performed. Additionally, Kolaczkowski et al. considered, for the sake of simplicity, Gaussian distributions of either localized or delocalized phonons, which are not sufficiently good reflections of a phonon sideband shape in a single-site spectrum. Today the parameters of electron-phonon and electron-[intra-molecular vibration] coupling (phonon sideband shape, frequencies, and Huang-Rhys factors S of PSB and intra-molecular vibrations) are sufficiently well-known from SHB [134, 135] and Fluorescence Line Narrowing (FLN and ΔFLN) experiments, [136-138] and one can synthesize single site spectra and calculate relevant spectral overlaps numerically.

The spectral overlap dependence on the donor-acceptor ZPL gap can be calculated taking into account that such dependence is essentially equal to a convolution of the absorption single-site spectra of the donor and acceptor (provided there is mirror symmetry between emission and absorption single site spectra). If the latter two spectra are normalized, the proper normalization of the overlap integral dependence on the D-A gap can be easily determined via

$$\int_0^\infty (A_A(E) \otimes A_D(E))dE = \int_0^\infty A_A(E)dE \times \int_0^\infty A_D(E)dE \qquad (9)$$

where $\otimes$ denotes convolution; A_D is the donor absorption; and other variables are as in Eq 8. In particular, if both single-site spectra are normalized to one on energy scale as required by Eq 8, the overlap integral **dependence** on the donor-acceptor gap (NB: not the overlap itself) also will be normalized to one.

The prevalence of given overlap (i.e. of given rate) depends on the prevalence of the pigment pairs possessing given donor-acceptor gap, defined as ZPL-ZPL gap. In other words, it depends on the SDF of donor and acceptor pigments. Figure 18 resembles that from [126] and considers a hypothetical case of two pigments, possessing identical (degenerate) site distribution functions (SDF), and connected by EET (i.e. belonging to the same complex; similar situation, but with three pigments, most likely arises for the lowest-energy states in the trimeric FMO complex, see Section 4.4.2.). In a given complex one or another pigment can be lower in energy due to disorder, and their energies are independent. Solid overlapping curves (a) and (b) (labeled as a/b) represent identical true full SDF of pigments 1 and 2, respectively. (We use term “true full” to distinguish these SDF from sub-SDF introduced below). Curve (c) reflects the probability that the energy of a chromophore 1 (or 2) is lower than the energy on the x-axis.

Essentially, curve (c) represents a properly normalized integral of curve (a/b), or so called cumulative distribution. The SDF of a sub-ensemble of pigments 2 (or 1) capable of downhill EET to pigments 1 (or 2) (curve d) is the product of the curves (b) and (c), representing the probability to find pigment 2 (1) at given energy and the probability to find pigment 1 (2) at the energy lower than given energy. Curve (e), the SDF of a sub-ensemble of pigments being the lowest-energy pigments in their complexes, is the difference of curves (b) and (d). Summarizing, curve (d) reflects the sub-SDF of pigments 1 and 2 capable of downhill EET, and curve (e) reflects the sub-SDF of the pigments 1 and 2 incapable of EET (since they are the lowest-energy ones in a complex).

The above treatment can be easily extended to the case of several competing acceptors. The lifetime of the excited state of the donor will be determined by the sum of the rates of energy transfer from the donor to every available acceptor. It is known from statistics that the probability distribution for the sum of two or more independent variables is the convolution of the distribution functions for every variable. Note that the rate distributions, not the overlap distributions, have to be convoluted. Determination of these, as well as calculation of the line widths in the one donor and one acceptor case, requires knowledge of the inter-pigment interaction energies, V, not just the spectral overlap distributions discussed above. These energies are obviously system-dependent, and one would have to consider particular complexes, as we will do in sections 4.4.1 and 4.4.2 for CP43 and FMO, respectively. In the case of several independent donors with quasi-degenerate SDFs, the resulting distribution can be obtained by adding the distribution functions obtained in the previous step for every donor separately, weighted by the magnitudes of the contribution of each donor at ω_B.

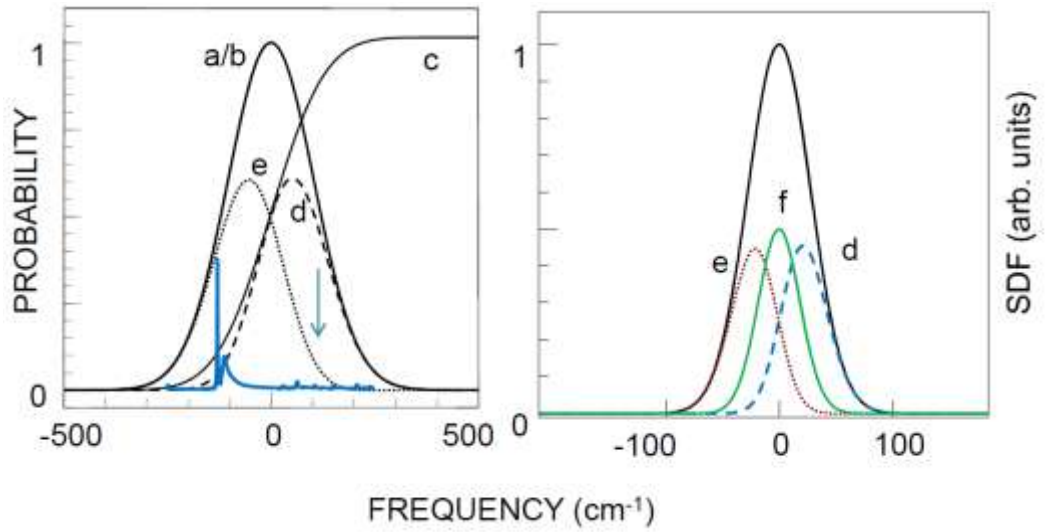

Figure 18A. Total SDF and sub-SDF in the case of two pigments with identical SDF. Blue curve is the absorption spectrum of a molecule with ZPL relatively low in energy, which is excited at higher energy via its phonon sideband or vibronic replicas. **Figure 18B:** the full SDF of three identical pigments with FMO 825 nm band parameters and three sub-SDF corresponding to the lowest-energy pigments (e), pigments with one donor and one acceptor (f) and highest-energy, two-acceptor pigments (d). Zero corresponds to 12116 cm^{-1}.

4.3.2. Non-resonant burning without burning via EET. In our earlier simulations of EET-influenced SHB in CP43 [60] the EET rate distributions have been calculated once, at burn wavelength. This is, however, appropriate only for the analysis of the resonant holes. (Since only the resonant holes have been simulated in [60], the results presented for CP43 in Section 4.4.1 are still correct.) By the time we started working on FMO, Section 4.4.2, we recognized that for the analysis of non-resonant parts of the spectrum (pseudo-PSB and burning following the EET) one needs to introduce frequency-dependent EET-rate distributions.

Suppose we illuminate the system depicted in Figure 18A at the blue edge of the joint SDF of two identical pigments (a/b), blue vertical arrow. The absorption at this wavelength will be dominated by pigments having a lower-energy partner and

experiencing downhill EET (curve d). The distribution of EET rates at burn wavelength will determine the evolution of the resonant hole. However, the pseudo-PSB contribution to the hole spectrum originates from pigments excited via their phonon- or vibration sidebands. The absorption spectrum of a molecule contributing to pseudo-PSB is shown by a blue curve. Assuming the HB occurs in vibrationally relaxed state, the HB yield distribution for such molecules will be determined by the wavelength of the ZPL (burnt via their PSB or vibronic replicas), not by the burn wavelength. As probability of EET decreases towards longer wavelengths, the average HB yield should increase (see eq. 5). One can generate multiple sub-SDF, each one corresponding to just one of all possible EET rates. The sub-SDF for zero EET rate would be, in the case of two identical pigments depicted in Figure 18A, just the curve (e). However, sub-SDFs can be calculated also for all other rates. The sum of all sub-SDF for non-zero rates will yield curve (d). These sub-SDF are in general non-Gaussian. Figure 19 shows a set of distributions for a dimer with inter-pigment coupling V=3cm^{-1} and other parameters from FMO complex, section 4.4.2. It is clear that for some EET rates / homogeneous widths the sub-SDF are even two-headed. For each fixed-rate sub-SDF the effect of the EET rate on HB yield (see Eq. 5) is also fixed, and not wavelength-dependent. The sub-SDF for zero EET rate (curve e in Figure 18A) is not shown here, as its integral intensity is equal to the integral intensity of all curves in the Figure 19 combined. The sum of all curves in the Figure 19 yields curve d in Figure 18A.

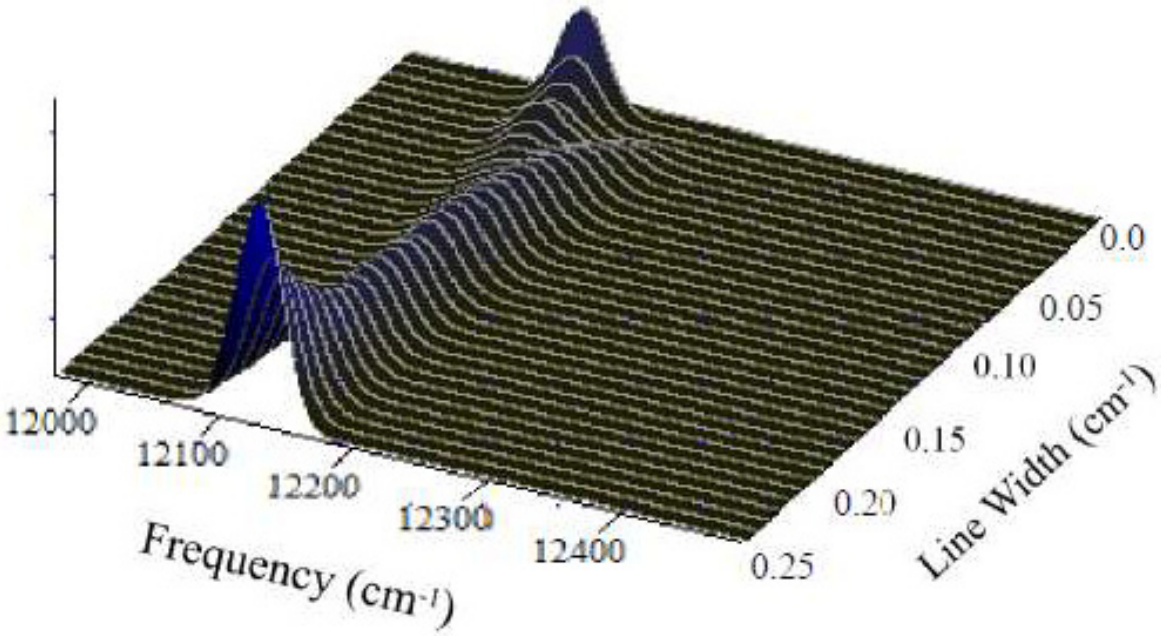

Figure 19. Example of sub-SDF for different EET rates for one-donor-one-acceptor pigments (V=3 cm^{-1}, the width SDF is 65 cm^{-1} and the SDF peak position: 12116 cm^{-1}). "ZPL width" includes only EET contribution to the width; pure dephasing and width corresponding to fluorescence lifetime are not included.

In the case of trimeric complex (e.g. FMO), one has to consider the case of three, rather than two, identical overlapping bands. For three pigments one can think of one donor and two potential acceptors, remember that EET rates have to be summed, and that the distribution of the sum of two independent variables is the convolution of the respective distributions. The resulting distribution will start at twice the minimal rate (most likely still zero) and end at twice the maximal rate for a dimer. The three pigment analog of Figure 18A is presented in Figure 18B. For the sake of consistency with Figure 18A, the lowest-energy of the three sub-SDF is still labeled (e) and the highest-energy sub-SDF is labeled (d). The middle sub-SDF, corresponding to the pigments with one donor and one acceptor, is labeled (f).

Combining various sub-SDF with proper weights determined by the emission probabilities

$$p_{em} = \tau_{fl}^{-1} / (\tau_{fl}^{-1} + \tau_{EET}^{-1})$$

one can obtain the emission origin and, convoluting it with the single site emission – the bulk emission spectrum. Obviously, the contribution of non-zero EET rate sub-SDFs to the emission origin will strongly depend on the inter-pigment coupling. This allows for an estimate of inter-pigment coupling based on the emission spectrum.

Also, we took into account that protein phonons are delocalized and same phonon is coupled to both donor and acceptor pigments. As a result, the phonon part of the overlap function should resemble the single site spectrum rather than convolution of the donor and acceptor single-site spectra [139].

4.3.3. Burning via EET – two pigments system. The above discussion involved burning of pigments via their own PSB or vibronic replicas. Proper modeling of the whole hole spectra in multi-pigment systems, including the part to the red of the resonant ZPH, requires introduction of NPHB of the acceptor molecule following EET from one pigment to another. This will be done by establishing additional contributions to the single-site spectrum in the exponential of Eq. 4. First we consider the case of two pigments: In the exponential in Eq. 4, $e^{-P\sigma\phi(\lambda,\Gamma)L(\omega_B-\omega,\tau_{EET})t\cos^2\alpha}$ the HB yield describes the probability that the pigment (with ZPL at ω) will experience NPHB while in excited electronic state. The rest of the exponential describes the number of photons that a pigment with ZPL at ω will absorb at λ_B (within time t). Once the photon is absorbed, the energy can be either emitted as fluorescence or transferred to another

pigment with ZPL at ω'. In both cases, the pigment may experience NPHB while it is in the excited state.

The probability that the pigment with ZPL at ω will transfer energy to pigment with ZPL at ω' can be calculated from the spectral overlap dependence on donor ZPL – acceptor ZPL gap. (As stated above, one is supposed to use PSB part of the single-site spectrum rather than overlap of two PSB in the spectral region of delocalized phonons.) This spectral overlap dependence on $(\omega-\omega')$ can be converted into the dependence of EET probability on $(\omega-\omega')$ according to

$$p_{EET}(\omega-\omega') = \tau_{EET}^{-1} / (\tau_{fl}^{-1} + \tau_{EET}^{-1}) .$$

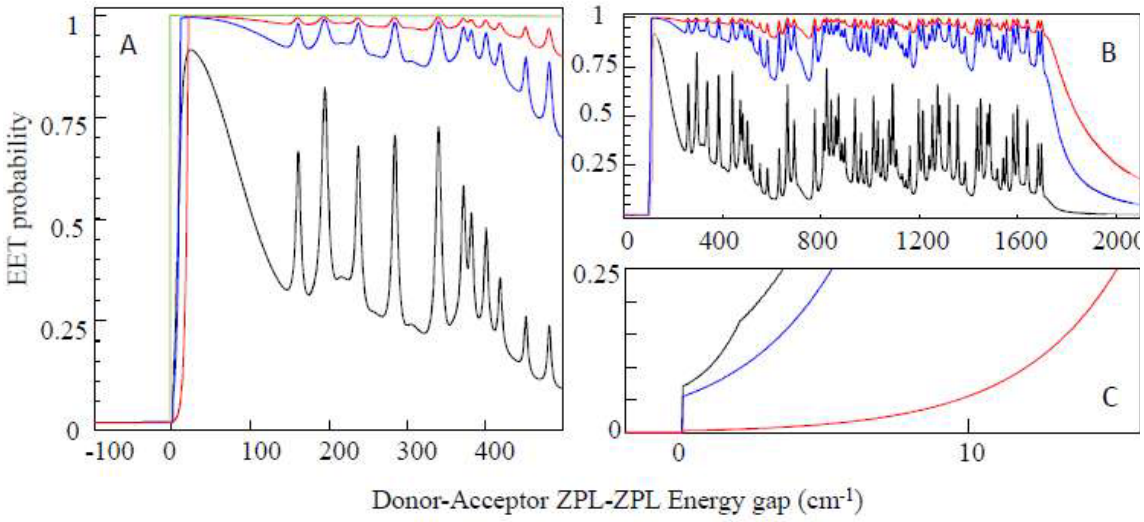

Figure 20. Dependence of the probability of EET on donor-acceptor ZPL gap for different values of inter-pigment coupling (where the probability functions for V=1cm^{-1}, V=5cm^{-1} and V=10cm^{-1} are the black, blue and red curve respectively; the green curve is the probability function resembling the step function of Jankowiak et al); all single-site spectrum parameters from FMO.

The dependence of p_{EET} on donor-acceptor energy gap for several values of inter-pigment coupling is depicted in Figure 20. We stress that dependence presented in Figure 20 reflects only the dependence of probability of EET on the ZPL-ZPL energy gap, but

does not include the probabilities of various gaps. As can be seen, for V~10 cm^{-1} the probability function resembles the step function of Jankowiak et al (green). Below 10cm^{-1}, the shape of the EET probability function bears some memory of the single-site spectrum.

In order to calculate the probability that excitation at ω_B will result in burning of pigment with ZPL at ω' via EET, one needs to sum the probabilities, for all possible combinations where $\omega_B - \omega'$ is fixed, of i) exciting, at ω_B, the donor pigment with ZPL at ω and ii) EET from ω_B to ω'. The former one (labeled * in the following discussion) is proportional to the product of the single molecule emission spectrum peaked at ω_B (note ω_B argument of single-site spectrum $L(\omega)$ in the exponential in Eq. 4) and the sub-SDF of the donor molecules (curve (d) in Figure 18) at ω. The sum of probabilities can be imagined as the overlap of $p_{EET}(\omega - \omega')$ and the above product (*). By analogy with calculating the spectral overlap dependence on donor ZPL - acceptor ZPL gap, the dependence on ω' of probability of exciting pigment with ZPL at ω' via EET following excitation at ω_B will be proportional to convolution of $p_{EET}(\omega - \omega')$ with mirror image of function (*). If we label the latter convolution $L'(\omega')$, then SDF of molecules burnt via EET only will be described with

$$G_0(\omega')e^{-P\sigma\phi(\lambda,\tau_{fl})L'(\omega_B-\omega')t\cos^2\alpha}.$$

Note that HB yield does not depend on the wavelength here, as this expression applies only to the sub-SDF with no further EET, G_0 (curve (e) in Figure 18). Pigments described by other sub-SDF are donors, and in the two-pigment case they cannot be burnt via EET. The total effect on the sub-SDF (e) is described with

$$G_0(\omega')e^{-P\sigma\phi(\lambda,\tau_{fl})[L'(\omega_B-\omega')+L(\omega_B-\omega)]t\cos^2\alpha}\cdot$$

and it is obvious that deeper pseudo-PSB hole is expected due to EET than without taking EET into account.

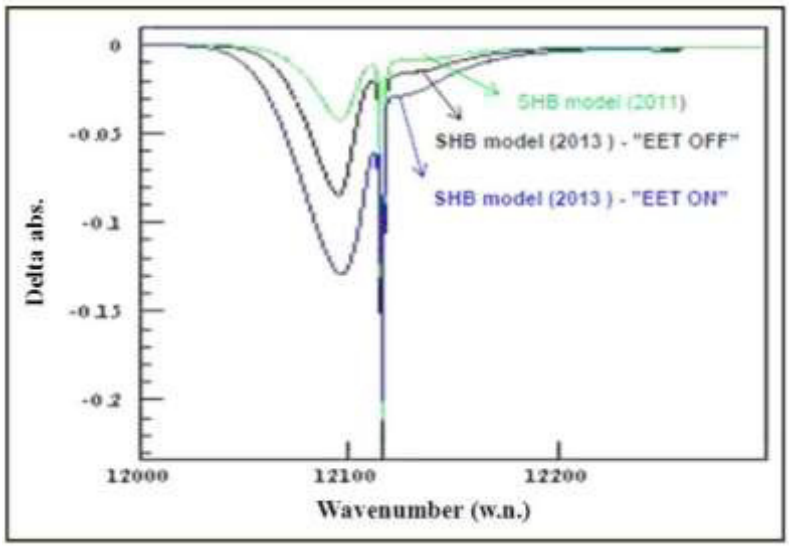

Figure 21. HB spectra taking EET into account to different degrees. V=3 cm^{-1} and no anti-hole was considered; the illumination dose was same in all three cases, The green curve has been obtained with SHB model that included the EET rate distributions at burn wavelength and no burning via EET, [60]; the black curve has been calculated including only wavelength dependent EET rate distribution; the blue curve has been calculated considering both the wavelength dependent EET rate distribution and burning via EET.

Concerning the proper normalization of *L'(ω')* one could argue that we are re-using the same excitations which were absorbed by the (EET-capable fraction of the) sample, curve (d) in Figure 18, in the first place. The total number of photons absorbed by the EET-capable pigments is proportional to the area under the product of the single-site emission spectrum peaked at ω_B and the sub-SDF of the donor molecules (* above). (This area is proportional to donor absorption at ω_B). These excitations, minus the losses to emission, are redistributed over the acceptor molecules (e) with ZPL at energies lower than ω_B. Thus, the $L'(\omega_B-\omega')$ has to be normalized in such way that the area under the

product of $L'(\omega_B-\omega')$ and the acceptor sub-SDF (curve (e) in Figure 18) is the average EET probability times the area under the product of single-site emission spectrum and the sub-SDF of the donor molecules (*).

The situation gets somewhat more complicated in the case of the trimer. The EET contribution to burning of the lowest-energy pigment due to exciting the pigments with one donor and one acceptor (curve (f) in Figure 18) can be calculated as described above, except the sub-SDF of the one-donor-one-acceptor pigments (curve (f) in Figure 18) should be used instead of the sub-SDF of donor pigments of the two-pigment case (and the sub-SDF for the lowest-energy pigments will be somewhat different, see curve (e) in Figure 18).

At the first glance the burning of one-donor-one-acceptor pigments (f) and of the lowest-energy pigments (e) due to direct transfer from the highest-energy, two-acceptor pigments (curve (d) in Figure 18) should follow the same logic. However, one has to take into account that in reality EET is limited to within one single trimer, and the excitation can be transferred to either one of the acceptors, it is a competitive process. The fractions of excitation transferred in one step to one-donor-one-acceptor pigments (f), and directly to the lowest-energy pigments (e) scale as $\tau_{EETf}^{-1}/(\tau_{EETf}^{-1}+\tau_{EETe}^{-1})$ and $\tau_{EETe}^{-1}/(\tau_{EETf}^{-1}+\tau_{EETe}^{-1})$, respectively (subscripts match the band labeling in Figure 18). And these fractions will generally be not identical due to difference in spectral overlaps. The smaller fraction of energy absorbed by the highest-energy pigments (d) will follow directly to the lowest-energy pigments in the trimer (e), and the larger fraction will follow to one-donor-one-acceptor pigments (f). The latter fraction can be redistributed over one-donor-one-acceptor sub-SDF corresponding to different rates of EET according

to their relative areas (see Figure 18). The excitations transferred from the highest-energy pigment to one-donor-one-acceptor pigment can then further follow to the lowest-energy pigment… Note that the photon absorbed by the highest-energy, two-acceptor pigment has three chances of causing NPHB, and the photon absorbed by the one-donor-one-acceptor pigment has two chances of causing NPHB!

The shape of the curve $L''(\omega_B-\omega'')$, the analog of the single site spectrum for sequential, two-step, transfer to the lowest-energy pigments at ω' can be calculated as follows: By analogy with the above, one has to sum the probabilities, for all possible combinations for which $\omega_B-\omega''$ is fixed, of i) exciting, at ω_B, the highest-energy pigment with ZPL at ω and ii) EET from ω to ω'', where ω'' is the ZPL frequency of the pigment with one donor and one acceptor and iii) EET from pigments with ZPL at ω'' to pigments with ZPL at ω'. To do that, one has to first calculate $L'(\omega_B-\omega')$ with ω'' being the ZPL frequency of the pigment with one donor and one acceptor, and find the product of this curve with the sub-SDF of one-donor-one-acceptor pigments. This product, an analog of (*), is proportional to the probability that excitation ends up on a one-donor-one-acceptor pigment with ZPL at ω''. Then, the mirror image of the latter product has to be convoluted with the function describing EET probability between pigments with ZPL at ω'' and ω', respectively.

4.3.4. Treatment of EET in the case of small donor-acceptor gaps. The issue of EET in the case when pigments have resonant ZPLs is relatively unexplored. Obviously, some ZPL-ZPL overlap can be present only if inter-pigment coupling is small. Otherwise excitonic splitting will ensure that degeneracy is removed, at least in the case of a dimer. The relaxation from higher to lower excitonic states will be described by coherent

population oscillations [140]. For weakly coupled, well spatially separated pigments, the Förster approximation should be sufficient. The detailed expression for the Förster EET rate can be found in Parson [140].

$$k_{rt} = \frac{2\pi}{\hbar}|V|^2[\sum_n \sum_m \frac{\exp(-E_{vib,n,1}/k_B T}{Z_1}|\langle \chi_{1m}|\chi_{1n}\rangle|^2 \times$$

$$\times \sum_u \sum_w \frac{\exp(-E_{vib,u,2}/k_B T}{Z_2}|\langle \chi_{1w}|\chi_{1u}\rangle|^2]\delta(\Delta E_1 - \Delta E_2)$$

Here *n* and *m* label vibrational levels of molecule 1, *u* and *w* label vibrational levels of molecule 2. χ are vibrational wavefunctions, $E_{vib,n,1}$ and $E_{vib,w,2}$ are energies of vibrational levels *n* and *w* of molecules 1 and 2, respectively, relative to the zero-point levels of molecules 1 and 2. The delta-function ensures conservation of energy and *Z* are vibrational partition functions. The above equation contains Franck-Condon factors for various vibronic transitions. As the 0-0 transitions are not excluded, one should consider ZPL-ZPL overlap as part of the whole spectral overlap of the Förster model.

In [60] the overlap integral dependence of the donor-acceptor ZPL gap has been calculated simply as a convolution of the single site absorption spectra for donor and acceptor, including ZPL. Then it was multiplied by V^2 and a normalization constant accounting for fundamental constants and unit conversions. The result was the homogeneous line width dependence on donor-acceptor gap. However, it is easy to see that while this procedure gives correct line widths for gaps over several cm^{-1}, it does not work correctly when ZPLs are nearly in resonance. As shown in Figure 22, if the dephasing-limited width is used for both spectra being convoluted, then the peak of the dependence of EET-determined line width on the energy gap corresponds to a line width

of 13.4 cm^{-1} (blue curve; peak is truncated to allow showing details of corrected situation). But the ZPL contribution to this line width dependence is obviously much narrower than that. Another way to look at it is that we are trying to correctly calculate the homogenous line width / EET rate for small donor acceptor overlap. However, in order to get the correct result, we need to convolute two Lorentzians of correct widths, which we do not *a priori* know.

The ZPL contribution to the overlap dependence on donor-acceptor gap can be constructed in the following way: First we ignore excitonic effects and note that, in this case, the ZPL contribution to overlap or line width dependence on the ZPL-ZPL gap is Lorentzian, as it is a result of the convolution of two Lorentzian functions and its width is the sum of the widths of the two original Lorentzians. One of the latter, belonging to the acceptor, has a dephasing-limited width, while the other, belonging to the donor, has a width determined by the EET rate.

Normalized to an area of one, the Lorentzian function can be described by

$$\frac{1}{\pi}\left[\frac{2\Gamma}{4(x-x_0)^2+\Gamma^2}\right]$$

where Γ is FWHM and the peak value is $2/\pi\Gamma$. The ZPL part of the overlap dependence on the donor-acceptor gap has to satisfy the conditions that

$$\frac{C}{\pi}\left[\frac{2\Gamma}{4(x-x_0)^2+\Gamma^2}\right]=\Gamma$$

or

$$\frac{C\cdot 2}{\pi\cdot width}=peak\_overlap$$

where the normalization factor C depends on inter-pigment coupling and can be determined from the not yet corrected overlap function. Here *peak overlap* and *width* are

characteristics of one and the same overlap function, for example, the one with an "incorrect" ZPL part reported in Figure 22 (blue). The width is assumed to be the sum of the ZPL widths of two single-site spectra used in the overlap calculation.

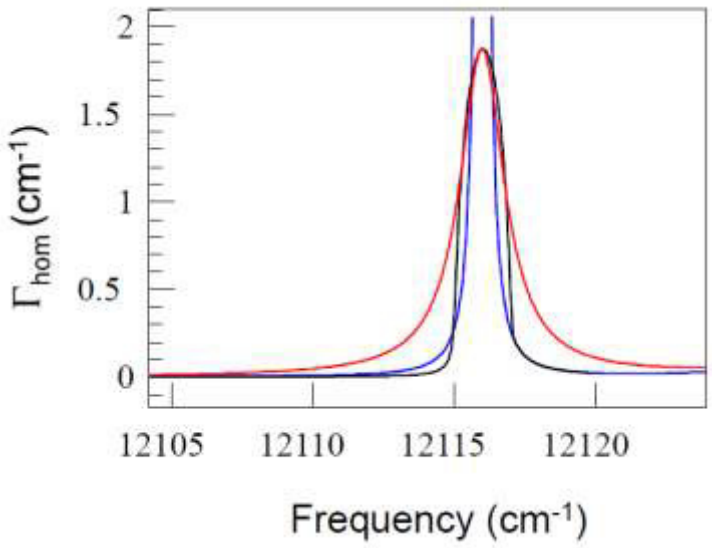

Figure 22. Blue: the result of convolution of two single-site spectra; with the width of the (truncated) peak being much smaller than the height. Black: corrected ZPL-ZPL contribution to spectral overlap (or line width) dependence on donor-acceptor gap. Red: Lorentzian function with same width and peak magnitude, for comparison.

A more elaborate treatment recognizes that the (ZPL region of the) correct curve should obey

$$\frac{C}{\pi}\left[\frac{2(\Gamma+2\Gamma_{dephasing})}{4(x-x_0)^2+(\Gamma+2\Gamma_{dephasing})^2}\right]=\Gamma,$$

where Γ is determined solely by EET, since both donor and acceptor lines have pure dephasing contribution to the width. From here,

$$\frac{C}{\pi}2(\Gamma+2\Gamma_{dephasing})=(4(x-x_0)^2+(\Gamma+2\Gamma_{dephasing})^2)\Gamma$$

$$(\Gamma+2\Gamma_{dephasing})^2)\Gamma+4(x-x_0)^2\Gamma-\frac{2C}{\pi}\Gamma-\frac{4C}{\pi}\Gamma_{dephasing}=0$$

$$\Gamma^3+4\Gamma^2\Gamma_{dephasing}+(4\Gamma_{dephasing}{}^2+4(x-x_0)^2-\frac{2C}{\pi})\Gamma-\frac{4C}{\pi}\Gamma_{dephasing}=0$$

Our software solves this cubic equation for Γ (which is simultaneously the value of the homogeneous EET-determined width (proportional to overlap) at point *x* and the width of the EET contribution to the width dependence on ZPL-ZPL overlap) as a function of *x*. Note that the corrected curve (black curve in Figure 20) is flattened at the top. This reflects the fact that if the EET rate is fast enough, the donor homogeneous width is large enough, and small detuning of a narrow acceptor line with respect to a broad donor line practically does not affect the ZPL-ZPL overlap. On the other hand, once detuning reaches certain threshold, the overlap falls off faster than a Lorentzian. Lorentzian with peak magnitude being same as its width is shown in red in Figure 22 for comparison.

Next, one has to take into account that due to excitonic effects, gaps smaller than $2V$ are impossible in the dimer case (but possible for a trimer). This means that if we consider a pair of pigments with zero ZPL-ZPL gap in the absence of interaction, the EET rate for this pair will be determined by the overlap between two single-site spectra, including the Lorentzian ZPL, separated by $2V$. Technically, this means stretching the overlap (for the purpose of determining line width distributions) from [0+$2V$ to end] to occupy [0 to end] interval in agreement with $\Delta E = 2V\sqrt{1+(\delta/2V)^2}$, with 0 being the ZPL peak location where δ is the site energies difference. For generating the EET probability function (see Section 4.3.3) one has to un-stretch the result back, so that the

step would be located at $2V$. For the trimer, the degenerate excitonic states are possible [141] and the homogeneous width dependence on donor-acceptor gap was calculated without the latter correction.

4.3.5. NPHB anti-hole treatment. Since our model describes non-photochemical HB, the absorption of burnt molecules is redistributed, the anti-hole is formed and the expected NPHB spectrum is conservative (integral=0; total hole area = total anti-hole area). Our software recalculates the sub-SDF (as well as EET-based corrections to single site spectra, see section 4.3.3) after every step of the burning process. To clarify the latter statement – the sum of all sub-SDF is not changed as a result of this additional recalculation, but individual sub-SDF are changed. This allows for taking into account that as a result of the blue shift of the lowest-energy pigment other pigment in the complex may become the lowest-energy one.

HB model of [60] implies lack of spectral memory. If spectral memory were present, some molecules would be cycled back and forth between two (or more) frequencies, and, as long as all frequencies available to them are lower than the burn frequency, the net burning would be reduced, except for the region close to burn frequency, including the resonant hole and PSB (see Section 4.3.2). Incorporation of spectral memory into HB models has been demonstrated in [108]. However, the model of [126] does not include the distribution of homogeneous line widths (EET rates) or burning via EET. Merging the two approaches results in increased computational power requirements (work in progress).

4.4. Manifestations of EET rate distributions in various systems

4.4.1. Effects of the distribution of excitation energy transfer rates on NPHB spectra of CP43 complex. The PSII core of all plants, algae and cyanobacteria contains two core antenna complexes, CP43 and CP47. The CP43 complex binds 13 chlorophyll *a* molecules. These chlorophylls are grouped on the opposite sides of the membrane. Thus, 9 Chl molecules are observed near the stroma and the other 4 Chls towards the luminal side of the membrane [18, 19, 77]. Figure 23A shows the structure of PSII core antenna CP43. The main function of CP43 is to funnel the excitation energy from the Chl *a/b* light-harvesting antennae (LHCII, CP24, CP26 and CP29) to the reaction centre of PSII [18, 19, 93].

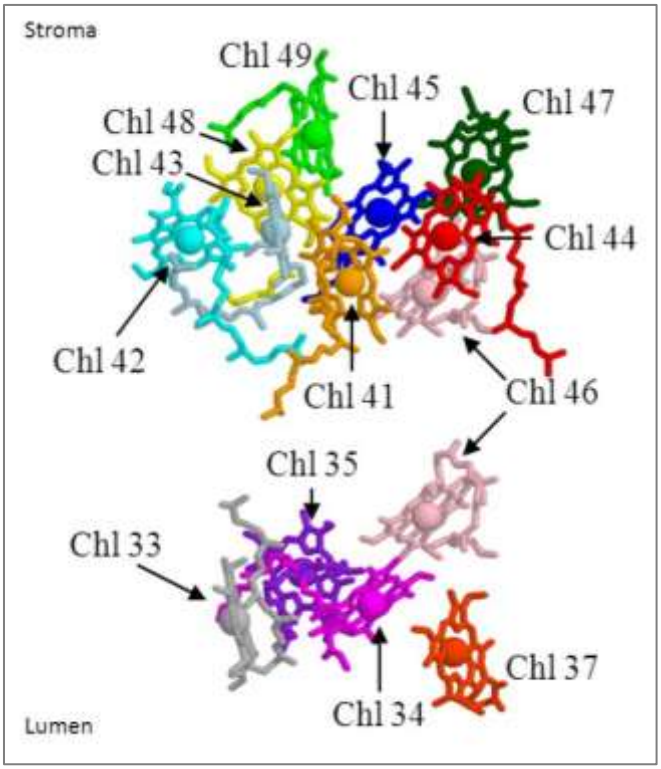

Figure 23. The structure of the core antenna complex CP43. The increased spacing between luminal and stromal parts of the complex is introduced for clarity; note that Chl 46 (notation by Loll, ref. 93), located somewhat in between lumenal and stromal groups of pigments, is shown twice (pink). Reprinted with permission from ref.142. Copyright (2008) American Chemical Society.

4.4.2.1. Experimental methods. The CP43 samples were purified and isolated by Dr. R. Picorel, Zaragoza, following the procedures reported in ref. 142 and ref. 143. The CP43 samples were obtained using an additional chromatography column at the end of the earlier purification procedure. Prior to experiment the concentrated samples were diluted with buffer (Bis-Tris, pH 6.0, plus 0.03% (w/v) n-dodecyl-β-D-maltoside DM, [142]). Detergents like DM solubilize membrane proteins which present hydrophobic side surfaces. As all spectroscopic experiments have been performed at low temperatures the diluted samples have been mixed with glycerol at a ratio of 1:2 buffer/glycerol. Glycerol-based systems are biological cryopotectants well known for their ability to form a high-quality optical amorphous state over a wide range of temperatures [144-148]. Thus, chlorophylls are surrounded by proteins which are (partially) surrounded by detergent micelle which is in turn embedded in buffer/glycerol glass. There is no evidence of protein denaturing or otherwise exhibiting any major structure changes upon cooling, including at the temperature of phase transition of water-glycerol mixture. The data in figure 24 is consistent just with the increase of homogeneous line width and electron-phonon coupling with temperature. As can be seen in figure 24, our 5 K spectra are in good agreement with those of [150] (shown) as well as [101].

The hole burning (HB) spectra have been measured in both fluorescence excitation mode at high resolution and in transmission / absorption mode at lower resolution [66]. In high-resolution experiments the beam from a tunable Spectra-Physics (Sirah) Matisse Dye Laser has been used for both excitation and scanning of the spectral holes and HGK. The Matisse DS ring dye laser operates in TEM_{00} spatial mode and enables single-frequency scanning over 45 GHz at a time while maintaining stable power

output and without mode hopping [149]. More importantly, drifts can be stabilized to less than 30 MHz for hours in HGK measurements [71]. This is sufficient as typical homogeneous line widths at 5 K are of the order of one GHz due to pure dephasing. In high-resolution experiments the spectral holes and the HGK were recorded with a Hamamatsu PMT/photon counter while in low-resolution the spectra were measured with a Varian Cary 5000 spectrophotometer at a resolution of 0.5 nm. For all experiments the excitation intensity was stabilized using a laser beam power stabilizer (Brockton Electro-Optics Corp). All spectra have been measured at low temperature (5K). It is important to mention that in our set-up the temperature can be kept approximately constant over an extended period of time (t_{burn} >>1h). The holes can be erased by heating the sample in the dark to ~ 150K [71].

4.4.1.2. Electrostatic coupling between pigments of the core antenna CP43 complex responsible for A and B states. Figure 24 (frame A) depicts the 5 K absorption spectrum of our CP43 sample. The Q_y absorption band contains two lowest-energy overlapping bands which are referred to as A and B states. Jankowiak et al. [101] proposed that both quasi-degenerate lowest-energy states of CP43 are localized on separate Chl *a* molecules and are not connected by fast energy transfer (based on the fact that one could burn dephasing-limited width holes all over the spectral range covering A and B bands). Groot et all [150] suggested that state A is delocalized over at least three strongly coupled Chl molecules, while state B is localized on a single chlorophyll. In this model state A has oscillator strength equal to that of three Chl molecules and peaks at 679.8 nm (A3 in Figure 24). This will be referred to as the A3B1 model in the following discussion. In contrast, Hughes et al. [151] suggested that state B is the lowest energy

state of the excitonically coupled pigment system, while state A is monomeric. In the latter ("A1B3") model, the oscillator strength of the lowest B state is approximately 1 Chl equivalent just by coincidence and two other excitonic states of this multimer peak at 676.6 (B" in Figure 24) and 681.7 nm (B' in Figure 24), and they have, respectively, significantly increased and significantly reduced oscillator strengths. The various deconvolutions suggested for the lowest-energy part of the spectrum by these models are shown in Figure 24.

In ref. 126 Zazubovich and Jankowiak demonstrated that, based on the shapes of the SDFs corrected for EET, one cannot distinguish between the above three possibilities but that the requirement of slow/negligible EET between A and B [101] is unnecessary. Narrow holes can be burnt at unexpectedly blue wavelengths due to disorder, not lack of inter-pigment coupling. In ref. 153, based on extensive modeling of various non-resonant, hole-burned spectra, it was concluded that bands A and B are strongly localized on Chls 44 and 37 (Loll's notation, [93]), respectively. For our EET rate / line width distribution calculations, it is important to note that the electrostatic coupling between Chls 37 and 44 is 5.7 cm^{-1}, [152] (or up to 7.6 cm^{-1} if one does not take into account the dielectric constant of the protein). This magnitude of coupling is in reasonable agreement with the EET time of ~10 ps observed for the counterparts of the A and B bands in the CP43' of the PSI-CP43' supercomplex [127]. Below we determine if the consideration of EET distributions will provide additional arguments in favor of any of the above models and in favor of assignment of chlorophylls 37 and 44 to B and A bands [60].

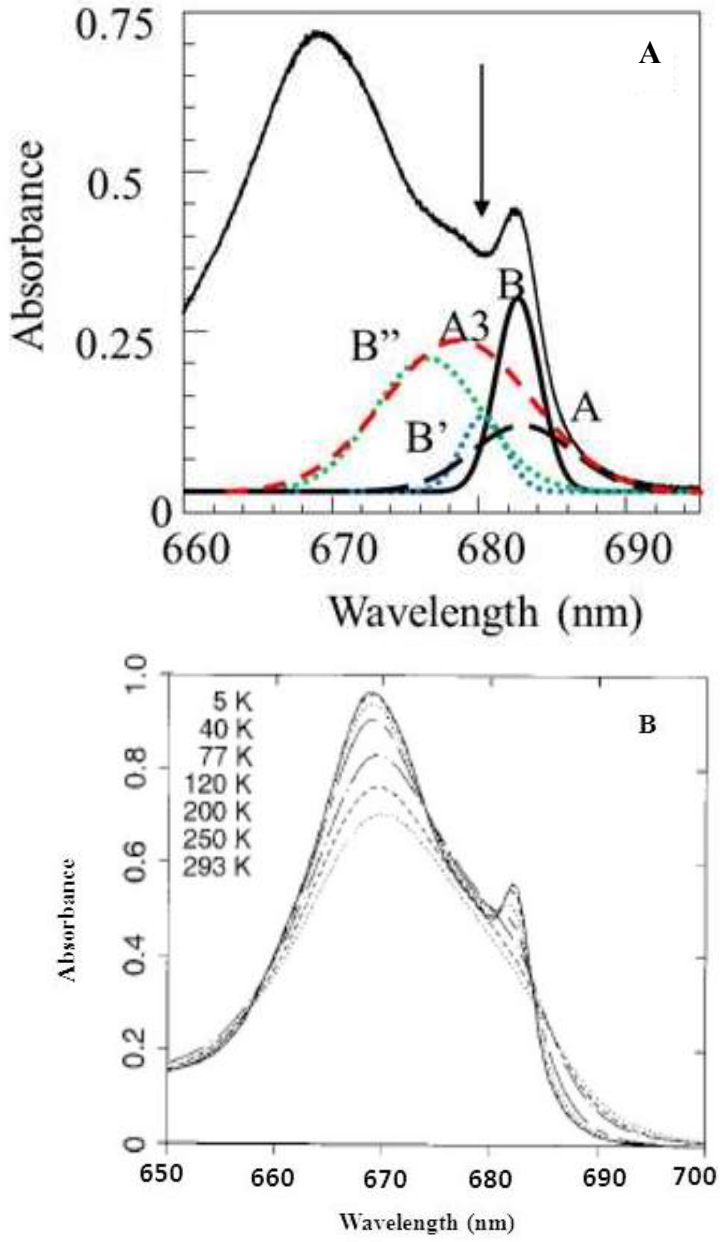

Figure 24A The absorption spectrum of CP43 as well as the SDFs of the lowest-energy states according to various models discussed in the text (Reprinted with permission from ref.60. Copyright (2011) American Chemical Society. **Figure 24B.** The Q_y absorption band of CP43 at different temperatures (Reprinted from ref. 150, Copyright (1999), with permission from Elsevier); the lowest-energy band peaked at ~ 683-nm is clearly resolved only in spectra measured at liquid nitrogen and helium temperatures (T < 77 K).

Figure 25 presents the SDFs of the two bands (similar to the A [solid red curve] and B [solid blue curve] states of CP43 determined via hole burning action spectra) as well as the overlap dependence on the D-A gap (black solid curve). Parameters of the

single-site spectra used for overlap simulations belong to A and B states of the CP43 complex and are summarized in Table 2; they were determined by independent lower-resolution hole burning experiments [101,116]. We used the frequencies and Huang-Rhys factors of the Chl *a* intramolecular modes as determined by Rätsep et al. for CP29 antenna complex of green plants [138]. The only exception is the 90 cm^{-1} mode, which does not manifest in the HB spectra of CP43. Thus, the *S*-factor for this mode has been reduced 10-fold.

Table 2. Hole simulation parameters for CP43 (from ref. 60)

CP43 band	**SDF peak; width (cm^{-1})**	**Oscillator strength (Chl eq.)**	**Excited state lifetime (ns)**	**S_{PSB}**	**ω_m; Γ_{Gauss}; $\Gamma_{Lorentz}$ (cm^{-1})**	**λ_0**	**σ**
A	14643; 180	1	3.5	0.30±0.05	17; 11; 70	10.2±0.1	1.0±0.1
B	14643, 65	1.2	3.5	0.30±0.05	24; 15; 70	9.7±0.3	1.0±0.1

The spectral overlap dependence based on Kolaczkowski et al. [133] is presented for comparison (dash-dotted green curve). It is clear that the latter curve strongly underestimates the spectral overlap and EET rates for most of the D-A gaps, except the smallest ones. As 99% of the B state SDF is located to the red with respect to the burn wavelength, 99% of the burning into the A state is affected by EET. On the other hand, only 80% of the A state SDF is located to the red with respect to burn wavelength. Consequently, 20% of burning into the B state at 680 nm is not affected by EET and can result in the formation of narrow, dephasing-limited holes, even though this wavelength

is 3 nm to the blue with respect to the B band peak. The overlap values for various energy gaps were assigned probabilities according to the acceptor SDF and binned.

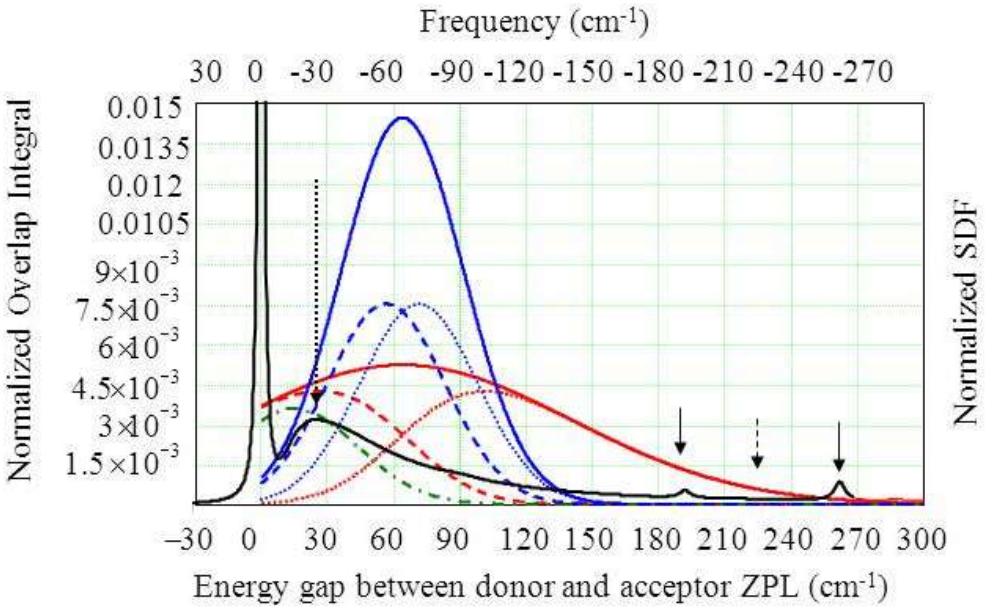

Figure 25. Spectral overlap dependence on the ZPL-ZPL energy gap (black curve) for the single site spectra parameters in Table 2, two SDFs (solid red and blue curves), and deconvolution of those SDFs into sub-SDFs of fractions capable (dashed line) or incapable (dotted line) of EET. The dash-dotted green curve is the overlap integral dependence on energy gap according to Kolaczkowski et al, [133].Vertical solid arrows indicate contributions to the overlap from localized vibrations; the dashed arrow indicates minimal overlap. The dotted arrow indicates maximal overlap within the range of Fig.26. Reprinted with permission from ref. 60 . Copyright (2011) American Chemical Society.

Resulting overlap distributions, normalized to one, are presented in Figure 26. The red curve corresponds to B→A EET and contains a 20% contribution of the zero EET rate (indicated by the dashed horizontal arrow). The blue curve corresponds to A→B EET.

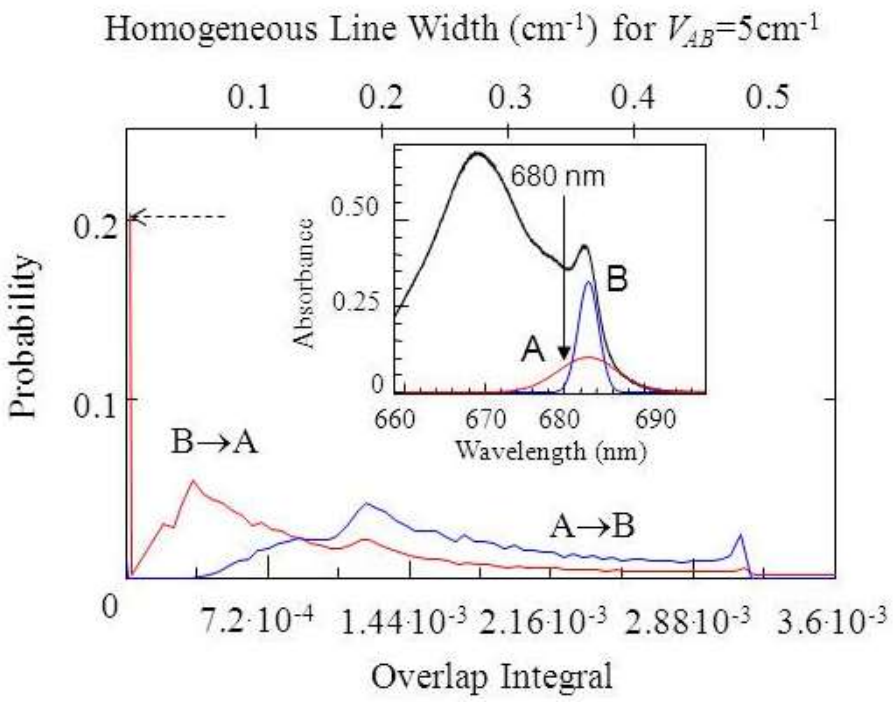

Figure 26. Overlap distributions (lower scale) and homogeneous line width distributions with V_{AB} = 5 cm^{-1} for EET between two bands with the SDFs resembling those of the two lowest-energy states of the CP43 complex (the inset contains its absorption spectrum and two SDFs). The blue curve is the distribution for A→B EET for λ_B = 680 nm, while the red curve is the distribution for B→A EET. The horizontal dashed arrow indicates the ~20% contribution of B-type pigments incapable of EET at λ_B. Reprinted with permission from ref. 60 . Copyright (2011) American Chemical Society.
N.B: Homogeneous line width reported in the figure does not include pure dephasing contribution (e.g, 1 GHz or 0.033 cm^{-1} at 5 K, [101]).

Both distributions are clearly asymmetrical. Higher values of the overlap (these would be located beyond the right edge of Figure 26) correspond to the ZPL-ZPL contribution but are very unlikely due to excitonic splitting. Note that one can also, in principle, use logic similar to that employed above and construct line width distributions at any wavelength from the energy gap dependences of the EET rates calculated in various Redfield frameworks [128]. Returning to Főrster EET, A to B and B to A, two line width distributions for each burn wavelength and each interaction energy V were calculated within the hole burning simulator software based on the SDF, single-site

spectral parameters, and the burn wavelength, and these are used for subsequent modeling of simultaneous burning into two (uncorrelated) bands.

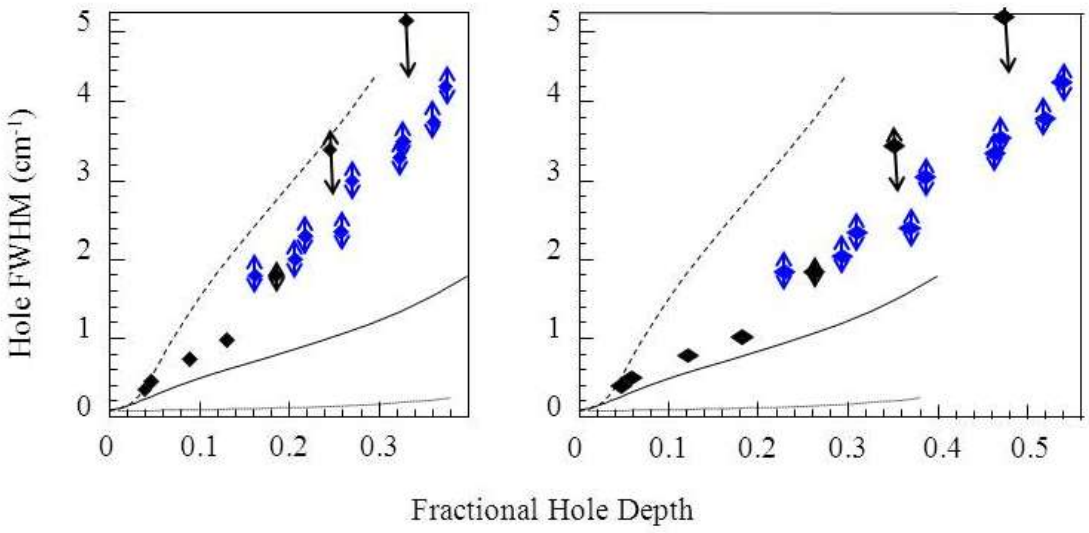

Figure 27. Left frame - Experimental dependence of the hole width on hole depth for λ_B = 680.15 nm. Black diamonds: high-resolution data. Blue diamonds: low-resolution data, corrected for the spectrometer resolution. The solid curve is the theoretical dependence for V_{AB}=5cm^{-1}, and the dashed curve is the theoretical dependence for V_{AB} =10 cm^{-1}. The dotted curve was obtained in the absence of the line width distribution.
Right frame –The dependence of the hole width on hole depth corrected for contribution of states other than A and B at λ_B = 680.15 nm.

Figure 27 depicts the hole width dependence on the fractional hole depth. The dependence is composed of two parts: the shallow hole part was measured in fluorescence excitation mode at high resolution (black diamonds). The deeper/broader hole part of the dependence is obtained using holes registered in an absorption mode with a spectrophotometer at 0.05 nm (1.08 cm^{-1}) resolution (blue diamonds). Assuming that the error of corrected hole widths is the same as that of uncorrected ones, the error bars were set to 0.5 cm^{-1} for lower-resolution holes while for high-resolution holes (narrowest holes), the errors are actually smaller than symbol size. However, for two broadest holes of the high-resolution set the errors are large (hole width is comparable to scan range;

40GHz x 3=~4 cm^{-1}). The widths (and depths) of the holes extracted from the spectra measured at low resolution were corrected for spectrophotometer resolution before being plotted in Figure 27. Apart from the deepest holes measured at high resolution and the shallowest hole measured at low resolution, the data in Figure 27 can be fitted with a single curve. Figure 27 also depicts the theoretical width/depth dependences calculated for V_{AB}= 5 cm^{-1} (solid curve) and 10 cm^{-1} (dashed curve). All other parameters are summarized in Table 2. The dotted curve corresponds to the fractional hole width dependence in the absence of any line width distribution. It can easily be seen that the experimental results are located between the theoretical curves for V_{AB} = 5 and 10 cm^{-1}.

First, in the A3B1 model, the absorption at 680 nm will include only A and B contributions, with S~0.3. Thus, unless we employ an extremely broad distribution with a large fraction of very large EET rates for which there is no experimental or excitonic calculation basis, it is impossible to explain why the maximal achievable hole depth is only ~40% (results not shown) given that the electron-phonon coupling is weak (S ~ 0.3). Once we rule the A3B1 model unlikely, we note that not all of the absorption at 680 nm is supposed to belong to the A and B states or to be burnable. Higher states will transfer energy down to A and B and therefore will burn poorly (see Eq. 4). Thus, the true A + B fractional depths corresponding to each width are larger than shown in Figure 27 (experimental). Consequently, V_{AB} is closer to 5 cm^{-1} than to 10 cm^{-1}, which is in perfect agreement with our earlier assignment of Chls 44 and 37 to A and B states, respectively [152]. As seen in Table 3, there are other pairs of chlorophylls with ~ 5 cm^{-1} coupling. However, modeling the optical spectra assuming these assignments of the lowest-energy

bands does not lead to a reasonable agreement between theoretical and experimental spectra [152].

Table 3. Inter-pigment couplings between Chl a molecules in CP43 complex, in cm^{-1}.

	Chl 33	Chl 34	Chl 35	**Chl 37**	Chl 41	Chl 42	Chl 43	**Chl 44**	Chl 45	Chl 46	Chl 47	Chl 48	Chl 49
Chl 33	???	-8.68	-3.13	-1.59	-3.28	12.43	12.31	1.23	-7.91	2.39	-1.82	-0.78	-0.11
Chl 34		???	-23.7	74.51	1.0	0.81	88.33	5.67	22.48	65.87	10.77	-5.68	-0.93
Chl 35			???	-18.96	-1.79	-1.16	-4.37	-5.31	-5.38	-18.55	-5.51	15.64	4.65
Chl 37				???	1.51	3.2	1.7	**5.72**	-1.2	23.99	2.52	-2.45	3.2
Chl 41					???	-15.51	-65.57	-16.67	19.73	-3.01	-1.25	2.27	-3.35
Chl 42						???	50.95	9.48	-19.7	9.18	3.73	-5.44	6.85
Chl 43							???	-8.76	58.92	-1.21	-5.57	24.17	-15.65
Chl 44								???	39.7	48.04	47.8	-16.45	8.3
Chl 45									???	-35.99	86.89	17.72	-5.67
Chl 46										???	-58.08	-8.92	8.19
Chl 47											???	-15.95	8.74
Chl 48												???	-45.46
Chl 49													???

Also note that for S = 0.3 the 39% maximum hole depth corresponds to 50% of the absorption at 680 nm belonging to burnable bands. Thus, (i) the A1B3 model of the Krausz group does not appear very feasible, as in that model >60% of absorption at 680 nm belongs to higher components of B (supposedly featuring very fast relaxation to the lowest B component), and (ii) since in the A1B1 model A and B states contribute less than 50% to the absorption, the results indicate that there is an additional state (most likely the third-lowest exciton state of CP43) contributing to the absorption at 680 nm, which features couplings to A and B pigments in the same 5-10 cm^{-1} range. Returning to the A1B3 model from the Krausz group, [151] our results still may be consistent with B being a multimer with a weak narrow component at ~680 nm (i.e., with higher excitonic components not in this region but at much higher energy, [152]). This will allow for

agreement with the CD data. The third B-component observed by Krausz in δ-CD spectra most likely resulted either from not taking into account the antiholes of the first two B-components or from an excitonic band peaking at ~676 nm, which is not part of the B-manifold and exhibits relatively slow EET to A and B (see discussion on A1B1 model above).

4.4.1.3. Conclusions. The effects of the line width distributions resulting from Förster-type EET between weakly interacting pigments with uncorrelated site distribution functions on the NPHB process were explored both theoretically and experimentally in isolated CP43 antenna from spinach. It was proven that inclusion of such a EET rate distributions strongly affects the dependence of the hole width on the fractional hole depth and allows for the extraction of approximate values of inter-pigment couplings. In addition, it was demonstrated that validation or rejection of the lowest-energy A and B bands assignment to different Chl molecules in CP43 are possible when this type of distribution is considered in the SHB modeling.

4.4.2. Effects of the distribution of excitation energy transfer rates on resonant and non-resonant NPHB spectra from FMO

4.4.2.1. Introduction. The peripheral antenna complex of the green sulfur bacteria, the Fenna–Matthews–Olson (FMO) protein, is a water-soluble trimeric protein. Until recently it was believed that it contains seven bacteriochlorophyll *a* (BChl*a*) molecules per monomer [9, 32-34]. The structure of the FMO protein is presented in Fig. 28. However, the recent X-ray studies on the structure of FMO have revealed the eighth BChl *a* molecule which is placed near the chlorosome (ref. 33 and references therein). As

FMO interfaces the membrane of the green sulfur bacteria and the chlorosomes, its main role is to transfer the excitation energy from the chlorosomes to the membrane-embedded bacterial reaction center [8, 9, 32-34].

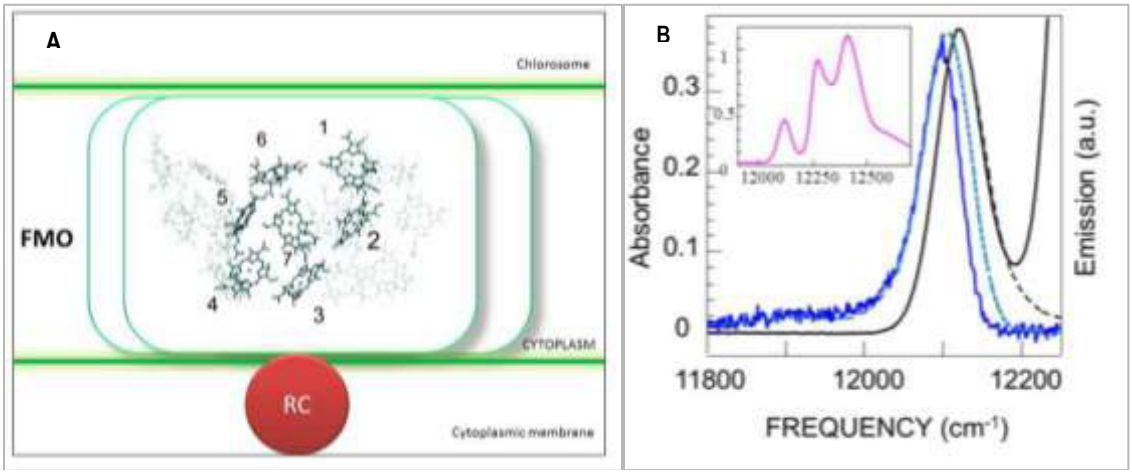

Figure 28. Frame A - The locations of BChl molecules in a FMO monomer (Adapted from ref.32, Copyright (2006), with permission from Elsevier). The pigments within one selected monomer are highlighted, the pigments of other two monomers are presented as fainter shapes. **Frame B** - The low temperature absorption spectra of FMO protein. Dashed black curve: fit to the 825 nm band absorption (see text). Blue solid curve: emission spectrum measured for the same sample as absorption. Dashed blue curve: emission spectrum predicted assuming that emission origin coincides with the full 825 nm band SDF (i.e., there is no intra-825 nm-band, inter-monomer, EET). Insert shows the entire Q_y absorption band of *C. tepidum* FMO complex.

4.4.2.2 Experimental details. The Fenna-Matthews-Olson protein from green bacteria *Chlorobium tepidum* has been isolated and purified as described in ref.153 by Blankenship's group at Washington University, Saint Louis. Absorption spectra of FMO from *C. tepidum* have been measured at KSU using Bruker HR125 FTIR spectrometer at 1 cm^{-1} resolution. Emission spectrum has been measured using Acton 0.3 m spectrograph and Princeton Instruments Spec 10 nitrogen-cooled spectroscopic back-illuminated CCD camera. Reported emission spectra were corrected for wavelength dependence of CCD sensitivity. Spectra measured on different days exhibited up to a nanometer shifts with respect to each other. However, the absorption and emission peaks moved in concert,

with apparent Stokes shift staying constant. Care has been taken to analyze together only the spectra measured on the same day.

4.4.2.3 Results and discussion. The low-temperature (5 K) absorption spectrum of FMO proteins from the green sulfur bacterium *C. tepidum* shows several bands in the 800-830 nm spectral region (insert of Fig. 28B). The shape of the spectrum is mostly determined by the strong excitonic interactions between the BChl molecules of the same monomer as well as by the interactions between the BChl and the protein [9, 32-34, 154].

The nature of the lowest-energy band of the FMO complex, the presence or absence of inter-monomer excitation energy transfer in trimeric FMO, and the exact origins of various hole burning (HB) and fluorescence line narrowing (FLN) and ΔFLN spectra [155] are not fully understood. Even if trimeric nature of FMO and resulting inter-monomer excitation energy transfer (EET) are considered important for explaining its spectroscopic properties, different groups treat the lowest-energy 825 nm band as sum of three bands with either different or identical parameters. Competing evidence in favor of different interpretations is available, while spectral holes are notoriously difficult to fit in any of the available models.

Figure 28B contains the absorption and emission spectra of FMO at 5 K. Smooth curve is the fit to absorption spectrum produced assuming that the lowest-energy band can be treated as either due to monomeric chlorophyll, or as belonging to three chlorophylls possessing identical site-distribution functions (SDF). In principle, one could achieve the same result also using three non-identical SDF for monomers of the trimer, as long as the sum of these SDF has the same shape as the SDF in the monomer / identical trimer cases, i.e. is a Gaussian peaked at 12116 cm^{-1} and with the width of 65

cm^{-1}. Dashed curve is the calculated emission spectrum obtained by dressing the whole same SDF with same phonons and local vibrations (see below for details).

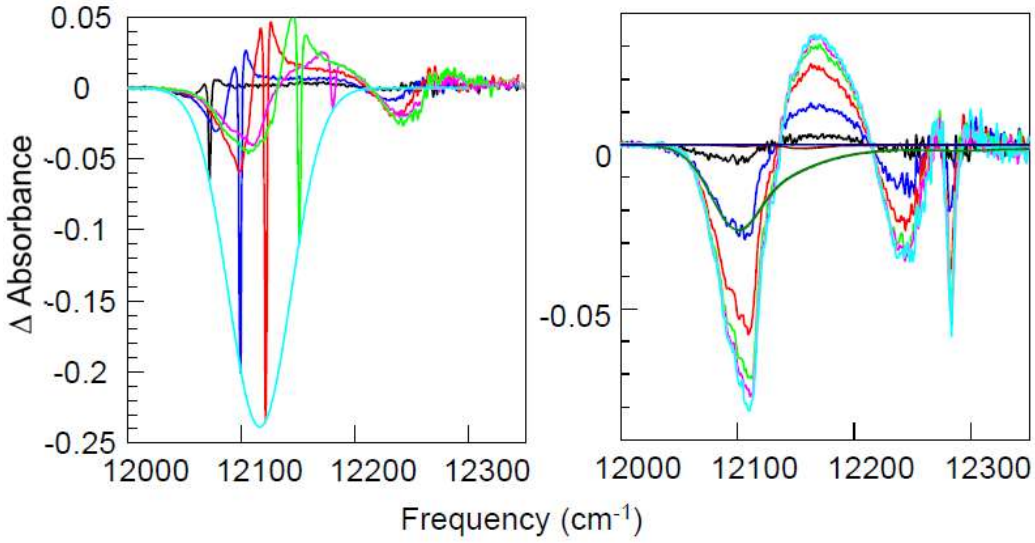

Figure 29A: Holes burnt at 821.0 (magenta), 823.0 (green), 825.0 (red), 826.5 (dark blue) and 828.4 (black) nm with a fluence of about 120 J/cm^2. Light-blue curve is the inverted full SDF of the 825 nm band. **Figure 29B:** Non-resonant holes produced by illumination at 814 nm with varying fluence. Smooth dark green curve represents the theoretical non-resonant hole in the presence of EET and the absence of an anti-hole.

Figure 29A presents the hole spectra obtained for λ_B of 821.0, 823.0, 825.0, 826.5 and 828.4 nm with 120 J/cm^2. The total SDF (see above) is presented for comparison. It is immediately clear that the hole depths follow the SDF. This appears to be an indication that inter-monomer intra-825 nm band EET is not present, as this EET should reduce the HB yield. However, a quick look at Figure 28B indicates that such a conclusion would be premature. Namely, the emission spectrum predicted in the no-EET model is too blue-shifted and, more importantly, too broad compared to the experimental one. While positions of the bands can be adjusted by adjusting electron-phonon coupling, the mirror image law (applied to the 825 nm band alone) dictates that in the absence of intra-band EET the width of the emission spectrum must be approximately equal to the width of the

absorption spectrum, and this is not the case. The width of the absorption band is ~75cm^{-1}, while the width of the emission band is ~60 cm^{-1}. Note that the absorption, hole and emission spectra reported here were measured on the same day and therefore the discrepancies between calculated and experimental emission spectra cannot be attributed to differences in sample preparation. By analogy with CP43 and CP43' (*IsiA* protein surrounding the cyanobacterial PSI core in case of iron-deficient environment), one could suggest that intra-band EET is actually present, and that emission occurs (mostly) from the lowest-energy pigment of the trimer [7, 189].

One should also note a satellite hole at 12243 cm^{-1} (816.8 nm), which is located to the blue of all the burn wavelengths and therefore must be due to the excitonic effects (in the first approximation – it is the higher excitonic component of 825 nm state). Both lowest-energy and 816.8 nm holes are not conservative, with blue-shifted anti-hole exhibiting much smaller integral intensity than the hole itself. This suggests coexistence of at least two hole-burning mechanisms. Regular NPHB is responsible for small blue (on average) shifts, resulting in anti-holes in the vicinity of λ_B. These anti-holes can easily be seen next to the resonant holes obtained at the longest burn wavelengths. As described in [152, 156] the blue NPHB shift of the lowest-energy pigment in an excitonically coupled system results in a blue shift of the higher exciton states (e.g. 816.8 nm band). An additional mechanism removes pigments from the 825 nm band region. The exact mechanism of this removal is unclear. Either some Bchl experiences reversible photochemical burning of unknown nature (this could be expected in a reaction center protein, like PS I, see Chapter 5, but not in the antenna proteins), or it experiences NPHB with a drastic blue shift, taking its absorption far out of the original 825 nm band SDF.

Figure 29B contains holes obtained with varying burn doses and λ_B of 814 nm, outside of the lowest-band SDF. EET results in a low-energy hole peaked at 12105 cm^{-1} (somewhat dose-dependent), accompanied by a higher-energy hole at 12243 cm^{-1} (816.8 nm). Just like the spectra in Figure 29A, the hole spectra are clearly non-conservative. The energy splitting between two broad holes is about 135 cm^{-1}. The integral intensity of these two broad holes is approximately twice the integral intensity of the positive feature located between the holes. This offers an interesting possibility that removal of the lowest-energy bacteriochlorophyll (e.g. most likely Bchl 3 [157]) would result in the red shift of the second lower energy Bchl 4 absorption. The sign of the proposed Bchl 3 (contributing 87.5% to the lowest state) to Bchl 4 coupling (ref. 158) is in agreement with the lower-energy hole being deeper. Here one can note that HB results are not in agreement with Hamiltonian from ref. 159 with 175 cm^{-1} difference in site energies and –62 cm^{-1} coupling between Bchl 3 and 4, the lowest-energy pigments in the complex. As couplings are generally more trustworthy than site energies, our results put site energies in FMO by Fleming and Vulto [157, 158] under doubt. For the above Bchl 4 red shift hypothesis to be correct, the site energies of two lowest-energy bacteriochlorophylls in FMO monomer have to be nearly identical. In any case, it is clear that the hole spectra are non-conservative and therefore any NPHB-based model, however well-developed, will not be sufficient to perfectly fit all the hole spectra. In the following we will, however, use improved model of HB in the presence of slow EET [60] to estimate the inter-monomer couplings from the emission spectra. Combining various sub-SDF with proper weights determined by the emission probabilities

$$p_{em} = \tau_{fl}^{-1} / (\tau_{fl}^{-1} + \tau_{EET}^{-1})$$

one can obtain the emission origin and, convoluting it with the single site emission – the bulk emission spectrum.

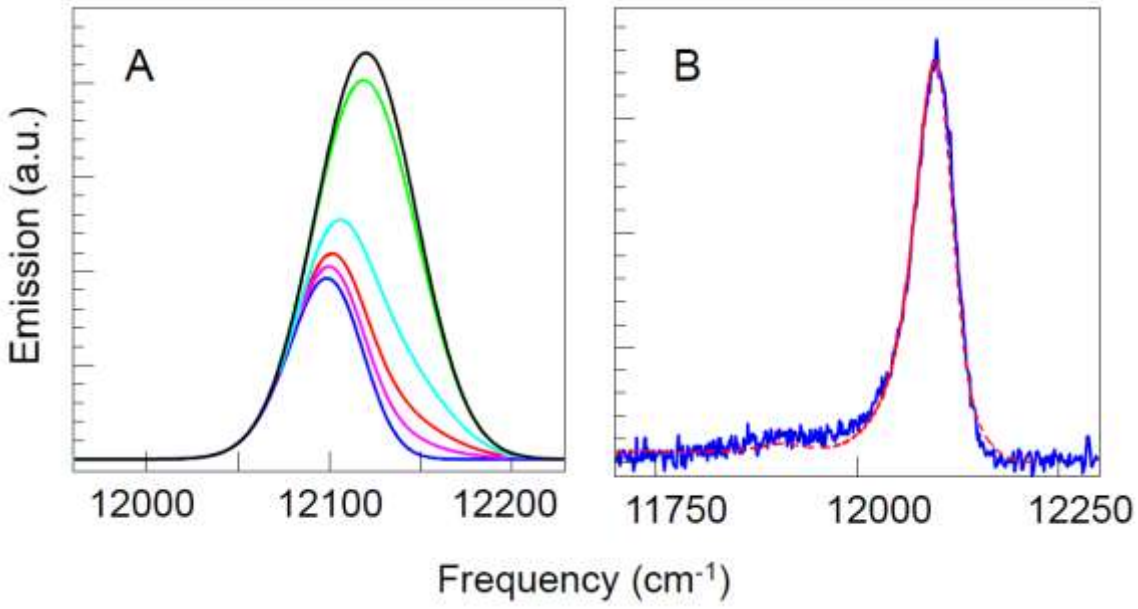

Figure 30A: Emission origin calculated in trimeric model with slow EET: Black: total SDF of the 825 nm band of FMO, emission origin in case inter-monomer coupling is zero. Light green: $|V|=0.1$ cm^{-1}, Light blue: $V=0.5$ cm^{-1}, Red: $V=1.0$ cm^{-1}; Magenta: $V=2.0$ cm^{-1}; Blue: curve (e) from Figure 18B, valid for $V=3.0$ cm^{-1} and above. **Figure 30B:** best fit (red) to the FMO 5K emission spectrum (blue), $V=1.2$ cm^{-1}.

Obviously, the contribution of non-zero EET rate sub-SDFs to the emission origin will strongly depend on the inter-pigment coupling. This allows for a rough estimate of inter-pigment coupling based on the emission spectrum. Figure 30A depicts the shapes of the emission origin in FMO for various values of inter-pigment coupling within 825 nm band. For $V>3$ cm^{-1} the emission origin is practically indistinguishable from the zero-EET sub-SDF (blue curve in Figure 30A; curve (e) in Figure 18B). Dashed red curve in Figure 30B represents the emission spectrum calculated for FMO assuming slow EET is possible due to inter-pigment coupling of ~1.2 cm^{-1} (best fit to the emission spectrum).

One can utilize similar logic, and derive, using Eq. 5, the "origin" of non-resonantly burnt lowest-energy hole in Fig. 29B. Different sub-SDF will have to be added with weights proportional to the HB yields (Eq.5). Since the NPHB rate is much smaller than both fluorescence and EET rates, the shape of the "non-resonant hole origin" will be nearly identical to the shape of the emission origin. Dressing the "non-resonant hole origin" with phonons and vibrations one can reproduce the non-resonantly-burnt hole spectra from Figure 29B, dark green curve. Sharp features causing discrepancies between theoretical and experimental curves are most probably ZPL burnt through local vibrational modes when exciting at 814 nm. One should note that although the shapes of non-resonant holes apparently support the inter-monomer EET hypotheses, one can explain the non-resonant HB results also without invoking inter-monomer EET. However, there is a fundamental difference in what one has to do and to assume in order to simulate the non-resonant holes in the presence and in the absence of inter-monomer EET. In the absence of EET, the lower-energy hole can be produced assuming just ~10 cm^{-1} average shift between the original hole (dark green curve in Fig 30 dressed with phonons and vibrations) and the anti-hole, solid black curves in Figure 31A. In the presence of EET one has to assume ~60 cm^{-1} average shift, Figure 31B. Note that in the latter case small NPHB shifts are still allowed as long as spectral memory is present, and molecules that experienced small shift can be returned to original wavelength by a subsequent act of small-shift NPHB following EET from 814 nm pigments to 825 nm pigments. We are going to use information on these shifts as initial guesses for anti-hole function in resonant hole fitting. The fractions of absorption "disappearing" in the process of hole burning are 25% in the presence of EET and 9% in the case of no EET.

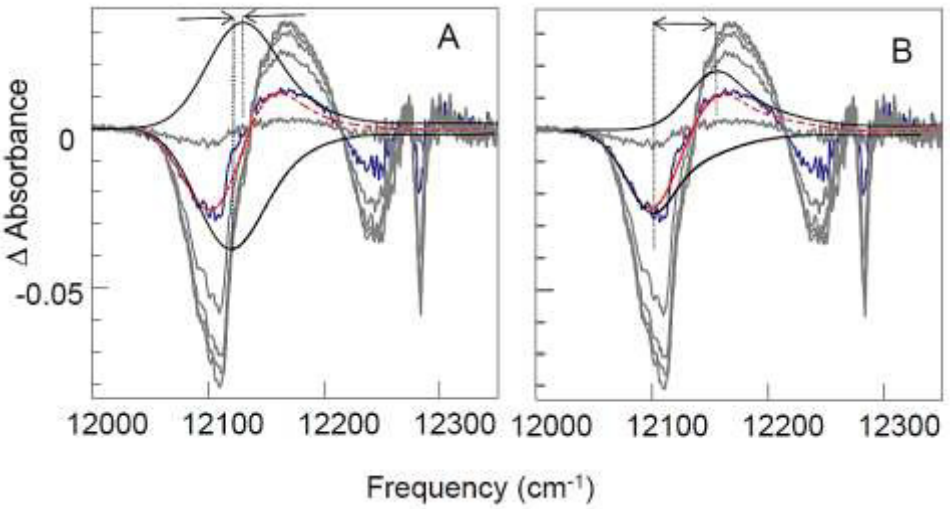

Figure 31A: ΔAbsorption of non-resonantly burned molecules and anti-holes (solid black curves) and their sum (dashed red curve) compared to a representative HB spectrum (blue) in the absence of EET. Non-resonantly burned spectra for other fluences are presented in grey. **Figure 31B:** Similar spectra as frame A, but in the presence of EET.

Figure 32A presents the 821 nm holes simulated assuming no inter-monomer EET. As determined above, the average blue shift upon burning is 10 cm^{-1} in this case. Obviously, the lowest-energy holes are the least affected by potential EET (as there are no more lower-energy acceptors) and therefore would look nearly identical regardless of the presence or absence of EET. These are the bluest, shortest-λ_B holes that should be affected by EET the most, if EET is present. Blue curve was produced using no-memory model of [59], while the red curve was produced using perfect spectral memory model [160]. The burn intensities have been chosen to produce the resonant hole of the same fractional depth as in the experimental spectrum. Note that in the case of perfect spectral memory, where the anti-hole absorption burns and returns back to original pre-burn frequency (except for 10% we allowed to escape far to the blue, see above), the pseudo-PSB part of the hole is strongly suppressed compared to the experiment, while in the no-memory case the pseudo-PSB is too intense. In both limiting cases, memory-wise, one

can see that the broad pseudo-PSB feature is peaked at too high energy (too close to the burn frequency) if the HB yield is constant across the whole 825 nm band (result of no EET). Thus, in the more realistic case of partial spectral memory (i.e. the case where more than two, but still finite number of spectral positions are available to each pigment molecule) one would expect the pseudo-PSB to be too blue-shifted as well. Figure 32B presents the simulations of the 821nm hole assuming presence of inter-monomer EET, with V=1.2 cm^{-1}, average blue shift of 60 cm^{-1} and no spectral memory. Here we have added another feature not present in the model of [60] – burning via EET. Burning via EET is introduced via corrections to $L(\omega_B-\omega)$ in the exponent in Eq.4 (see chapter 4.3.3). Qualitatively, allowing for burning via EET results in enhancement of the hole features at energies lower than the laser frequency. One could also note that in the presence of EET one photon absorbed by the highest-energy one of the three pigments has three chances to cause hole burning! Overall, it is clear that the fit in the Fig. 32B, though not perfect, is better than either of the fits in Fig. 32A. Note that one cannot exclude the presence of small, ~10 cm^{-1} shifts in addition to ~60 cm^{-1} shifts in the case of inter-monomer EET. These shifts are likely dominant for the lowest-energy holes. For lower-energy holes, ~10 cm^{-1} shifts move the ZPL of a significant fraction of burnt molecules to the blue of the burn frequency, while for higher-energy holes the molecules remain to the red with respect to burn frequency after the 10 cm^{-1} shift. If spectral memory is present, the latter molecules are eventually returned to pre-burn condition. Note how presence of spectral memory reduces **apparent** HB effectiveness in Fig. 32A. ("Apparent" as the same values of HB yield were used in both cases.) On the other hand an important fault of simulated spectra in Fig. 32B is that the resonant hole burning is reduced at higher energies, in

disagreement with the experiment (see also Fig. 27). Is there a meaningful way explain this discrepancy without abandoning EET?

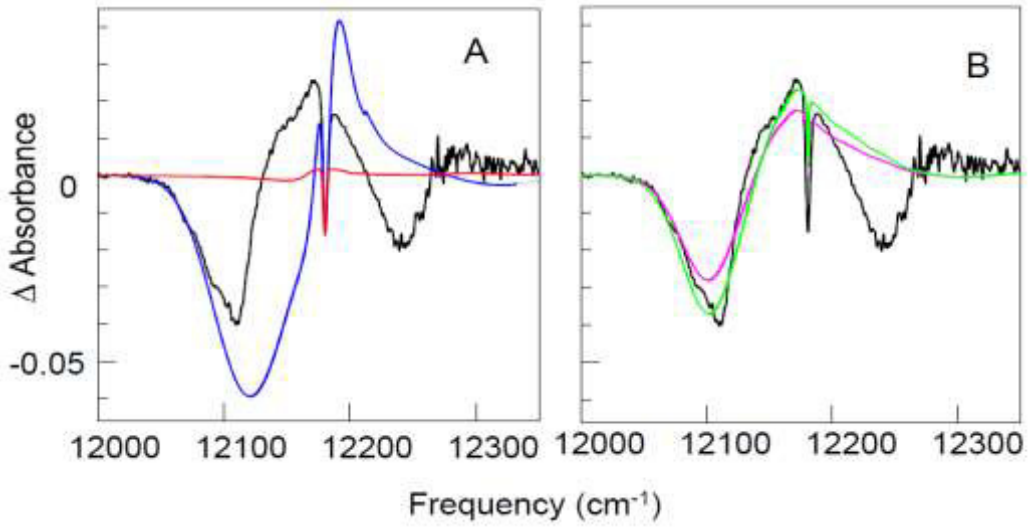

Figure 32A: Hole burnt at 821 nm and modeling results in the absence of EET and aberage blue shift of the anti-hole of 10 cm^{-1}. Red curve: perfect spectral memory [139], blue curve: no spectral memory. **Figure 32B:** Same hole and modeling results for two irradiation doses in the presence of EET. The small ~10 cm^{-1} shifts are not included, as it was assumed that their contribution is small when spectral memory in present (see red curve in frame A). We did not attempt to simulate the higher-energy satellite hole at 816 nm.

The model as described above does not include excitonic effects. They may affect the shape of the function describing burning via EET. Most importantly, as shown by Reppert [156], in an excitonically coupled system the shift of the site energy of the lowest-energy pigment (due to NPHB) results in the shift of all the exciton states, including the higher ones. We demonstrate it here for a dimer, for the sake of clarity:

The energies of transitions to the two exciton states of a dimer can be expressed as:

$$E\pm = (E_H + E_L)/2 \pm \sqrt{V^2 + ((E_H - E_L)/2)^2}\ , \qquad (10)$$

where E_H and E_L are site energies (transition energies in the absence of interaction) of higher and lower-energy pigments in the dimer, respectively. Differentiating the above

equation, if NPHB results in the shift of the site energy E_L by ΔE_L, the energy of the higher exciton state will shift by

$$\Delta E_{+} = \frac{\Delta E_L}{2}\left(1 + \frac{(E_L - E_H)}{\sqrt{4V^2 + ((E_H - E_L))^2}}\right) \qquad (11)$$

Note that $E_L - E_H < 0$ and the square root is defined as positive.

We assume that additional HB of the higher-energy pigments would be observable when the spectral shift of the higher exciton state is larger than the homogeneous line width. The fraction of systems experiencing observable excitonic burning effect depends on inter-pigment coupling V, the SDF parameters and the distribution of shifts (anti-hole function). If V is small and the donor-acceptor gap is large, the small shift of the lower-energy pigment has almost no effect on the higher energy state. On the other hand, if the anti-hole function is broad enough (for instance, when pigments are free to shift within the whole SDF and beyond), this "excitonic higher-state burning" may be present in a large fraction of trimers even for small coupling V. We also need to stress that due to this effect the higher-energy states will appear to be burning resonantly with the same rate as the lower-energy states [152, 156], see Eq. 5 with $\tau_{EET}^{-1}=0$. Interestingly, this would mean that there would be no preference for resonant burning of pigments with the slowest EET or no EET in this system, and the widths of even shallow holes would reflect the average EET rate, not necessarily the slower end of the EET rate distribution. The average EET time calculated for V=1.2 cm^{-1} for the middle of the 825 nm band is 270 ps, which can be compared to 135 ps reported in [161]. Achieving agreement with [161] requires increasing inter-

monomer coupling to ~1.7 cm^{-1}, which results in slightly poorer fit to the emission spectrum (maximum 2-3 cm^{-1} too red), but slightly better fits to hole spectra.

It is not clear if this indirect resonant burning of higher states attributable to excitonic effect was ever observed in any system. Apparent absence of effect was considered in [156] as evidence in favor of Redfield EET models. However it may be quite possible that FMO possesses the necessary combination of small coupling (justifying Főrster EET), small SDF width (ensuring large E_H–E_L are unlikely) and anti-hole function with large average spectral shift.

Figure 33A depicts the results of simulations for the trimer with FMO parameters, V=3 cm^{-1} and the NPHB shift of the lowest-energy pigment of 10 cm^{-1} to the blue. One can see that under these conditions more than half of the trimers exhibit middle state shifts, and about 1/3 exhibit higher state shifts which are higher than 0.25 cm^{-1}. Such shifts are larger than homogeneous line width and thus would be detectable as hole burning, not just hole broadening. The probability distributions of shifts of the second-lowest (one donor one acceptor), and the highest (two acceptors), states of the trimer of pigments with identical FMO-like SDF upon 60 cm^{-1} shift of the lowest-energy pigment to the blue and coupling V=1.5 cm^{-1} is presented in figure 33B. Most of the higher state shifts are to the blue. Occasionally, red shifts are possible when the shift of the lowest-energy pigment changes the order of pigments (e.g. the lowest-energy one becomes the second-lowest, etc)

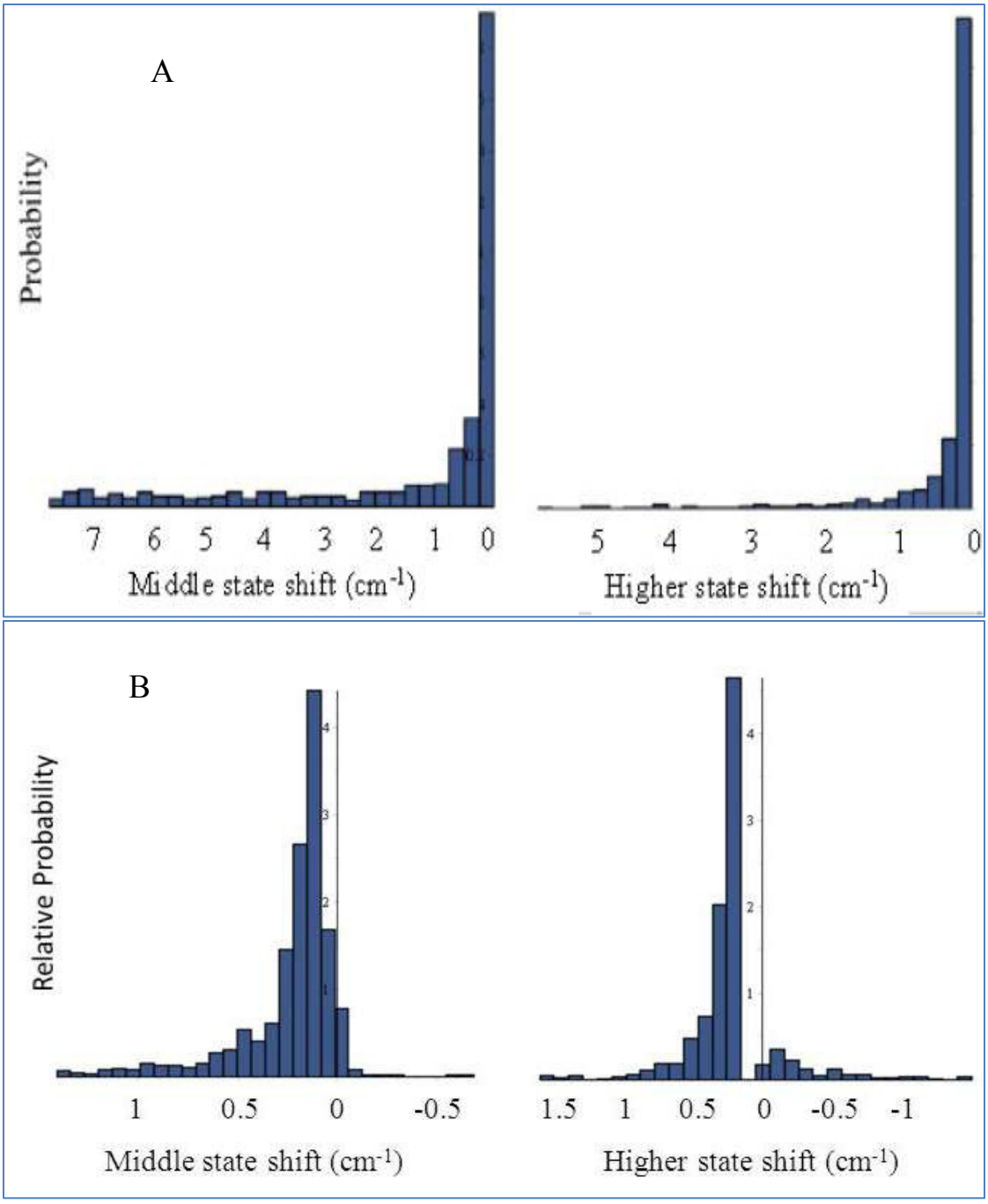

Figure 33. The shift probability distributions for the middle (one donor and one acceptor) and higher (two acceptors) excitonic states of the trimer with identical FMO-like SDF parameters. **Frame A -** The NPHB shift of the lowest-energy pigment was assumed to be 10 cm^{-1} to the blue, and coupling V= 3 cm^{-1}. **Frame B** - The NPHB shift of the lowest-energy pigment was assumed to be 60 cm^{-1} to the blue and coupling V=1.5cm^{-1}. Courtesy of Stephanie Larocque.

Rigorously including this effect into simulation of HB spectra at high resolution is subject of future publications, as it requires combining burning via EET, presence spectral memory (approaches similar to those employed in [160] can be used to keep track of excitonic interactions in a trimer) and more than one tier of the protein energy landscape in the same program.

One can note that inter-pigment coupling of 1.2-1.7 cm^{-1} is lower than 3 cm^{-1} predicted for Bchl 3 of adjacent monomers by excitonic calculations, see Table 4. (The matrix is not symmetric with respect to diagonal since FMO is a trimer and rows and columns belong to different monomers.) This may mean either that the dielectric constant of the substance between these pigments has not been estimated properly, or that due to contributions from other pigments the transition dipole of the 825 nm excitonic state has less favorable orientation than that of "pure" Bchl 3, or that the widespread assignments of the 825 nm band to Bchl 3 are incorrect. With respect to the latter possibility, however, it is clear that, besides Bchls 1 and 6, there are no better candidates for the 825 nm band than Bchl 3, coupling-wise. Bchl 1 has never been proposed as the origin of the 825 nm band [162] (apparently, assuming BChl 1 is the lowest-energy one does not lead to meaningful absorption, CD, etc spectra), while Bchl 6 has not been considered the lowest-energy one since the end of the 90-ies [163] before the orientation of FMO with respect to the RC has been determined [153] and it became clear that BChl 3 is close to the RC, while Bchls 1 and 6 are closer to the baseplate (See figure 28A). Having the lowest-energy pigment of FMO away from the RC would represent an unnecessary obstacle for fast EET from chlorosome to FMO to RC.

Table 4. Couplings between Bchls of adjacent trimers in cm^{-1} calculated assuming effective $\mu^2 = 30\ D^2$. Couplings between identical Bchls are highlighted. The Bchl3-Bchl3 coupling is -3.0 cm^{-1}.

	1A	2A	3A	4A	5A	6A	7A	8A
1C	1.6	0.7	-0.7	0.9	3.4	1.8	1.5	25.7
2C	2.3	-0.3	-3.5	-2.6	11.1	7.0	3.1	5.0
3C	2.1	0.5	-3.0	6.8	6.6	2.9	6.3	0.7
4C	0.4	0.7	0.7	2.9	-1.1	-0.4	2.9	-1.5
5C	0.9	1.3	1.7	-0.4	2.7	-0.1	-1.1	4.0
6C	0.0	1.0	1.0	2.2	-2.3	-2.0	2.7	-9.6
7C	0.5	0.5	-0.9	7.0	-2.5	0.3	9.0	-11.3
8C	0.0	0.8	1.0	-1.4	1.8	-1.5	-3.4	5.2

4.4.2.4. Conclusions. We argue that NPHB results obtained for 825 nm band in trimeric FMO of *C. Tepidum* are consistent with the presence of relatively slow EET, and with weak (~1.5 cm^{-1}) coupling between identical pigments from different monomers. Improved NPHB simulation approach, based on HB master equation (Eq. 4), but also including frequency-dependent EET rate distributions and burning following EET, allows for reasonable fits to experimental data. Further improvements, however, critically depend on our understanding of protein energy landscapes, which determine the distributions of spectral shifts and respective HB yields, as well as the degree of spectral memory involved.

Qualitatively, the hole burning in FMO involves two processes. The first one involves small, <10 cm^{-1} spectral shifts, with high degree of spectral memory. In addition, either higher-tier large blue shift NPHB or reversible photochemical hole burning results in major shifts of the lowest-energy states in the monomers. The latter, in turn, results in some spectral shifts of all states of the trimer due to coupling between pigments of each monomer responsible for the 825 nm band. The shape of the NPHB satellite hole structure contradicts the widely accepted sets of site energies [159].

The software developed for this project also has additional features that were not directly employed. For instance, it allows simulations of δ-FLN spectra in the presence of burning via EET, using realistic functions describing wavelength dependence of the EET probabilities, as opposed to step function of [164]. As first demonstrated in [164] one would expect the EET to create an illusion of the increase of electron-phonon coupling with frequency observed via δ-FLN [155]. Also, the program recalculates all sub-SDF after every step of burning. This allows one to recalculate the emission origin and the emission spectrum after each step of burning as well. This is important as now one can model the evolution of the shape of non-resonantly excited emission spectrum with time as the sample is illuminated (in a hole burning experiment or in the process of alignment before the measurement of fluorescence spectrum). Drift of the fluorescence spectrum to the blue with time has been noticed for many complexes (LHCII, PS I, etc; unpublished results; in all those measurements care has been taken to minimize the alignment time or to erase the effects of NPHB prior to final fluorescence measurement). If one assumes the absence of drift while in fact the drift is present (e.g. if alignment before fluorescence spectrum measurement took too long and some burning occurred), this results in incorrect estimations of electron-phonon coupling, Stokes shift and/or inter-pigment coupling in dimer and trimer models.

4.5. PSII RC Distributions of charge separation rates – competing views. 680 and 684 nm bands

4.5.1. Introduction. Photosystem II (PSII) is a multiunit trans-membrane protein essentially made up of a dimeric core and an assortment of peripheral antennae

complexes. Each monomer of the PSII core contains several major subunits including the reaction center (RC) and the core antenna proteins (CP43 and CP47), [8-15]. A PSII-RC is made up from several polypeptides including the D1 (PsbA), D2 (PsbD) polypeptides and cytochrome b-559. PSII RC contains two pheophytins *a* (Pheo *a*), one or two β-carotene molecules and one non-heme Fe atom [165]. By analogy with the two bacteriochlorophyll molecules in the RC of purple bacteria forming a "special pair", structurally similar chlorophylls in PSII RC were initially referred to as "special pair" (P680) as well. However it was demonstrated by Durrant et al. [37] that comparable short distances (10-11 Å) between coupled pigments in the PSII RC and comparable couplings lead to multimer formation, and now it is generally accepted that there is no well-defined "special pair" in PSII-RC. D_1/D_2 proteins also bind two additional chlorophylls *a* (Chl_{D1}/Chl_{D2}) and two pheophytin molecules ($Pheo_{D1}/Pheo_{D2}$) [8-15, 165-169]. Further, unlike bacterial RC, PSII RC contains two peripheral chlorophylls, which absorb at around 670 nm, are weakly coupled to the other pigments, and transfer energy to other pigments relatively slowly [8-15, 165-169].

In principle, the charge separation occurs between the primary electron-donor and the primary electron-acceptor. The initial electron transfer results in the formation of the primary radical pair and the subsequent electron transfer processes lead to the water oxidation that powers the photosynthetic organism and oxygen formation [8-15, 29, 88, 165-167]. Since the primary electron donor is considered to be a multimer and the static disorder of the protein causes energetic differentiation among reaction center cofactors, two different charge separation pathways are possible in the PSIIRC from higher plants.

Recently, Romero et al [88] identified the two different charge separation pathways in the PSIIRC from spinach as follows (Figure 34):

$$(Chl_{D1}Phe_{D1})^{*} \rightarrow Chl_{D1}^{+}\,Phe_{D1}^{-} \rightarrow P_{D1}^{+}\,Phe_{D1}^{-}\ ;$$

this CS pathway is referred to as Chl_{D1} path, and

$$(P_{D1}P_{D2}Chl_{D1})^{*} \rightarrow P_{D2}^{+}\,P_{D1}^{-} \rightarrow P_{D1}^{+}\,Chl_{D1}^{-} \rightarrow P_{D1}^{+}\,Phe_{D1}^{-};$$

this is referred to as P_{D1} pathway.

Thus, in the latter case the primary electron donor is P_{D1} and the primary electron acceptor is Phe_{D1}. In the former case chlorophyll molecule Chl_{D1} first donates electron to Phe_{D1} acceptor and then accepts electron from P_{D1} [88]. The P_{D1} pathway primary charge separation appears to be somewhat faster, 1 ps versus 3 ps. Finally, it needs to be stressed that in the intact PSII cores [168 and ref. therein] the primary donor band seems to be located at 685 nm rather than 680 nm. Thus, it might be possible that isolation introduces sufficient disturbance to PSII RC and changes the nature of the primary donor, or at least the proportions in which two electron transfer pathways described above are present. In [86] multiple arguments were presented to show that properties of the 680 nm main band and 684 nm shoulder (see Figure 35) in isolated PSII RC are very similar, and P684 model has been proposed. In this model the shoulder at 684 nm represents the lowest state and primary electron donor of the remnant of the RCs least disturbed during isolation.

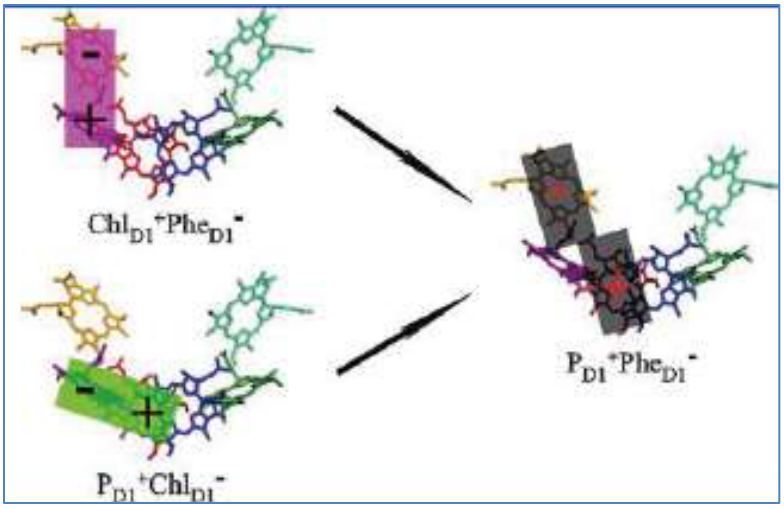

Figure 34. The diagram of the two different charge separation pathways in the PSII RC from spinach. Reprinted with permission from ref. 88. Copyright (2010) American Chemical Society

4.5.2. Experimental details. Plant PSII RC (6-Chl per 2 pheophytin molecules) samples have been isolated and purified as described in ref. 86. Just before the experiments the samples have been diluted with buffer (MES; pH 6.5; 2mM dodecyl-maltoside and 5mM imidazole) and glycerol 1:2 to ensure formation of high optical quality glasses at liquid helium temperatures (for more details see chapter 4.4.2.1). Hole growth kinetics curves for the lowest states of PSII RC from spinach have been measured at low temperature (5 K) in fluorescence excitation mode and in transmission mode at high resolution using the high-resolution optical setup and the cryostat presented in chapter 4.4.2.1. The fluorescence signal was detected through AELP-730 interference long-pass filter (Omega Optical) and conventional long-pass filters (LOMO)) with a Hamamatsu PMT/photon counter placed at 90^0 with respect to the excitation beam. Transmission signal was detected with the same photomultiplier at 180^0, the intensity was regulated by neutral density filters (LOMO).

4.5.3. Results and Discussion. The absorption spectrum of isolated PSII RC from spinach is presented in Figure 35. The main features of the spectrum are a narrow peak at 680 nm, a broad band at 670 nm, and a weak preparation-dependent shoulder at ~684 nm. As stated in the Introduction to the chapter 4.1, SHB, [86] and photon echo [87] results obtained for the lower-energy spectral region of the isolated RC of PSII may be interpreted in a consistent fashion, assuming an extremely broad distribution of charge separation times from a couple of picoseconds to several nanoseconds, although, admittedly, in recent two-dimensional (2D) electronic spectroscopy experiments on isolated PSII RC at 77 K, [89] a much narrower heterogeneous distribution of time scales associated with charge transfer was observed than the one based on photon echo results, [87].

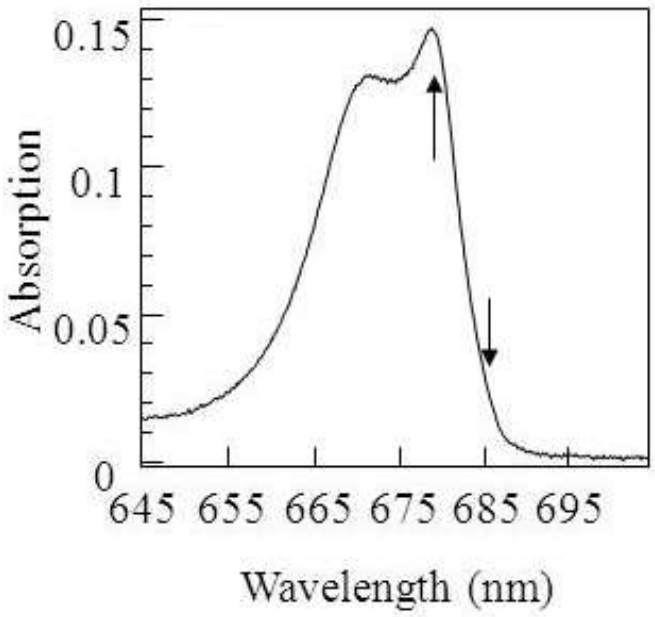

Figure 35. The absorption spectrum of the isolated PSII RC complex. The arrows indicate the burn wavelengths of 680 and 686 nm, the latter within a weak shoulder at ~684 nm, Reprinted with permission from ref. 60. Copyright (2011) American Chemical Society.

In ref 86, using less sophisticated modeling tools than are now at our disposal, Riley et al fitted the triplet bottleneck holes burnt at 684-686 nm and suggested that the ~684 nm band can be attributed to the lowest-energy state of a multimer involved in charge separation in the case of less disturbed RC preparations, referred to as P684. Studies of intact oxygen-evolving PSII cores (also containing CP43 and CP47) place that state at ~684-685 nm, [168] and suggest that isolation of the RCs results in the shift of this band to 680 nm (hence P680) in most, but not all, RCs. In this example, we analyze if the distribution of line widths following from ref. 87 can also be used to fit the persistent holes burned at 686 nm in the spectrum of the PSII RC. Figure 36 shows HGK curves obtained at 686 nm and 5 K with various burn intensities, in transmission and fluorescence excitation modes. The numbers next to either the curves or the data points refer to excitation intensities in mW/cm^2. The data points belonging to the same "discrete" data set were obtained by consecutive burning, measuring the hole spectrum, and then burning at the same wavelength again with, in most cases, increased intensity.

The fastest two HGK curves (red and magenta) were obtained in fluorescence excitation mode; other data sets were measured in transmission/absorption mode. It is clear that the hole burning rate is strongly intensity- and acquisition mode dependent. This is a manifestation of the ease with which the transient triplet bottleneck hole burning occurs in this system and an evidence for charge separation being quite probable upon excitation at 686 nm. While the system is in the triplet state (following charge separation and recombination), it is unavailable for absorbing photons at burn wavelength; i.e., it is experiencing an analogue of saturation. As a result, the apparent burning rate is reduced. A simple theory of triplet-related saturation, independent of the particular mechanism of

the triplet state emergence, involves application of Poisson statistics. Namely, the otherwise potentially absorbable photon will really be absorbed only if it arrives at least $\tau_{triplet}$ after the previous photon, where $\tau_{triplet}$ is the triplet lifetime, which is on the order of 1 ms in PSII RC [169]. In other words, we are interested in the probability of seeing one or fewer photons in the time interval equal to the triplet lifetime for given total photon flux.

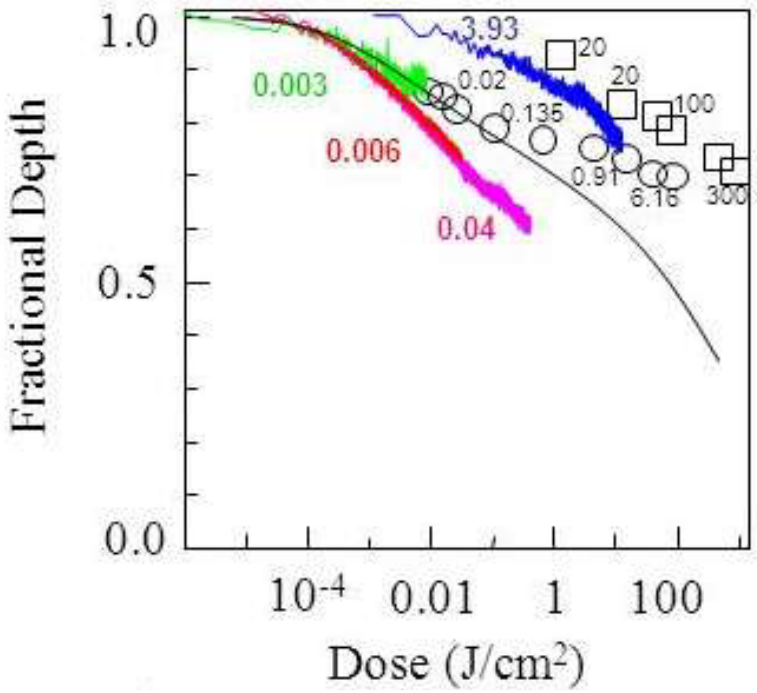

Figure 36. Persistent hole depth versus irradiation dose data for λ_B = 686 nm. The noisy curves are HGK curves; symbols refer to data extracted from the hole spectra. The numbers refer to the intensity (in mW/cm^2) used to obtain the data.
The fastest two HGKs (red and magenta) were obtained in fluorescence excitation mode. Also presented is the best fit (solid black line) to the lowest-intensity transmission mode data (noisy green curve + open circles). See the text for line width distribution details, Reprinted with permission from ref. 60 . Copyright (2011) American Chemical Society

This probability is described by the cumulative Poisson distribution

$$\rho = e^{-\bar{n}} \sum_{k=0}^{1} \frac{\bar{n}^k}{k!} \qquad (12)$$

where $\bar{n}$ is the average number of potentially absorbable photons (if triplet formation was impossible) incident on the pigment molecule per triplet lifetime. Note that the sum has only two terms which have to be taken into account, for k = 0 and 1.

Also note that $\bar{n}$ is dependent on the shape of the single site spectrum, L(ω), because for resonant ZPL excitation absorption occurs much easier than for PSB excitation. Summarizing, to take triplet saturation-related effects into account, the exponent in Eq 4 has to be multiplied by the probability

$$\rho(\omega, \tau_{triplet}, \alpha) = e^{-P\sigma L(\omega)\tau_{triplet}\cos^2\alpha}\left[P\sigma L(\omega)\tau_{triplet}\cos^2\alpha + 1\right] \qquad \textbf{(13)}$$

Here all variables are as in Eqs 4 and 5. Obviously, for very short triplet lifetime or very small photon flux, ρ ≈1, and no correction to HB yield has to be made. Unfortunately, ρ depends on the angle α between the laser polarization and the pigment's transition dipole, and introducing correction for saturation would negate the approximation (Eq. 7) for angular distribution treatment in HB master equation (Eq. 4), and require a 10- to 30-fold increase in the calculation time. For this reason we did not attempt to perfect the fits to the triplet bottleneck holes from ref 86 in this work, which was our original intention, as the triplet bottleneck holes would likely be affected not only by the line width distribution but also by saturation effects. Note that saturation would decrease and broaden the ZPL contribution to the transient holes, causing the illusion of stronger electron-phonon coupling. Thus, our suggestion of moderate electron-phonon coupling for the charge-separating state of PSII RC [86] still stands.

Table 5. Hole simulation parameters for PSII RC

band	SDF peak; width (cm^{-1})	Oscillator strength (Chl eq.)	Excited state lifetime (ns)	S_{PSB}, S_{80}	ω_m; Γ_{Gauss}; $\Gamma_{Lorentz}$ (cm^{-1})	λ_0	σ
684 nm	14605; 90	2	6.0	0.80±0.05, 0.2	17; 11; 17	10.4±0.2	1.1± 0.2
680^{+} nm	14699; 110	2*	6.0	0.80±0.05, 0.2	17; 11; 17	10.4 ±0.2	1.1± 0.2

[+] the parameters of the 680 nm band do not affect burning at 686 nm significantly, and no attempt was made to vary them to achieve a better fit.
[*]additionally, the amplitude of the 680 nm band is three times larger than for the 684 nm band due to sample heterogeneity, not different oscillator strength.
The pure dephasing-limited homogeneous line width was set to 0.033 cm^{-1} (1 GHz),[28]

The increased apparent hole burning rate in the fluorescence excitation mode is also in agreement with charge separation occurring in a fraction of complexes upon 686 nm excitation: only the complexes with the slowest charge separation rates (or zero rate) contribute to fluorescence, while the complexes experiencing fast charge separation do not fluoresce. And those complexes contributing to fluorescence are preferentially detected in fluorescence excitation mode. In summary, to avoid saturation and to simultaneously probe complexes with all possible charge separation rates, one has to apply our model to the HGK and width versus depth data obtained in transmission mode with the lowest-possible excitation intensity.

Figure 36 also contains the best fit (black solid curve) to the lowest-intensity transmission mode data set (green noisy curve + open circles). The SDF and electron-phonon coupling parameters of the 684 and 680 nm bands were adopted from ref 69 and

are presented in Table 5. The available values of the lifetime corresponding to the slowest depopulation of the excited state (in the absence of charge separation) range from 2 ns, [89] to 20 ns, [88]. We used a value of 6 ns, in agreement with refs 83, 120, and 171. It is evident from the figure 36 that for higher burn intensities saturation effects cause discrepancies between calculations and experimental data. It can be demonstrated that the onset of the discrepancy is in agreement with the saturation described by Eqs 12 and 13 given the photon budgets of our experiments and a triplet lifetime of 1 ms. Figure 37 shows the experimental data and its fit for hole width vs depth dependence. The (solid) curve, providing the best fit for the 686 nm data (open and solid circles correspond to two different complementary data sets), was obtained with the same parameters as the theoretical HGK curve in figure 36.

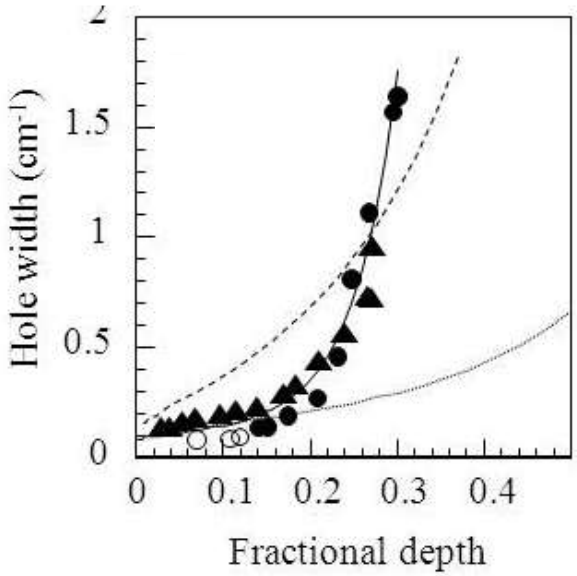

Figure 37. Experimental persistent hole width vs depth data (open and solid circles represent two complementary data sets) for λ_B = 686 nm and theoretical fits with the same distribution as in figure 36 (solid curve), with the distribution from ref 87 (dashed curve) and without any line width distribution (dotted curve). The solid triangles represent the experimental data obtained at 680 nm. The data was obtained at high resolution (~30 MHz) with 4 cm^{-1} scan range. Therefore, errors do not exceed the size of the symbols Reprinted with permission from ref. 60. Copyright (2011) American Chemical Society

The dashed curve was obtained using the whole distribution from ref 87. The dotted curve was obtained without any line width distribution. It is clear that distribution from ref 87 is not applicable to the 684 nm band. The more realistic distribution (resulting in the solid curve in figure 36) contains only zero charge separation rate (i.e., slower than 160 ps, see below; relative weight 45%) and very fast (a Gaussian peaking at 3.3 cm^{-1} [1.5 ps], with the FWHM of 1 cm^{-1}, relative weight 55%) components. This latter Gaussian matches the slower side of the Weibull distribution used in ref 86 to fit the triplet bottleneck holes. Note that in triplet bottleneck hole measurements the persistent holes are usually saturated prior to the transient hole burning, and therefore transient holes are expected to contain only the fastest end of the broad line width / inverse lifetime distributions. Concerning the zero charge separation rate component, we note that SHB is unable to distinguish between hundreds of picoseconds charge transfer times and hundreds of picoseconds excited state lifetimes shortened just by pure dephasing, a phenomenon present in any amorphous system, [69] in the absence of any charge transfer. Note that the typical 5 K pure dephasing-broadened homogeneous line widths are on the order of 1 GHz, [101] which corresponds to 160 ps. Charge separation slower than that will have only a minor effect on the SHB data.

Surprisingly, the full distribution from ref. 87 does not provide a good fit for the HB data obtained at 680 nm (triangles) either. The latter data set resembles the 686 nm one (circles) fairly well, suggesting only a minor contribution of intermediate (tens of picoseconds [87, 89]) charge separation rates to the 680 nm distribution. It can also be demonstrated (results not shown) that agreement between experimental 680 nm data and results of simulations involving the recent charge separation rate distribution from ref 150

is extremely poor. The presence of a fairly large fraction of RCs exhibiting very slow charge separation rates seems to be required to fit the hole burning data. Concerning the tens of picoseconds contribution observed in the time-domain experiments, [87-89] we should note that SHB delivers exclusively the characteristic time of the primary charge separation process, which affects the lifetime of the excited state directly resulting from the absorption of light. Time domain methods, on the other hand, are also sensitive to secondary charge separation processes, as they obviously cause additional evolution of the spectra in time. Thus, taking into account that the tens of picoseconds component has been assigned to the secondary charge separation processes, [88, 89] its absence in our SHB data is understandable.

We also compared our results obtained above for CP43 (Section 4.4.1 and refs 71, 66) and PSII RC with those reported by Hughes et al for intact oxygen-evolving PSII cores (fully-functional RC+CP43+CP47) [172]. Hughes et al claimed that spectral hole burning in the intact PSII cores is unusually fast, and proposed a modified HB mechanism involving charge separation in the RC triggering conformational changes in CP43 and CP47. Figure 38 shows the experimental persistent HGK curves obtained for λ_1=691.6nm, λ_2=685.2nm and λ_2=684.7nm in a spinach PSII core at 2.5 K as reported in ref. 172. We superimpose our HGK data for CP43 for burning wavelength λ_B=686nm and the theoretical fit to HGK curve measured in transmission at the lowest intensity (T= 5 K, λ_B = 686 nm) in isolated PS II RC (fig.38). It is clear that although the HB rate in the PS II core [172] may indeed depend on the oxidation state of the RC in the core, the HB rate reported in ref. 172 is not exceptionally fast. In fact, the HGK is faster in isolated CP43 than in the core. EET from CP43 to RC in the cores should reduce the HB yield (Eq. 5).

On the other hand, burning in CP43 should be somewhat faster at 2.5 K than at 5 K, due to narrower homogeneous line width [66]. With these corrections, the HB rates observed in [172] in the PSII cores are similar to those reported by us in CP43.

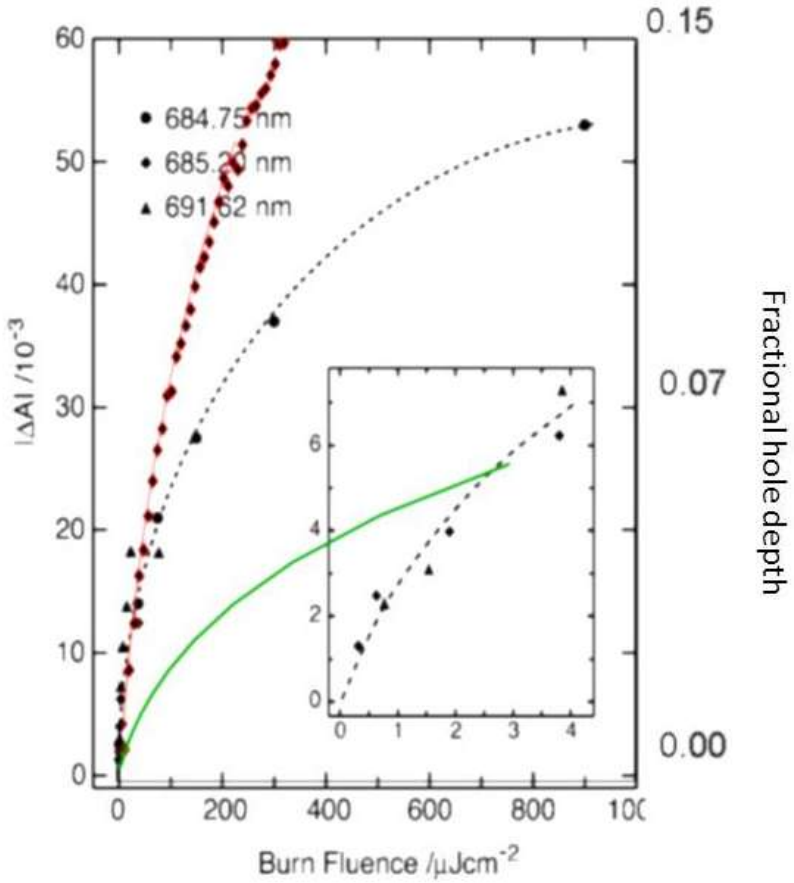

Figure 38. Absorbance difference vs. burn fluence (Figure 11 Reprinted with permission from ref. 172. Copyright (2004) American Chemical Society and fractional hole depth vs. burn fluence (our data) for PSII core (RC+CP43+CP47) from spinach in $S_1(QA^-)$ at T= 2.5 K and 5 K, respectively. Black line, triangles, and circles: HGK in PSII core from spinach, in $S_1(QA^-)$ state, Red line and diamonds: HGK curve obtained at T= 5K and λ_B = 686 nm in CP43 (our data); Green: fit to HGK curve measured in transmission at the lowest intensity, T= 5K, λ_B = 686 nm; isolated PS II RC (our data).

4.5.3. Conclusions. In summary, without going into the details of the charge separation processes in PSII RC, our results are in qualitative agreement with ref 88, where the coexistence of two different charge separation pathways in the PSII RC at low temperature was proposed, each pathway leading to either slow (activated) or fast (activationless) charge separation. It seems plausible that the fraction of the RCs exhibiting slow charge separation could increase with the decrease of temperature. This might explain quantitative disagreement between the magnitudes of different contributions obtained at 5 K and at 77 K [88, 89]. However, such a difference cannot be quantitatively evaluated, as it is well-known that the relative contributions from P680 and P684 vary from sample to sample, and ref 89 did not provide 77 K absorption spectra for comparison with our data. A detailed discussion on the charge-separation pathways is beyond the scope of this research, which focused on line width distributions, but it will be attempted in future studies. We note, however, that the data presented here offers one more similarity between the hole-burning properties of the 680 and 684 nm states and can be treated as further evidence in support of the P680/P684 model suggested in ref 86, namely that P680 is the lowest excitonic state of RCs somewhat disturbed by the isolation and purification procedures, while P684 is characteristic for less disturbed systems, including so-called PSII cores.

5. Hole Burning and Thermocycling Experiments in Photosystem I

5.1. Introduction. Photosystem I (PSI) is one of the two major membrane protein complexes involved in oxygenic photosynthesis whose main function is to catalyze light-driven electron transport through the thylakoid membrane (from the lumen to the stroma) [8, 20-29, 92]. PSI is one of the largest and most complex membrane proteins for which functional information and detailed 3D structure is now available, both for cyanobacteria and plants [8, 20-29]. A structural comparison between cyanobacterial and plant PSI shows interesting similarities as well as major differences [2, 7, 11, 20-29, 92]. PSI in plants is a monomer, while in cyanobacteria PSI usually occurs in a trimeric form [2, 7, 11, 20-29, 92]. Another major and the most striking structural difference between cyanobacterial and plants PSI is found in the light harvesting peripheral antenna network. In cyanobacterial PSI the membrane-intrinsic peripheral antennae do not exist but there is a large membrane-extrinsic antenna system referred to as the phycobilisomes [2, 11, 20-29, 92]. In plants, the peripheral antennae system referred to as the Light Harvesting Complex, LHC I consists of four chlorophyll-binding proteins (Lhca 1-4) closely connected to one side of the monomeric PSI core [2, 11, 20-29, 92].

The PSI core subunits PsaA/PsaB are surrounded by several small membrane-intrinsic subunits whose main function likely is to maintain the stability of the protein and of the antenna network, and mediate trimerization of cyanobacterial PSI [2, 11, 20-29, 92]. Thus, the small membrane-intrinsic subunits are somewhat different in cyanobateria and plants. As all the protein subunits are tightly connected, the PSI core is a robust supercomplex difficult to fractionate further [20].

In all oxygenic photosynthetic organisms the reaction center of photosystem I (PSI-RC) is integral part of the PSI core (respective cofactors belong to PsaA and PsaB subunits) rather than a separate protein entity, like in PSII. The PSI-RC components include the primary electron donor and several cofactors that form the electron transfer chain. The primary electron donor is the "special pair" (P700), a chlorophyll *a*/ chlorophyll *a'* heterodimer which is located close to the luminal side of the membrane [2, 11, 20-29]. The efficient transfer of the excitation energy within the chlorophyll molecules network of PSI leads to the charge separation between the primary electron donor, P700, and primary acceptor, A_0 (Chl *a*). The re-reduction of $P700^+$ by A_0^- is avoided by a fast electron transfer to the intermediate electron acceptor A_1 (quinone), [26, 173, 174].The electron is further transferred across the membrane to Fx and then to the terminal electron acceptor F_B/F_A (Fe_4S_4 clusters).

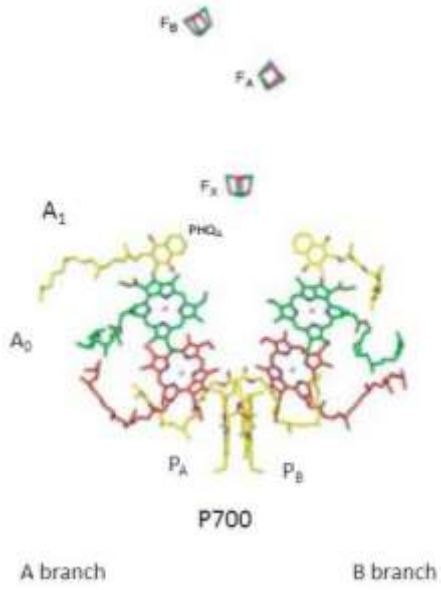

Figure 39. Structural arrangement of the cofactors in the reaction center of Photosystem I, where P_A and P_B designate the two components of the special pair (primary electron donor, P700); A_0 refers to the primary electron acceptor (Chl a) and A_1 is the phylloquinone (PhQ_A); the terminal electron acceptors are three iron-sulfur clusters Fx, F_A and F_B. Adapted from ref. 174, Copyright (2002), with permission from Elsevier

The low temperature (5 K) absorption spectra of PSI from plants and cyanobacteria [175-181] show the existence of several chlorophylls that absorb at longer wavelengths than the primary donor P700. These chlorophylls are known as "red chlorophylls" and their number and distribution over wavelengths varies between species. The red shift of these states is attributed to excitonic interactions. Thus, the states are assigned to groups of pigments (strongly coupled dimers or trimers) rather than to individual pigments with peculiar interactions with protein.

At physiological temperature these states easily transfer energy to the P700, but at low temperature they act as competing energy traps [175-181]. It is believed that the purpose of these chlorophylls is to extend the range of harvested wavelengths. Several spectroscopy techniques including SHB have been used to identify, locate and assign the red chlorophylls in several species of cyanobacteria and plants [175-181]. In plants the red most emission maximum of PSI-200 (200 refers to the number of chlorophylls per P700 in the monomeric core plus in peripheral antenna) is placed at 730 nm (F730) and it has been attributed to peripheral antennae complexes Lhca3 and Lhca4 [175]. In cyanobacteria the lowest-energy states have to be assigned to the core, as peripheral antenna is not present. The lowest-energy states of PSI from several cyanobacteria have been identified and assignments of these states to particular pairs of the strongly coupled Chls have been proposed [175-181]. *Synechocystis* PCC 6803 exhibits two pools of red chlorophylls which are referred to as C708 and C714 [177] while *T. elongatus* has three red antenna states which have been labeled as C708, C715 and C719 according to their peak absorption wavelengths [176]. C719 of *T. elongatus* and C714 of *Synechocyctis* PCC6803 exhibit multiple similar properties (very strong electron-phonon coupling,

strong band or hole shift under pressure, strong Stark effect [176, 177, 183]) which indicates that these states likely originate from the same chlorophyll group and possess some charge transfer character.

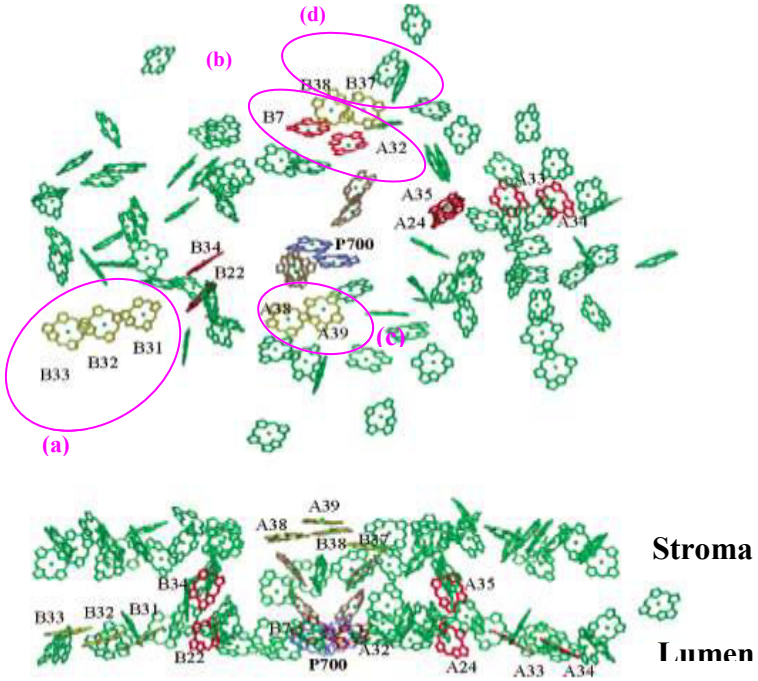

Figure 40. Red chlorophyll assignment in PSI from cyanobacteria where in the notation of Krauß et all chlorophylls B31, B32 and B33 are referred to as trimer **a**. The dimers **b, c** and **d** are made up of chlorophylls A32/ B7, A38/A39 and B37/B38 (from ref. 175, 177, 180). The three-fold axis of symmetry is perpendicular to the page and located above the top view of PSI. Adapted with permission from ref. 180. Copyright (2002) American Chemical Society

However, which of them are the origins of the red antenna states is unclear. Theories with different levels of complexity (dipole-dipole approximation is too crude for small inter-pigment distances) assign the highest couplings to different groups of pigments. Moreover, there is also no agreement about the site energies (transition energies in the absence of interaction) of the chlorophylls. Therefore, assignment of the red states requires comparisons between structural and spectroscopic data. Most of these comparisons were performed for *T. elongatus*, for which the X-ray structure is readily

available. Figure 40 depicts a number of chlorophyll groups which are most likely red states candidates, based on all available data.

There appears to be general agreement about the lowest-energy state (C719 in *T. elongatus* and C714 in *Synechocystis* PCC6803) being attributed to the dimer **b**, B7-A32, Figure 40, [176]. For example, it is known that the relative intensity of the C719 state is sensitive to monomerization, and therefore respective chlorophylls must be located close to the symmetry axis of the PSI trimer. Additionally, Brecht et al have recently (2011) reported that the fluorescence of the red-most antenna states in cyanobacterial PSI (i.e., C719 in *T. elongatus*) is effectively quenched by oxidized P700 [181], indicating that this group of chlorophylls must be located close enough to the special pair as well. Figure 41 from ref. 181 shows the fluorescence spectra of *T. elongatus* PSI with reduced and oxidized P700. As can be seen, the peak of the emission band shifts by almost 10 nm depending on oxidation state of P700. The results depicted in Figure 41 can be interpreted as $P700^+$ quenching the fluorescence of the red-most state of PSI (C719 state) significantly better than reduced P700 does [181 and references therein]. Thus, for oxidized P700, the lowest state emitting at 741 nm is quenched and the emission spectra are dominated by fluorescence from the second-lowest C715 state, emitting at 732 nm. The C708 state of *T. elongatus* PSI exhibits low electron-phonon coupling, and as indicated by SPCS experiments emits around 710-712 nm. $P700^+$ absorbs lower in energy than C719 state and downhill EET from this state to $P700^+$ is possible and rather likely. Fluorescence of other red states is less sensitive to the oxidation state of P700 and their origins are less clear.

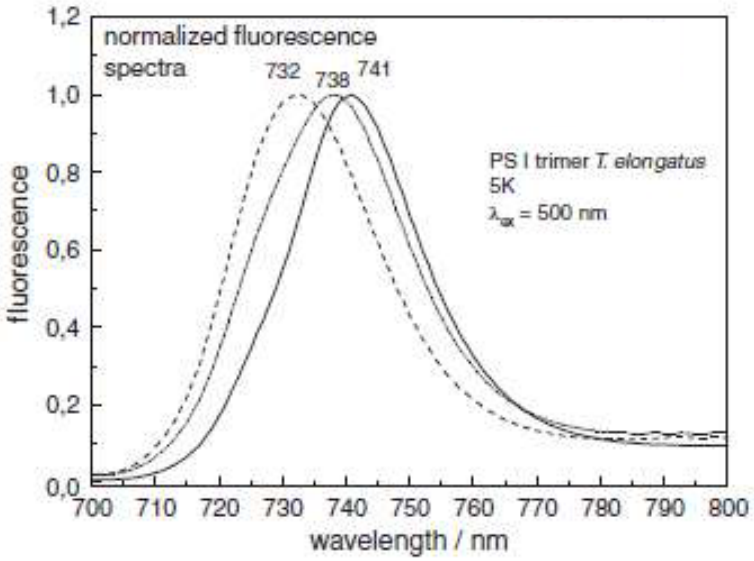

Figure 41. 5 K fluorescence spectra of PS I trimers from *T. elongatus* with P700 in the reduced (solid line), oxidized (dashed line) and mixture of reduced-oxidized state (dash–dotted line). Reprinted from ref. 181, Copyright (Year), with permission from Elsevier

PSI is a "good" SPCS object. Due to the presence of "red antenna states" and the strong electron-phonon coupling of the lowest state(s), the emission is red-shifted with respect to absorption. Among interesting SPCS observations are switching between alternating energy transfer pathways most probably as a result of conformational changes in the protein, as well as dependence of spectral diffusion (line jumps) on the composition of amorphous host surrounding the protein (regular versus deuterated buffer, etc). Based on the latter result Brecht et al concluded that dynamics observed in SPCS experiments involves protons. This is in disagreement with our conclusions based on SHB in a number of other pigment-protein complexes (Chapter 3.4). Thus, it would be interesting to explore protein dynamics in PSI by means of SHB and compare it with SPCS observations. This, however, is not an easy task. The lowest-energy state of PSI exhibits very strong electron-phonon coupling and it is questionable if one can burn much of a zero-phonon hole into it. (In the light of ref. 181 placing the emission of the C719

state at 741 nm, the ZPH observed so far [176, 178] at around 720 nm may actually belong to the C715 state.) Thus, HGK would suffer from low dynamic range. The lifetimes of other states are affected by energy transfer to the lowest red antenna state and/or P700, and the EET rate distributions for them (see Chapter 4) are unknown. Determining these distributions is of interest to us as well. An interesting way to explore these issues is to investigate the satellite hole structures emerging upon burning in PSI. It is usually assumed [175-179] that the formation of the satellite holes at wavelengths longer than the burn wavelength ($\lambda > \lambda_B$) is due to the downhill energy transfer, as is the case for FMO, see Section 4.4.2. But this would explain only the satellite holes corresponding to the lowest-energy bands. Higher-energy bands would transfer energy downhill, and their HB rate would be drastically reduced, see Eq. 5 above. Therefore, the satellite hole structure most likely involves also the upper excitonic components of the lowest-energy states, as well as electrochromic shifts of the bands belonging to some pigments in the vicinity of either the P700, or possibly in the vicinity of the pigments responsible for the red states, as the latter possess significant charge-transfer character [176-178]. Thus, we explored the satellite hole structures resulting from illumination at various wavelengths, as well as dependence of those structures on thermocycling.

5.2. Experimental Details. We performed several low-temperature (5 K) SHB and thermocycling experiments on PSI from both *T. elongatus* and *Synechocystis* PCC6803. The *T. elongatus* sample was produced by dissolving the ultra-pure crystals of PSI employed in X-ray diffraction experiments supplied by Petra Fromme, ASU. *Synechocystis* samples were never crystallized and were produced by more conventional

protocol [177]. The SHB experiments have been performed in both fluorescence excitation mode at high resolution and in transmission / absorption mode at lower resolution. The absorption spectra have been measured with Varian Cary 5000 spectrophotometer at 0.25 nm resolution while the fluorescence excitation spectra have been measured with a Hamamatsu PMT/photon counter module through 750 nm long-pass interference filter (Omega). Two laser systems have been used during the low resolution experiments. The tunable Spectra Physics model 3900 Titanium-Sapphire laser (~30 GHz) has been used for hole burning at wavelengths longer than 730 nm while the frequency-doubled CW Nd:YAG Laser has been used for burning at 532 nm. The tunable Spectra-Physics (Sirah) Matisse dye (LDS698 for 675-730 nm) laser (< 1 MHz) has been used for both hole burning and reading the spectra (at low intensity) in fluorescence excitation mode. As the laser system setup and the spectrophotometer are located in different laboratories, the laser light has been guided using single-mode optical fibers. In more recent experiments (see further sections for details) care has been taken to minimize the amount of light reaching the sample prior to measurements, especially those involving exploration of $P700^+$ formation. The sample compartment of the spectrophotometer was carefully isolated from room light, with only aperture covered by 730 or 750 nm interference long-pass filters (Omega). For all these experiments the temperature inside of the sample chamber was cycled using UTREX temperature regulator.

5.3. Spectral hole burning and thermocycling experiments on PSI. The satellite hole spectra of PSI for *Synechocystis PCC 6803* and *T. elongatus* upon excitation at high energy are shown in Figure 42.

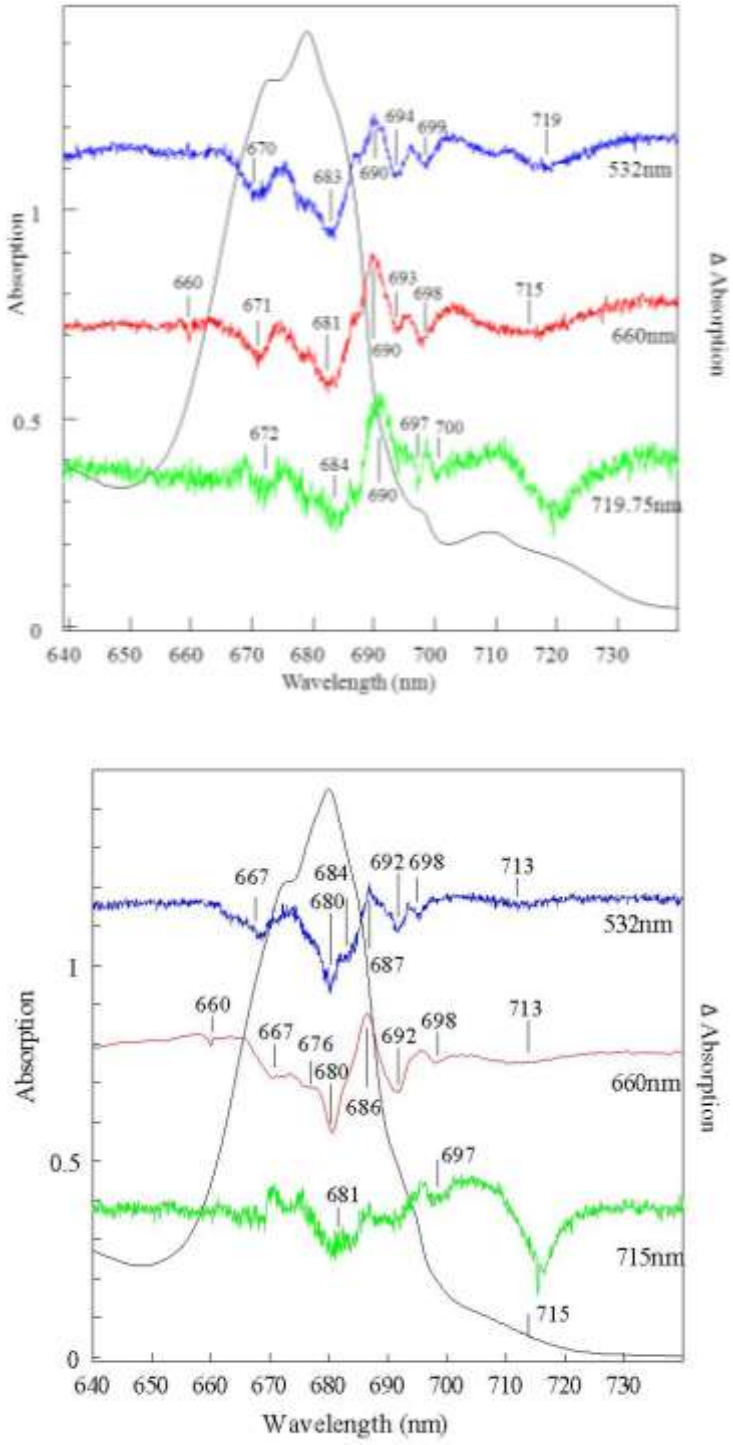

Figure 42. The low-temperature (5 K) absorption and non-resonant hole structures for PSI from *T. elongatus* (frame A) and *Synechocystis PCC 6803* (frame B). Hole spectra are labeled (to the right) with illumination wavelengths

These complex structures likely are superpositions of structures originating from all energy traps, including both red antenna states and P700. However, at the first glance no signature of P700, with characteristic bleach at 703 nm, is observed in any spectra. The same is true about the hole spectra reported over the years [176-178]. It is not clear if the $P700^+$ minus P700 signature was truly not present, or if it was masked by other features of the spectra, for instance by the NPHB anti-holes associated with the lowest-energy spectral holes. In the further discussion we address this question and conclude that unless some effort has been made, the samples used in this work had P700 predominantly in the oxidized state.

5.3.1. The signature of P700 oxidation. Two types/batches of *T. Elongatus* samples have been explored. Samples A had unknown state of P700 oxidation, but based on fluorescence spectra peaked at 732 nm (not shown) and difficulty of producing any additional oxidation of P700 (see below) one can argue that they were predominantly oxidized. Samples B represent an attempt to produce samples with P700 in reduced state [181]. Unfortunately, due to limited amount of high-quality material, we were unable to produce a sample with F_A and F_B FeS clusters perfectly chemically pre-reduced (this makes P700 oxidation fully reversible with characteristic times of 170 μs and several ms, respectively, due to recombination of $P700^+A_1^-$ and $P700^+F_x^-$, and no P700 contribution is expected for persistent holes.) Unexpectedly, illumination of this partially reduced sample yielded a strong signature of $P700^+$ minus P700, with prominent bleach peaked at 703 nm, prominent positive feature at 691 nm, negative feature at 684 nm, as well as a number of smaller and narrower features. Based on both peak magnitude and integral intensity of the 703 nm bleach, we estimate that in about 10% of complexes P700 could

be photo-oxidized by reducing terminal FeS clusters. Judging by fluorescence peaked at 741 nm (Figure 43), in the rest of the complexes in this sample the P700 were likely in reduced state. However, our fluorescence spectrum is slightly broader on the low-energy side than that of [181], indicating the presence of contribution from second-lowest state emission and the presence of some oxidized P700. One can also notice that the shape of our $P700^+$ minus P700 signature does match very closely with that presented in [182].

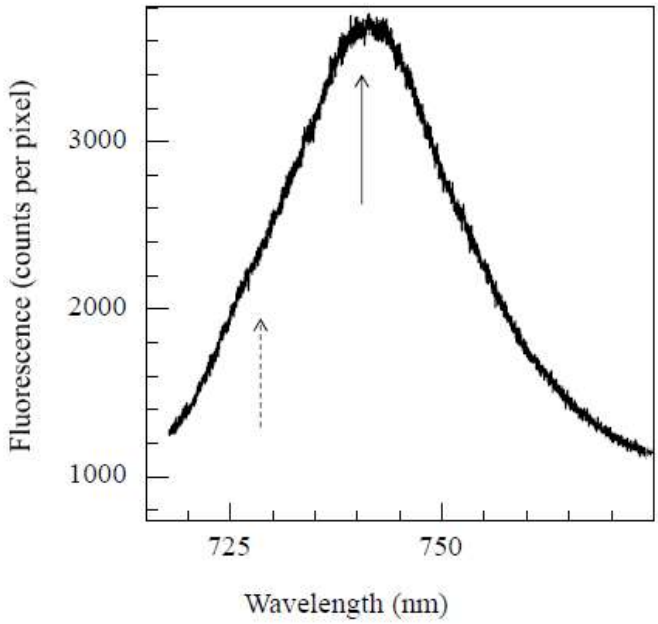

Figure 43. 5 K fluorescence spectrum of mostly reduced sample B. Comparison with figure 41 (from [181]) above shows that while the sample mostly has P700 in reduced state (hence the peak at 741 nm, solid arrow) some contribution from samples with oxidized P700 is also present, yielding a shoulder at ~730 nm, dashed arrow.

This signature difference spectrum could be produced by exceedingly weak as well as by fairly red-shifted illumination. The $P700^+$ minus P700 spectra are depicted in Figure 44. Green curve in frame A is the difference spectrum produced just by scanning the spectrum with spectrophotometer once (difference between second and first absorption spectra measured after cooling the sample to 5 K in the dark). Blue curve is the difference spectrum produced by one minute exposure to the dimly lit (one computer

monitor facing away from the cryostat) room (without any filters; see below). The intensity of this dim light reaching the sample was estimated at several nW/cm^2, all wavelengths combined. However, deliberate illumination of the sample with the laser produces P700$^+$ minus P700 spectrum of larger amplitude. Note that complexes which have either oxidized P700 from the beginning or successfully pre-reduced FeS clusters would not contribute to the P700 signature. The former are already oxidized, and the latter recover in milliseconds [181 and refs therein] and do not contribute to persistent holes. This signature originates from complexes which originally had P700 in reduced state as well as had FeS clusters available.

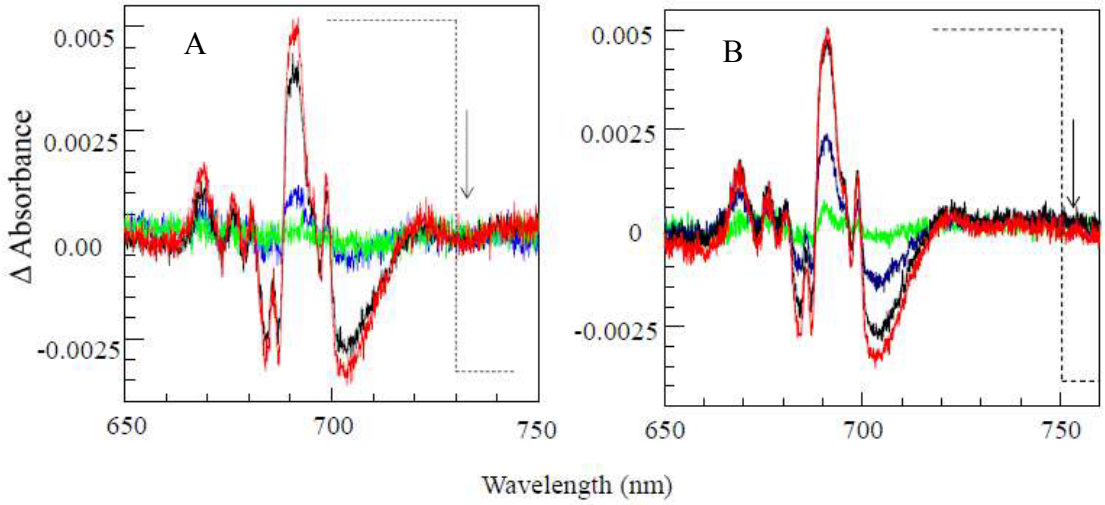

Figure 44. Frame A: Green curve: difference between two consecutively measured spectra. Blue: result of exposure of the sample to dim room light (several nW/cm^2). Black: after one minute of illumination at 732 nm. Red: after 16 minutes of illumination at 732 nm. Dashed line indicates the cut-off wavelength of a long-pass filter, 730 nm. **Frame B:** NPHB-free P700$^+$ minus P700 spectra produced with illumination at 753 nm through 750 nm long-pass filter. Green: difference between the first two spectrometer scans. Blue: after seven spectrometer scans, further scanning does not increase the hole. Black: after 10 minutes of illumination at 753 nm. Red: after further 20 minutes of illumination at 753 nm.

Black curve in frame A is a result of one minute exposure to 20 mW/ cm^2 of light at 735 nm. 730 nm long-pass filter was used to ensure that light at shorter wavelength is not reaching the sample. Red curve results from additional 15 minutes of illumination. Similar curves can be produced with light up to 753 (Figure 44B). In the latter case 750 nm long-pass filter has been employed to ensure that $P700^+$ formation is not due to parasitic light of lower wavelengths (see below).

Manifestations of the ongoing P700 oxidation could also be seen in fluorescence excitation mode, with detection at wavelengths longer than 750 nm. Scanning the laser over the PSI absorption band (from about 735 to 670 nm) with read intensity of tens of nanowatts per cm^2 results in a decrease of the signal at all wavelengths, with C719 band decreasing faster than others. Attempts to measure HGK at any wavelength or HB action spectra resulted in the same effect. Qualitatively, these observations are consistent with ongoing increase of the fraction of oxidized P700 which in turn reduces the fluorescence yield of the C719/F740 state, whose fluorescence, peaked at 741 nm (Figure 41) is preferentially detected in fluorescence excitation experiments. Absence of the sample with either 100% reduced or 100% oxidized P700 prevented us from measuring reliable HGK data. Observed HGK curves clearly contained multiple components, i.e., they were a superposition of NPHB and overall signal decrease due to $P700^+$ formation.

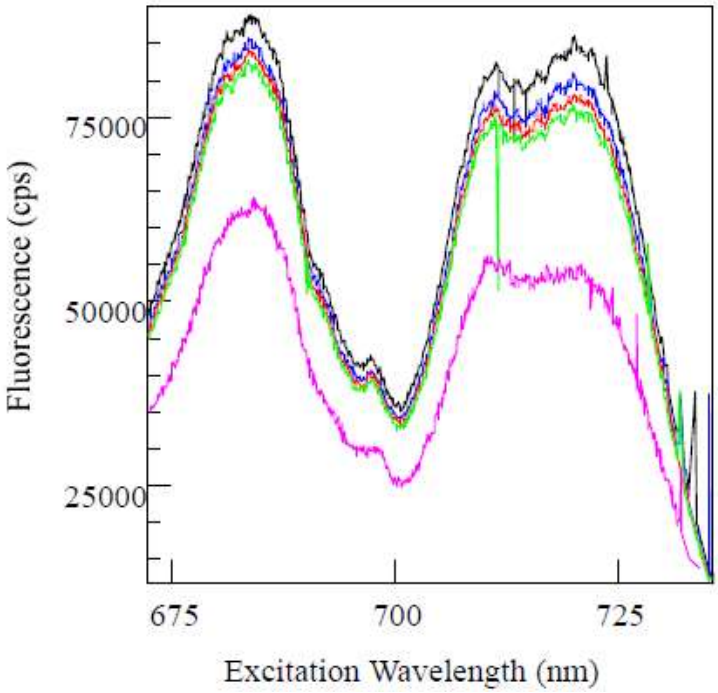

Figure 45. Fluorescence excitation spectra of sample B, cooled down in the dark. Black to green curves represent consecutive scans from 735 to 670 nm. Magenta curve was recorded after an attempt to measure the HB action spectrum covering 735 to 700 nm range. Spectra are equally distorted (longer-wavelength range is amplified) by the transmission dependence on wavelength of the supposedly neutral density filters used for beam attenuation. The spectra were left uncorrected since in uncorrected spectra the red state region is artificially amplified and its evolution is clearer.

As photo-oxidation of P700 in a fraction of complexes proved extremely easy, we needed to estimate the amount of parasitic light (mostly fluorescence of the Ti-Sapphire crystal, scattered pump laser light, etc) which might leak into the optical fiber between the laser system and spectrometer and be responsible for $P700^+$ formation. In order to do that, we measured the amount of light passing through a fiber and a combination of 700 nm long-pass and 720 nm short-pass interference filters when illuminated with 15 mW of 745 nm laser light (here and below all powers are per powermeter area, 0.65 cm^2). This transmitted amount was approximately 220 nW. Approximately 150 nW out of these 220 nW are expected to belong to 745 nm light transmitted through the 720 nm short-pass filter, as the attenuation of this filter at 745 nm is 100,000 times. Thus, approximately 70

nW of parasitic light per 20 nm spectral window would be expected under these conditions. The 730 or 750 nm long-pass filters used in the above experiments on PSI have attenuation of at least 100,000 times below 730 nm or below 750 nm, respectively. Thus, the amount of parasitic shorter-wavelength excitation reaching the sample through the long-pass filters must not have exceeded single picowatts per cm^2. With typical illumination times of ~10-30 minutes, one cannot explain observed P700 oxidation with parasitic light alone. Thus, P700 absorption extends to at least 753 nm. This is comparable to RT results [182 and references therein] and much longer wavelength than reported earlier for 5 K. Minimizing the amount of light impinging on (mostly oxidized) samples A prior to measurement allowed us to observe the $P700^+$ formation also in these samples. The amplitude of the respective hole spectrum, however, was several times lower and the spectra are not shown here due to much poorer signal to noise ratio. Finally we note that in the light of the above it is not surprising that Small and co-workers [176-178, 183] never observed any signature of P700 oxidation in their spectra. A Fourier-transform spectrometer was utilized by their group, which constantly illuminates the sample with relatively intense white light. Thus, if samples used in [176-178, 183] contained any fraction of reduced P700 capable of being semi-permanently oxidized, it was oxidized prior to the first measurement.

5.3.2. Persistent HB and thermocycling

Measurements described below were performed using sample A, likely predominantly oxidized. Exposure to dim (~nW/cm^2) room light, which is known to cause detectable $P700^+$ formation in the partially reduced sample, did not cause

noticeable effects. Weak 700^+ minus P700 signature (similar to the one shown in Fig. 44B) could still be produced by illumination at 733 nm through 730 nm long-pass filter, indicating that P700 is not perfectly oxidized from the beginning. After further illumination at 733 nm did not enhance the $P700^+$ minus P700 signature any more, additional burning was attempted at 725 nm (without the 730 nm long-pass filter). Illumination at this wavelength is expected to probe only the C719 state. The response to burning is still very weak (blue curve), in line with the lifetime of C719 being shortened due to quenching by $P700^+$ [181] and the HB yield being reduced. The only clearly observable item in addition to the resonant hole and its anti-hole is a positive feature at 689.4 nm. This feature is different with respect to the positive 691 nm feature of the $P700^+$ minus P700 signature (shown in red for comparison). It is not clear if this positive feature is associated with the negative feature to the blue or to the red of it (see also comments on *Synechocystis* below). In the latter case, the 689 nm feature will be the anti-hole of the higher excitonic component of the C719 state. The higher excitonic state hole itself might be masked by the anti-hole of the original hole. It is also possible, however, that some conformational change in the protein moves the absorption of C719 pigments to 689 nm. This would result in C715 becoming the lowest-energy state of the complex.

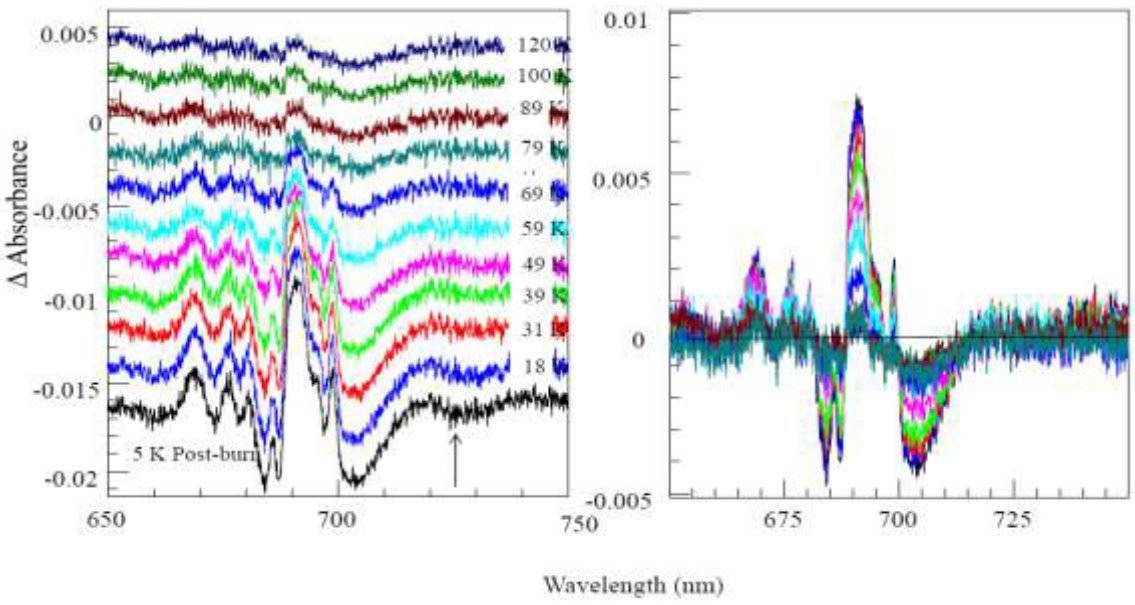

Figure 46. Left Frame: Hole spectra after thermocycling to indicated excursion temperatures. Spectra are shifted along vertical axis for clarity. Arrow indicates the burn wavelength of 725 nm. Right frame: several hole spectra (color coding same as in the left frame) overlaid together.

Black curve in Figure 47 is the hole spectrum for λ_B=714.5 nm. Again, prior to this burn the sample was illuminated by 733 nm light through 730 nm long-pass filter to oxidize remaining P700. At 714.5 nm wavelength both C715 and C719 states are populated either directly or via energy transfer. The C708 state is not probed. The electron-phonon coupling for C708 state is weak, the absorption band is narrow, and therefore the origin of this state is not too far from 708 nm. Thus, C708 absorption at 714.5 nm is expected to be negligible. Zero-phonon hole is clearly visible at burn wavelength, even at 0.25 nm resolution, indicating that electron-phonon coupling for the C715 state is weaker than for C719 state. As for the 725 nm hole spectrum (blue), the 714.5 nm hole spectrum (black) exhibits features that do not resemble those of the $P700^+$ minus P700 spectrum (red). Most of the features of the 725 and 714.5 nm hole spectra are similar, and probably belong to C719 group of chlorophylls. However, one clear

difference is the presence of a strong negative feature at 682.5 nm in the 714.5 nm hole spectrum. Thus, we propose that the higher excitonic band of the C715 state is at 682.5 nm. A combination of weak positive feature at 661 nm and negative feature at 671 nm also seem to be associated with C715 state. None of the hole spectra in Figure 47 clearly indicate that the higher excitonic state of the respective chlorophyll group is much stronger than the lowest-energy state. According to excitonic calculations [105], the lowest excitonic band of the B7-A32 dimer possesses larger oscillator strength than its higher-energy exciton band, while for A38-A39 and B37-B38 dimers the lower exciton state has to be the weaker one. Thus, at the first glance, our results seem to indicate that A38-A39 and B37-B38 dimers unlikely are the origin of either C719 or C715. However, the energy difference between higher and lower-energy bands belonging to the same group of chlorophylls is significantly larger than twice the inter-pigment coupling (~700 cm^{-1} versus ~2x150 cm^{-1} for C715 state). This indicates that the site energies (in the absence of interactions) of respective chlorophylls are significantly different, the C715 state is somewhat localized on the lower-energy pigment in the dimer, and therefore the difference in oscillator strengths of higher and lower excitonic bands should be much smaller than predicted in [105].

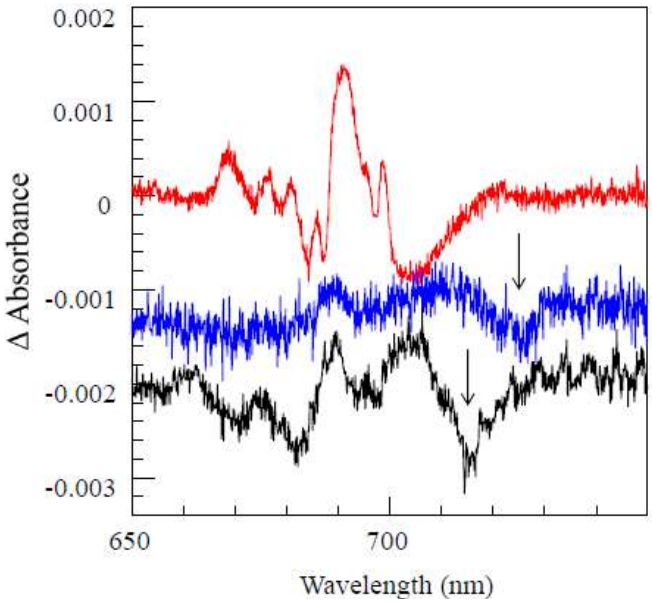

Figure 47. Sample A with mostly oxidized P700. Black: hole spectrum after illumination at 714.5 nm, probing both C715 and C719 states. Blue: hole spectrum after illumination at 725 nm, probing only C719 state. Arrows indicate burn wavelengths. Red: $P700^+$ minus P700 signature from sample B, Figure 44, presented for comparison.

Figure 48 depicts the results of a thermocycling experiment with the hole burnt at 719 nm, for sample A, with mostly reduced P700. Here the sample was not deliberately subjected to any long-wavelength illumination (supposedly oxidizing the remaining P700) prior to burning. On the other hand, no effort has been made to keep the sample in the dark, and it is possible that sample was exposed to a flashlight during adjustment. Again, ZPH is clearly visible in the hole spectrum, indicating contribution from C715 state in addition to that of C719 state. These spectra are still mostly free of $P700^+$ minus P700 contribution. If that contribution were present, it could be hidden behind the NPHB features, in particular the bleach at 703 nm could be hidden under the anti-hole of the original hole.

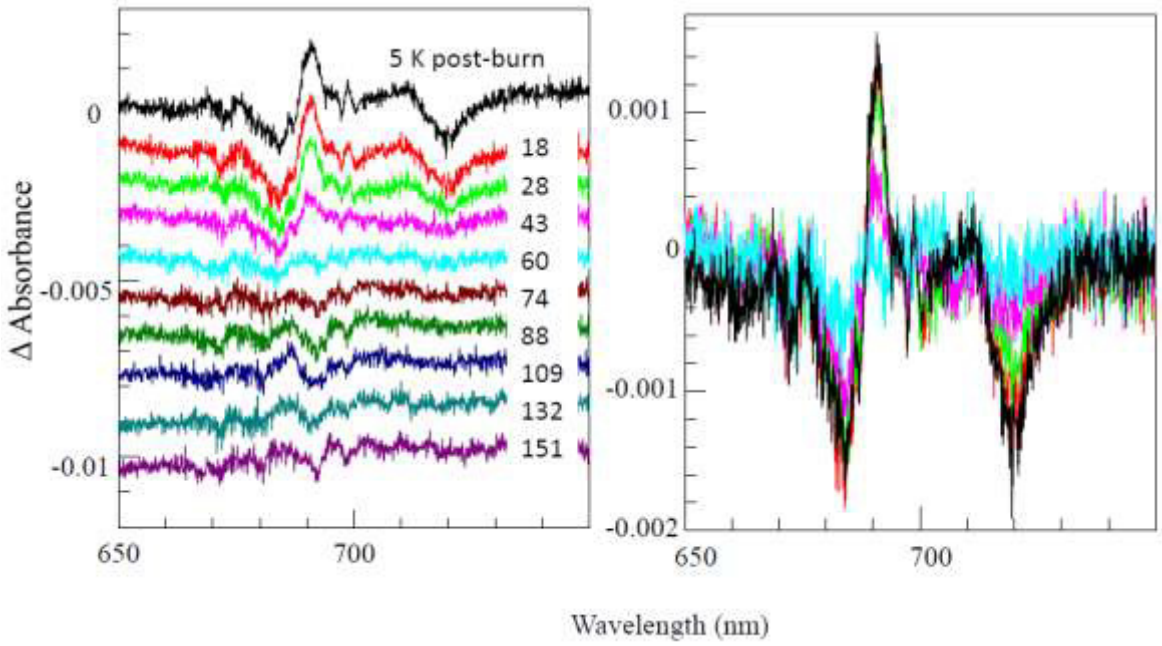

Figure 48. Left Frame: Hole spectra with λ_B=719 nm after thermocycling to indicated excursion temperatures. Spectra are shifted along vertical axis for clarity. The burn wavelength was 719 nm. Right frame: several hole spectra (color coding same as in the left frame) overlaid together.

However, mutual compensation of the P700 hole and the anti-hole of the resonant hole is unlikely. First, that would imply comparable rates of P700 oxidation and NPHB, which is unlikely, given that these are vastly different processes. It is unclear why nearly perfect compensation should occur in several samples, for several burn wavelengths and various illumination doses. However, the NPHB hole (together with its anti-hole) seems to recover by 60 K, but the P700 bleach hole does not emerge in the process of thermocycling (see in particular light blue spectrum). The left part of the Figure 48 contains hole spectra shifted with respect to each other for clarity. The right part of the figure contains spectra for cycling temperatures up to 60 K, overlaid to make the differences in the rates of recovery of various features more obvious. It is apparent that all the main features of the spectrum recover at different rates, and the ratios of those

rates are not the same as for the $P700^+$ minus P700 feature, Figure 44. By the time resonant C715/C719 hole is almost recovered (cyan; 60 K), the 684 nm negative feature has recovered only by ~50%. Interestingly, after cycling to higher temperatures, the difference spectra develop a weak positive feature at 684 nm and weak negative feature at 690 nm. These persist till 151 K. It is quite likely that some $P700^+$ has been formed in the sample in the process of alignment, even before the pre-burn spectrum of the series has been measured, and then experienced recovery.

The discrepancies in the recovery rate of higher- and lower-energy features associated with C715 and/or C719 states indicate that hole recovery involves more complicated process than just the return of a pigment blue-shifted as a result of NPHB to its original wavelength. It appears that the satellite hole structures are formed due to a "domino effect", where NPHB-induced structural changes in the vicinity of one pigment trigger changes in the vicinity of the other pigment. The latter may not fully recover immediately when the first pigment and its environment return to the original conformational sub-state.

Figure 49A shows satellite hole structures obtained as a result of burning at 532 nm and 660 nm. The satellite hole structures for short burn wavelengths may contain contributions from all three red antenna states as well as from P700 oxidation, if the latter is still possible. The absorption around 532 nm is dominated by carotenoids, which then transfer energy to chlorophylls. The spectra are normalized to the same intensity of the lowest-energy hole (C719), although they were almost normalized to begin with. Frame B shows the difference of the two above spectra. Both spectra clearly possess a 709 nm hole, matching the respective peak in the absorption spectrum (C708). This component of

the satellite hole structure is present for lower illumination doses as well, indicating that C708 is always a weak trap, in agreement with SPCS results by [185-188], not only after the C719 is burnt away. Again, as in the case of burning at shorter wavelengths, the hole spectra are non-conservative. The bleach at 703 nm is missing. We note that in sample B, where P700 was predominantly reduced, illumination at short wavelengths produced the satellite hole structure still dominated by $P700^{+}$ minus P700 signature (results not shown), even if there was prior illumination at >730 nm. Thus, we believe that in sample A the latter contribution was truly negligible.

The most prominent difference between 532 nm and 660 nm spectra is that the 710 nm and 719 nm holes are poorly separated in the latter. The difference spectrum in Frame B exhibits lowest-energy hole at 712.6 nm. Although the easiest interpretation would be to still assign this hole to the C715 state, the comparison with the difference between spectra with λ_B of 714.5 nm and 725 nm Figure 47, frame C in Figure 49 (this difference would be dominated by the satellite hole structure associated with C715), shows that the whole satellite hole structure is different in these two cases. Thus, our results can be considered as preliminary evidence for still another red antenna state. Note that the combined intensity of the red region in *T. elongatus* PSI is equal to that of 8-9 Chls per monomer [182], and not all oscillator strength of all chlorophyll groups is concentrated in the red state region [105]. Thus, presence of the fourth red antenna state is in principle feasible. Apparently, excitation via carotenoids at 532 nm does not bring excitation into the vicinity of this group of pigments. Byrdin et al [105] reported the distances between chlorophylls of PSI and carotenoids. In the PSI carotenoids seem to be evenly distributed, and only a small fraction of chlorophylls are further away from the

nearest carotenoid than 7Å. None of the chlorophyll groups usually proposed as origin of the red antenna states (see Figure 40) is composed of chlorophylls which are consistently very far from any carotenoids. There are two groups of pigments exhibiting sufficiently strong couplings which are far from carotenoids. These are A36-A37 and B14-B15 [105] and they were not seriously considered as origin of any red antenna states before.

Finally, we compare the spectra with λ_B of 714.5 and 532 nm, frame D. The hole spectrum with λ_B of 714.5 is dominated by C715 and C719 states, while the spectrum with λ_B of 532 nm also contains contribution from C708 (and, if the additional red state is present, see above paragraph, the 532 nm spectrum contains reduced contribution from that state.) The spectra have been normalized in the low-energy, C719 region. The difference spectrum may contain contributions from C708 and C715. It appears that the C708 hole is accompanied by strong features around 683, 678 and 671 nm. These features appear stronger than the C708 hole itself, suggesting that C708 state originates from one of the chlorophyll groups for which the weaker lower exciton state is predicted.

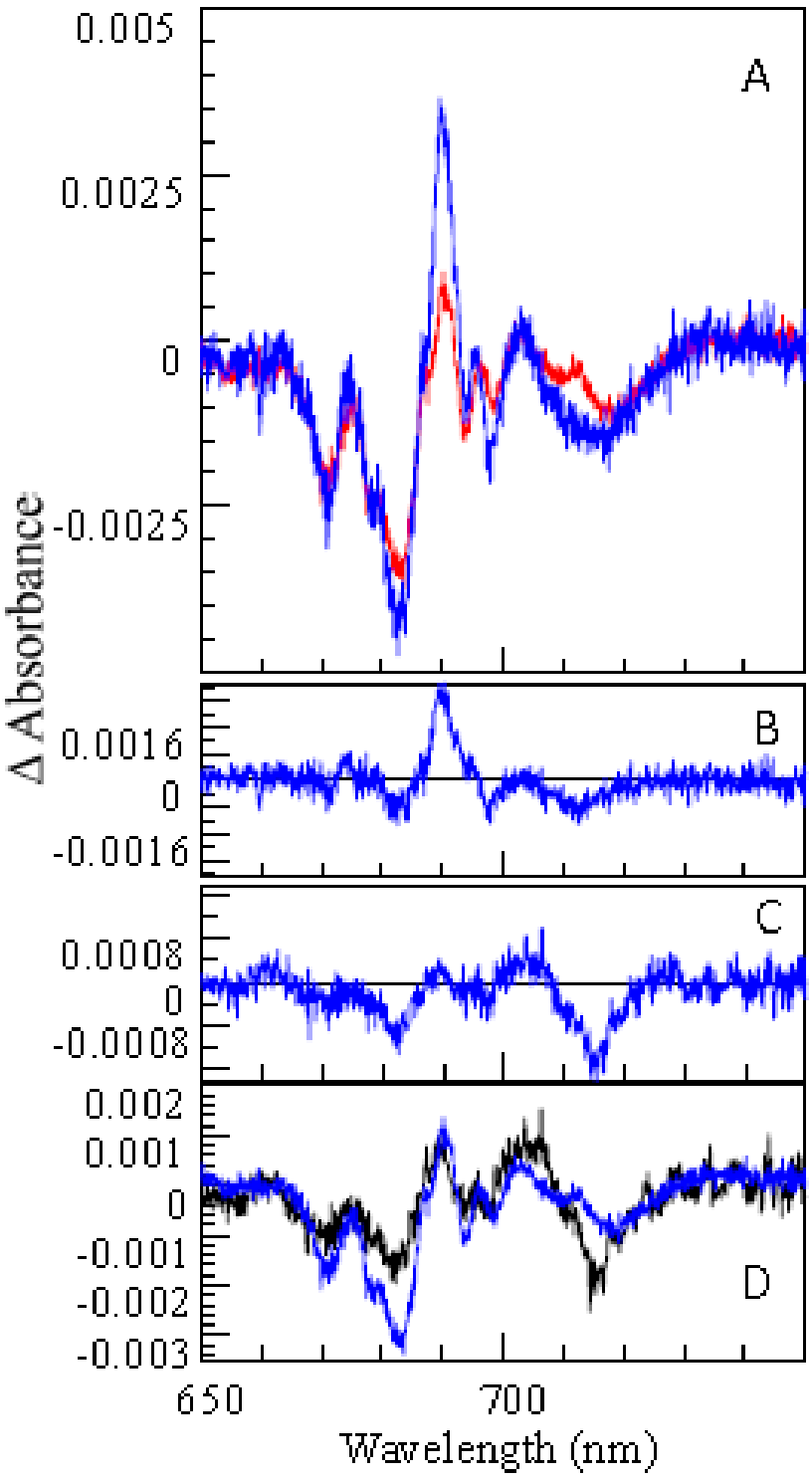

Figure 49 Frame A: Hole spectra for λ_B of 660 nm (blue) and 532 nm (red). **Frame B:** the difference between spectra in frame A. **Frame C:** The difference between spectra for λ_B of 714.5 and 725 nm (see Figure 47). **Frame D:** the hole spectra for λ_B of 714.5 nm (black) and 532 nm (blue).

Similar experiments have been performed also on PSI of *Synechocystis PCC6803*. Chronologically, these experiments were performed earlier than those on *T. elongatus*, and no effort has been made to alter the oxidation state of P700 using either chemical reagents or light. Overall, the satellite hole spectra for two organisms qualitatively resemble each other relatively closely, except the NPHB spectra ($P700^+$ minus P700 signature was not observed, indicating that most of the PSI was probably oxidized) obtained for *Synechocyctis* are shifted by several nm to the blue. A notable exception is the absence of a strong positive feature (analog of the 689 nm feature in *T. elongatus*), in the long burn wavelength spectrum, see Figure 42. This provides additional argument in favor of "domino-effect", multi-step conformational changes suggested above.

5.4. Conclusions. We demonstrated that oxidation of P700 can occur upon illumination at >750 nm even at cryogenic temperatures. Achieving perfect control over oxidation state of P700 in PSI samples is essential for proper SHB measurements, including both resonant (such as HGK measurements for the purpose of protein energy landscapes exploration) and non-resonant burning. We succeeded in obtaining the isolated signatures of C719 and C715 states, including higher excitonic components. Additionally, we present preliminary evidence for the fourth red antenna state, with the band peaked at 712.5 nm. Obtaining separate satellite hole signatures of various red states allows for narrowing the range of possible site energies, and provides additional constraints for structure-based modeling of various optical spectra. Interestingly, many of the above hole structures appear to have similar features at similar wavelengths. Although it might be just a coincidence (it is difficult to fit 96 chlorophylls into a relatively narrow spectral region and not to have some similar spectra), it is tempting to

speculate that red antenna states having higher exciton states in resonance with those of P700 might have some evolutionary advantage, by somewhat increasing the probability of EET from the red states to P700. So-called extended Förster EET models, describing EET between groups of strongly coupled pigment molecules [107-109] involve the overlaps between whole densities of states (including the higher exciton levels) rather than the overlaps between emission and absorption spectra of regular Förster theory. Finally we note that there is also evidence that the observed C719 and C715 signatures may be affected by "domino effect", and are not just a result of NPHB-induced blue shift of the absorption of the lowest-energy pigment in the group.

Conclusions

Effects of the distributions of excitation energy transfer (EET) rates (homogeneous line widths) on the nonphotochemical spectral hole burning (NPHB) processes have been theoretically explored and experimentally determined for several oxygenic photosynthetic chlorophyll protein complexes. We have proven that the quantitative analysis of the effects of the line width distributions resulting from Förster-type EET between weakly interacting pigments with uncorrelated site distribution functions, on the NPHB spectra of isolated CP43 antenna from spinach allows for the extraction of approximate values of inter-pigment couplings and rejection of some band-to-pigment assignments. In particular, the coupling between A and B states is of the order of 5 cm^{-1}, which is in agreement with these states being localized on pigments 44 and 37, respectively. The effects of the distribution of frequency-dependent EET rates on resonant and non-resonant NPHB spectra from Fenna-Mathews-Olson (FMO) antenna complex of green bacteria have also been investigated. We demonstrated that inclusion of additional feature, burning following EET, into the HB master equation allows for reasonable fits to experimental data. The hole and emission spectra are very sensitive to the presence of even slow EET, and their analysis allows for determination of inter-pigment coupling. We argue that NPHB results obtained for 825 nm band in trimeric FMO of *C. Tepidum* are consistent with the presence of relatively slow EET and with weak (~1.5 cm^{-1}) coupling between identical lowest-energy pigments from adjacent monomers. The discrepancy between measured and calculated couplings may be explained by use of incorrect dielectric constant of the protein in calculations. Dielectric constant can be measured in a simpler system, for example cytochrome b6f, containing

only two weakly-interacting chlorophyll molecules, by comparing calculated coupling and coupling obtained via emission and HB spectra analysis described here.

We also explored the effects of the distribution of charge transfer rates on PSII RC from spinach. Our findings are consistent with the assumption that two different charge separation pathways in the PSII RC coexist at low temperatures, with each pathway leading to either slow (activated, characteristic time longer than 160 ps) or fast (activationless, characteristic lifetime several ps) charge separation. Moreover, our SHB data support the idea that P680 is the lowest excitonic state of RCs somewhat disturbed by the isolation and purification procedures, while the shoulder at 684 nm represents P684, characteristic for less disturbed systems, including so-called PSII cores.

Some features of the protein energy landscapes have been explored for the lowest-energy pigments of cyanobacteria *Thermosynechococcus elongatus* by means of high and low resolution hole burning spectroscopy. We analyzed the effects of the P700 oxidation on the resonant and nonresonant holes in PSI and, in particular, the satellite hole structures emerging upon burning in PSI have been measured and thermocycling experiments have been performed. Most importantly, the isolated signatures of C719 and C715 states, including higher excitonic components, as well as preliminary evidence for the fourth red antenna state, with the band peaked at 712.5 nm, have been reported in this research. Obtaining isolated satellite hole signatures of various red states has particular importance as it limits the range of possible site energies, and provides additional constraints for structure-based modeling of various optical spectra.

There are several future directions of research which will enhance our understanding of EET and protein dynamics in photosynthetic complex. First, the model and software developed here for calculation of both resonant and non-resonant hole spectra in the presence of Förster-type EET between pigments in pigment-protein complexes has to be refined and improved by including spectral memory and excitonic effects. Inclusion of spectral memory into HB models will allow some molecules to be cycled back and forth between two (or more) frequencies. This effect will result in a reduced net burning of molecules with lower frequencies than the burn frequency, except for the region close to burn frequency. Incorporation of the effect of indirect resonant burning of higher states attributable to excitonic effect into simulation of HB spectra at high resolution is a subsequent step as it requires spectral memory presence. Thus, it will provide a concrete way to track the excitonic interactions in a trimer. However, since spectral memory approach uses more than one tier of the protein energy landscape its development requires more knowledge about protein dynamics of photosynthetic complexes.

For Photosystem I the first obvious step would be reconfirming the observations presented here using samples with P700 perfectly reduced and perfectly oxidized. Once proper sample preparation is mastered, we will follow our original plan and explore protein dynamics and energy transfer between the “red states”. The experience gained with the EET rate distributions in the course of this work will help us with the latter task. As some features of the spectral diffusion behavior may reflect the dynamics of the amorphous host surrounding the protein (i.e., the frozen buffer/glycerol glass), rather than

of the protein itself, we will have to extend our experiments to Photosystem I in deuterated buffer and/or glycerol.

Additionally, to achieve better understanding of the protein dynamics and energy landscapes in chlorophyll-protein complexes will we perform HB, recovery and thermocycling experiments in a simple trans-membrane protein involved in photosynthesis, Cytochrome b_6f (possessing one Chl *a* molecule per protein monomer) as well as in chlorophyll-doped organic glasses (as a control experiment). As Cytochrome b_6f is a dimer, it may also be possible to explore slow EET (similar to that between monomers in FMO) and measure the protein's dielectric constant.

Tables and figures

Table 1. Tunneling distribution parameters used to fit the HGK curves (from ref. [59] and [71]).

	LH2[a]	**CP43, A-state**	**CP29**	**LHCII monomer**	**LHCII trimer**
λ_0	10.3±0.2	10.2±0.2[b]	10.2 ±0.2	11.3±0.2	11.2±0.2
σ_λ	0.7±0.2	1.0±0.05	1.4±0.2	2.0±0.2	2.3±0.2
S	0.45 ± 0.05	0.30±0.05	0.60±0.05	0.80±0.05	1.3±0.1

[a] from [59]
[b] corrected value for CP43 is given according to [71].

Table 2. Hole simulation parameters for CP43 (from ref. 60)

CP43 band	**SDF peak; width (cm^{-1})**	**Oscillator strength (Chl eq.)**	**Excited state lifetime (ns)**	**S_{PSB}**	**ω_m; Γ_{Gauss}; $\Gamma_{Lorentz}$ (cm^{-1})**	**λ_0**	**σ**
A	14643; 180	1	3.5	0.30±0.05	17; 11; 70	10.2±0.1	1.0±0.1
B	14643, 65	1.2	3.5	0.30±0.05	24; 15; 70	9.7±0.3	1.0±0.1

Table 3. Inter-pigment couplings between Chl a molecules in CP43 complex, in cm^{-1}.

	Chl 33	Chl 34	Chl 35	**Chl 37**	Chl 41	Chl 42	Chl 43	**Chl 44**	Chl 45	Chl 46	Chl 47	Chl 48	Chl 49
Chl 33	???	-8.68	-3.13	-1.59	-3.28	12.43	12.31	1.23	-7.91	2.39	-1.82	-0.78	-0.11
Chl 34		???	-23.7	74.51	1.0	0.81	88.33	5.67	22.48	65.87	10.77	-5.68	-0.93
Chl 35			???	-18.96	-1.79	-1.16	-4.37	-5.31	-5.38	-18.55	-5.51	15.64	4.65
Chl 37				???	1.51	3.2	1.7	**5.72**	-1.2	23.99	2.52	-2.45	3.2
Chl 41					???	-15.51	-65.57	-16.67	19.73	-3.01	-1.25	2.27	-3.35
Chl 42						???	50.95	9.48	-19.7	9.18	3.73	-5.44	6.85
Chl 43							???	-8.76	58.92	-1.21	-5.57	24.17	-15.65
Chl 44								???	39.7	48.04	47.8	-16.45	8.3
Chl 45									???	-35.99	86.89	17.72	-5.67
Chl 46										???	-58.08	-8.92	8.19
Chl 47											???	-15.95	8.74
Chl 48												???	-45.46
Chl 49													???

Table 4. Couplings between Bchls of adjacent trimers in cm^{-1} calculated assuming effective μ^2 = 30 D^2. Couplings between identical Bchls are highlighted. The Bchl3-Bchl3 coupling is -3.0 cm^{-1}.

	1A	2A	3A	4A	5A	6A	7A	8A
1C	1.6	0.7	-0.7	0.9	3.4	1.8	1.5	25.7
2C	2.3	-0.3	-3.5	-2.6	11.1	7.0	3.1	5.0
3C	2.1	0.5	-3.0	6.8	6.6	2.9	6.3	0.7
4C	0.4	0.7	0.7	2.9	-1.1	-0.4	2.9	-1.5
5C	0.9	1.3	1.7	-0.4	2.7	-0.1	-1.1	4.0
6C	0.0	1.0	1.0	2.2	-2.3	-2.0	2.7	-9.6
7C	0.5	0.5	-0.9	7.0	-2.5	0.3	9.0	-11.3
8C	0.0	0.8	1.0	-1.4	1.8	-1.5	-3.4	5.2

Table 5. Hole simulation parameters for PSII RC

band	SDF peak; width (cm^{-1})	Oscillator strength (Chl eq.)	Excited state lifetime (ns)	S_{PSB}, S_{80}	ω_m; Γ_{Gauss}; $\Gamma_{Lorentz}$ (cm^{-1})	λ_0	σ
684 nm	14605; 90	2	6.0	0.80±0.05, 0.2	17; 11; 17	10.4±0.2	1.1± 0.2
680[+] nm	14699; 110	2*	6.0	0.80±0.05, 0.2	17; 11; 17	10.4 ±0.2	1.1± 0.2

[+] the parameters of the 680 nm band do not affect burning at 686 nm significantly, and no attempt was made to vary them to achieve a better fit.
[*]additionally, the amplitude of the 680 nm band is three times larger than for the 684 nm band due to sample heterogeneity, not different oscillator strength.
The pure dephasing-limited homogeneous line width was set to 0.033 cm^{-1} (1 GHz),[28]

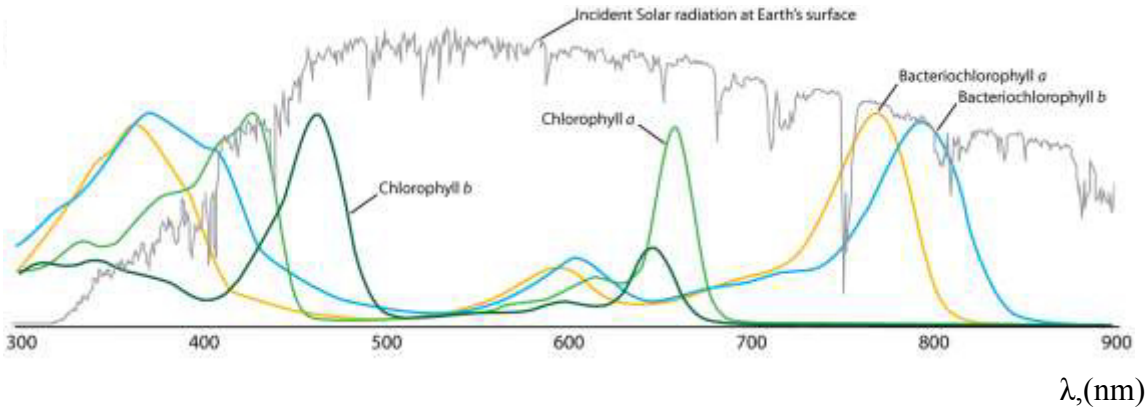

Figure 1. Absorption spectra of chlorophylls *a* and *b* and bacteriochlorophylls *a* and *b* in methanol and ethanol. For comparison, the solar radiation spectrum is presented as well. Reprinted from ref. 13, Copyright (2010), with permission from Elsevier

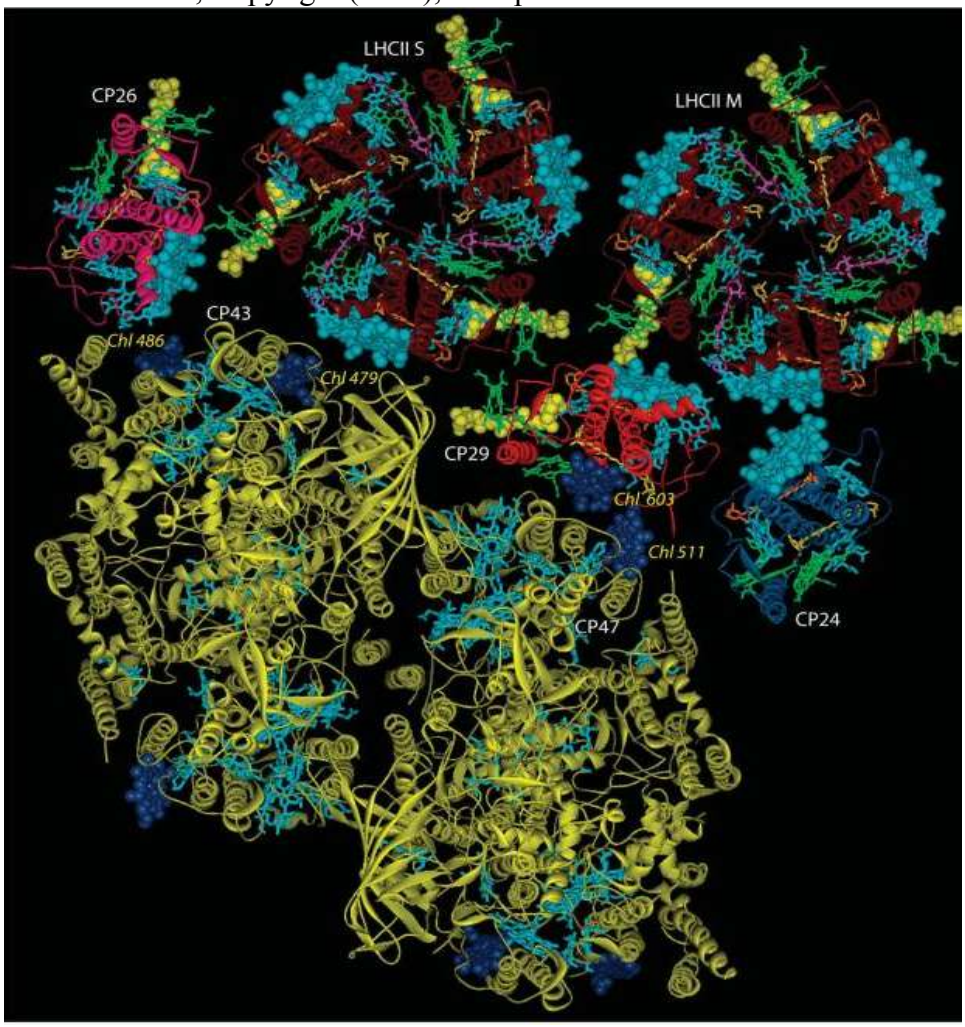

Figure 2. The structure of the PSII in plants where the yellow ribbon diagram shows the structure of PSII- core (from ref. 14). Note that the core is dimeric. Reprinted by permission from Macmillan Publishers Ltd: EMBO, ref. 14, copyright (2009).

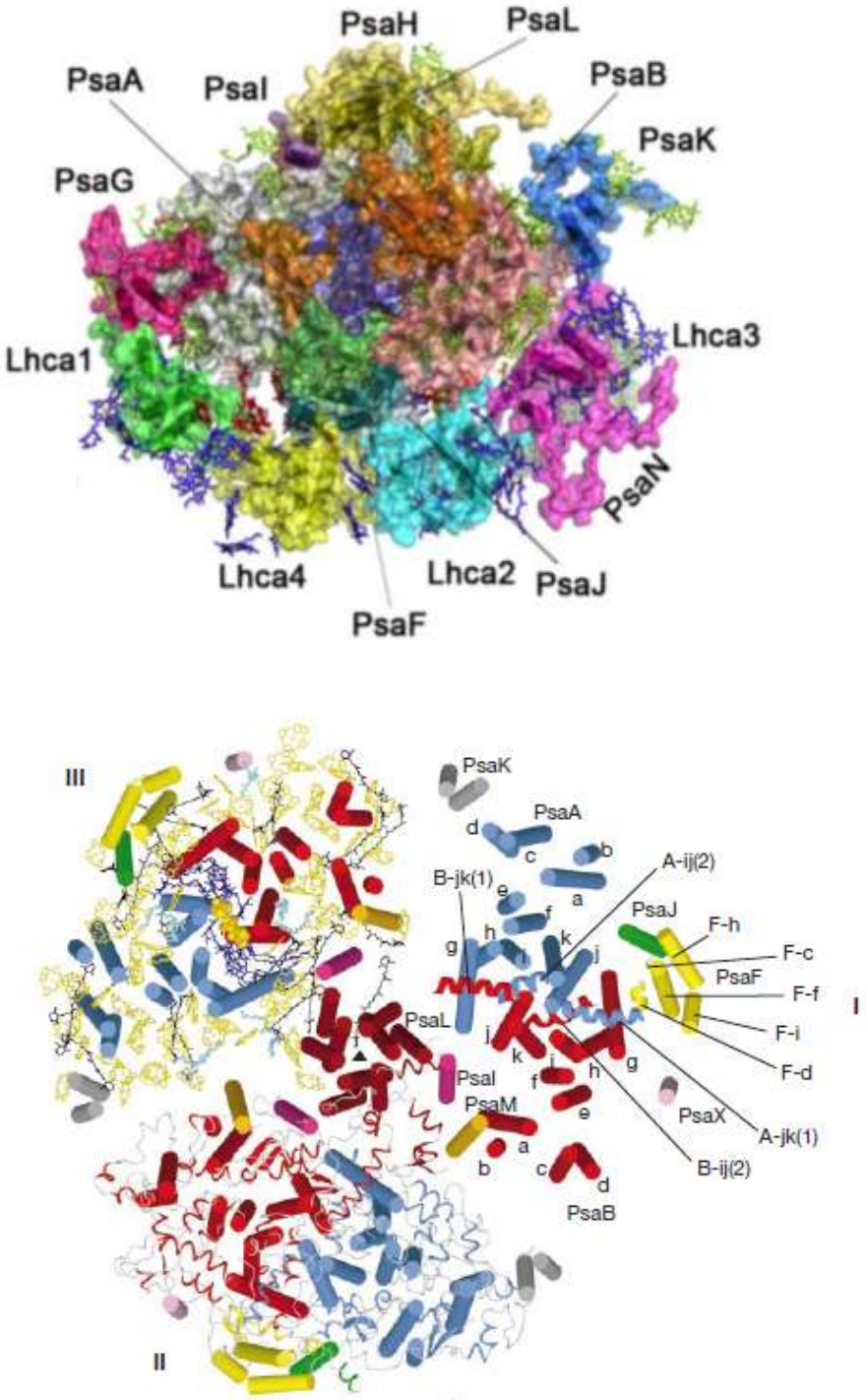

Figure 3. Structural details of PSI from plants (top; from Ref. 21, reprinted with permission from American Society for Biochemistry and Molecular Biology) and cyanobacteria *Thermosynechococcus elongatus* (bottom; Reprinted by permission from Macmillan Publishers Ltd: Nature, ref. 29, copyright (2001). Monomers are oriented with PsaL protein subunits towards three-fold symmetry axis.

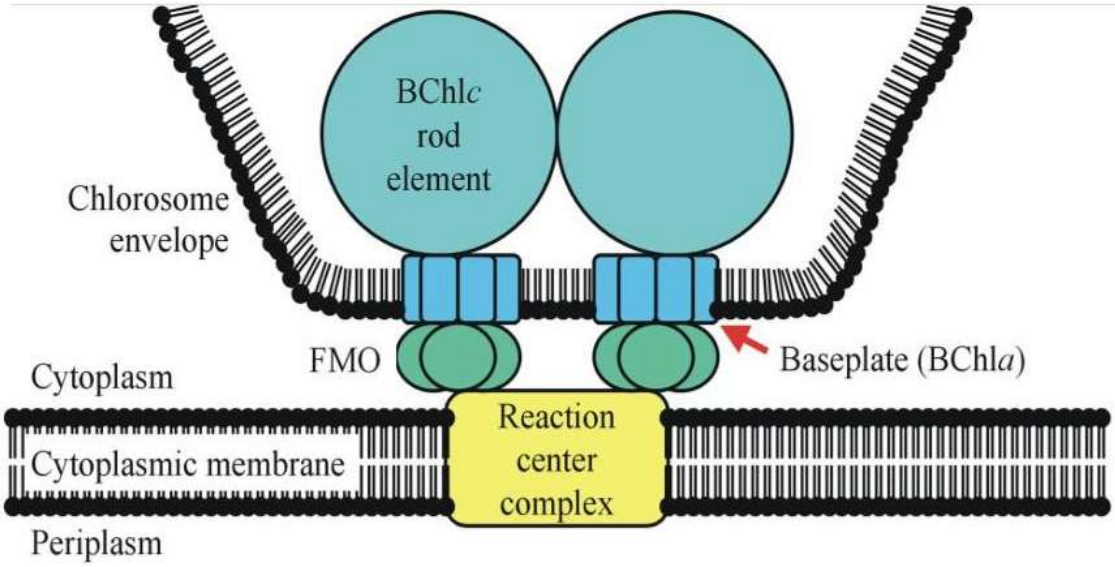

Figure 4. Structure of the photosynthetic apparatus including the light-harvesting antenna complexes in green sulphur bacteria. Reprinted with permission from ref. 33 Copyright (2007) National Academy of Sciences, USA.

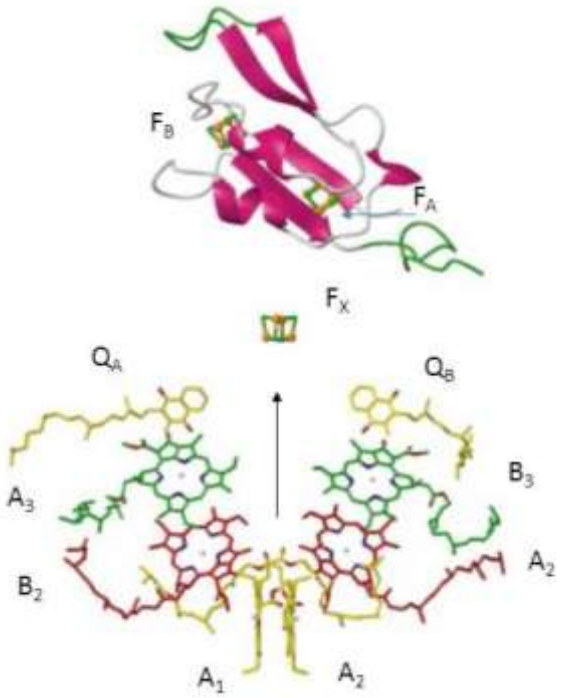

Figure 5. The "special pair" and other cofactors in the PSI-RC from cyanobacteria *Thermosynechococcus elongatus*. The labels A and B refer to the two branches of the electron transfer chain. The QX (X=A or B) and F_Y (Y = X or A or B) indicate the quinone and iron-sulfur clusters. Reprinted by permission from Macmillan Publishers Ltd: Nature, ref. 29, copyright (2001).

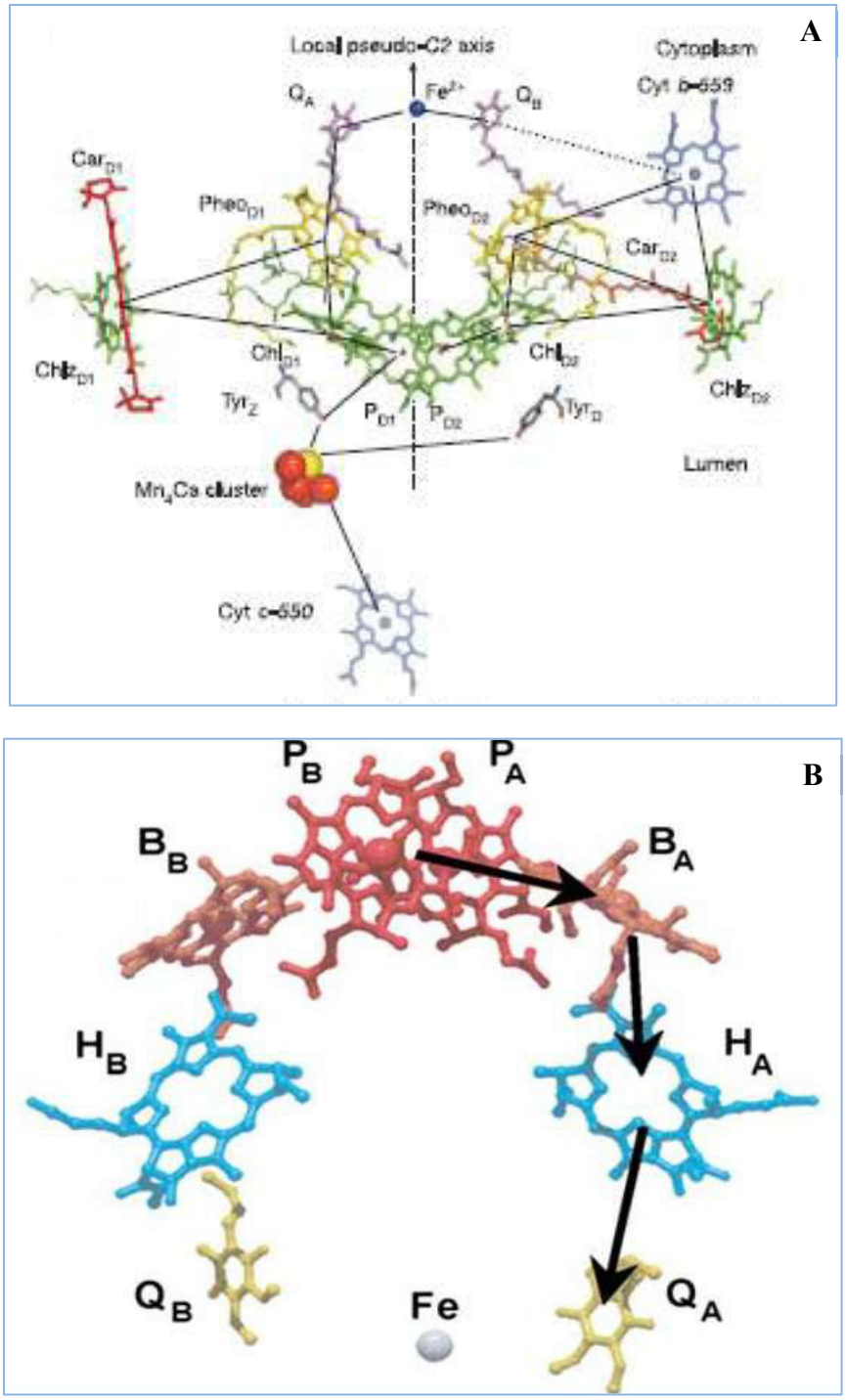

Figure 6. **Frame A** cofactors of PSII from cyanobacteria *Thermosynechococcus elongatus.* The labels D1 and D2 refer to the two branches of the RC. Electron transfer occurs along the D1-branch. Also shown are the Mn_4Ca cluster and cytochrome c-550 Reprinted by permission from Macmillan Publishers Ltd: Nature, ref. 35, copyright (2005) **Frame B** The RC cofactors from purple bacteria *Rb. Sphaeroides*. Q_A and Q_B are immobile and mobile quinones, respectively. Arrows indicate the pathway of electron transfer. Reprinted from ref.39, Copyright (2002), with permission from Elsevier

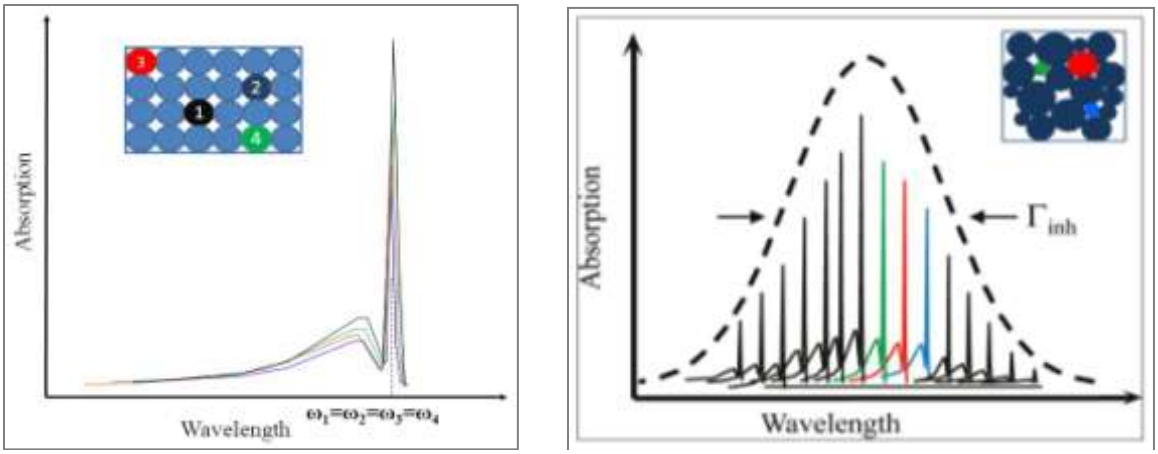

Figure 7. Spectra of the impurity centers in a crystalline matrix (left) and amorphous matrix (right).

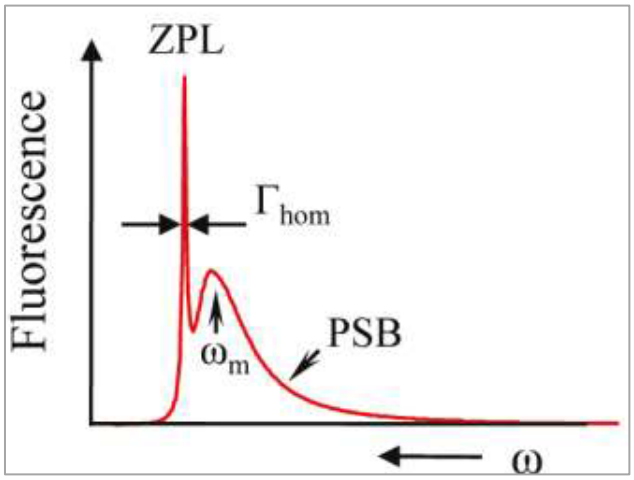

Figure 8. Spectral line shape of an impurity center in a solid matrix at low temperature. Γ_{hom} is the homogeneous line width, and ω_m is the mean phonon frequency. Reprinted with permission from ref.7. Copyright (2011) American Chemical Society.

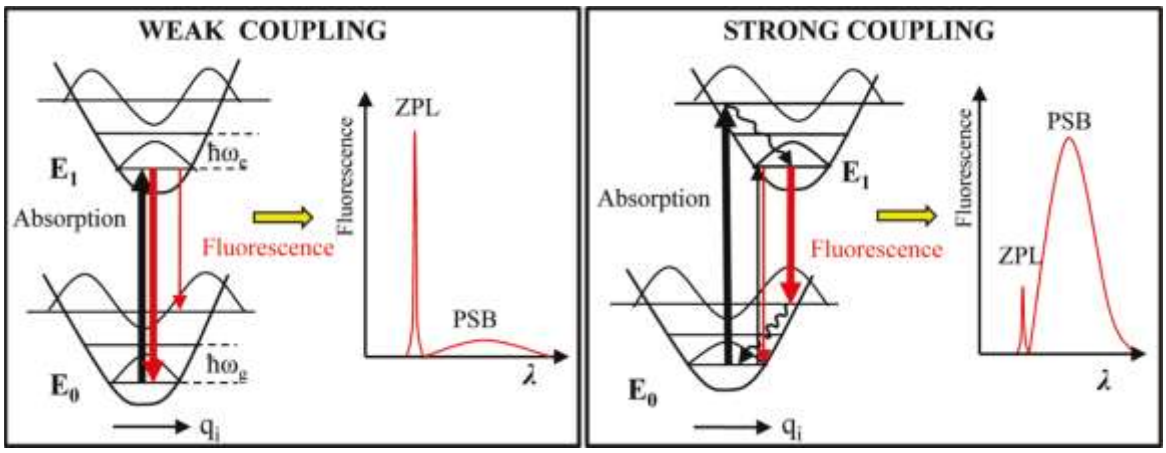

Figure 9. Features of the single impurity spectral line (zero-phonon line and phonon side-band) depending on the strength of electron-phonon coupling. Reprinted with permission from ref.7. Copyright (2011) American Chemical Society.

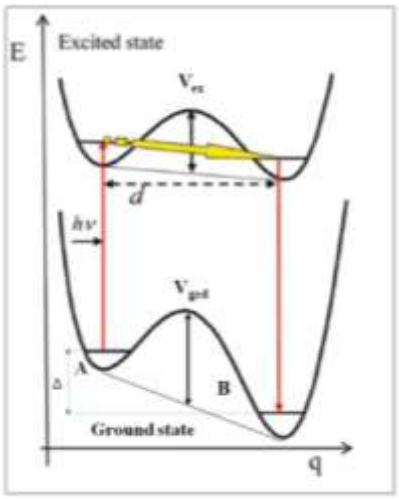

Figure 10. Two-Level System model; where the barriers height in the ground and excited states are V_{grd} and V_{ex}; displacement between the two potential minima is denoted by d; the asymmetry of the TLS is Δ and hν is the excitation energy of the chromophore initially found in conformation A of the ground state. The tunneling frequency is $W=\omega_0 exp(-\lambda)$. Reprinted with permission from ref.7. Copyright (2011) American Chemical Society.

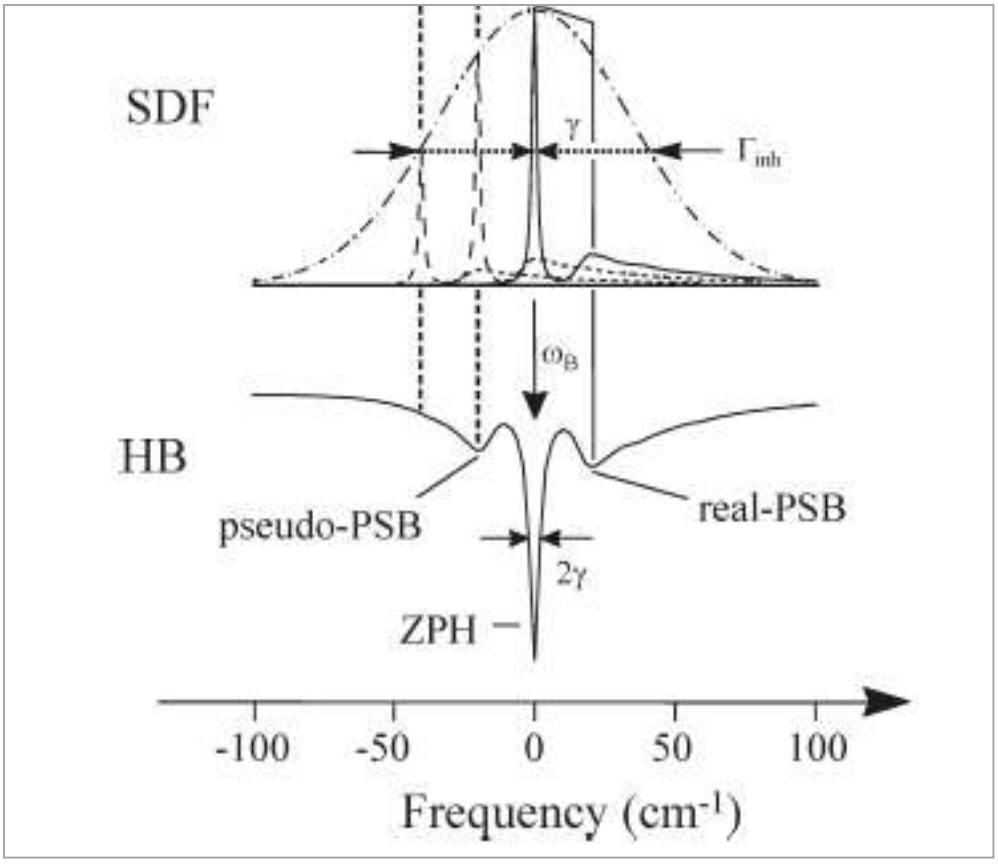

Figure 11. The spectral - hole profile (SDF is Site Distribution Function with Γ_{inh} being the inhomogeneous width, γ is the homogeneous width and 2γ is the hole width. Width is defined here and everywhere else within this thesis as the Full Width at Half Maximum, FWHM). Reprinted with permission from ref.7. Copyright (2011) American Chemical Society.

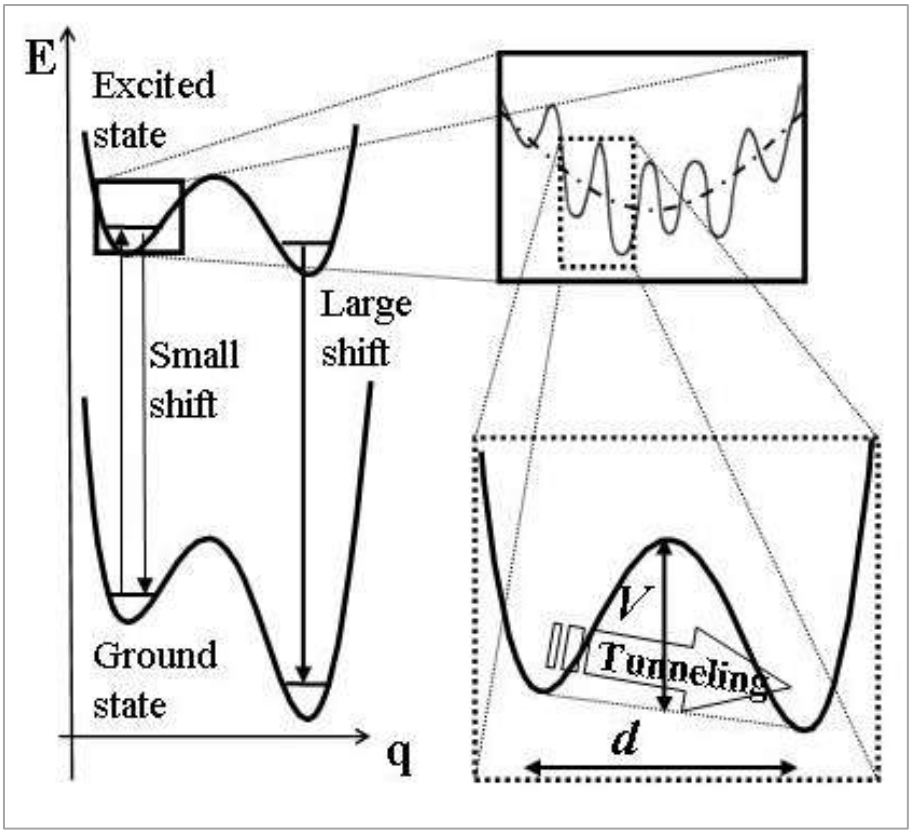

Figure 12. NPHB mechanisms accounting for two different hierarchical tiers on the energy landscape. Adapted with permission from ref. 66. Copyright (2012) American Chemical Society.

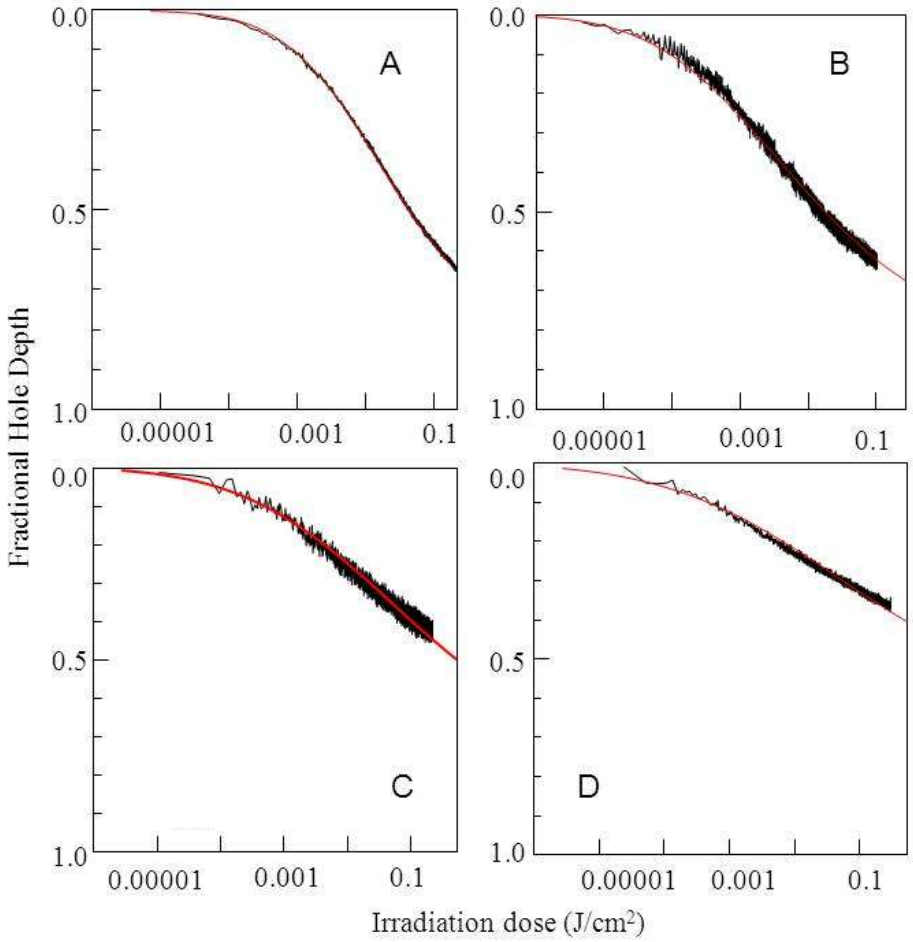

Figure 13. (A) HGK curve (noisy black curve) and its fit (red) for CP43 at 686.8 nm. (B) HGK curve (noisy black curve) and its fit (red) for CP29 at 681.7 nm. (C) HGK curve (noisy black curve) and its fit (red) for monomeric LHCII at 683.1 nm. (D) HGK curve (noisy black curve) and its fit (red) for trimeric LHCII at 684.2 nm. Reprinted with permission from ref.71. Copyright (2011) American Chemical Society.

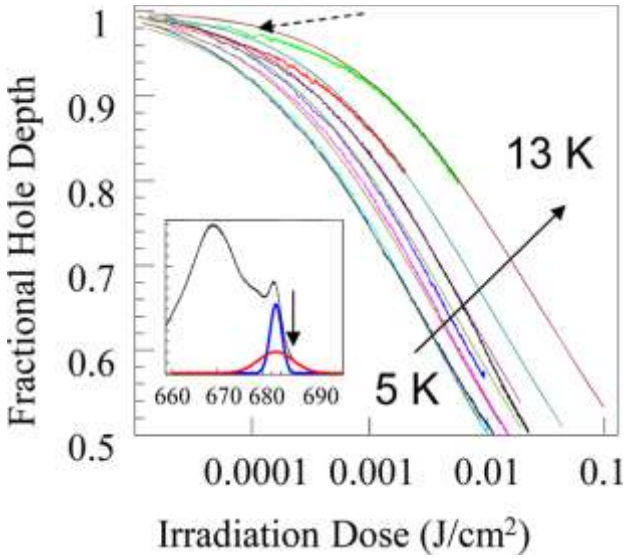

Figure 14. HGK curves for 5, 6, 7, 8, 10, and 13 K. The smooth curves are the fits to HGK curves. The parameters of the Gaussian λ-distribution obtained from the fit to 5K HGK curve are λ_0=10.2±0.1, σ_λ=1.1±0.1, with S=0.35±0.05. The insert depicts the absorption spectrum of CP43 (black) with the site distribution function of the A-band (red) and the B-band (blue). The down arrow indicates the burn wavelength. Reprinted with permission from ref.66. Copyright (2012) American Chemical Society.

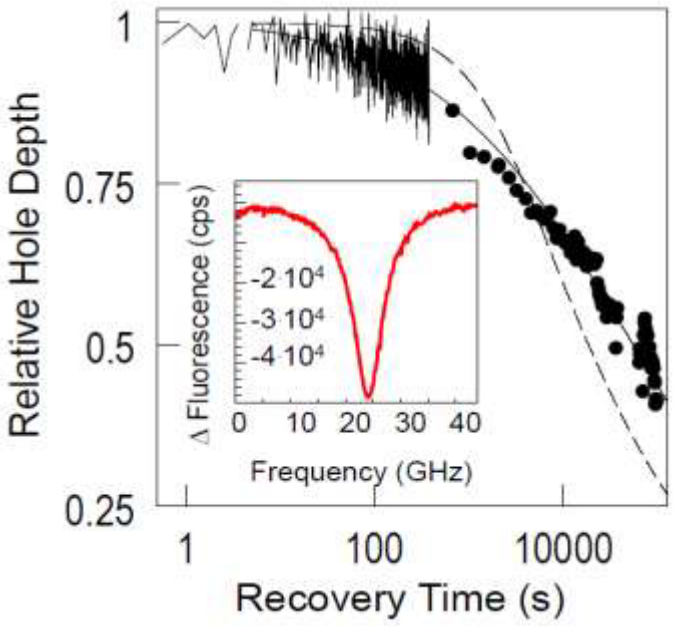

Figure 15. Hole-recovery data for 21%-deep hole, noisy curve and circles. Smooth solid curve (good fit to experimental data) results from modeling in Gaussian λ-distribution framework (see Fig. 16A), while dashed curve results from modeling in uniform λ-distribution framework (see Fig. 16B). The insert represents a sample hole spectrum (ref. 15, 66, 71). The datapoints presented as circles are result of averaging of about 40 points of the raw data. The size of the symbols is approximately equal to the size of potential error bar, ~0.02.

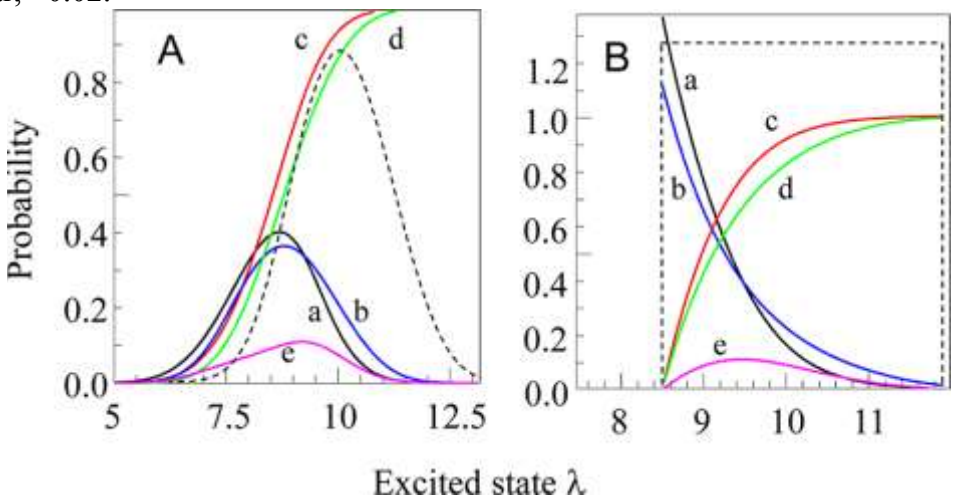

Figure 16. (A) Calculated excited-state partial λ-distributions for Gaussian true full λ-distributions (black: 20% deep hole, a; blue: 55% deep hole, b). Areas under curves are normalized to 1. The red (c) and green (d) curves are integrals of the black and blue curves, respectively. The magenta curve (e) is the difference between these integrals. The dashed curve is the true full λ-distribution. (B) Same for the uniform λ-distribution. Reprinted with permission from ref.66. Copyright (2012) American Chemical Society.

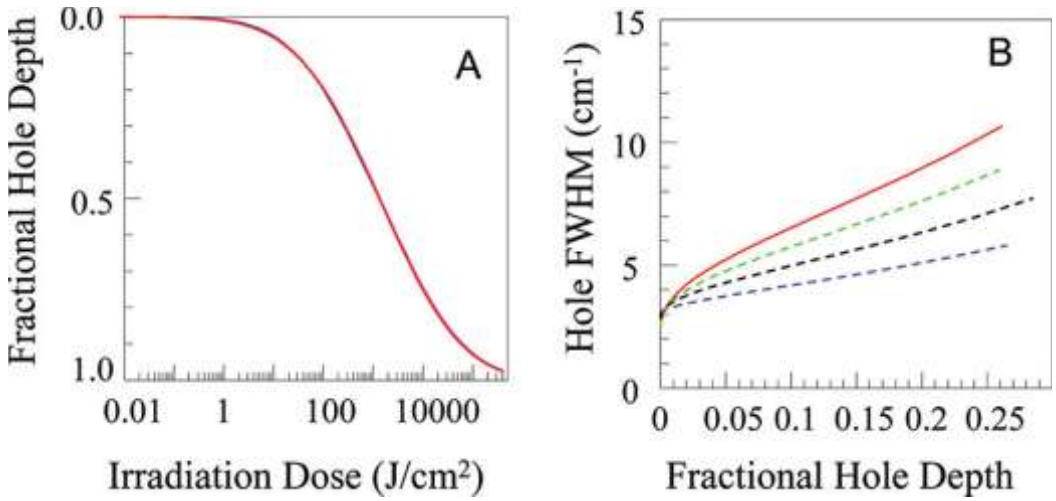

Figure 17. **Frame A:** Indistinguishable HGK curves for different combinations of λ-distribution and line width distribution parameters (see below). **Frame B:** Easily distinguishable hole width dependences on the hole depth for the same parameters as in frame A. Red curve: line width distribution peaking at 3.0 cm^{-1} with fwhm = 3.0 cm^{-1}, λ_0= 10.0, and σ_λ = 1.0. Green: line width distribution peaking at 2.5 cm^{-1} with fwhm =2.1 cm^{-1}, λ_0 = 10.15, and σ_λ = 1.0. Black: line width distribution peaking at 2.0 cm^{-1} with fwhm = 1.3 cm^{-1}, λ_0 = 10.2, and σ_λ = 1.0. Blue: single line width 1.5 cm^{-1}, λ_0 = 10.5, and σ_λ = 1.0. Reprinted with permission from ref.60. Copyright (2011) American Chemical Society.

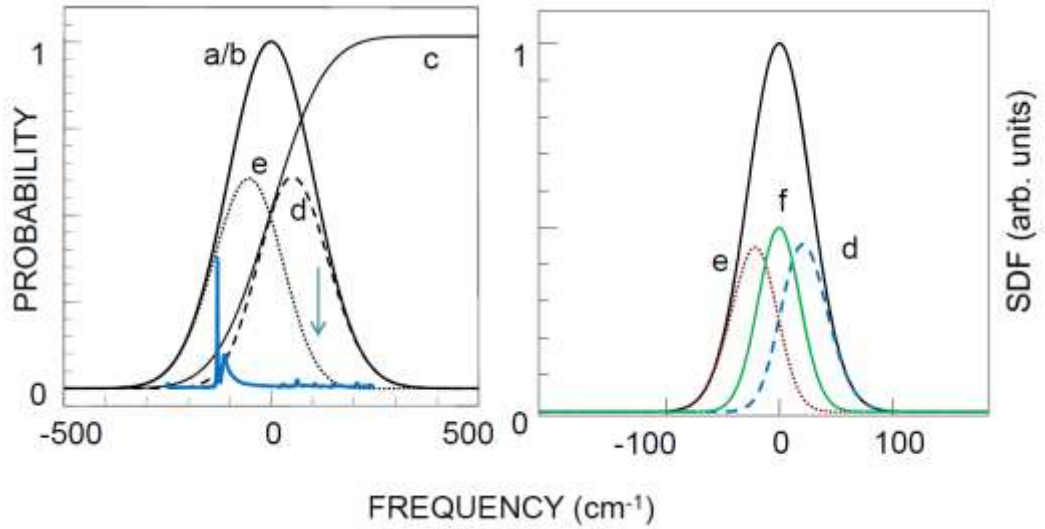

Figure 18A. Total SDF and sub-SDF in the case of two pigments with identical SDF. Blue curve is the absorption spectrum of a molecule with ZPL relatively low in energy, which is excited at higher energy via its phonon sideband or vibronic replicas. **Figure 18B:** the full SDF of three identical pigments with FMO 825 nm band parameters and three sub-SDF corresponding to the lowest-energy pigments (e), pigments with one donor and one acceptor (f) and highest-energy, two-acceptor pigments (d). Zero corresponds to 12116 cm^{-1}.

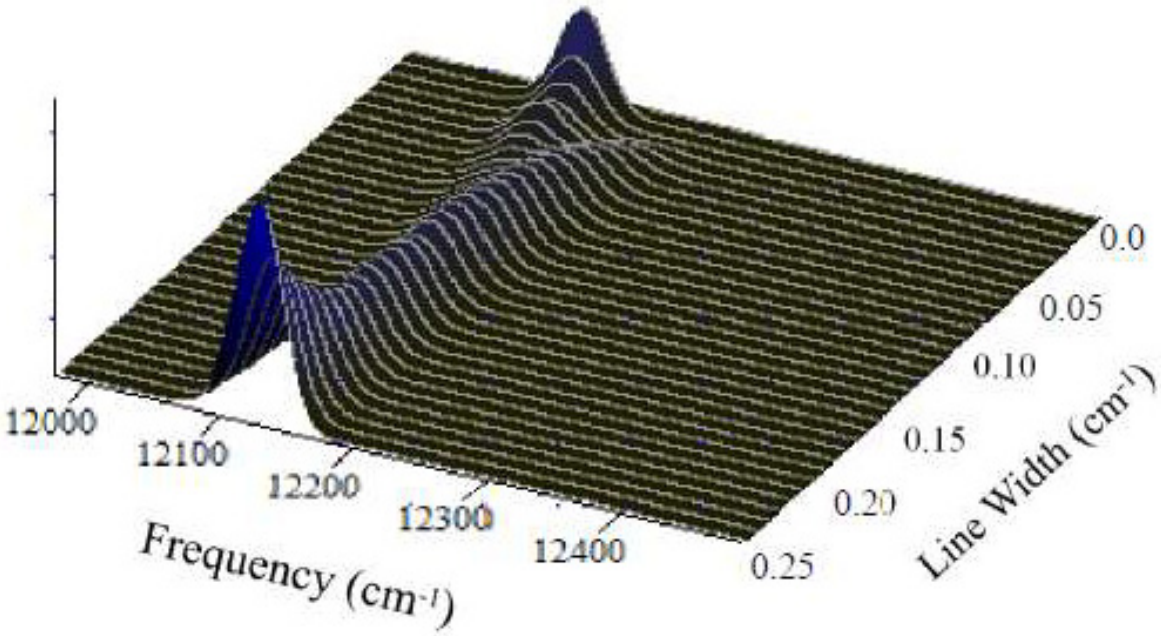

Figure 19. Example of sub-SDF for different EET rates for one-donor-one-acceptor pigments (V=3 cm^{-1}, the width SDF is 65 cm^{-1} and the SDF peak position: 12116 cm^{-1}). "ZPL width" includes only EET contribution to the width; pure dephasing and width corresponding to fluorescence lifetime are not included.

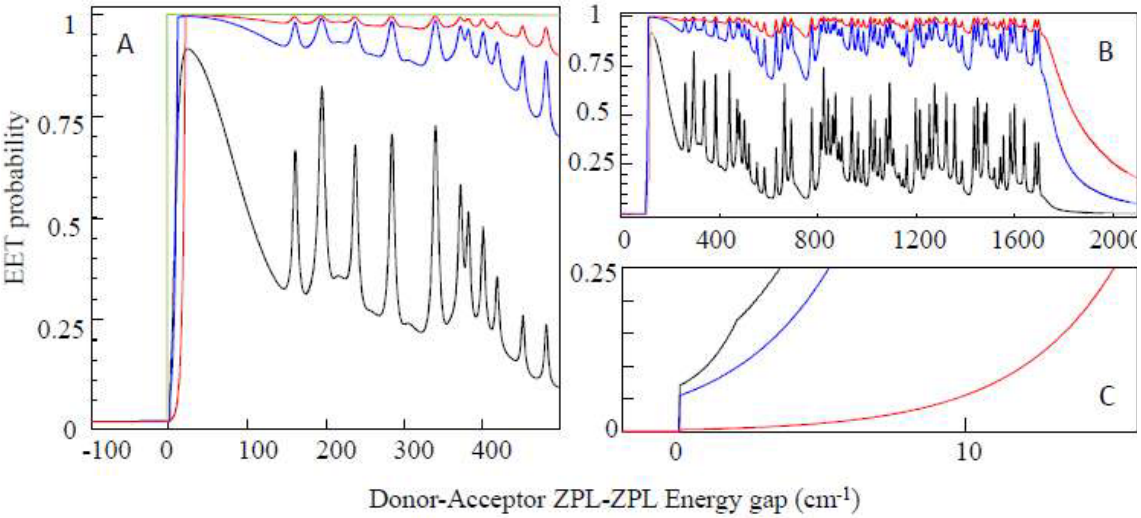

Figure 20. Dependence of the probability of EET on donor-acceptor ZPL gap for different values of inter-pigment coupling (where the probability functions for V=1cm^{-1}, V=5cm^{-1} and V=10cm^{-1} are the black, blue and red curve respectively; the green curve is the probability function resembling the step function of Jankowiak et al); all single-site spectrum parameters from FMO.

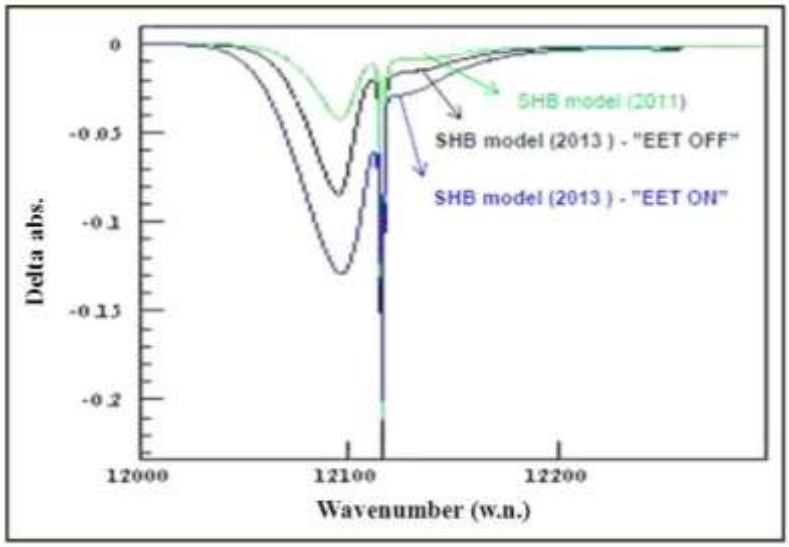

Figure 21. HB spectra taking EET into account to different degrees. V=3 cm^{-1} and no anti-hole was considered; the illumination dose was same in all three cases, The green curve has been obtained with SHB model that included the EET rate distributions at burn wavelength and no burning via EET, [60]; the black curve has been calculated including only wavelength dependent EET rate distribution; the blue curve has been calculated considering both the wavelength dependent EET rate distribution and burning via EET.

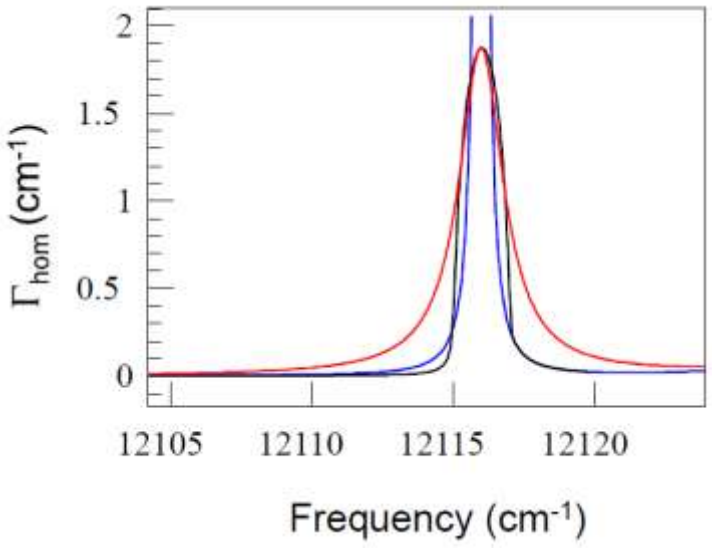

Figure 22. Blue: the result of convolution of two single-site spectra; with the width of the (truncated) peak being much smaller than the height. Black: corrected ZPL-ZPL contribution to spectral overlap (or line width) dependence on donor-acceptor gap. Red: Lorentzian function with same width and peak magnitude, for comparison.

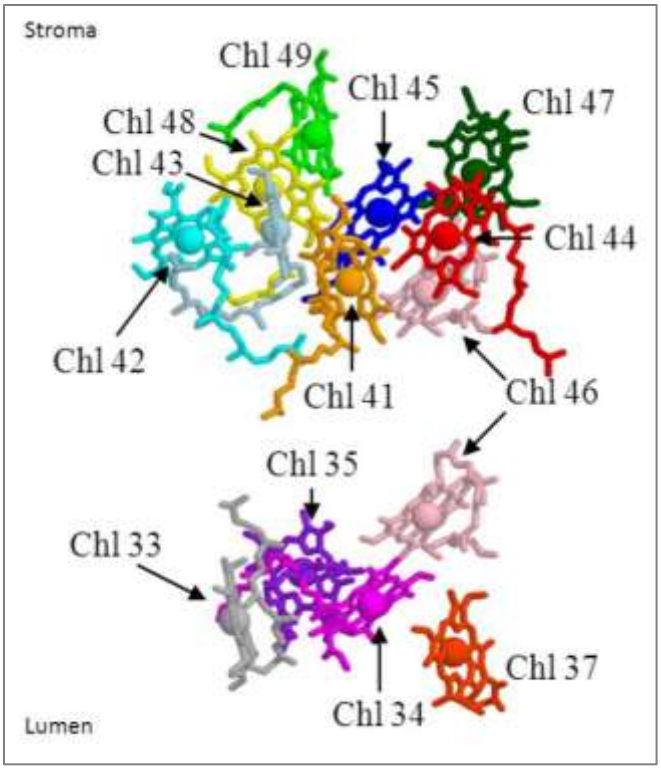

Figure 23. The structure of the core antenna complex CP43. The increased spacing between luminal and stromal parts of the complex is introduced for clarity; note that Chl 46 (notation by Loll, ref. 93), located somewhat in between lumenal and stromal groups of pigments, is shown twice (pink). Reprinted with permission from ref.142. Copyright (2008) American Chemical Society.

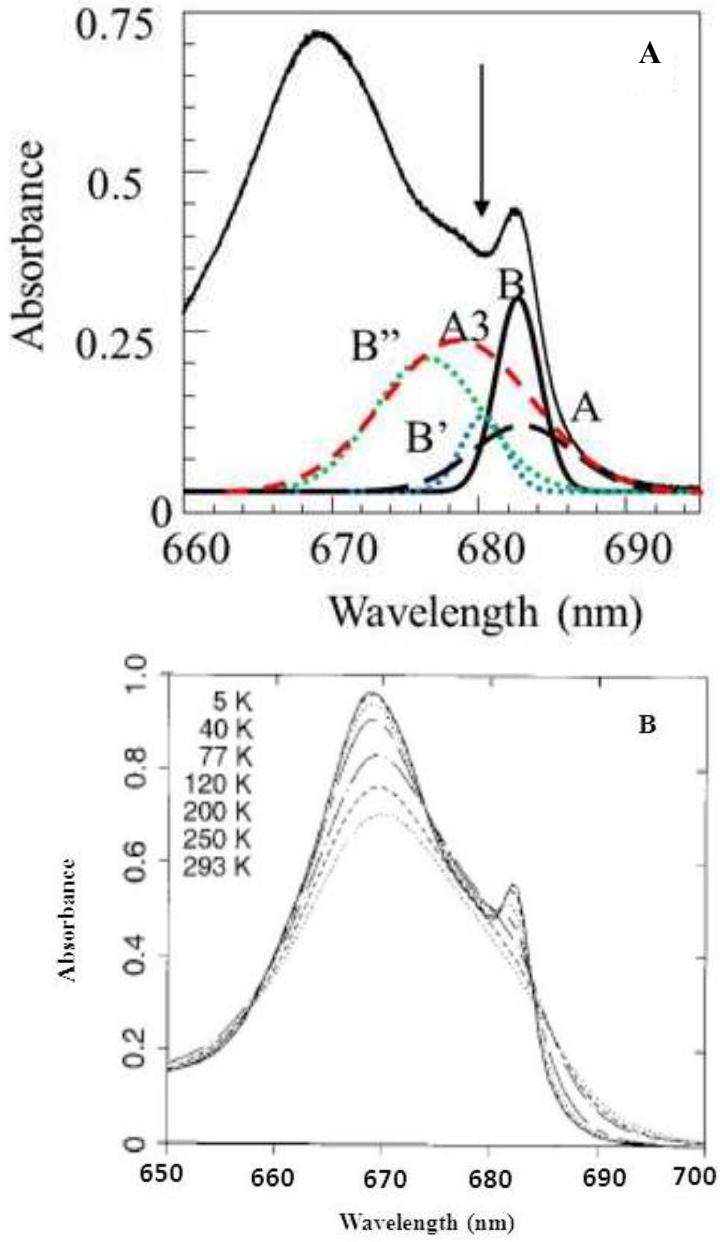

Figure 24A The absorption spectrum of CP43 as well as the SDFs of the lowest-energy states according to various models discussed in the text (Reprinted with permission from ref.60. Copyright (2011) American Chemical Society. **Figure 24B.** The Q_y absorption band of CP43 at different temperatures (Reprinted from ref. 150, Copyright (1999), with permission from Elsevier); the lowest-energy band peaked at ~ 683-nm is clearly resolved only in spectra measured at liquid nitrogen and helium temperatures (T < 77 K).

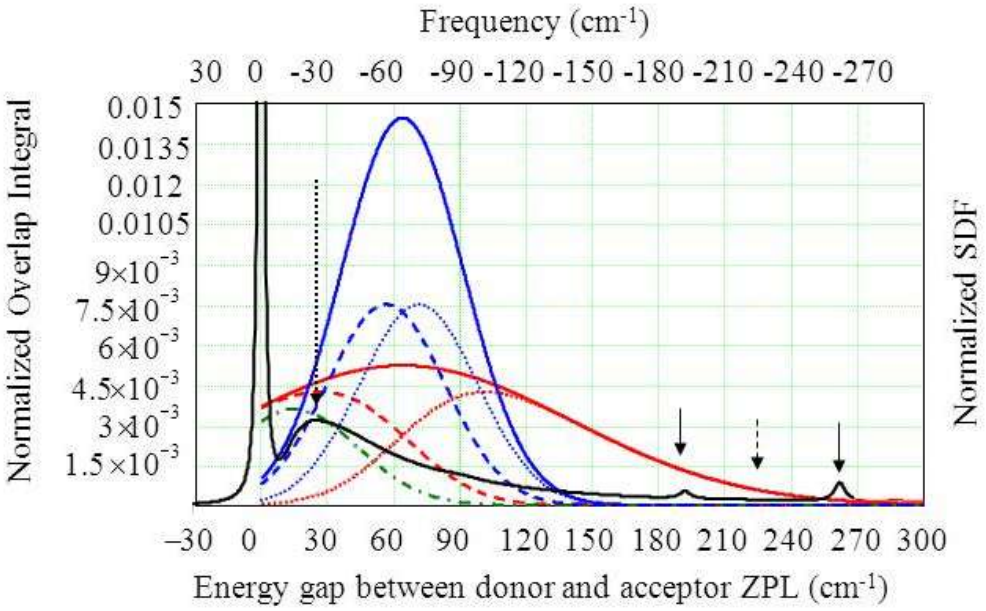

Figure 25. Spectral overlap dependence on the ZPL-ZPL energy gap (black curve) for the single site spectra parameters in Table 2, two SDFs (solid red and blue curves), and deconvolution of those SDFs into sub-SDFs of fractions capable (dashed line) or incapable (dotted line) of EET. The dash-dotted green curve is the overlap integral dependence on energy gap according to Kolaczkowski et al, [133].Vertical solid arrows indicate contributions to the overlap from localized vibrations; the dashed arrow indicates minimal overlap. The dotted arrow indicates maximal overlap within the range of Fig.26. Reprinted with permission from ref. 60 . Copyright (2011) American Chemical Society.

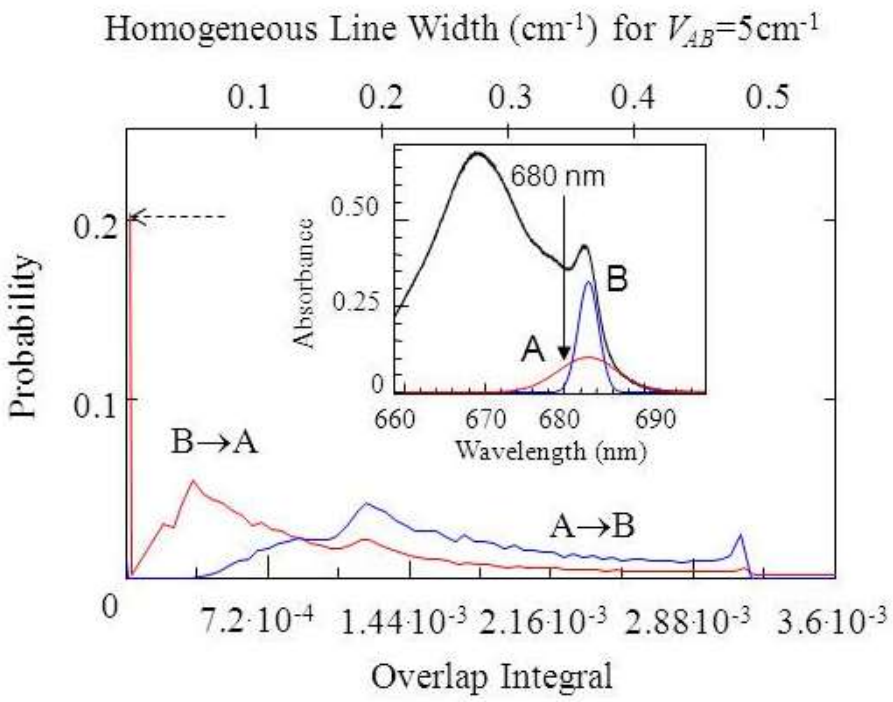

Figure 26. Overlap distributions (lower scale) and homogeneous line width distributions with V_{AB} = 5 cm^{-1} for EET between two bands with the SDFs resembling those of the two lowest-energy states of the CP43 complex (the inset contains its absorption spectrum and two SDFs). The blue curve is the distribution for A→B EET for λ_B = 680 nm, while the red curve is the distribution for B→A EET. The horizontal dashed arrow indicates the ~20% contribution of B-type pigments incapable of EET at λ_B. Reprinted with permission from ref. 60 . Copyright (2011) American Chemical Society.
N.B: Homogeneous line width reported in the figure does not include pure dephasing contribution (e.g, 1 GHz or 0.033 cm^{-1} at 5 K, [101]).

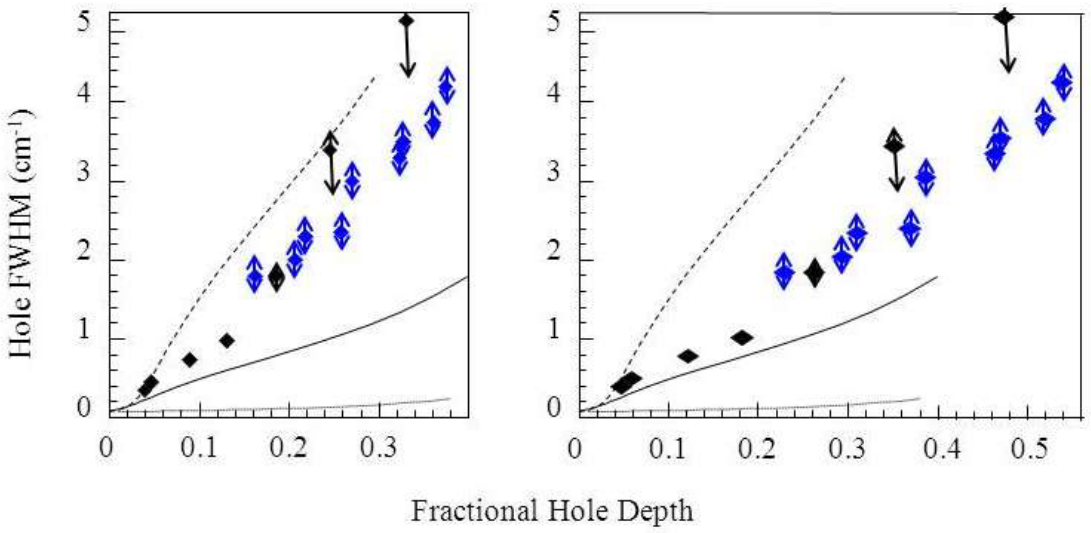

Figure 27. Left frame - Experimental dependence of the hole width on hole depth for λ_B = 680.15 nm. Black diamonds: high-resolution data. Blue diamonds: low-resolution data, corrected for the spectrometer resolution. The solid curve is the theoretical dependence for V_{AB}=5cm^{-1}, and the dashed curve is the theoretical dependence for V_{AB} =10 cm^{-1}. The dotted curve was obtained in the absence of the line width distribution.
Right frame –The dependence of the hole width on hole depth corrected for contribution of states other than A and B at λ_B = 680.15 nm.

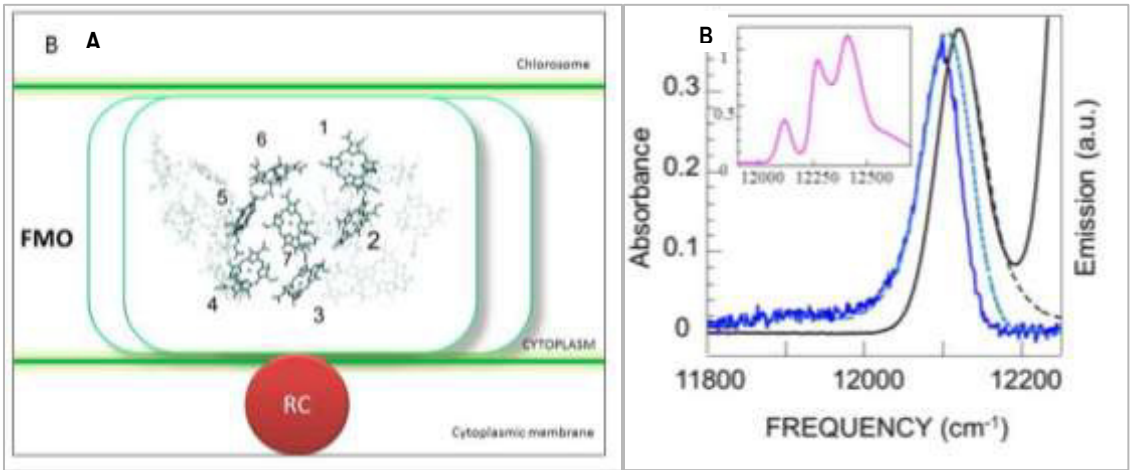

Figure 28. Frame A - The locations of BChl molecules in a FMO monomer (Adapted from ref.32, Copyright (2006), with permission from Elsevier). The pigments within one selected monomer are highlighted, the pigments of other two monomers are presented as fainter shapes. **Frame B** - The low temperature absorption spectra of FMO protein. Dashed black curve: fit to the 825 nm band absorption (see text). Blue solid curve: emission spectrum measured for the same sample as absorption. Dashed blue curve: emission spectrum predicted assuming that emission origin coincides with the full 825 nm band SDF (i.e., there is no intra-825 nm-band, inter-monomer, EET). Insert shows the entire Q_y absorption band of *C. tepidum* FMO complex.

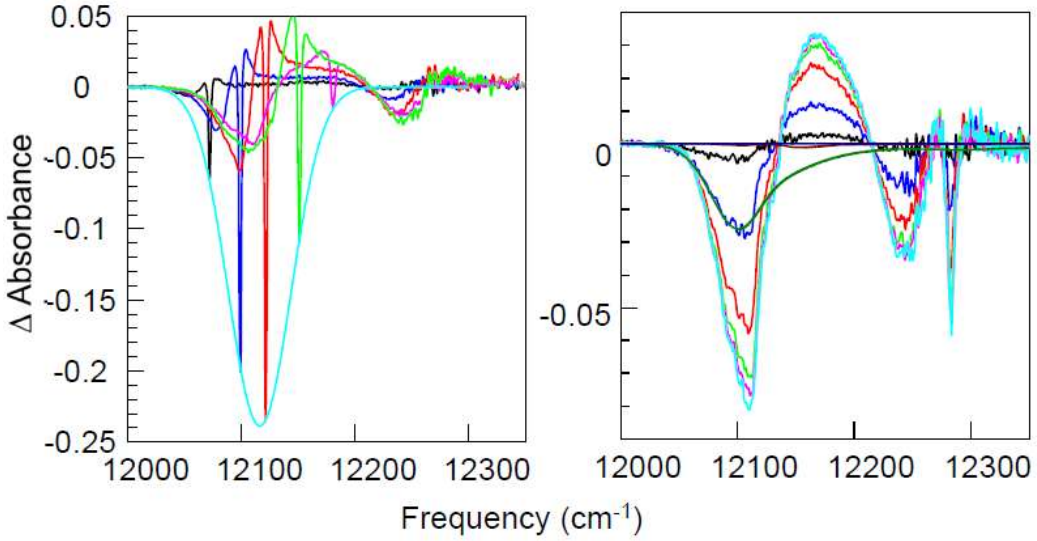

Figure 29A: Holes burnt at 821.0 (magenta), 823.0 (green), 825.0 (red), 826.5 (dark blue) and 828.4 (black) nm with a fluence of about 120 J/cm^2. Light-blue curve is the inverted full SDF of the 825 nm band. **Figure 29B:** Non-resonant holes produced by illumination at 814 nm with varying fluence. Smooth dark green curve represents the theoretical non-resonant hole in the presence of EET and the absence of an anti-hole.

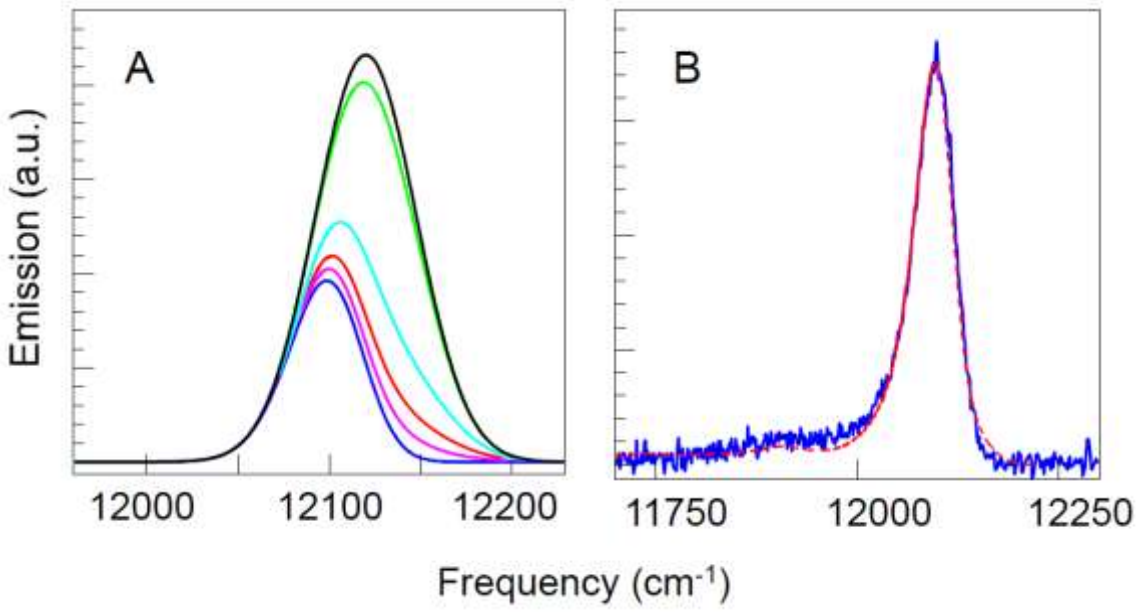

Figure 30A: Emission origin calculated in trimeric model with slow EET: Black: total SDF of the 825 nm band of FMO, emission origin in case inter-monomer coupling is zero. Light green: |V|=0.1 cm^{-1}, Light blue: V=0.5 cm^{-1}, Red: V=1.0 cm^{-1}; Magenta: V=2.0 cm^{-1}; Blue: curve (e) from Figure 18B, valid for V=3.0 cm^{-1} and above. **Figure 30B:** best fit (red) to the FMO 5K emission spectrum (blue), V=1.2 cm^{-1}.

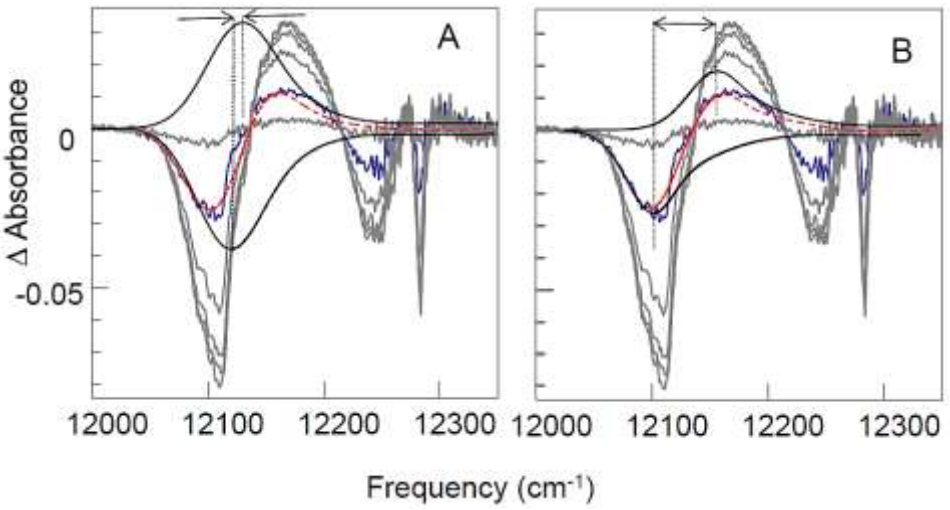

Figure 31A: ΔAbsorption of non-resonantly burned molecules and anti-holes (solid black curves) and their sum (dashed red curve) compared to a representative HB spectrum (blue) in the absence of EET. Non-resonantly burned spectra for other fluences are presented in grey. **Figure 31B:** Similar spectra as frame A, but in the presence of EET.

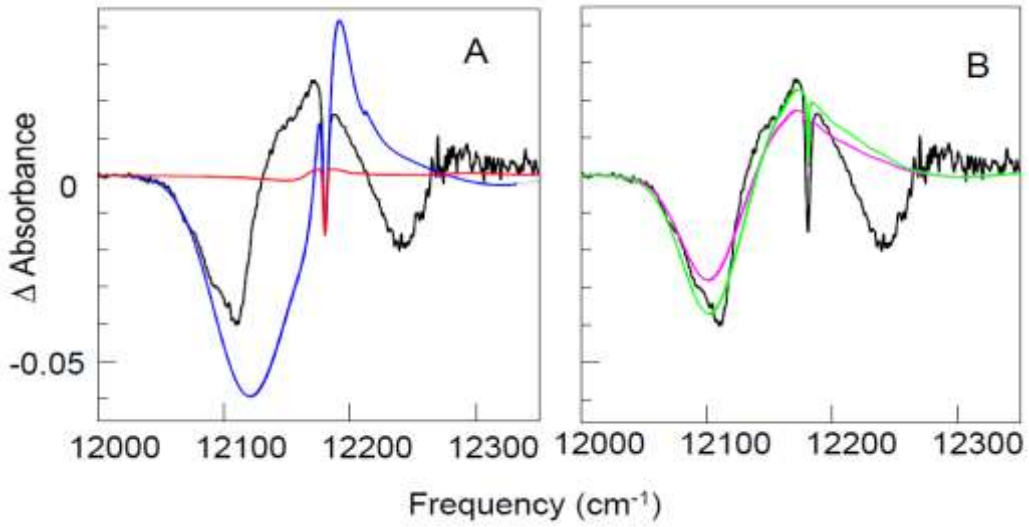

Figure 32A: Hole burnt at 821 nm and modeling results in the absence of EET and aberage blue shift of the anti-hole of 10 cm^{-1}. Red curve: perfect spectral memory [139], blue curve: no spectral memory. **Figure 32B:** Same hole and modeling results for two irradiation doses in the presence of EET. The small ~10 cm^{-1} shifts are not included, as it was assumed that their contribution is small when spectral memory in present (see red curve in frame A). We did not attempt to simulate the higher-energy satellite hole at 816 nm.

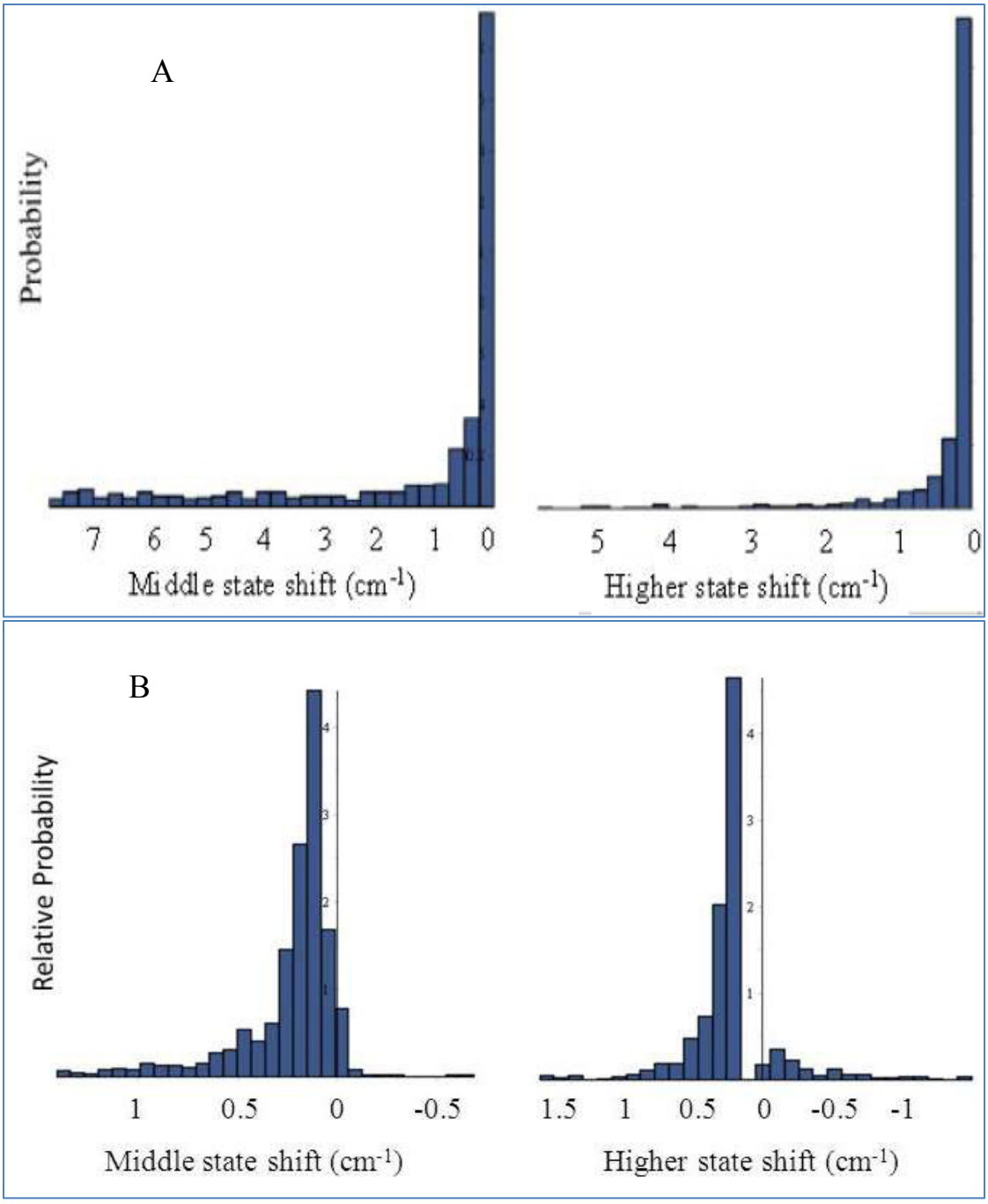

Figure 33. The shift probability distributions for the middle (one donor and one acceptor) and higher (two acceptors) excitonic states of the trimer with identical FMO-like SDF parameters. **Frame A -** The NPHB shift of the lowest-energy pigment was assumed to be 10 cm^{-1} to the blue, and coupling V= 3 cm^{-1}. **Frame B** - The NPHB shift of the lowest-energy pigment was assumed to be 60 cm^{-1} to the blue and coupling V=1.5cm^{-1}. Courtesy of Stephanie Larocque.

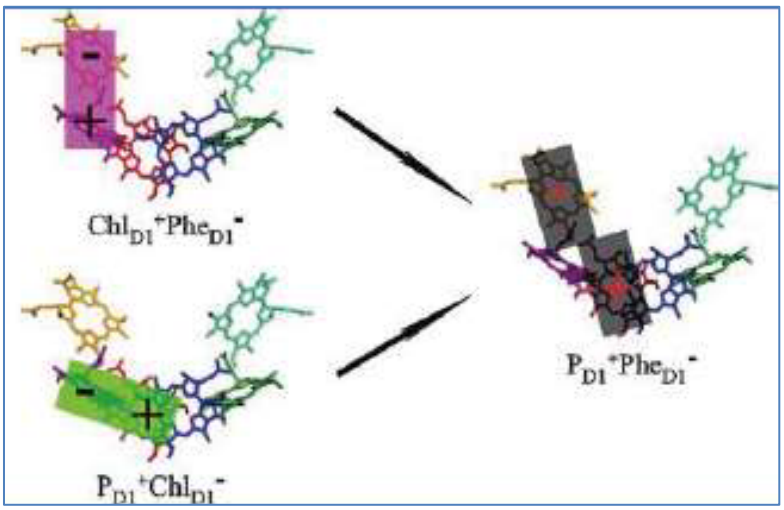

Figure 34. The diagram of the two different charge separation pathways in the PSII RC from spinach. Reprinted with permission from ref. 88. Copyright (2010) American Chemical Society

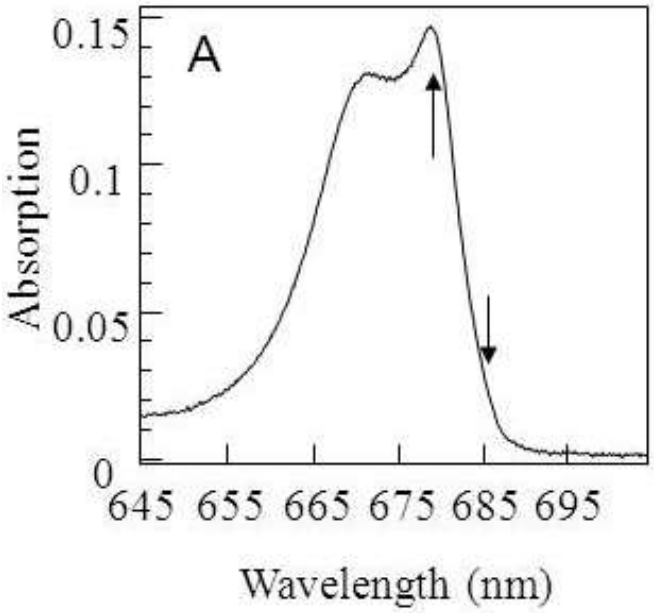

Figure 35. The absorption spectrum of the isolated PSII RC complex. The arrows indicate the burn wavelengths of 680 and 686 nm, the latter within a weak shoulder at ~684 nm, Reprinted with permission from ref. 60. Copyright (2011) American Chemical Society.

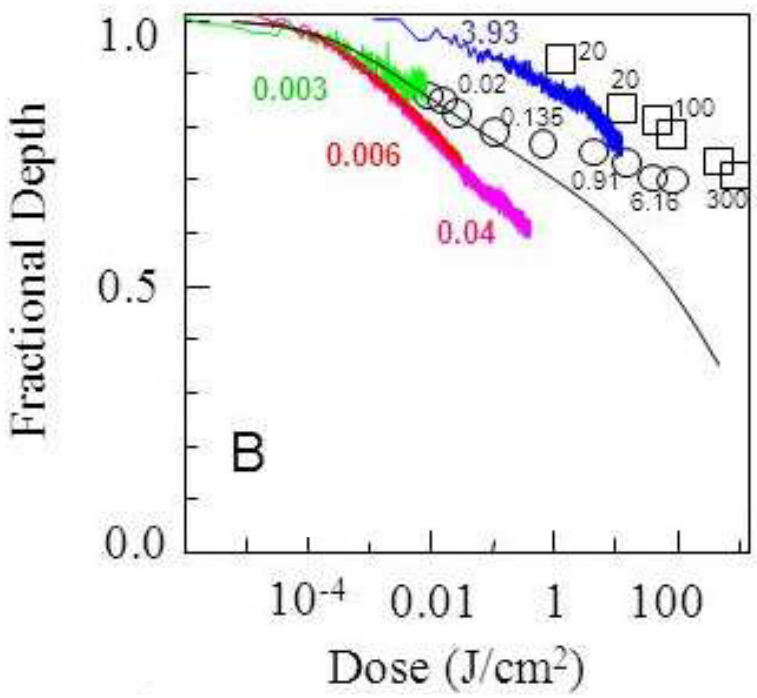

Figure 36. Persistent hole depth versus irradiation dose data for λ_B = 686 nm. The noisy curves are HGK curves; symbols refer to data extracted from the hole spectra. The numbers refer to the intensity (in mW/cm^2) used to obtain the data.
The fastest two HGKs (red and magenta) were obtained in fluorescence excitation mode. Also presented is the best fit (solid black line) to the lowest-intensity transmission mode data (noisy green curve + open circles). See the text for line width distribution details, Reprinted with permission from ref. 60 . Copyright (2011) American Chemical Society

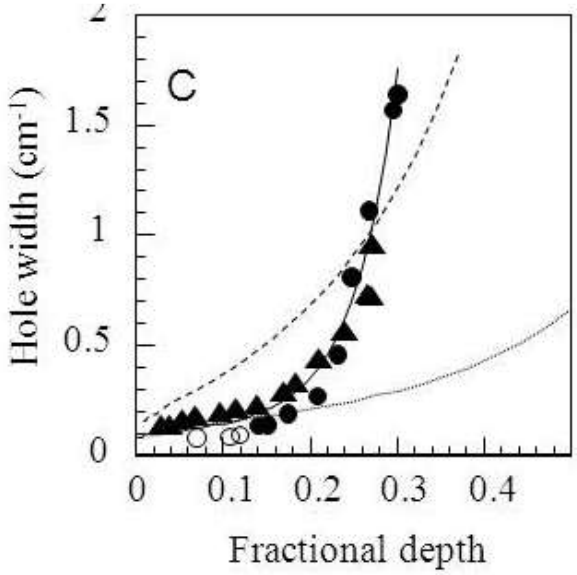

Figure 37. Experimental persistent hole width vs depth data (open and solid circles represent two complementary data sets) for λ_B = 686 nm and theoretical fits with the same distribution as in figure 36 (solid curve), with the distribution from ref 87 (dashed curve) and without any line width distribution (dotted curve). The solid triangles represent the experimental data obtained at 680 nm. The data was obtained at high resolution (~30 MHz) with 4 cm^{-1} scan range. Therefore, errors do not exceed the size of the symbols Reprinted with permission from ref. 60. Copyright (2011) American Chemical Society

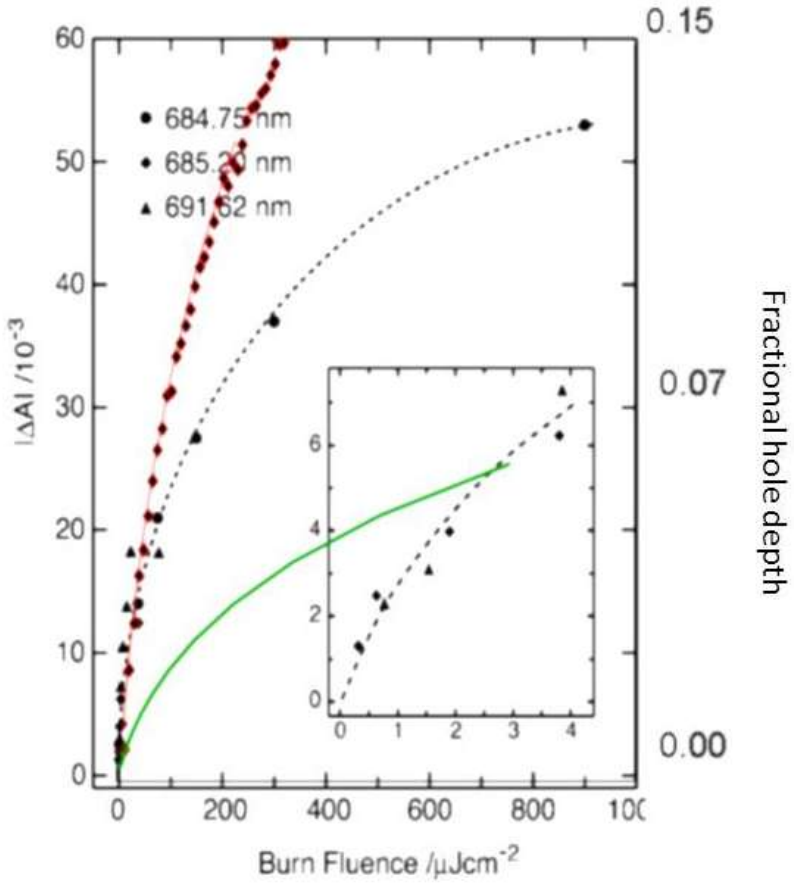

Figure 38. Absorbance difference vs. burn fluence (Figure 11 Reprinted with permission from ref. 172. Copyright (2004) American Chemical Society and fractional hole depth vs. burn fluence (our data) for PSII core (RC+CP43+CP47) from spinach in $S_1(QA^-)$ at T= 2.5 K and 5 K, respectively. Black line, triangles, and circles: HGK in PSII core from spinach, in $S_1(QA^-)$ state, Red line and diamonds: HGK curve obtained at T= 5K and λ_B = 686 nm in CP43 (our data); Green: fit to HGK curve measured in transmission at the lowest intensity, T= 5K, λ_B = 686 nm; isolated PS II RC (our data).

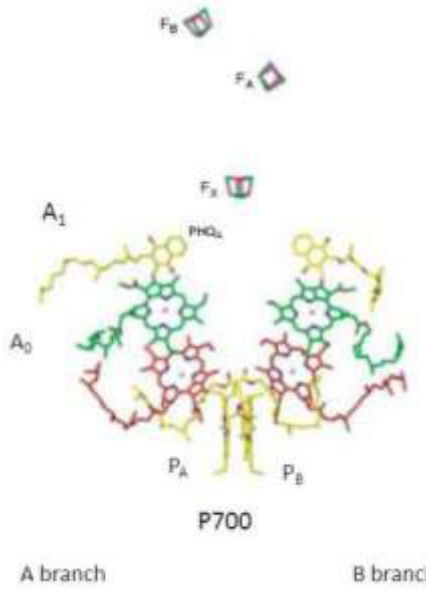

Figure 39. Structural arrangement of the cofactors in the reaction center of Photosystem I, where P_A and P_B designate the two components of the special pair (primary electron donor, P700); A_0 refers to the primary electron acceptor (Chl a) and A_1 is the phylloquinone (PhQ_A); the terminal electron acceptors are three iron-sulfur clusters Fx, F_A and F_B. Adapted from ref. 174, Copyright (2002), with permission from Elsevier

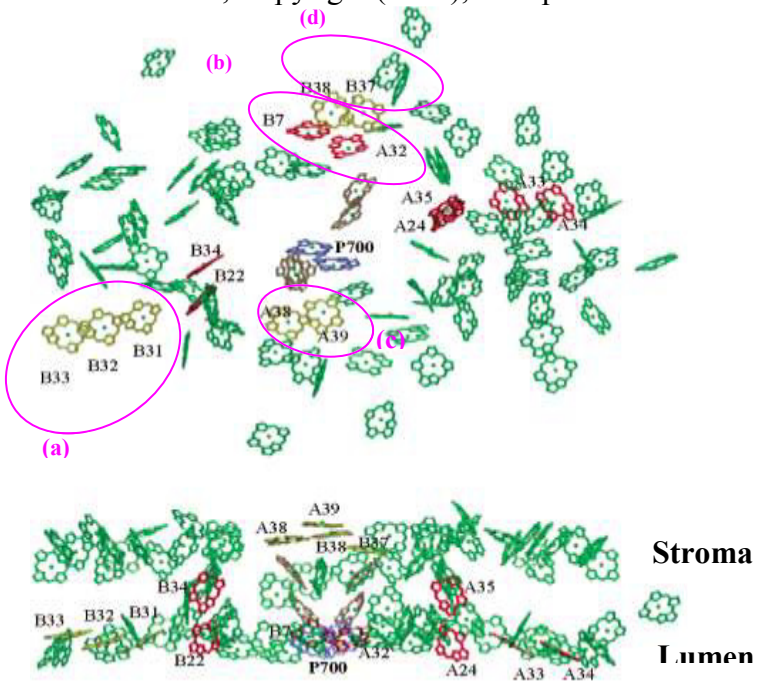

Figure 40. Red chlorophyll assignment in PSI from cyanobacteria where in the notation of Krauß et all chlorophylls B31, B32 and B33 are referred to as trimer **a**. The dimers **b, c** and **d** are made up of chlorophylls A32/ B7, A38/A39 and B37/B38 (from ref. 175, 177, 180). The three-fold axis of symmetry is perpendicular to the page and located above the top view of PSI. Adapted with permission from ref. 180. Copyright (2002) American Chemical Society

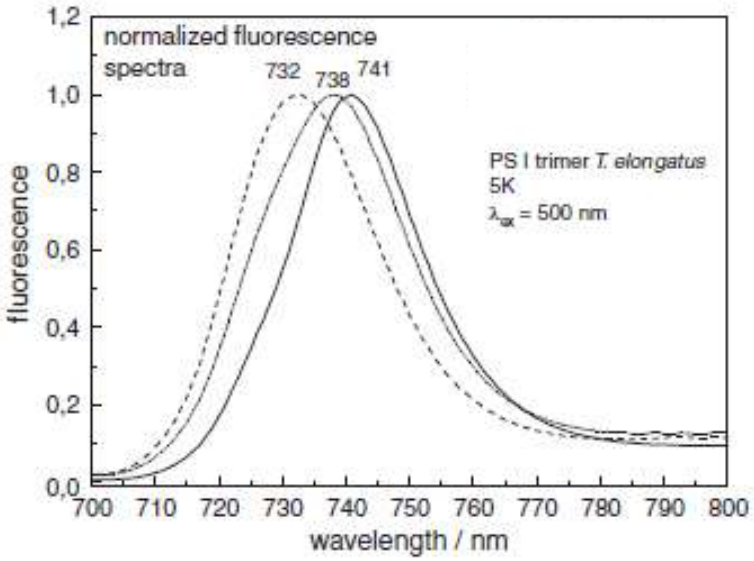

Figure 41. 5 K fluorescence spectra of PS I trimers from *T. elongatus* with P700 in the reduced (solid line), oxidized (dashed line) and mixture of reduced-oxidized state (dash–dotted line). Reprinted from ref. 181, Copyright (Year), with permission from Elsevier

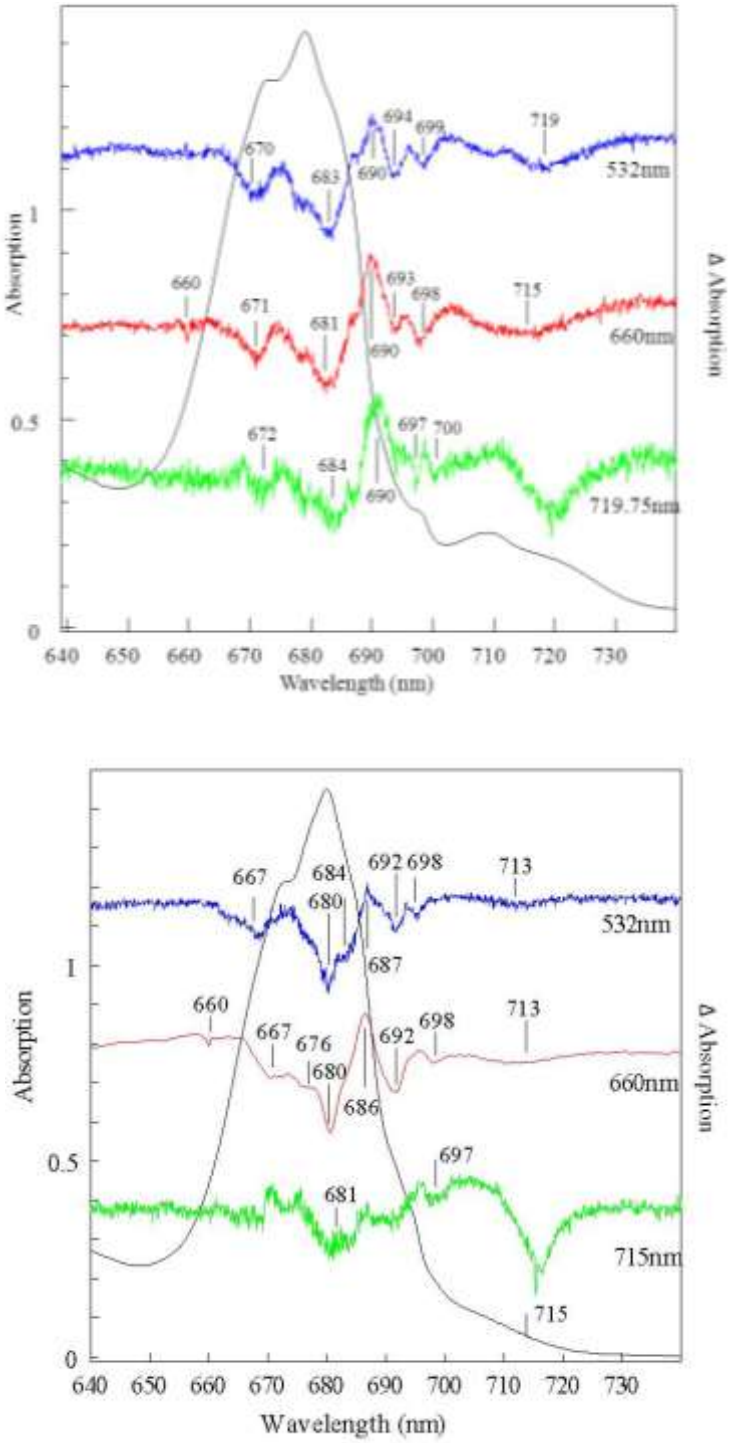

Figure 42. The low-temperature (5 K) absorption and non-resonant hole structures for PSI from *T. elongatus* (frame A) and *Synechocystis PCC 6803* (frame B). Hole spectra are labeled (to the right) with illumination wavelengths

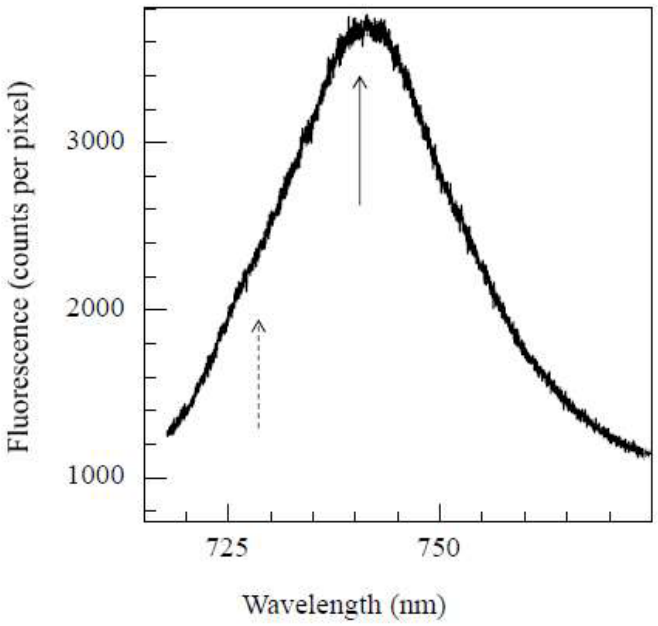

Figure 43. 5 K fluorescence spectrum of mostly reduced sample B. Comparison with figure 41 (from [181]) above shows that while the sample mostly has P700 in reduced state (hence the peak at 741 nm, solid arrow) some contribution from samples with oxidized P700 is also present, yielding a shoulder at ~730 nm, dashed arrow.

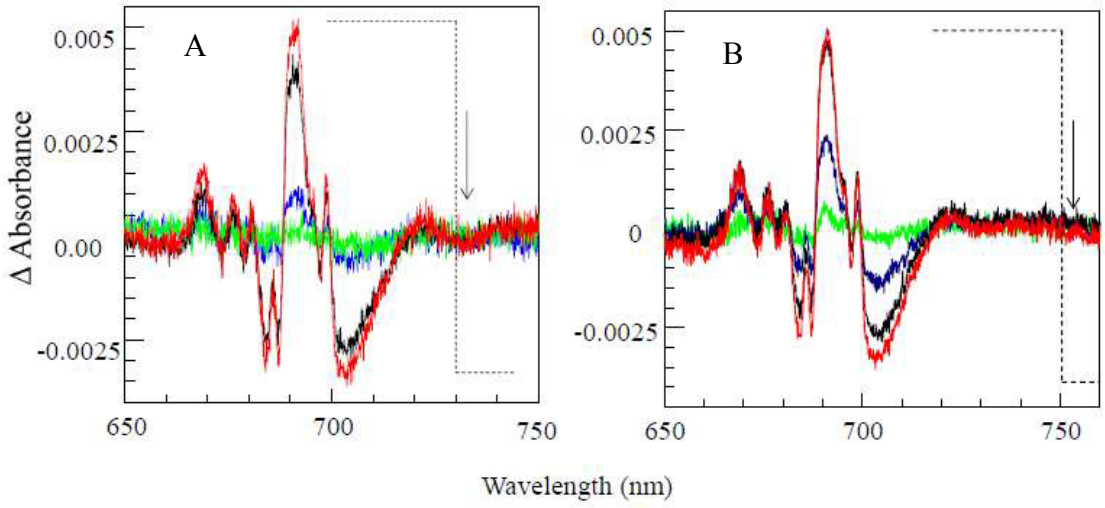

Figure 44. Frame A: Green curve: difference between two consecutively measured spectra. Blue: result of exposure of the sample to dim room light (several nW/cm^2). Black: after one minute of illumination at 732 nm. Red: after 16 minutes of illumination at 732 nm. Dashed line indicates the cut-off wavelength of a long-pass filter, 730 nm. **Frame B:** NPHB-free P700$^+$ minus P700 spectra produced with illumination at 753 nm through 750 nm long-pass filter. Green: difference between the first two spectrometer scans. Blue: after seven spectrometer scans, further scanning does not increase the hole. Black: after 10 minutes of illumination at 753 nm. Red: after further 20 minutes of illumination at 753 nm.

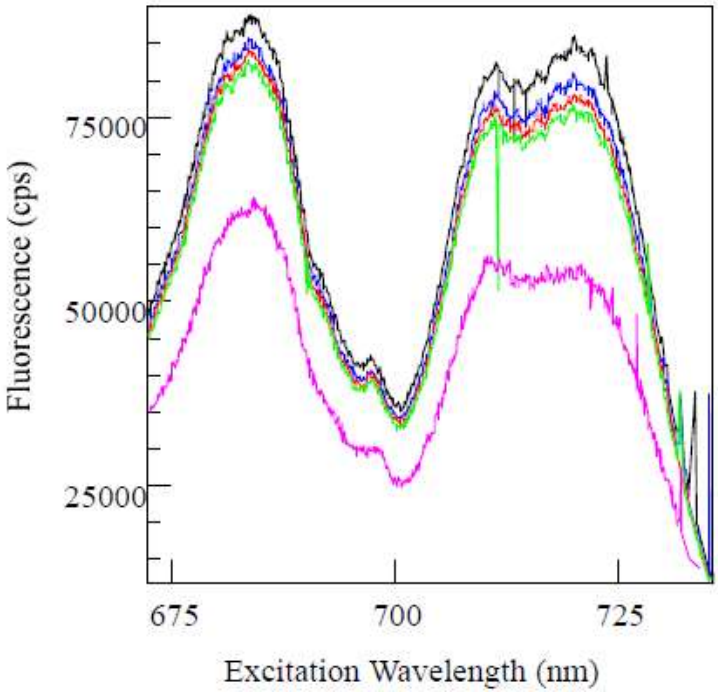

Figure 45. Fluorescence excitation spectra of sample B, cooled down in the dark. Black to green curves represent consecutive scans from 735 to 670 nm. Magenta curve was recorded after an attempt to measure the HB action spectrum covering 735 to 700 nm range. Spectra are equally distorted (longer-wavelength range is amplified) by the transmission dependence on wavelength of the supposedly neutral density filters used for beam attenuation. The spectra were left uncorrected since in uncorrected spectra the red state region is artificially amplified and its evolution is clearer.

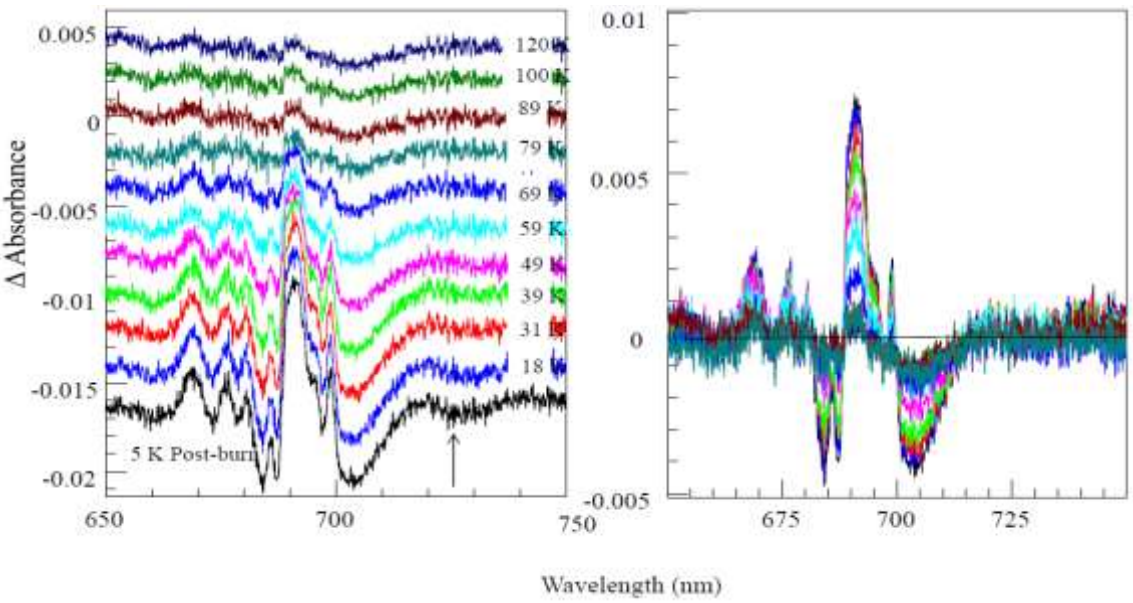

Figure 46. Left Frame: Hole spectra after thermocycling to indicated excursion temperatures. Spectra are shifted along vertical axis for clarity. Arrow indicates the burn wavelength of 725 nm. Right frame: several hole spectra (color coding same as in the left frame) overlaid together.

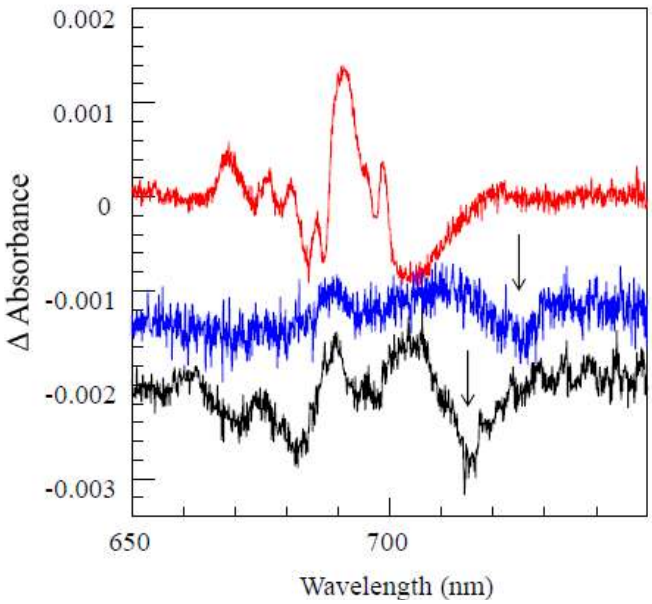

Figure 47. Sample A with mostly oxidized P700. Black: hole spectrum after illumination at 714.5 nm, probing both C715 and C719 states. Blue: hole spectrum after illumination at 725 nm, probing only C719 state. Arrows indicate burn wavelengths. Red: $P700^{+}$ minus P700 signature from sample B, Figure 44, presented for comparison.

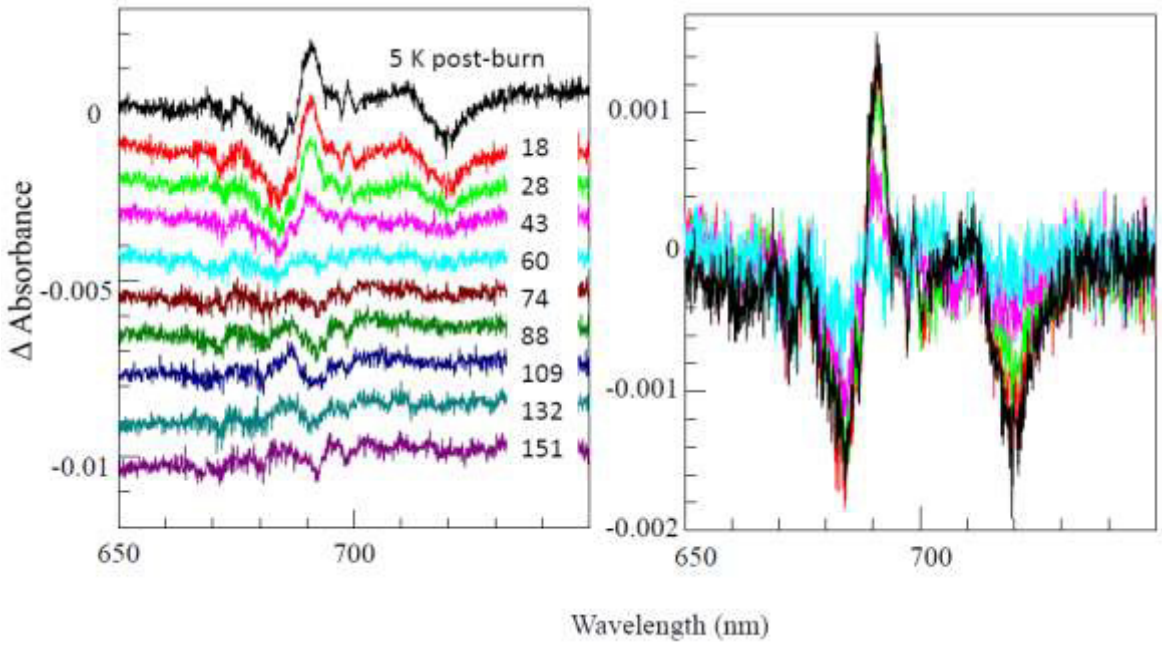

Figure 48. Left Frame: Hole spectra with λ_B=719 nm after thermocycling to indicated excursion temperatures. Spectra are shifted along vertical axis for clarity. The burn wavelength was 719 nm. Right frame: several hole spectra (color coding same as in the left frame) overlaid together.

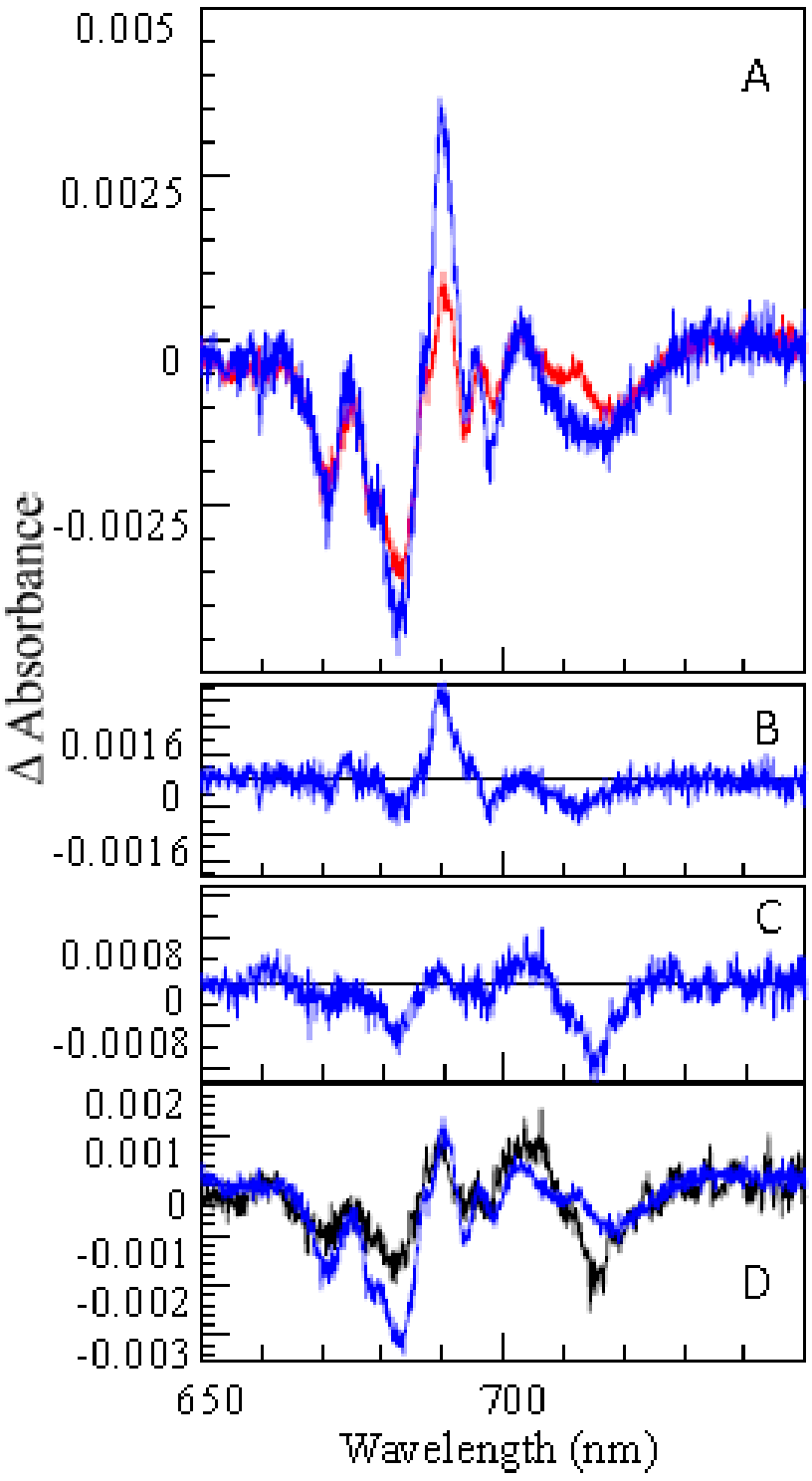

Figure 49 Frame A: Hole spectra for λ_B of 660 nm (blue) and 532 nm (red). **Frame B:** the difference between spectra in frame A. **Frame C:** The difference between spectra for λ_B of 714.5 and 725 nm (see Figure 47). **Frame D:** the hole spectra for λ_B of 714.5 nm (black) and 532 nm (blue).

References:

1. D. G. Nocera Living healthy on a dying planet, Chem Soc Rev 38, 13-15, 2009
2. M. Hambourger, G. F. Moore, D. M. Kramer, D. Gust, A. L. Moore, T. A. Moore Biology and technology for photochemical fuel production, Chem Soc Rev, 38, 25-35, 2009
3. L. S. Nathan, (chair) Basic research needs for solar energy utilization, Report on the Basic Energy Sciences Workshop on Solar Energy Utilization, California Institute of Technology, 2005
4. W. Moomaw, Renewable Energy and Climate Change An Overview, IPCC Scoping Meeting on Renewable Energy Sources – Proceedings, Lubeck, Germany, 20 – 25 January, 2008
5. R. Mechler, Insights from the IPCC Special Report on Managing the Risks of Extreme Events and Disasters to Advance Climate Change Adaptation (SREX), A multidisciplinary approach to tackling extreme events in climate adaptation, Rio de Janeiro, June 15, 2012
6. G. D. Scholes, G. R. Fleming, A.Olaya-Castro, R. van Grondelle, Lessons from nature about solar light harvesting, Nature Chemistry, 3, 763-774, 2011
7. R.Jankowiak, M. Reppert, V. Zazubovich, J. Pieper, T. Reinot, Site Selective and Single Complex Laser-Based Spectroscopies: A Window on Excited State Electronic Structure, Excitation Energy Transfer, and Electron Phonon Coupling of Selected Photosynthetic Complexes, Chem. Rev, 111, 4546-4598, 2011
8. R.E. Blankenship, Molecular mechanisms of photosynthesis. Blackwell Science, Oxford, 2002

9. H.van Amerongen, L.Valkunas, R. van Grondelle, Photosynthetic Excitons. Singapore, 2000
10. R.O. Donald, C. F. Yocum (Eds.), Oxygenic Photosynthesis: The Light Reactions, Advances in Photosynthesis, Vol.4, Kluwer Academic Publisher, 1996
11. B. Grimm, R.J. Porra, W.Rüdiger, H. Scheer, (Eds.) Advances in Photosynthesis and Respiration, Chlorophylls and Bacteriochlorophylls, Vol. 25, Springer, 2006
12. H. Scheer (Eds.) Chlorophylls, CRC Press, 1991
13. I. McConnell, G. Li, G. W. Brudvig, Energy Conversion in Natural and Artificial Photosynthesis, Chem Biol, 17, 5, 434-447, 2010
14. S. Caffarri, R. Kouril, S. Kereiche, E. J Boekema, R. Croce, Functional architecture of higher plant photosystem II supercomplexes, The EMBO Journal, 28, 3052-3063, 2009
15. V. Zazubovich , R. Jankowiak, Biophotonics of Photosynthesis, ed. D. Andrews, Wiley 2013, in press.
16. J. W. Murray, J. Duncan, J. Barber, CP43-like chlorophyll binding proteins: structural and evolutionary implications, Trends in Plant Science, 11, 3, 152-158, 2006
17. F. J. Kleima, C. C. Gradinaru, F. Calkoen, I. H. M. van Stokkum, R. van Grondelle, H. van Amerongen, Energy Transfer in LHCII Monomers at 77K Studied by Sub-Picosecond Transient Absorption Spectroscopy, Biochemistry, 36, 15262-15268, 1997
18. J. Pieper, R. Schodel, K-D Irrgang, J. Voigt, G. Renger, Electron-Phonon Coupling in Solubilized LHC II Complexes of Green Plants Investigated by Line-Narrowing and Temperature-Dependent Fluorescence Spectroscopy, J. Phys. Chem. B, 105, 7115-7124, 2001

19. X. Pan et all, Structural insights into energy regulation of light-harvesting complex CP29 from spinach**,** Nature structural & molecular biology, 18, 3, 309-316, 2011
20. A. Amunts, O. Dorory, N. Nelson, The structure of a plant photosystem I supercomplex at 3.4Å resolution, Nature, 447, 58-63, 2007
21. A. Amunts, H. Toporik, A. Borovikova, N. Nelson Structure Determination and Improved Model of Plant Photosystem I, The Journal of Biological Chemistry, 285, 5, 3478–3486, 2010
22. I. Grotjohann, P. Fromme, Structure of cyanobacterial Photosystem I, Photosynthesis Research, 85, 51–72, 2005
23. P. Fromme*,* P. Mathis, Unraveling the Photosystem I reaction center: a history, or the sum of many efforts, Photosynthesis Research, 80, 109–124, 2004
24. C. Jolley, A. Ben-Shem, N. Nelson, P. Fromme, Structure of Plant Photosystem I Revealed by Theoretical Modeling, Journal of Biological Chemistry, 280, 39, 33627-33636, 2005
25. P. Fromme I. Grotjohann, The protein Complexes of Oxygenic Photosynthesis, Photosynthetic Protein Complexes Edited by P. Fromme, Wiley, 10-21, 2008
26. N. Krauß, Structure and Function of Cyanobaterial Photosystem I, Photosynthetic Protein Complexes Edited by P. Fromme, Wiley, 23-52, 2008
27. A. Amunts, O. Drory, N. Nelson, A Glimpse into the Atomic Structure of Plant Photosystem I, Photosynthetic Protein Complexes Edited by P. Fromme, 65-77, 2008
28. M. K. Sener, C. Jolley, A. Ben-Shem, P. Fromme, N. Nelson, R. Croce, K. Schulten, Comparison of the Light-Harvesting Networks of Plant and Cyanobacterial Photosystem I, Biophysical Journal, 89, 3, 1630–1642, 2005

29. P. Jordan, P. Fromme, H. T. Witt, O. Klukas, W. Saenger, N. Krauβ, Three-dimensional structure of cyanobacterial photosystem I at 2.5 Å resolution, Nature, 411, 909–917, 2001

30. Y. Tian, R. Camacho, D. Thomsson, M. Reus, A. R. Holzwarth, I. G. Scheblykin, Organization of Bacteriochlorophylls in Individual Chlorosomes from Chlorobaculum tepidum Studied by 2-Dimensional Polarization Fluorescence Microscopy, J. Am. Chem. Soc, 133, 17192-17199, 2011

31. K-H Tang, L. Zhu, V. S. Urban, A. M. Collins, P. Biswas, R. E. Blankenship Temperature and Ionic Strength Effects on the Chlorosome Light-Harvesting Antenna Complex, Langmuir, 27, 4816-4828, 2011

32. J. Adolphs, T. Renger, How Proteins Trigger Excitation Energy Transfer in the FMO Complex of Green Sulfur Bacteria, Biophysical Journal, 91, 2778–2797, 2006

33. F. Müh, El-Amine Madjet, M. Adolphs, J. Abdurahman, A. Rabenstein, B. Ishikita, H. Knapp, E-Wr and T. Renger, α-Helices direct excitation energy flow in the Fenna–Matthews–Olson protein, PNAS, 104, 16862–16867, 2007

34. A. Camara-Artigas, R. E Blankenship, J. P. Allen, The structure of the FMO protein from *Chlorobium tepidum* at 2.2 Å resolution, Photosynthesis Research, 75, 1, 49-55, 2003

35. B. Loll, J. Kern, W. Saenger, A. Zouni, J. Biesiadka, Towards complete cofactor arrangement in the 3.0 Å resolution structure of photosystem II, Nature, 438, 1040-1044, 2005

36. R. J. Cogdell, Photosynthetic Reaction Centers, Ann. Rev. Plant Physiol, 34, 21-45, 1983

37. J.R. Durrant, D.R Klug, S.L. Kwa, R.vanGrondelle, G.Porter, J. P. Dekker, Amultimermodel for P680, the primary electron donor of photosystem II, Proc. Natl. Acad. Sci. USA, 92, 4798–4802, 1995

38. R. Jankowiak, Probing electron-transfer times in photosynthetic reaction centers by hole-burning spectroscopy, J. Phys. Chem. Lett, 3, 1684−1694, 2012

39. M. R. Jones, P. K. Fyfe, A. W. Roszak, N. W. Isaacs, R. J. Cogdell, Protein–lipid interactions in the purple bacterial reaction centre, Biochimica et Biophysica Acta, 1565 206– 214, 2002

40. R.H. Austin, S. Erramilli, Low-Temperature Spectroscopy, Methods in Enzymology, 246, 131-168, 1995

41. L. A. Rebane Low-Temperature Spectroscopy of Organic Molecules in Solids by Photochemical Hole Burning, Appl. Phys. B, 29, 235-250, 1982

42. K. K. Rebane, Purely electronic zero-phonon line as the foundation stone for high resolution matrixspectroscopy, single impurity molecule spectroscopy, persistent spectral hole burning, J. Lumin, 100, 219–232, 2002

43. Y. G. Vainer, A. V. Naumov, M. Bauer, L. Kador, Dynamics of amorphous polymers at low temperatures and temporal evolution of spectra of single impurity molecules: I. Experiment, Optics and Spectroscopy, 94, 6, 864–872, 2003

44. S. Volker, Hole-Burning Spectroscopy, Annu. Rev. Phys. Chern. 40, 499-530, 1989

45. H.C. Meijers, D.A. Wiersma, Low temperature dynamics in amorphous solids: a phonon echo study, J. Chem. Phys, 101, 8, 6927 – 6943, 1994

46. J. Friedrich, D. Haarer Photochemical Hole Burning: A Spectroscopic Study of Relaxation Processes in Polymers and Glasses, Angew. Chem. Int. Ed. Engl. 23, 113-140, 1984

47. J. Friedrich, Hole Burning Spectroscopy and Physics of Proteins, Methods in Enzimology, 246, 226 – 259, 1995

48. J. Kohler, A.M. van Oijen, M. Ketelaars, C. Hofmann, M. Matsushita, T.J. Aartsma Optical Spectroscopy of Individual Photosynthetic Pigment Protein Complexes, Intl. J. Modern Phys. B, 15, 28-30, 3633-3636, 2001

49. R. Purchase, S. Völker, Spectral hole burning: examples from photosynthesis Photosynth Res, Photosynth. Res, 101, 245-266, 2009

50. V. Personov, R.I. Ai'Shits. E.I. L.A. Bycovskaia, The Effect of Fine Structure Appearance in Laser-Excited Fluorescence Spectra of Organic Compounds in Solids Solutions Optics Communications, 6, 2, 169-173, 1972

51. J.M. Hayes, G. J. Small, Non-photochemical hole burning and impurity site relaxation processes in organic glasses, Chem. Phys, 27, 151-157, 1978

52. R. I. Personov, B. M. Kharmalov, Photochemical and Photophysical Hole Burning in Electronic Spectra of Complex Organic Molecules, Laser Chem, 6, 181-201, 1986

53. L. A. Rebane, A. A. Gorokhovskii, J. V. Kikas, Low-Temperature Spectroscopy of Organic Molecules in Solids by Photochemical Hole Burning, Appl. Phys. B, 29, 235-250, 1982

54. T. Reinot, J. M. Hayes, G. J. Small, Fundamentals of Nonphotochemical Hole Burning Spectroscopy and Application to Complex Systems, Photon. Sci. News, 6, 83–99, 2000

55. R. Jankowiak, J. M. Hayes, G. J. Small, Spectral Hole-Burning Spectroscopy in Amorphous Molecular Solids and Proteins, Chem. Rev, 93, 1471-1502, 1993

56. C. Hofmann, T.J. Aartsma, H. Michel, J. Köhler, Direct observation of tiers in the energy landscape of a chromoprotein: A single-molecule study, Proc Natl Acad Sci USA, 100,15534–15538, 2003

57. H. Frauenfelder, S. G. Sligar, G. Peter, The Energy Landscapes and Motions of Proteins, Science, New Series, 254, 5038, 1598-1603, 1991

58. G. D. Scholes, G. R. Fleming, On the Mechanism of Light Harvesting in Photosynthetic Purple Bacteria: B800 to B850 Energy Transfer, J. Phys. Chem. B, 104, 1854-1868, 2000

59. D.Grozdanov, N. Herascu, T. Reinot, R. Jankowiak, V. Zazubovich, Low-Temperature Protein Dynamics of the B800 Molecules in the LH2 Light-Harvesting Complex: Spectral Hole Burning Study and Comparison with Single Photosynthetic Complex Spectroscopy, J. Phys. Chem, 114, 3426-3438, 2010

60. N. Herascu, S. Ahmouda, R. Picorel, M. Seibert, R. Jankowiak, V. Zazubovich, Effects of the Distributions of Energy or Charge Transfer Rates on Spectral Hole Burning in Pigment-Protein Complexes at Low Temperatures, J. Phys. Chem. B, 115, 15098–15109, 2011

61. H. Oikawa, S. Fujiyoshi, T. Dewa, M. Nango, Matsushita, How deep is the potential well confining a protein in a specific conformation? A single-molecule study on temperature dependence of conformational change between 5 and 18 K, J. Am. Chem. Soc, 130, 4580−4581, 2008

62. V.V. Ponkratov, J. Friedrich, J.M. Vanderkooi, Hole burning experiments with proteins: Relaxations, fluctuations and glass-like features, Journal of Non-Crystalline Solids, 352, 4379–4386, 2006

63. J.L. Skinner, J. Friedrich, J. Schlicher, Spectral Diffusion in Proteins: a Simple Phenomenological Model, J. Phys. Chem. A, 103, 2310-2311, 1999

64. W. Köhler, J. Friedrich, Probing of conformational relaxation processes of proteins by frequency labeling of optical states, J. Chem. Phys, 90, 2, 1270-1273, 1989

65. W. Köhler, J. Friedrich, Distribution of Barrier Heights in Amorphous Organic Materials, Physical Review Letters, 59, 19, 2199-2202, 1987

66. M. Najafi, N. Herascu, M. Seibert, R. Picorel, R. Jankowiak, V. Zazubovich, Spectral Hole Burning, Recovery, and Thermocycling in Chlorophyll−Protein Complexes: Distributions of Barriers on the Protein Energy Landscape, J. Phys. Chem. B, 116, 11780-11790, 2012

67. W. Köhler, J. Friedrich, H. Scheer, Conformational barriers in low-temperature proteins and glasses, Physical Review A, 37, 2, 660–662, 1988

68. P. Schellenberg, J. Friedrich, J. Kikas, Thermal recovery and spectral diffusion of photochemical holes in polymorphic systems, J. Chem. Phys,101, 9262-9270, 1994

69. T. Reinot, V. Zazubovich, J. M. Hayes, G. J. Small, New Insights on Persistent Nonphotochemical Hole Burning and Its Application to Photosynthetic Complexes, J. Phys. Chem. B, 105, 5083-5098, 2001

70. T. Reinot, N. C. Dang, G. J. Small, A model for persistent hole burned spectra and hole growth kinetics that includes photoproduct absorption: Application to free base

phthalocyanine in hyperquenched glassy ortho-dichlorobenzene at 5 K, J. Chem. Phys, 119, 19, 10404-10414, 2003

71. N. Herascu, M. Najafi, A. Amunts, J. Pieper, K.-D. Irrgang, R. Picorel, M. Seibert, V. Zazubovich, Parameters of the protein energy landscapes of several light-harvesting complexes probed via spectral hole growth kinetics measurements, J. Phys. Chem. B, 115, 2737–2747, 2011.
72. T. Reinot, G. Small, Non-Lorentzian zero-phonon holes and new insights on nonphotochemical hole burning: Al-phthalocyanine in hyperquenched glassy water, J. Chem. Phys, 114, 9105–9114, 2001
73. N. C. Dang, T. Reinot, M.; Reppert, R. Jankowiak, Temperature Dependence of Hole Growth Kinetics in Aluminum-Phthalocyanine-Tetrasulfonate in Hyperquenched Glassy Water, J. Phys. Chem. B, 111, 1582–1589, 2007
74. T. Reinot, J. M. Hayes, G. Small, Laser-induced hole filling and spectral diffusion of aluminum phthalocyanine tetrasulfonate in hyperquenched glassy films, J. Chem. Phys, 110, 4820–4827, 1999
75. T. Reinot, N. C. Dang, G. Small, A model for persistent hole burned spectra and hole growth kinetics that includes photoproduct absorption: Application to free base phthalocyanine in hyperquenched glassy ortho-dichlorobenzene at 5 K, J. Chem. Phys, 119, 10404–10414, 2003
76. S. P. Love, C. E. Mungan, A. J. Sievers , J. A. Campbell, Persistent infrared spectral hole burning of Tb^{3+} in the glasslike mixed crystal $Ba_{1-X-Y}La_xTb_yF_{2+x+y}$, J. Opt. Soc. Am. B, 9, 5, 794-799, 1992

77. R. Kiyanagi, H.Kimura, M.Watanabe, Y. Noda, T.Mochida, T.Sugawara, Indication of Tunneling State of Hydrogen Atom in Hydrogen-Bonded Material 5-Bromo-9-hydroxyphenalenon Studied by X-ray and Neutron Diffractions, J. Phys. Soc. Jpn, 77 064602 (1−7), 2008

78. W. C. Hamilton, J.A. Ibers, Hydrogen Bonding in Solids; Benjamin: New York, Amsterdam, The Netherlands, 1968

79. Y. Berlin, A. Burin, J. Friedrich, S. Kohler, Spectroscopy of proteins at low temperature. Part I: Experiments with molecular ensembles, J. Physics of Life Reviews, 3, 262−292, 2006

80. J. Baier, M. F. Richter, R. J. Cogdell, S. Oellerich, Kohler, Determination of the spectral diffusion kernel of a protein by single-molecule spectroscopy, J. Phys. Rev. Lett, 100, 018108 (1−4), 2008

81. A. Heuer, P Neu,. Tunneling dynamics of side chains and defects in proteins, polymer glasses, and OH-doped network glasses, J. Chem. Phys, 107, 8686−8696, 1997

82. H. van der Laan, C. De Caro, Th. Schmidt, R. W.Visschers, R. van Grondelle, G. J. S. Fowler, C. N. Hunter, S. Volker, Excited-state dynamics of mutated antenna complexes of purple bacteria studied by hole-burning, Chem. Phys. Lett, 212, 569–580, 1993

83. M. L.Groot, J. P. Dekker, R. van Grondelle, F. T. H. den Hartog, S. Volker, Energy Transfer and Trapping in Isolated Photosystem II Reaction Centers of Green Plants at Low Temperature. A Study by Spectral Hole Burning, J. Phys. Chem, 100, 11488–11495, 1996

84. M. Ratsep, R. E. Blankenship, G. J. Small, Energy Transfer and Spectral Dynamics of the Three Lowest Energy Q_y-States of the Fenna-Matthews-Olson Antenna Complex, J. Phys. Chem. B, 103, 5736–5741, 1999

85. H-M.Wu, S. Savikhin, N. R. S. Reddy, R. Jankowiak, R. J. Cogdell, W. S. Struve, G. J. Small, Femtosecond and Hole-Burning Studies of B800's Excitation Energy Relaxation Dynamics in the LH2 Antenna Complex of *Rhodopseudomonas acidophila* (Strain 10050), J. Phys. Chem, 100, 12022–12033, 1996

86. K. Riley, R. Jankowiak, M. Ratsep, G. J. Small, V. Zazubovich, New Insights on Persistent Nonphotochemical Hole Burning and Its Application to Photosynthetic Complexes, J. Phys. Chem. B, 108, 10346–10356, 2004

87. V. I. Prokhorenko, A. R. Holzwarth, Primary Processes and Structure of the Photosystem II Reaction Center: A Photon Echo Study, J. Phys. Chem. B, 104, 11563–11578, 2000

88. E. Romero, I. H. M. van Stokkum, V. I. Novoderezhkin, J. P. Dekker, R.van Grondelle, Two Different Charge Separation Pathways in Photosystem II, Biochemistry, 49, 4300–4307, 2010

89. J. A. Myers, K. L. M. Lewis, F. D. Fuller, P. F. Tekavac, C. F. Yocum, J. P. Ogilvie, Two-Dimensional Electronic Spectroscopy of the D1-D2-cyt b559 Photosystem II Reaction Center Complex, J. Phys. Chem. Lett, 1, 2774–2780, 2010

90. T. Reinot, V. Zazubovich, J. M. Hayes, G. J. Small, New Insights on Persistent Nonphotochemical Hole Burning and Its Application to Photosynthetic Complexes, J. Phys. Chem. B, 105, 5083–5098, 2001

91. J. M. Hayes, P. A. Lyle, G. J. Small, A Theory for the Temperature Dependence of Hole-Burned Spectra, J. Phys. Chem, 98, 7337–7341, 1994

92. R. J. Cogdell, A. T. Gardiner, H. Hashimoto, T. H. P. Brotosudarmo, A comparative look at the first few milliseconds of the light reactions of photosynthesis, Photochem. Photobiol. Sci, 7, 1150–1158, 2008

93. B. Loll, J. Kern, A. Zouni, W. Saenger, J.Biesiadka, K.-D. Irrgang, The Antenna System of Photosystem II From *Thermosynechococcus elongatus* at 3.2 Å Resolution, Photosynth. Res, 86, 175–184, 2005

94. A. Ben-Shem, F.Frolow, N.Nelson, Crystal structure of plant photosystem I, Nature, 426, 630–635, 2003

95. G. McDermott, S. M. Prince, A. A. Freer, A. M. Hawthornthwarte-Lawless, M. Z. Papiz, R. J. Cogdell, N. W. Isaacs, Crystal structure of an integral membrane light-harvesting complex from photosynthetic bacteria, Nature, 374, 517–521, 1995

96. M. K. Sener, D. Lu, T. Ritz, S. Park, P. Fromme, K, Schulten, Robustness and Optimality of Light Harvesting in Cyanobacterial Photosystem I, J. Phys. Chem. B, 106, 7948–7960, 2002

97. A. Damjanovic, H. M. Vaswani, P. Fromme, G. R. Fleming, Chlorophyll Excitations in Photosystem I of *Synechococcus elongatus*, J. Phys. Chem. B, 106, 10251–10262, 2002

98. S. Vasil'ev, P. Orth, A. Zouni, T. G. Owens, D. Bruce, Excited-state dynamics in photosystem II: insights from the x-ray crystal structure, Proc. Natl. Acad. Sci. USA, 98, 8602–8607, 2001.

99. R. G. Alden, E. Johnson, V. Nagarajan, W. W. Parson, C. J. Law, R. G. Cogdell, Calculations of Spectroscopic Properties of the LH2 Bacteriochlorophyll−Protein

Antenna Complex from *Rhodopseudomonas acidophila*, J. Phys. Chem. B, 101, 4667–4680, 1997

100. K. Sauer, R. J. Cogdell, S. M. Prince, A. A. Freer, N. W. Isaacs, H. Scheer, Structure-Based Calculations of the Optical Spectra of the LH2 Bacteriochlorophyll-Protein Complex from *Rhodopseudomonas acidophila,* Photochem. Photobiol, 64, 564–576, 1996

101. R. Jankowiak, V. Zazubovich, M. Ratsep, S. Matsuzaki, M. Alfonso, R. Picorel, M. Seibert, G. J, Small, The CP43 Core Antenna Complex of Photosystem II Possesses Two Quasi-Degenerate and Weakly Coupled Qy-Trap States, J. Phys. Chem. B, 104, 11805–11815, 2000

102. M. Di Donato, R. van Grondelle, I. H. van Stokkum, M. L. Groot, Excitation Energy Transfer in the Photosystem II Core Antenna Complex CP43 Studied by Femtosecond Visible/Visible and Visible/Mid-Infrared Pump Probe Spectroscopy, J. Phys. Chem. B, 111, 7345–7352, 2007

103. K. J. Riley, T. Reinot, R. Jankowiak, P. Fromme, V. Zazubovich, Red antenna states of photosystem I from cyanobacteria *Synechocystis* PCC 6803 and *Thermosynechococcus elongatus*: single-complex spectroscopy and spectral hole-burning study, J. Phys. Chem. B, 111, 286–292, 2007

104. V. Zazubovich, S. Matsuzaki, T. W. Johnson, J. M. Hayes, P. R. Chitnis, G. Small, Red antenna states of photosystem I from cyanobacterium *Synechococcus elongatus*: a spectral hole burning study, J. Chem. Phys, 275, 47–59, 2002

105. M. Byrdin, P. Jordan, N. Krauβ, P. Fromme, D. Stehlik, E. Schlodder, Light harvesting in photosystem I: modeling based on the 2.5-A structure of photosystem I from *Synechococcus elongatus*, Biophys. J, 83, 433–457, 2002

106. A. F. Elli, F. Jelezko, C. Tietz, H. Studier, M. Brecht, R. Bittl, J. Wrachtrup, Red Pool Chlorophylls of Photosystem I of the Cyanobacterium *Thermosynechococcus elongatus*: A Single-Molecule Study, Biochemistry, 45, 1454–1458, 2006

107. S. Jang, M. D. Newton, R. Silbey, Multichromophoric Foerster Resonance Energy Transfer, J. Phys. Rev. Lett, 92, 218301 (1-4), 2004

108. G. D. Scholes, G. R. Fleming, On the Mechanism of Light Harvesting in Photosynthetic Purple Bacteria: B800 to B850 Energy Transfer, J. Phys. Chem. B, 104, 1854–1868, 2000

109. K. Mukai, S. Abe, H. Sumi, Theory of Rapid Excitation-Energy Transfer from B800 to Optically-Forbidden Exciton States of B850 in the Antenna System LH2 of Photosynthetic Purple Bacteria, J. Phys. Chem. B, 103, 6096–6102, 1999

110. A. M.van Oijen, M. Ketelaars, J. Kohler, T. J. Aartsma, J. Schmidt, Spectroscopy of individual light-harvesting 2 complexes of *Rhodopseudomonas acidophila*: diagonal disorder, intercomplex heterogeneity, spectral diffusion, and energy transfer in the B800 band, Biophys. J, 78, 1570–1577, 2000

111. M. Hussels, M. Brecht, Evidence for direct binding of glycerol to Photosystem I, FEBS Letters**,** 585, 2445-2449, 2011

112. J. Baier, M. F. Richter, R. J. Cogdell, S. Oellerich, J. Kohler, Do proteins at low temperature behave as glasses? A single-molecule studyJ. Phys. Chem. B, 111, 1135–1138, 2007

113. F. L. de Weerd, I. H. M. van Stokkum, H. van Amerongen, J. P.Dekker, R. van Grondelle, Pathways for energy transfer in the core light-harvesting complexes CP43 and CP47 of photosystem II, Biophys. J, 82, 1586–1597, 2002

114. S. R. Greenfield, M. Seibert, M. Wasielewski, Pathways for energy transfer in the core light-harvesting complexes CP43 and CP47 of photosystem II, J. Phys. Chem. B, 103, 8364–8374, 1999

115. S. A. P. Merry, S. Kumazaki, Y. Tachibana, D. M. Joseph, G. Porter, K. Yoshihara, J.Barber, J. R. Durrant, D. R. Klug, Sub-picosecond equilibration of excitation energy in isolated photosystem II reaction centers revisited: Time-dependent anisotropy, J. Phys. Chem, 100, 10469–10478, 1996

116. M. L. Groot, N. P. Pawlowicz, L. J. G. van Wilderen, J. W. Breton, I. H. M. van Stokkum, R. van Grondelle, Initial electron donor and acceptor in isolated Photosystem II reaction centers identified with femtosecond mid-IR spectroscopy, Proc. Natl. Acad. Sci.U.S.A, 102, 13087–13092, 2005

117. J. M. Salverda, M. Vengris, B. P. Krueger, G. D. Scholes, A. R. Czarnoleski, V. Novoderezhkin, H. van Amerongen, R. van Grondelle, Energy transfer in light-harvesting complexes LHCII and CP29 of spinach studied with three pulse echo peak shift and transient grating, Biophys. J, 84, 450–465, 2003

118.K. Gibasiewicz, R. Croce, T. Morosinotto, J. A. Ihalainen, I. H. M. vaStokkum, J. P. Dekker, R. Bassi, R. van Grondelle, Excitation Energy Transfer Pathways in Lhca4, Biophys. J, 88, 1959–1969, 2005

119. A. D. Stahl, M. Di Donato, I. H. M. van Stokkum, R.van Grondelle, M. L. Groot, A Femtosecond Visible/Visible and Visible/Mid-Infrared Transient Absorption Study of the Light Harvesting Complex II, Biophys. J, 97, 3215–3223, 2009

120. A. R. Holzwarth, M. G. Muller, M. Reus, M. Nowaczyk, J. Sander, M. Rogner, Kinetics and mechanism of electron transfer in intact photosystem II and in the isolated reaction center: Pheophytin is the primary electron acceptor, Proc. Natl. Acad. Sci. USA, 103, 6895–6900, 2006

121. R. Croce, M. G. Muller, R. Bassi, A. R. Holzwarth, Chlorophyll *b* to Chlorophyll *a* Energy Transfer Kinetics in the CP29 Antenna Complex: A Comparative Femtosecond Absorption Study between Native and Reconstituted Proteins,Biophys. J, 84, 2508–2516, 2003

122. M. Ratsep, T. W. Johnson, P. R. Chitnis, G. J. Small, The Red-Absorbing Chlorophyll *a* Antenna States of Photosystem I: A Hole-Burning Study of *Synechocystis* sp. PCC 6803 and Its Mutants, J. Phys. Chem. B, 104, 836–847, 2000

123. T. Reinot, G. J. Small, Modeling of dispersive nonphotochemical hole growth kinetics data. Al-phthalocyanine tetrasulphonate in hyperquenched glassy water, J. Chem. Phys, 113, 10207–10214, 2000

124. T. Reinot, N. C. Dang, G. J. Small, Non-photochemical versus photochemical hole burning in hyperquenched glassy water and cubic ice, J. Lumin, 98, 183–188, 2002

125. T. Förster, Zwischenmolekulare Energiewanderung und Fluoreszenz, Ann. Phys, 437, 55–75, 1948

126. V. Zazubovich, R. Jankowiak, On the energy transfer between quasi-degenerate states with uncorrelated site distribution functions: an application to the CP43 complex of Photosystem II, J. Lumin, 127, 245–250, 2007

127. K. J. Riley, V. Zazubovich, R. Jankowiak, Frequency-Domain Spectroscopic Study of the PS I-CP43' Supercomplex from the Cyanobacterium Synechocystis PCC 6803 Grown under Iron Stress Conditions, J. Phys. Chem. B, 110, 22436–22446, 2000

128. V. I. Novoderezhkin, R. van Grondelle, Physical origins and models of energy transfer in photosynthetic light-harvesting, Phys. Chem. Chem. Phys, 12, 7352–7365, 2010

129. A. Ishizaki, G. R. Fleming, On the adequacy of the Redfield equation and related approaches to the study of quantum dynamics in electronic energy transfer, J. Chem. Phys, 130, 234110 (1-9), 2009

130. A. Ishizaki, G. R. Fleming, Unified treatment of quantum coherent and incoherent hopping dynamics in electronic energy transfer: reduced hierarchy equation approach, J. Chem. Phys, 130, 234111 (1-10), 2009

131. M. Yang, G. R. Fleming, Influence of phonons on exciton transfer dynamics: comparison of the Redfield, Forster, and modified Redfield equations, Chem. Phys, 275, 355–372, 2002

132. V. I. Novoderezhkin, M. A. Palacios, H. van Amerongen, R. van Grondelle, Energy-Transfer Dynamics in the LHCII Complex of Higher Plants: Modified Redfield Approach, J. Phys. Chem. B, 108, 10363–10375, 2004

133. S. V. Kolaczkowski, J. M. Hayes, G. J. Small, A Theory of Dispersive Kinetics in the Energy Transfer of Antenna Complexes, J. Phys. Chem, 98, 13418–13425, 1994

134. J. K. Gillie, G. J. Small, J. H. Golbeck, Nonphotochemical hole burning of the native antenna complex of photosystem I (PSI-200), J. Phys. Chem, 93, 1620–1627, 1989

135. V. Zazubovich, I. Tibe, G. J. Small, Bacteriochlorophyll *a* Franck-Condon Factors for the S0 - S1(Q*y*) Transition, J. Phys. Chem. B, 105, 12410–12417, 2001

136. M. Wendling, T. Pullerits, M. A. Przyjalowski, S. I. E.Vulto, T. J. Aartsma, R. van Grondelle, H. van Amerongen, Electron−Vibrational Coupling in the Fenna−Matthews−Olson Complex of *Prosthecochloris aestuarii* Determined by Temperature-Dependent Absorption and Fluorescence Line-Narrowing Measurements, J. Phys. Chem. B, 104, 5825–5831, 2000

137. E. J. G. Peterman, T. Pullerits, R. van Grondelle, H.van Amerongen, Electron-phonon coupling and vibronic fine structure of light-harvesting complex II of green plants: temperature dependent absorption and high-resolution fluorescence spectroscopy, J. Phys. Chem. B, 101, 4448–4457, 1997

138. M. Ratsep, J. Pieper, K.-D. Irrgang, A. Freiberg, Excitation Wavelength-Dependent Electron-Phonon and Electron-Vibrational Coupling in the CP29 Antenna Complex of Green Plants, J. Phys. Chem. B, 112, 110–118, 2008

139. J. M. Hayes, M. Ruehlaender, C. M. Soukoulis, G. J. Small, Monte carlo simulations of energy transfer rates: application to downward energy transfer within the 825 nm absorption band of the FMO complex of *Prosthecochloris aestuarii,* J Lumin, 98, 246–255, 2002

140. W.W. Parson, Modern Optical Spectroscopy: With Exercises and Examples from Biophysics and Biochemistry, Springer, ISBN-10: 3540958959, 2009

141. H-M. Wu, M. Ratsep, I-J. Lee, R. J. Cogdell, G. J. Small, Exciton Level Structure and Energy Disorder of the B850 Ring of the LH2 Antenna Complex, J. Phys. Chem. B, 101, 7654-7663, 1997

142. N. C. Dang, V. Zazubovich, M. Reppert, B. Neupane, R. Picorel, M. Seibert, R. Jankowiak, The CP43 Proximal Antenna Complex of Higher Plant Photosystem II Revisited: Modeling and Hole Burning Study. I, J. Phys. Chem. B, 112, 9921–9933, 2008

143. M. Alfonso, G. Montoya, R. Cases, R. Rodriguez, R. Picorel, Core Antenna Complexes, CP43 and CP47, of Higher Plant Photosystem II. Spectral Properties, Pigment Stoichiometry, and Amino Acid Composition, Biochemistry, 33, 10494–10500, 1994

144. B. Zelent, N. V. Nucci, J. M. Vanderkooi, Liquid and Ice Water and Glycerol/Water Glasses Compared by Infrared Spectroscopy from 295 to 12 K, J. Phys. Chem. A, 108, 11141-11150, 2004

145. K. Murata, H. Tanaka, Liquid–liquid transition without macroscopic phase separation in a water–glycerol mixture, Nature Materials, 11, 436-443, 2012

146. A. Inaba, O. Andersson, Multiple glass transitions and two step crystallization for the binary system of water and glycerol Thermochimica Acta, 461, 44-49, 2007

147. G. Zhaoa, X. Guo, L. He, Z. Liu, D. Gao, Comparative study of glass transformation of glycerol–H_2O–NaCl ternary system and glycerol–PBS complex system, Thermochimica Acta, 419, 131-140, 2004

148. A. Angell Supercooled liquids: Clearing the water, Nature Materials, 11, 362- 364, 2012

149. Matisse User's Guide, Sirah Laser- und Plasmatechnik GmbH, Version 1.6

150. M.-L. Groot, R. N. Frese, F. L. de Weerd, K. Bromek, Å. Petersson, E. J. G. Peterman, I. H. M. van Stokkum, R. van Grondelle, J. P. Dekker, Spectroscopic properties of the CP43 core antenna protein of photosystem II, Biophys. J, 77, 3328–3340, 1999

151. J. L. Hughes, R. Picorel, M. Seibert, E. Krausz, Photophysical behavior and assignment of the low-energy chlorophyll states in the CP43 proximal antenna protein of higher plant Photosystem II, Biochemistry, 45, 12345–12357, 2006

152. M.Reppert, V. Zazubovich, N.C. Dang, M. Seibert, R. Jankowiak, Low-energy chlorophyll states in the CP43 antenna protein complex: simulation of various optical spectra. II, J. Phys. Chem. B, 112, 9934–9947, 2008

153. J. Wen, J. Harada,K. Buyle, K. Yuan, H. Tamiaki, H. Oh-oka, R. A. Loomis, R. E. Blankenship, Characterization of an FMO Variant of Chlorobaculum tepidum Carrying Bacteriochlorophyll a Esterified by Geranylgeraniol, Biochemistry, 49, 5455–5463, 2010

154. A. Freiberg, S. Lin, K. Timpmann, R. E. Blankenship, Exciton Dynamics in FMO Bacteriochlorophyll Protein at Low Temperatures, J. Phys. Chem. B, 101, 37, 7211–7220, 1997

155. M. Rätsep, A. Freiberg, Electron-phonon and vibronic couplings in the FMO bacteriochlorophyll a antenna complex studied by difference fluorescence line narrowing, J. Lumin, 127, 251-259, 2007

156. M. Reppert Modeling of Resonant Hole-Burning Spectra in Excitonically Coupled Systems: The Effects of Energy-Transfer Broadening, J. Phys. Chem. Lett, 2, 21, 2716–2721**,** 2011

157. M. Cho, H. M. Vaswani, T. Brixner, J. Stenger, G. R. Fleming, Exciton Analysis in 2D Electronic Spectroscopy, J. Phys. Chem. B, 109, 10542-10556, 2005

158. S.Vulto, M. De Baat, R. Louwe, H. Permentier, T. Neef, M. Miller, H. van Amerongen, T. Aartsma, Exciton Simulations of Optical Spectra of the FMO Complex from the Green Sulfur Bacterium *Chlorobium tepidum* at 6 K, J. Phys. Chem. B, 102, 9577–9582, 1998

159. S. I. E, Vulto, M. A.de Baat, S. Neerken, F. R.Nowak, H. van Amerongen, J. Amesz, T. J. Aartsma, Excited State Dynamics in FMO Antenna Complexes from Photosynthetic Green Sulfur Bacteria: A Kinetic Model, J. Phys. Chem. B, 103, 8153-8161, 1999

160. T. Reinot, N. C Dang, G. J. Small, A model for persistent hole burned spectra and hole growth kinetics that includes photoproduct absorption: Application to free base phthalocyanine in hyperquenched glassy ortho-dichlorobenzene at 5 K, J. Chem. Phys, 119, 10404–10414, 2003

161. M., Rätsep, R., Blankenship, G. J., Small, Energy transfer and spectral dynamics of the three lowest energy Qy-states of the Fenna-Matthews-Olson antenna complex, J. Phys. Chem. B, 103, 5736–5741, 1999

162. M. T. W, Milder, B, Brüggemann, R, van Grondelle, J. L, Herek, Revisiting the optical properties of the FMO protein, Photosynth. Res, 104, 257-274, 2010

163. D. Gulen, Interpretation of the excited-state structure of the Fenna–Matthews–Olson pigment protein complex of *Prosthecochloris aestuarii* based on the simultaneous simulation of the 4K absorption, linear dichroism, and singlet–triplet absorption difference spectra: a possible excitonic explanation? J Phys Chem, 100, 17683–17689, 1996

164. M. Reppert.,V. Naibo, R. Jankowiak, Accurate modeling of fluorescence line narrowing difference spectra: Direct measurement of the single-site fluorescence spectrum, J. Chem. Phys, 133, 1, 014506 (1-9), 2010

165. O. Nanba, K. Satoh, Isolation of a photosystem II reaction center consisting of D-1 and D-2 polypeptides and cytochrome b-559, Proc. Natl. Acad. Sci. USA, 84, 109-112, 1987

166. A. Zouni, H-T Witt, J. Kern, P. Fromme, N. Krauβ, W. Saenger, P. Orth, Crystal structure of photosystem II from Synechococcus elongatus at 3.8 Å resolution, Nature, 409, 739-743, 2001,

167. J.P. Dekker, R. Van Grondelle, Primary charge separation in Photosystem II, Photosynthesis Research, 63, 195-208, 2000

168. E. Krausz, J. L. Hughes, P. Smith, R. Pace, S. Peterson Årskold, Oxygen-evolving Photosystem II core complexes: a new paradigm based on the spectral identification of the charge-separating state, the primary acceptor and assignment of low-temperature fluorescence, Photochem. Photobiol. Sci, 4, 744–753, 2005

169. Y. Takahashi, O. Hansson, P. Mathis, K. Satoh, Primary radical pair in the Photosystem II reaction centerBiochim. Biophys. Acta, 893, 49–59, 1987

170. R. Y. Pishchalnikov, M. G. Muller, A. R. Holzwarth, In Photosynthesis. Energy from the Sun: 14th International Congress on Photosynthesis; Allen, J. F., Gantt, E., Golbeck, J. H., Osmond, B., Eds.; Springer: New York, 163-166, 2008

171. M.-L. Groot, E. J. G. Peterman, P. J. M. van Kan, I. H. M. van Stokkum, J. P. Dekker, R. van Grondelle, Temperature dependent triplet and fluorescence quantum yields of the

photosystem II reaction center described in a thermodynamic model, Biophys. J, 67, 318–330, 1994

172. J.L. Hughes, B. J. Prince, E. Krausz, P. J. Smith, R. J. Pace, H. Riesen, Highly Efficient Spectral Hole-Burning in Oxygen-Evolving Photosystem II Preparations, J. Phys. Chem. B, 108, 10428-10439, 2004

173. J. Goldbeck, Structure and function of photosystem I, Annu. Rev. Plant Physiol. Plant Mol. Biol, 43, 293-324, 1992

174. W. Saenger, P. Jordan, N. Krauß, The assembly of protein subunits and cofactors in photosystem I, Current Opinion in Structural Biology, 12, 244–254, 2002

175. J. A. Ihalainen, M. Ratsep, P. E. Jensen, H. V. Scheller, R. Croce, R. Bassi, K. Tommola, E. I. Jouko, A. Freiberg, Red Spectral Forms of Chlorophylls in Green Plant PSI- A Site-Selective and High-Pressure Spectroscopy Study, J. Phys. Chem. B, 107, 9086-9093, 2003

176. V. Zazubovich, S.Matsuzaki, T.W. Johnson, , J.M. Hayes, P.R. Chitnis, G.J. Small, Red antenna states of photosystem I from cyanobacterium *Synechococcus elongatus*: a spectral hole burning study, Chemical Physics, 275, 47–59, 2002

177. M. Ratsep, T. W. Johnson, P. R. Chitnis, G. J. Small, The Red-Absorbing Chlorophyll *a* Antenna States of Photosystem I: A Hole-Burning Study of *Synechocystis* sp. PCC 6803 and Its Mutants, J. Phys. Chem. B, 104, 836-847, 2000

178. K. J. Riley, T. Reinot, R. Jankowiak, P. Fromme, V. Zazubovich, Red Antenna States of Photosystem I from Cyanobacteria *Synechocystis* PCC 6803 and *Thermosynechococcus elongatus*: Single-Complex Spectroscopy and Spectral Hole-Burning Study, J. Phys. Chem. B, 111, 286-292, 2007

179. K. Gibasiewicz, A. Szrajner, J. A. Ihalainen, M. Germano, J. P. Dekker, R. van Grondelle, Characterization of Low-Energy Chlorophylls in the PSI-LHCI Supercomplex from *Chlamydomonas reinhardtii*. A Site-Selective Fluorescence Study, *J. Phys. Chem. B*, *109,* 21180-21186, 2005

180. M. K. Sener, D. Lu, T. Ritz, S. Park, P. Fromme, K. Schulten, Robustness and Optimality of Light Harvesting in Cyanobacterial Photosystem I, J. Phys. Chem. B, 106, 32, 7948-7960, 2002

181. E. Schlodder, M. Hussels, M. Çetin, N. V. Karapetyan, , M. Brecht, Fluorescence of the various red antenna states in photosystem I complexes from cyanobacteria is affected differently by the redox state of P700, Biochimica et Biophysica Acta, 1807, 1423–1431, 2011

182. L-O Pålsson, C. Flemming, B. Gobets, R. van Grondelle, J.P. Dekker, E. Schlodder, Energy Transfer and Charge Separation in Photosystem I: P700 Oxidation Upon Selective Excitation of the Long-Wavelength Antenna Chlorophylls of *Synechococcus elongates*, Biophysical Journal, 74, 2611–2622, 1998

183. J.M. Hayes, S. Matsuzaki, M. Ratsep, G.J. Small, Red Chlorophyll a Antenna States of Photosystem I of the Cyanobacteriunm Synechocystis sp. PCC 6803, J. Phys. Chem. 104, 5625-5633, 2000

184. M. Brecht, V. Radics, J. B. Nieder, R. Bittl, Protein dynamics-induced variation of excitation energy transfer pathways, PNAS, 106, 29, 11857–11861, 2009

185. M. Brecht, H. Studier, A.F. Elli, F. Jelezko, R. Bittl, Assignment of Red Antenna States in Photosystem I from *Thermosynechoccocus elongatus* by Single-Molecule Spectroscopy, Biochem, 46, 799-806, 2007

186. M. Brecht, H. Studier, V. Radics, J. B. Nieder, R. Bittl, Spectral Diffusion Induced by Proton Dynamics in Pigment-Protein Complexes, J. Am. Chem. Soc, 103, 17487-17493, 2008

187. M. Brecht, V. Radics, J. B. Nieder, H. Studier, R. Bittl, Red Antenna States of Photosystem I from *Synechocystis* PCC6803, Biochem, 47, 5536-5543, 2008

188. M. Brecht, Spectroscopic Characterization of Photosystem I at the Single-Molecule Level, Molecular Physics: An Intenational Jurnal at the Interface between Chemistry and Physics, 107, 18, 1955-1974, 2009

189. X. Feng, B. Neupane, K. Acharya, V. Zazubovich, R. Picorel, M. Seibert, R. Jankowiak, Spectroscopic Study of the CP43' Complex and the PSI-CP43' Supercomplex of the Cyanobacterium Synechocystis PCC 6803, J. Phys. Chem. B 115, 13339–13349, 2011.